DOE/ER-0313/29
Distribution
Categories
UC-423, -424

FUSION MATERIALS
SEMIANNUAL PROGRESS REPORT
FOR THE PERIOD ENDING
December 31, 2000

Prepared for
DOE Office of Fusion Energy Sciences
(AT 60 20 00 0)

DATE PUBLISHED: APRIL 2001

Prepared for
OAK RIDGE NATIONAL LABORATORY
Oak Ridge, Tennessee 37831
Managed by
U.T.-Battelle, LLC
for the
U.S. DEPARTMENT OF ENERGY
under Contract DE-AC05-00OR22725

FOREWORD

This is the twenty-ninth in a series of semiannual technical progress reports on fusion materials science activities supported by the Fusion Energy Sciences Program of the U.S. Department of Energy. This report focuses on research addressing the effects on materials properties and performance from exposure to the neutronic, thermal, and chemical environments anticipated in the chambers of fusion experiments and energy systems. This research is a major element of the national effort to establish the materials knowledge base for an economically and environmentally attractive fusion energy source. Research activities on issues related to the interaction of materials with plasmas are reported separately.

The results reported are the product of a national effort involving a number of national laboratories and universities. A large fraction of this work, particularly in relation to fission reactor irradiations, is carried out collaboratively with partners in Japan, Russia, and the European Union. The purpose of this series of reports is to provide a working technical record for the use of program participants, and to provide a means of communicating the efforts of fusion materials scientists to the broader fusion community, both nationally and worldwide.

This report has been compiled and edited under the guidance of A. F. Rowcliffe by Gabrielle Burn, Oak Ridge National Laboratory. Their efforts, and the efforts of the many persons who made technical contributions, are gratefully acknowledged.

S. E. Berk
Facilities and Enabling Technologies Division
Office of Fusion Energy Sciences

CONTENTS

1.0 VANADIUM ALLOYS 1

1.1 STUDY OF THE LONG-TERM STABILITY OF MHD COATINGS FOR FUSION REACTOR APPLICATIONS – B. A. Pint, L. D. Chitwood, J. H. DaVan, and J. R. DiStefano (Oak Ridge National Laboratory 3

Bulk specimens of two candidate compositions, CaO and AlN, for insulating coatings in a lithium-cooled fusion reactor have been exposed to lithium in 1000h isothermal tests at 500°-800°C to determine the maximum temperature at which acceptable compatibility is likely. Specimens of AlN+0.04Y showed significant mass loss at 700° and 800°C but much less attack at 600°C. For\ testing at 600°C, changing from a V alloy capsule liner to a Mo liner or adding 1000 ppm N to the Li caused only minor differences in the mass change. Polished cross-sections indicated that a reaction layer had formed in each case. Single crystals of CaO showed massive losses at 600° and 700°C similar to results with polycrystalline specimens. With the addition of 1000 ppm O to the Li, there was a change in the amount of CaO dissolved during the 1000h exposure suggesting that doping Li may be an avenue for improved compatibility. All of these results are consistent with an analysis of the relevant thermodynamic solubility data.

1.2 DEVELOPMENT AND CHARACTERIZATION OF ELECTRICALLY INSULATING CaO COATINGS — K. Natesan, M. Uz, D. L. Rink, and D. L. Smith (Argonne National Laboratory) 9

As part of the Department of Energy's Fusion Reactor Program, studies have been in progress at Argonne National Laboratory (ANL) to develop electrically insulating coatings on V-Cr-Ti alloys, in particular, on V- 4Cr-4Ti which is the primary candidate for use in various structural applications, including in the first wall structure/blanket of a fusion reactor. The first wall will be in contact with liquid Li coolant and electrical conductivity across the wall will lead to magnetohydrodynamic, pressure losses during flow in the magnetic field. Hence, among the critical requirements of the rather stringent design criteria for the first wall material are that the coating on it be non-porous, tenacious, electrically insulating, and capable of maintaining its structural integrity while in use in a liquid Li environment at temperatures of 400-700°C. More information on the material requirements of fusion reactors is reported in an earlier publication. This report addresses the development and characterization of a CaO coating that was applied on V-4Cr-4Ti alloy by a vapor transport (or thermal/chemical vapor deposition) process. Several coupon and rod specimens were coated with CaO by a double Ca-deposition/oxidation process that was developed at ANL. The specimens were analyzed and the coating was characterized after each step of the process as well as before and after exposure to a liquid Li environment. The analysis and characterization involved the use of one or more of scanning electron microscopy (SEM), energy dispersive X-ray analysis (EDX), and X-ray diffraction (XRD) techniques. Results are presented, with emphasis on microstructural analysis of the samples and on the details of the developed experimental procedure.

1.3 STRUCTURAL ANALYSIS OF PLATE-SHAPED PRECIPITATES IN NEUTRON IRRADIATED V-4Cr-4Ti — D. T.Hoelzer and S. J Zinkle (Oak Ridge National Laboratory) 19

Neutron irradiation of V-4Cr-4Ti t ~510 °C and dose of ~4 dpa resulted in the formation of relatively high number density of plate shaped precipitates on {100}bcc habit planes.The TEM analysis showed that their average size was ~24 nm (+/-12 nm)in diameter and ~1-3 nm in thickness.Diffuse streaking from the precipitates was observed to lie parallel to <100>bcc directions and centered at 3 /4 <200>positions in electron diffraction patterns.Based on an orientation relationship observed between the precipitates and bcc matrix and a tilting experiment on one plate variant,the structural analysis indicated that the crystal structure of the plates was consistent with the fcc structure,which is the same for the golobular-shaped Ti-(OCN)phase. The analysis also showed that diffuse scattering observed at 2/3 <222>positions in electron diffraction patterns is not caused by the plate shaped phase.

1.4 HELIUM ANALYSIS FROM THE DHCE-1 SIMULATION EXPERIMENT — D. L. Smith (Argonne National Laboratory) 26

A detailed calculation of the predicted helium generation rates in unalloyed vanadium and the reference V-4Cr-4Ti alloy irradiated in the DHCE-1 Proof-of-Principle experiment has been performed with the available data base on fundamental properties. Results of these detailed calculations indicate that the experimentally measured helium concentrations are in good agreement with the calculated values. Approximately 90% of the measured values are within a factor of 0.5 to 1.5 of the calculated values, which is quite good agreement. The validity of the experiment is further verified by a comparison of the experimental results from the other alloys included in the experiment with calculated correlation factors for each of the seven capsules. This paper presents a summary of the comparison of the results from the detailed calculations with experimental helium concentrations in the vanadium alloys in the DHCE-1 proof-of-principle experiment.

1.5 QUANTITATIVE OXYGEN ANALYSES FOR V-4Cr-4Ti ALLOYS — Y. Yan, D. P. McGann, D. L. Smith, and H. Tsai (Argonne National Laboratory) 34

A quantitative oxygen analysis has been performed for V-4Cr-4Ti alloys. The oxygen concentration is about 210 wppm for Japan's NIFS-1 heat, 324 wppm for ANL's 832665 heat, and 385 wppm for the GA's 832864 heat. Our experiment indicates that, after cutting, the oxygen analysis specimen should be pickled to remove the surface oxide.

1.6 UNIAXIAL CREEP BEHAVIOR OF V-4Cr-4Ti ALLOY — K. Natesan, W. K. Soppet, and D. L. Rink (Argonne National Laboratory) 37

A systematic study is currently being conducted at Argonne National Laboratory (ANL) to evaluate the uniaxial creep behavior of V-Cr-Ti alloys as a function of temperature in the range of 650-800°C and at applied stress levels in the range of 75-380 MPa. At present, the principal effort has focused on the V-4Cr-4Ti alloy of Heat 832665; however, another heat of a similar alloy from General Atomics (GA) will also be used in the study. During this reporting period, additional creep tests were conducted at 700 and 800°C at lower stress levels than in earlier tests. In addition, the tested specimens are examined for O contamination, if any, by vacuum fusion analysis of the tested specimens and by micro hardness measurements of specimen cross-sections. The test results indicate that in the temperature range of 650-800°C, creep deformation follows a power-law creep with stress exponents indicative of a dislocation-climb-controlled process.

1.7 CHARACTERIZATION AND IMPACT PROPERTIES OF V-4Cr-4Ti LASER WELDMENTS* — Y. Yan, D. L. Smith, Z. Xu, and H. Tsai, (Argonne National Laboratory) and T. Nagasaka and T. Muroga (National Institute of Fusion Science, Japan) 41

The effects of alloy chemistry and microstructure on the Charpy-impact properties of laser weldments of three heats of V-4Cr-4Ti alloy were investigated. The impact properties of all three heats indicate similar behavior with a DBTT of approximately –200°C based on one-third size Charpy specimens in the annealed condition. However, The Charpy impact properties of the weldments, which have a significantly differentmicrostructure, indicate significantly different DBTT's for the three heats. Laser welds or bead-on-plate microstructures obtained with the laser beam provide a unique method for investigating the effects of microsturctural and trace element concentrations on the properties of these alloys. Chemical analyses for several trace elements have been performed on the three heats in an attempt to determine which elements affect the mechanical properties. Further research is in progress to investigate the sensitivity of the V-4Cr-4Ti alloy system to minor variations in trace element concentrations and microstructural variations produced by varying the heat treatment.

1.8 MICROSTRUCTURAL EXAMINATION OF IRRADIATED V-4CR-4TI PRESSURIZED CREEP TUBES — D. S. Gelles (Pacific Northwest National Laboratory) 45

Three pressurized tubes of V-4Cr-4Ti have been examined to determine microstructural development due to irradiation creep following irradiation in ATR at 300°C.

1.9 IMPACT PROPERTIES OF V-4Cr-4Ti LASER WELDMENTS FROM THE GA'S HEAT — Y. Yan, H. Tsai, A. D. Storey, D.L. Smith, and Z. Xu (Argonne National Laboratory) 50

Charpy-impact properties of laser weldments of GA heat 832864 V-4Cr-4Ti alloy were investigated. Impact testing was performed with annealed specimens of the both base metal and the laser weldment in as-machined (by electric discharge machining with water as the flushing fluid) condition. The ductile-to-brittle-transition temperature (DBTT) for the base metal is below –187°C and for the laser weld is about 0°C. Additional microstructure characterization on the laser weld is underway.

1.10 SUMMARY REPORT ON THE US/JAPAN JUPITER COLLABORATION INTEGRATED FOCUS ON FUNDAMENTAL STUDIES – VANADIUM INITIATIVE – H.L. Heinisch (Pacific Northwest National Laboratory •) and N. Sekimura (University of Tokyo) 55

IFFS-VI was initiated by the participants in the JUPITER Workshop on Theory and Modeling for Fusion Materials held October 30, 1997, during ICFRM-8 in Sendai, Japan. The original initiative is described, participants and collaborations are identified, and progress is summarized.

2.0 SILICON CARBIDE COOMPOSITE MATERIALS 62

2.1 EFFECT OF HEAT TREATMENT ON SILICON CARBIDE BASED JOINING MATERIALS FOR FUSION ENERGY — C. A. Lewinsohn and R. H. Jones (Pacific Northwest National Laboratory)• , T. Nozawa, M. Kotani, H. Kishimoto, Y. Katoh and A. Kohyama (Kyoto University, Japan). 63

Two general approaches to obtaining silicon carbide-based joint materials were used. The first method relies on reactions between silicon and carbon to form silicon carbide, or to bond silicon carbide powders together. The second method consists of pyrolysing a polycarbosilane polymer to yield an amorphous, covalently bonded material. In order to assess the long-term durability of the joint materials, various heat treatments were performed and the effects on the mechanical properties of the joints were measured. Although the joints derived from the polycarbosilane polymer were not the strongest, the value of strength measured was not affected by heat treatment. On the other hand, the value of the strength of the reaction-based joints was affected by heat treatment, indicating the presence of residual stresses or unreacted material subsequent to processing. Further investigation of reaction-based joining should consist of detailed microscopic studies; however, continued study of joints derived from polymers is also warranted.

2.2 MECHANICAL PROPERTIES OF HELIUM IMPLANTED SILICON CARBIDE- L L Snead (Oak Ridge National Laboratory), R. Scholz (JRC Ispra), A. Frias Rebelo (Whereabouts Unknown) 69

It has been long apparent that ceramics will undergo significant gas production, transmutation and material "burn-up" under high energy neutron irradiation. For example, the original calculations for pure SiC exposed to 1 MW-a/m^2 of 14.1 MeV monoenergetic neutrons yielded 1596 appm helium, 440 appm hydrogen, 458 appm magnesium, 234 appm beryllium and 72 appm aluminum, as well as some less significant transmutants. Clearly, helium is the largest product and, because of its limited diffusivity in SiC, may cause significant swelling and/or stress in the material. This paper will give preliminary results of the effect of high levels of helium on the mechanical properties of CVD SiC.

2.3 TENSILE TESTING OF UNIDIRECTIONAL SILICON CARBIDE COMPOSITES FOR FUTURE IRRADIATION EXPERMENTS— 74

T. Hinoki,[1] L.L. Snead,[2] E. Lara-Curzio,[2] Y. Katoh,1 and A. Kohyama[1] 1
(1) Institute of Advanced Energy, Kyoto University; (2) Oak Ridge National Laboratory

The SiC/SiC composites, which have three kinds of unidirectional stoichiometric SiC fibers and various fiber coating, were prepared by I-CVI method for future irradiation experiments. In-plane tensile bars and transthickness tensile specimens were cut from these materials. In-plane tensile tests, transthickness tensile tests and four point bend tests were carried out at ambient temperature. While the specimens, SCS-9A™ fibers were used, showed superior ultimate tensile stress, more than 1 GPa, to the other specimens, proportional limit stress of the specimens, Hi-Nicalon™ type-S fibers were used, was larger than the other specimens. The specimens, Tyranno™ SA fibers were used or multiple SiC fiber coating was applied, showed brittle fracture behavior. Correlation between tensile results and flexural results was discussed. Transthickness tensile tests were unsuccessful because of insufficient bond between fixture and epoxy.

3.0 FERRITIC MARTENSITIC STEELS 85

3.1 SUMMARY OF IEA WORKSHOP/WORKING GROUP MEETING ON FERRITIC/MARTENSITIC STEELS FOR FUSION — R. L. Klueh 86

(Oak Ridge National Laboratory)

The International Energy Agency (IEA) Working Group on Ferritic/Martensitic Steels for Fusion held a workshop in Tokyo, Japan, 2-3 November 2000. Participants came from Europe, Russia, the United States, and Japan to review the progress of the collaboration on reduced-activation ferritic/martensitic steels and the development of plans for future collaboration. At this workshop, data that have been obtained during the collaboration were reviewed, and it was generally agreed that the testing phase for the IEA heats of steel obtained for this collaboration is near completion. A database has been established on the completed work, and that database is available to the international community. Based partially on the work performed in this collaboration, the European Union has developed specifications for a new reduced-activation steel, EUROFER 97, which has been produced and is now being evaluated. The other material of interest at this workshop was oxide dispersion-strengthened (ODS) steel, which was the subject of presentations from Europe, Japan, and the United States. The consensus is that selective utilization of these steels offers the possibility of a ferritic martensitic steel that will allow higher operating temperatures for a fusion device, although it is recognized that ODS steels are still in the early stage of development.

3.2 RECENT RESULTS FOR THE FERRITICS ISOTOPIC TAILORING (FIST) EXPERIMENT — D. S. Gelles, M. L. Hamilton, B. M. Oliver, and L. R. Greenwood 93

(Pacific Northwest National Laboratory), S. Ohnuki (University of Hokkaido, Japan),
K. Shiba (JAERI Tokai, Japan), Y. Kohno (Muroran Institute of Technology, Japan),
A. Kohyama (Kyoto University, Japan) and J. P. Robertson (Oak Ridge National Laboratory)

The results of shear punch testing, microstructural examination, and hydrogen and helium analyses performed on irradiated isotopically tailored alloys are reported for specimens irradiated in the HFIR JP20 experiment.

3.3 SHEAR PUNCH PROPERTIES OF LOW ACTIVATION FERRITIC STEELS FOLLOWING IRRADIATION IN ORR — R. M. Ermi, M. L. Hamilton and D. S. Gelles (Pacific Northwest National Laboratory) and A. M. Ermi (COGEMA Engineering Corporation, Richland, WA) 103

Shear punch post-irradiation test results are reported for a series of low activation steels containing Mn following irradiation in the Oak Ridge Reactor at 330 and 400°C to ~10 dpa. Alloy compositions included 2Cr, 9Cr and 12Cr steels with V to 1.5% and W to 1.0%. Comparison of results with tensile test results showed good correlations with previously observed trends except where disks were improperly manufactured because they were too thin or because engraving was faulty.

3.4 LONG-TERM HIGH TEMPERATURE OXIDATION BEHAVIOR OF ODS FERRITICS — B. A. Pint (Oak Ridge National Laboratory) 107

Four ODS ferritic compositions were tested for up to 10,000h at 700°-1100°C. At 700°-800°C in air, the reaction rates were very low for all of the alloys. At 900°C, the addition of Y_2O_3, compared to Al_2O_3, showed a distinct benefit in improving the oxidation resistance, due to a reactive element effect. The absence of Ti and W in one alloy appeared to result in a thinner reaction product after oxidation at 800°C. One composition was tested in 10% water vapor at 900°C and at 1000°C and 1100°C in air. Under these higher temperature conditions, there was a significant increase in the rates of oxidation. With only 13-14at%Cr in these alloys, their corrosion-limited operating temperature is less than 1000°C.

4.0 COPPER ALLOYS 114

No contributions.

5.0 BCC REFRACTORY METALS AND ALLOYS 115

5.1 IMPROVEMENTS IN THE DUCTILITY OF MOLYBDENUM WELDMENTS BY ALLOYING ADDITIONS OF Zr, B and C — M. K. Miller*, E. A. Kenik*, K. F. Russell (Oak Ridge National Laboratory) and A. J. Bryhan (Applied Materials, Santa Clara, CA) 116

A significant improvement in the ductility of molybdenum weldments has been achieved through the addition of zirconium, aluminum, carbon, and boron at the parts per million level. A ductility of 20% has been obtained in gas-tungsten arc weldments in 6.35-mm-thick plate. This improvement over molybdenum's traditional 3% ductility has been achieved by improving the normally low fracture stress of grain boundaries. Atom probe tomography has revealed segregation of zirconium, boron and carbon to and the depletion of oxygen at the grain boundaries in the base metal and the heat affected zone.

6.0 AUSTENITIC STAINLESS STEELS 122

6.1 VOID SWELLING AT LOW DISPLACEMENT RATES IN ANNEALED X18H10T STAINLESS STEEL AT 4 to 56 dpa AND 280-332°C 123
F. A. Garner (Pacific Northwest National Laboratory*), S. I. Porollo, A. N. Vorobjev, Yu. V. Konobeev, and A. M. Dvoriashin (Institute of Physics and Power Engineering, Russia)

Various components of pressurized water power reactors (PWRs) and some proposed fusion devices such as ITER will operate at lower temperatures and displacement rates than are encountered in many test reactors such as EBR-II, FFTF and HFIR. The question arises if the presence and magnitude of void swelling can be predicted for such irradiation environments. Data on Russian steel can be used to address part of this question. In reactor applications where Western countries typically use annealed AISI 304 stainless steel, it is the Russian practice to use annealed X18H10T, a titanium-stabilized 18Cr-10Ni stainless steel analogous to AISI 321. Using a flow restrictor component from the low-flux breeder zone of the BN-350 reactor in Kazakhstan, it was possible to examine the behavior of void swelling at relatively low temperatures and low displacement rates after 12 years of irradiation. The temperature of this component ranged from 270-340°C with a peak dose rate of 1.6×10^{-7} dpa/sec and a peak dose of 56 dpa. Careful sectioning of the component has yielded a large number of microscopy specimens over a ITER-relevant range of temperatures and displacement rates. Microstructural data are presented and show that void swelling at 10 to 50 dpa persists down to ~306°C for dose rates on the order of 1×10^{-7} dpa/sec.

7.0 INSULATING CERAMICS AND OPTICAL MATERIALS 135

7.1 MICROSTRUCTURE OF SWIFT HEAVY ION IRRADIATED SiC, Si_3N_4 AND AlN – S. J. Zinkle, J.W. Jones (Oak Ridge National Laboratory) and V.A. Skuratov (Flerov Laboratory, Dubna, RF) 136

Cross-section transmission electron microscopy was used to investigate the microstructure of single crystal silicon carbide and polycrystalline silicon nitride and aluminum nitride following room temperature irradiation with either 245 MeV Kr or 710 MeV Bi ions. The fluences ranged from $1x10^{12}/cm^2$ (single track regime) to $1x10^{13}/cm^2$. Ion track formation was observed in the Bi ion-irradiated Si_3N_4 specimen in regions where the electronic stopping power exceeded a critical value of ~15 keV/nm (depths <24 µm). Ion track formation was not observed at any depth in 245 MeV Kr ion-irradiated Si_3N_4, in which the maximum electronic stopping power was 14.5 keV/nm. There was no evidence for track formation in either SiC or AlN irradiated with 710 MeV Bi ions, which indicates that the threshold electronic stopping power for track formation in these two ceramics is >34 keV/nm. The high resistance of SiC and AlN to track formation may be due to their high thermal conductivity, but further study is needed to quantitatively evaluate the suitability of the various track formation models.

8.0 BREEDING MATERIALS 143

No contriibutions.

9.0 RADIATION EFFECTS, MECHANISTIC STUDIES, AND EXPERIMENTAL METHOD 144

9.1 THE INFLUENCE OF PKA DIRECTION ON DISPLACEMENT CASCADE EVOLUTION — Roger E. Stoller (Oak Ridge National Laboratory) 145

Extended Abstract.

9.2 THE EFFECT OF TEST MACHINE COMPLIANCE ON THE MEASURED SHEAR PUNCH YIELD STRESS AS PREDICTED USING FINITE ELEMENT ANALYSIS — Mychailo B. Toloczko (Pacific Northwest National Laboratory, Katsunori Abe (Tohoku University, Japan), Margaret L.Hamilton, Frank A. Garner, and Richard J.Kurtz (Pacific Northwest National Laboratory) 148

In previous research involving the use of the shear punch test,it was assumed that the displacement of the punch tip was only slightly different than the crosshead displacement. The present work explores this assumption and its ramifications by simulating the shear punch test with finite element analysis (FEA).The simulations suggest that punch tip displacement is much less than previously assumed,and that for the test frames which have been used,crosshead displacement is over an order of magnitude greater than punch tip displacement.This difference in displacements is thought to be due to test machine and punch compliance,and a simple elasticity calculation of the compliance of the punch,the test machine,and a specimen gives a result which is in agreement with the FEA simulations. The effect of using punch tip displacement on the observed effective shear yield stress was evaluated using FEA simulated shear punch tests on several different metals.Yield was measured at several different offset shear strains with a 1.0%offset shear yield strength measurement providing the best correlation with 0.2%offset uniaxial yield strength.When using the 1.0%offset shear yield values,the previously observed material-to-material variability in the tensile-shear correlation all but disappeared.Based on this work,it appears that the material-to-material variations in prior correlations between uniaxial yield strength and shear yield strength is due to a combination of large test machine compliance and material-to-material differences in the work hardening exponent.

9.3 CORRELATION OF NANOINDENTATION AND CONVENTIONAL MECHANICAL PROPERTY MEASUREMENTS — P. M. Rice (IBM Almaden Research Center) and R. E. Stoller (Oak Ridge National Laboratory) 160

Extended Abstract.

9.4 EFFECT OF PERIODIC TEMPERATURE VARIATIONS ON THE MICROSTRUCTURE OF NEUTRON-IRRADIATED METALS- S.J. Zinkle, N. Hashimoto, D.T. Hoelzer, A.L. Qualls (Oak Ridge National Laboratory) and T. Muroga (National Institute for Fusion Science) 162

Specimens of pure copper, a high-purity austenitic stainless steel, and V-4Cr-4Ti were exposed to eight cycles of either constant temperature or periodic temperature variations during neutron irradiation in the High Flux Isotopes Reactor to a cumulative damage level of 4 to 5 displacements per atom. Specimens were exposed to a low temperature during the initial 10% of accrued dose in each of the eight cycles, and were exposed to a higher temperature during the remaining 90% of accrued dose in each cycle. Different specimens were exposed to low/high irradiation temperatures of 225/340˚C and 350/520˚C. The microstructure was compared with that of companion

1.0 VANADIUM ALLOYS

STUDY OF THE LONG-TERM STABILITY OF MHD COATINGS FOR FUSION REACTOR APPLICATIONS† -- B. A. Pint, L.D. Chitwood, J. H. DeVan and J. R. DiStefano (Oak Ridge National Laboratory)

† dedicated to the memory of J. H. DeVan

OBJECTIVE

The objective of this task is to assess the long-term, high-temperature compatibility of high electrical resistance coatings with lithium at high temperatures. Electrically insulating, magnetohydrodynamic (MHD) coatings on the first wall of magnetic confinement reactors are essential to reduce the MHD force that would otherwise inhibit the flow of the lithium coolant. Initial experimental work is being conducted on bulk ceramics to determine basic lithium compatibility and maximum-use temperatures of candidate ceramics such as AlN and CaO.

SUMMARY

Bulk specimens of two candidate compositions, CaO and AlN, for insulating coatings in a lithium-cooled fusion reactor have been exposed to lithium in 1000h isothermal tests at 500°-800°C to determine the maximum temperature at which acceptable compatibility is likely. Specimens of AlN+0.04Y showed significant mass loss at 700° and 800°C but much less attack at 600°C. For testing at 600°C, changing from a V alloy capsule liner to a Mo liner or adding 1000ppm N to the Li caused only minor differences in the mass change. Polished cross-sections indicated that a reaction layer had formed in each case. Single crystals of CaO showed massive losses at 600° and 700°C similar to results with polycrystalline specimens. With the addition of 1000ppm O to the Li, there was a change in the amount of CaO dissolved during the 1000h exposure suggesting that doping Li may be an avenue for improved compatibility. All of these results are consistent with an analysis of the relevant thermodynamic solubility data.

PROGRESS AND STATUS

Experimental Procedure

Current work focused on two compositions of bulk specimens. High purity AlN (0.9wt%O, 0.04wt% Y) from Tokuyama Corp (Shapal SH-50) was made by nitriding Al_2O_3. The AlN specimens measured 2x8x12mm, had an average grain size of 7-8µm and a density of 3.25g/cm^3. Single crystals of CaO were obtained from Commercial Crystal Laboratories (Naples, FL) and measured ≈2x6x12mm. Previous work on these materials had used AlN with 5wt%Y_2O_3 and polycrystalline CaO specimens.[1] Specimen dimensions and mass were measured before and after exposure. The mass gain accuracy was 0.01mg/cm^2.

The experimental procedure for lithium exposures has been outlined previously[2,3]. Bulk ceramic specimens were exposed for 1000h at 500°-800°C. In some tests, additions of Li_3N, Li_2O or Ca were made to increase the impurity levels in the lithium to nominally 1000ppmw of nitrogen, 1000ppmw oxygen or 1wt%Ca, respectively. In order to explore the effect of the vanadium inner capsule on the experiment, a molybdenum capsule that was expected to be more inert to reactions of interstitial impurities in the lithium was used for some experiments. After exposure to Li, specimens were distilled in vacuum at 500-550°C to remove any residual Li from the specimen. Additional characterization was performed on selected specimens. In this phase, cross-sections were made by mounting the AlN specimens in epoxy and then cutting and polishing to examine the reaction product.

Results and Discussion

Mass changes after the 1000h exposures to lithium are shown in Table I. Both materials have similar densities; thus a mass loss of ≈3.2 mg/cm^2 corresponds to a 10µm loss in material thickness. The results for AlN+0.04Y are significantly better than those reported for AlN+5wt%Y_2O_3.[1] However, the mass losses were still significant at 700°C. Because previous work[1] showed the Al content of the Li increased with exposure temperature but not the N content, there was some concern that the V alloy capsule was gettering N during the test. Therefore, testing was also performed with Mo capsules. The results at 700°C showed less mass loss with a Mo capsule but at 600°C there was a small mass loss instead of a gain, as with a V alloy capsule.

In order to increase the initial nitrogen content in the lithium and possibly improve compatibility, 1000ppm N was added to the lithium for several tests. With a V capsule, this resulted in an increased mass gain at 600°C and slightly less mass loss at 700°C, Table I. The specimen tested at 600°C appeared to have a thicker residue on the surface that was not removed by distillation. With a Mo capsule at 600°C, there was an increase in the amount of mass loss with the addition of N.

Table I. Mass changes of bulk ceramic specimens after 1000h exposures to lithium in a vanadium alloy capsule at various temperatures.

Conditions	AlN+0.04Y		poly xtal CaO		single xtal CaO	
	%	mg/cm^2	%	mg/cm^2	%	mg/cm^2
500°C	-0.06	-0.15			specimen broke	
600°C	+0.1	+0.26	-3.6	-10.3	-3.0	-7.0
600°C†	-0.04	-0.10				
600°C+1000ppm N	+0.6	+1.36				
600°C+1000ppm N†	-0.07	-0.17				
600°C+1000ppm O			-3.3	-9.51	-1.6	-3.9
600°C+1wt%Ca					+2.0	+3.9
700°C	-3.37	-8.16			-9.1	-16.7
700°C†	-0.65	-1.56				
700°C+1000ppm N	-3.20	-7.66				
700°C+1000ppm O					-2.3	-7.2
700°C+1wt%Ca					-6.9	-17.6
800°C	-8.6	-26.5	-8.0	-23.3		

† tested in a Mo capsule

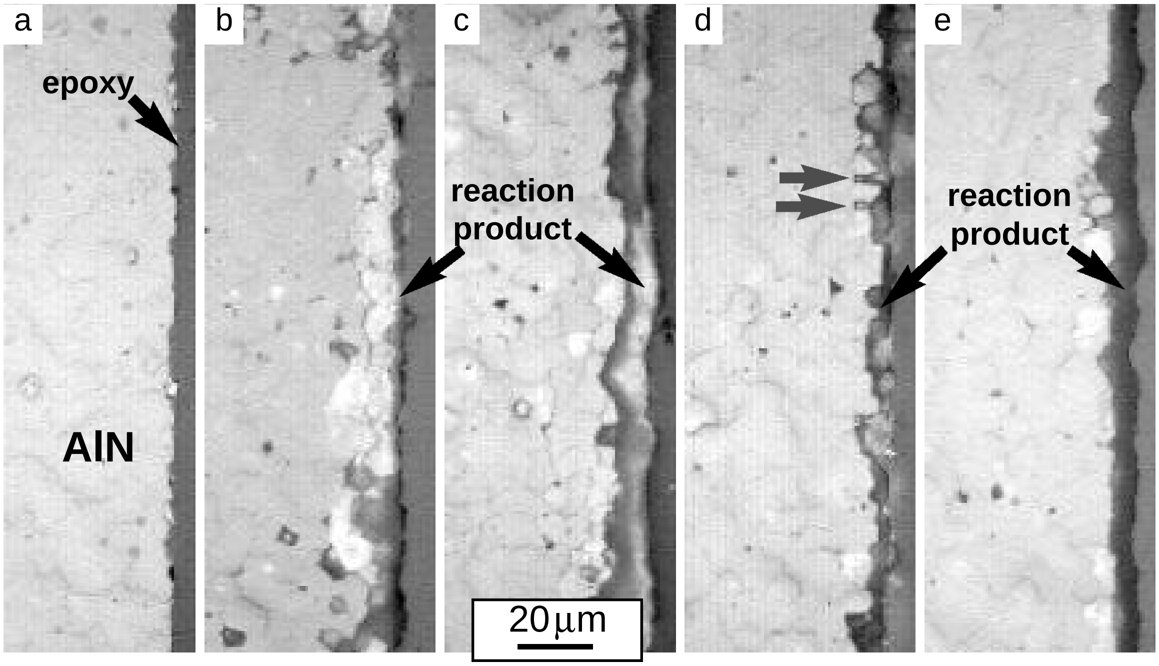

Figure 1. Light microscopy of polished cross-sections of AlN with (a) no exposure, and after 1000h at 600°C in (b) V capsule and undoped Li, (c) V capsule and Li + 1000ppm N, (d) Mo capsule and undoped Li, and (e) Mo capsule and 1000ppm N.

Because of the small mass changes at 600°C, cross-sections of the AlN specimens were made to further examine the reaction product. Figure 1 shows light microscopy images of the polished cross-sections. The cross-sections generally confirm the mass change numbers. For example, the highest mass gain was with a V capsule and a N addition which also showed the thickest reaction product, Figure 1c. The presence of a reaction product when a mass loss was measured (with Mo capsules), Figures 1d and 1e indicated that some AlN dissolved. The roughest interface was observed with a Mo capsule and undoped Li, Figure 1d. There also was some indication of attack along grain boundaries in this case (arrows). Further characterization of these specimens will be performed by Auger electron spectroscopy (AES) or by microprobe. Previous AES sputter depth profiling of the specimen shown in Figure 1b indicated a lithium aluminate layer at the surface.[1,3] Thus, it is necessary to confirm if the layers observed in cross-section also are oxides.

At 600°-800°C, significant mass losses were recorded for both polycrystalline and single crystal CaO, Table I. For either type of specimen, there was no indication of the specimen breaking or chipping and the amount of dissolution increased with test temperature. It is possible that the results for polycrystalline CaO (99.9% purity) reflected grain boundary attack or accelerated attack because the materials was only ≈95% dense. However, the similar results for single crystal CaO suggest that there was significant dissolution of CaO in undoped Li over this temperature range.

In an attempt to slow the rate of dissolution, Ca (1wt%) and O (1000ppmw) were added to the Li. While the addition of O did not change the mass loss for polycrystalline CaO, it did appear to reduce the mass loss for single crystal CaO at 600°C and 700°C, Table I. However, the amount of mass loss after 1000h at 600°C was still the equivalent of more than 10µm of lost material and, at 700°C, the equivalent of more than 20µm was lost.

The addition of Ca to the lithium had a minimal effect on the mass loss at 700°C but resulted in a mass gain at 600°C, Table I. Prior to exposure, the crystals appear greyish and opaque. After distillation, the specimen exposed to Li+1wt%Ca at 600°C was darker and appeared to have a surface layer which may account for the mass gain. Problems with charging in AES and XPS have prevented further characterization of these specimens. Additional experiments with higher O and Ca levels are presently being conducted.

The 400°C-450°C experimental results[4,5] and thermodynamic calculations[6-8] indicate CaO should be a good candidate material. However, rather than compare the reaction energy:

$$CaO + 2Li \leftrightarrow Ca + Li_2O \qquad [1]$$

the more relevant reactions are the dissolution reactions for the ceramics and the lithium until equilibrium is reached in solution:

$$CaO = (\underline{Ca})Li + (\underline{O})Li \quad \text{or} \qquad [2]$$

$$AlN = (\underline{Al})Li + (\underline{N})Li \qquad [3]$$

Thus, for CaO the relevant thermodynamic equations are:

$$k_r = a_{Ca} \cdot a_O \quad \text{and} \quad \Delta G = R \cdot T \cdot \ln k_r \qquad [4,5]$$

The reaction of the ceramic with lithium should occur until equilibrium is achieved in solution. Calculations using ThermoCalc software, Figure 2, provide equilibrium values using three different assumptions: (1) fixed Ca level of 5wt% in the lithium, (2) fixed O level of 500ppm in the lithium

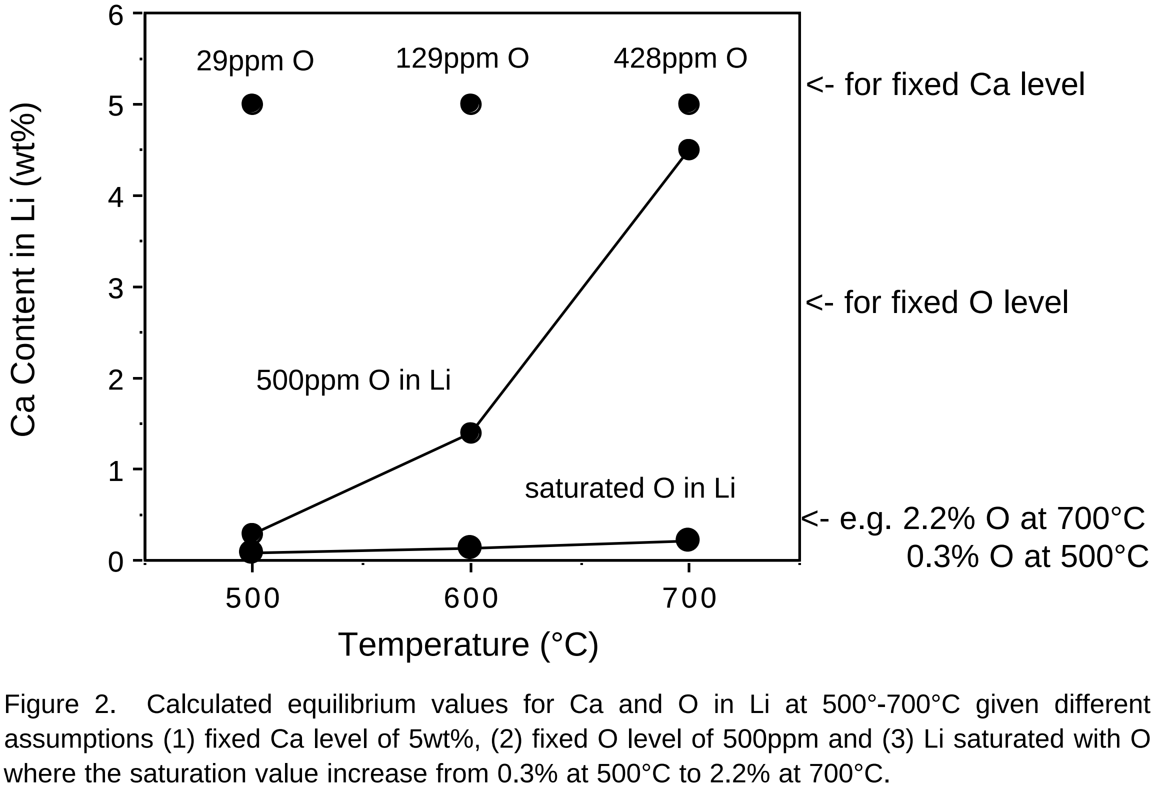

Figure 2. Calculated equilibrium values for Ca and O in Li at 500°-700°C given different assumptions (1) fixed Ca level of 5wt%, (2) fixed O level of 500ppm and (3) Li saturated with O where the saturation value increase from 0.3% at 500°C to 2.2% at 700°C.

and (3) Li saturated with O where the calculated saturation value increases from 0.3% at 500°C to 2.2% at 700°C. With the high levels of Ca and O in solution at equilibrium, these thermodynamic calculations suggest that the high dissolution rates of CaO in undoped Li are clearly possible. The calculations also indicate that corrosion control likely will depend upon maintaining the proper levels of corrosion product in the lithium. While it could be argued that pure lithium should result in lower corrosion rates, these calculations suggest that, rather than purifying the lithium, adding Ca and O to the lithium should lower the rate of corrosion. Of course, this hypothesis needs to be experimentally verified. The other concern with heavily doping the lithium is also revealed in Figure 2. If 5wt%Ca were added to Li in order to slow the dissolution of CaO, then the solubility of O will change radically from the hot leg to the cold leg of the system. This change in solubility would likely result in mass transfer by which dissolution would continue in the hot leg and deposition of Li_2O in the cold leg (due to the lower solubility of O at lower temperatures) could clog the Li flow.

Similar calculations were made for Al and N in lithium over the same temperature range, Figure 3. In this case, assuming 300ppm N in the lithium, the equilibrium values for Al are orders of magnitude lower, <15ppm at 700°C. This may explain why the mass losses at 600°C were significantly lower for AlN compared to CaO, Table I.

This combination of experimental results and thermodynamic analysis suggests a new strategy for selecting possible MHD coating materials. Elements which are highly soluble in Li may be more susceptible to dissolution at high temperature. Thus, one selection criteria could be cations which are insoluble in Li. Of course, looking for insoluble cations does not obviate the thermodynamic requirement suggested by Equation 1. As an example, a single crystal of CeO_2 was exposed in lithium for 1000h at 600°C and lost 20.7% of its mass. While Ce is expected to

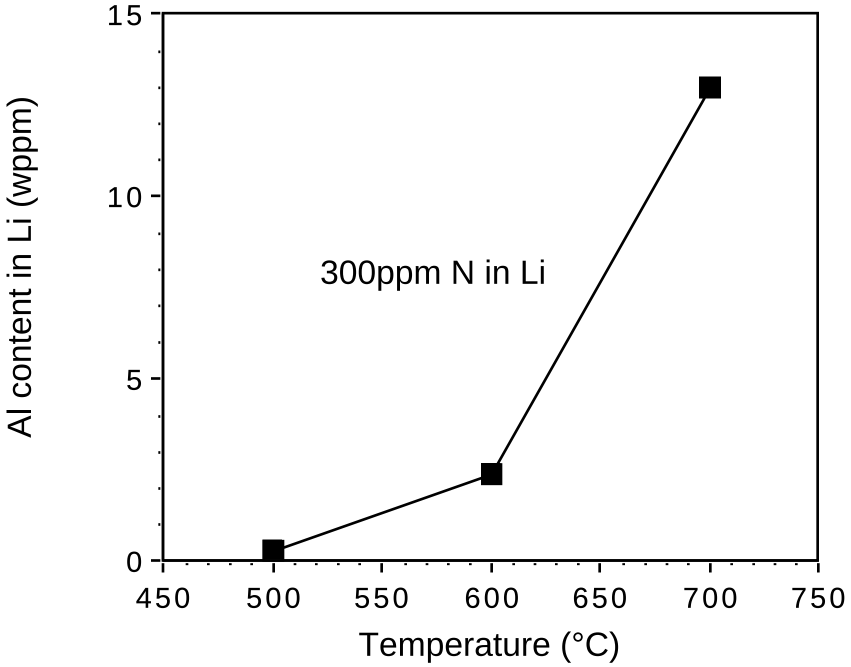

Figure 3. Calculated equilibrium values for Al in Li at 500°-700°C given a fixed N level of 300ppm. Note that the equilibrium Al levels are in wppm compared to up to 5wt% for Ca.

be relatively insoluble in Li, CeO_2 is less stable than Li_2O and thus dissolved during exposure. However, there are other oxides such as Sc_2O_3, Y_2O_3 and Er_2O_3, which have similar stabilities as CaO,[9] but have low solubilities which may make them more attractive candidates. These oxides would not be able to “self-heal” as no supply of cations could be provided in the lithium as is currently envisioned for CaO.[10] However, if the coating has exceptional Li compatibility and adhesion, there would be no need for healing.

REFERENCES

1. B. A. Pint, L.D. Chitwood, J. H. DeVan and J. R. DiStefano, DOE/ER-0313/28 (2000) 26.
2. B. A. Pint, L.D. Chitwood, J. H. DeVan and J. R. DiStefano, DOE/ER-0313/27 (1999) 49.
3. B. A. Pint, L. D. Chitwood and J. R. DiStefano, J. Nucl. Mater. in press (2001).
4. R. J. Lauf and J. H. DeVan, J. Electrochem. Soc. 139 (1992) 2087.
5. J. E. Battles, Intern. Mater. Rev. 34 (1989) 1.
6. I. Schreinlechner and F. Holub, in: Materials Behavior and Physical Chemistry in Liquid Metal Systems, H. U. Borgstedt (Ed.), Plenum Press, N.Y. 1982, p.105.
7. R. N. Singh, J. Amer. Ceram. Soc. 59 (1976) 112.
8. P. Hubberstey and T. Sample, J. Nucl. Mater. 248 (1997) 140.
9. K. Cvetkovic and A. Petric, Amer. Ceram. Soc. Bull. 79-4 (2000) 65.
10. J. H. Park and T. F. Kassner, J. Nucl. Mater. 233-237 (1996) 476.

DEVELOPMENT AND CHARACTERIZATION OF ELECTRICALLY INSULATING CaO COATINGS

K. Natesan, M. Uz, D. L. Rink, and D. L. Smith (Argonne National Laboratory)

OBJECTIVE

The objectives of this task are to (a) develop electrically insulating coatings, with emphasis on understanding the basic thermodynamic conditions and kinetic processes needed to develop stable coatings of CaO that are compatible in an Li/Li-Ca environment; (b) perform detailed postexposure analysis of the surface layers by several electron/optical techniques to characterize the elemental and phase compositions, quantify stratification in the layers, and establish the role of compositional changes in the coating and microstructure; (c) measure the electrical resistance of the coatings, before and after exposure to Li; and (d) establish optimal procedures from the standpoint of sample preparation, exposure time and temperature, and sequence of operations to obtain reliable and reproducible coatings with adequate electrical resistance for use in a Li environment.

SUMMARY

As part of the Department of Energy's Fusion Reactor Program, studies have been in progress at Argonne National Laboratory (ANL) to develop electrically insulating coatings on V-Cr-Ti alloys, in particular, on V-4Cr-4Ti which is the primary candidate for use in various structural applications, including in the first wall structure/blanket of a fusion reactor. The first wall will be in contact with liquid Li coolant and electrical conductivity across the wall will lead to magnetohydrodynamic, pressure losses during flow in the magnetic field. Hence, among the critical requirements of the rather stringent design criteria for the first wall material are that the coating on it be non-porous, tenacious, electrically insulating, and capable of maintaining its structural integrity while in use in a liquid Li environment at temperatures of 400-700°C. More information on the material requirements of fusion reactors is reported in an earlier publication.[1]

This report addresses the development and characterization of a CaO coating that was applied on V-4Cr-4Ti alloy by a vapor transport (or thermal/chemical vapor deposition) process. Several coupon and rod specimens were coated with CaO by a double Ca-deposition/oxidation process that was developed at ANL.[2] The specimens were analyzed and the coating was characterized after each step of the process as well as before and after exposure to a liquid Li environment. The analysis and characterization involved the use of one or more of scanning electron microscopy (SEM), energy dispersive X-ray analysis (EDX), and X-ray diffraction (XRD) techniques. Results are presented, with emphasis on microstructural analysis of the samples and on the details of the developed experimental procedure.

EXPERIMENTAL PROGRAM

The pertinent parts of the experimental setups used for depositing CaO coating on V-4Cr-4Ti alloy specimens by the He-flow and vacuum processes are shown in Figs. 1 and 2, respectively. The materials, system details, and experimental procedures used in this study are described below.

MATERIALS AND SYSTEM DETAILS

The nominal composition of the alloy used in this study was V-4 wt.%Cr-4 wt.%Ti. The samples were either 1-mm-thick coupons or 5-mm-diameter rods. All of the specimens were annealed for 1 h at 1000°C in 10^{-7} torr vacuum before use. The Ca metal was redistilled -6-mesh granules with a purity of 99.5% on the metals basis. Stainless steel wire screen with 1-mm square openings was used to fabricate the ≈20-mm-diameter cylindrical inner specimen chamber. The outer chamber, ≈35-mm in diameter, was a quartz tube for the vacuum process, and a stainless steel tube for the He-flow process. Stainless steel wire and bolts/nuts were used to hold the

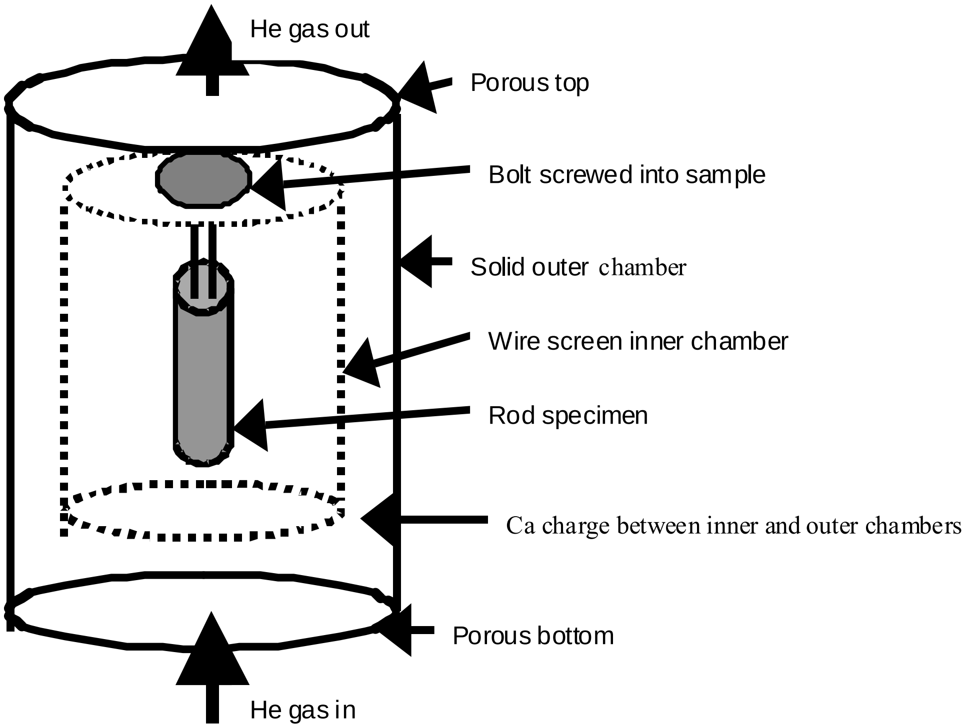

Fig. 1. Schematic illustration of experimental setup used during Ca-deposition steps of double Ca-deposition/oxidation process in He flow. All parts of setup were stainless steel.

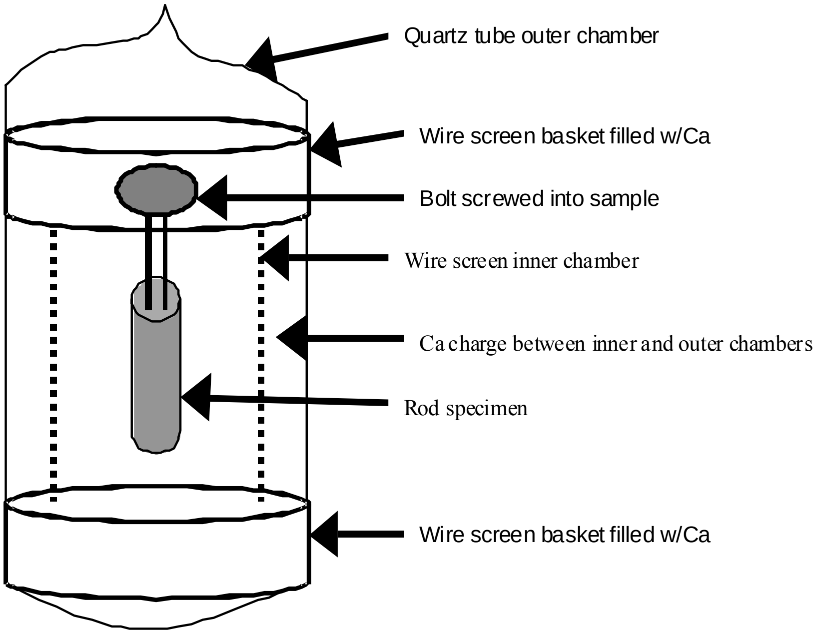

Fig. 2. Schematic illustration of experimental setup used during Ca-deposition steps of double Ca-deposition/oxidation process in vacuum. All parts of setup inside the quartz tube were stainless steel.

coupon samples and threaded rod samples, respectively, during the heating steps. A vertical high-temperature tube furnace, equipped with gas inlets/outlets, was used for Ca deposition by the He-flow process and for the oxidation step. A high-temperature muffle furnace was used to heat the sealed quartz tubes for Ca deposition by the vacuum process. The experimental environment consisted of flowing He or vacuum of 10^{-4} torr during the Ca-deposition steps and flowing Ar during the oxidation steps of the processes. Both He and Ar gases were 99.999% pure.

PROCEDURE

Calcium deposition by vapor transport relied on the relatively high vapor pressure of Ca metal at temperatures >700°C. As can be seen from Fig. 3, the vapor pressure of Ca metal is >0.1 torr at 700°C, and approaches 1 torr at 800°C. Also, Ca metal readily oxidizes in any of the environments used in this study. Evaluation, testing, and analysis of specimens coated by a single Ca deposition/oxidation process showed that CaO produced this way did not exhibit the desired insulating characteristics or stability in liquid Li. Therefore, two processes that involve double Ca deposition/oxidation steps were developed to successfully coat V-4Cr-4Ti alloy samples with stable CaO.

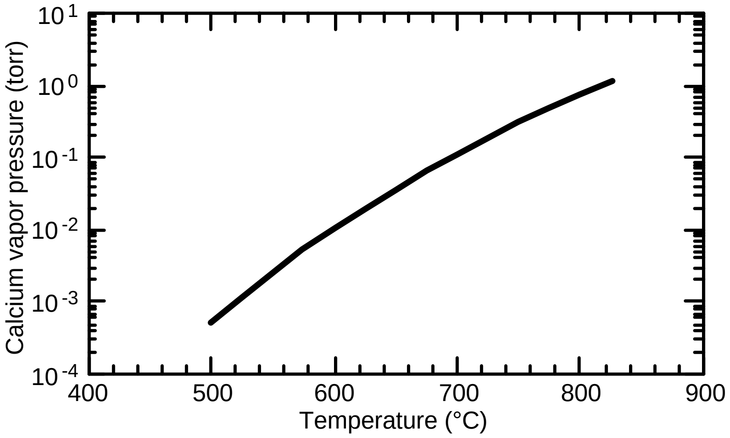

Fig. 3. Plot of Ca vapor pressure versus temperature.

He-flow process: The experimental setup used for Ca deposition in a flowing He environment is schematically illustrated in Fig. 1 with a rod specimen in place. The samples (coupons and/or rods) were hung vertically from the top of the wire screen inner chamber, which was placed inside the steel outer chamber that had a porous bottom and top. Granular Ca charge was placed between the inner and outer chambers. The first deposition of Ca was performed by heating the entire assembly in a flowing He environment at 775-800°C for 100-150 h. Photographs of the inner chamber with the sample in place and parts of the experimental assembly after the Ca-deposition step are shown in Figs. 4a and 4b, respectively. Calcium-deposited specimens were subsequently oxidized in flowing Ar at ≈700°C for 130-200 h in a quartz chamber inserted into a vertical resistance-wound furnace. The sequence of Ca deposition followed by oxidation was repeated to complete the double Ca deposition/oxidation process in He flow to obtain samples that were fully coated with stable CaO.

Vacuum process: A schematic representation of the experimental setup for depositing Ca during the vacuum process in shown in Fig. 2. The setup consists of a wire screen sample chamber that was scaled in a quartz tube with a vacuum of $^{10-}$4 torr. Granular Ca charge was placed around the inner chamber and in a cylindrical wire basket at the bottom, as shown in the figure A. A wire basket filled with Ca granules was also placed above the.

(a) **(b)**

Fig. 4. Photographs of experimental set up after Ca-deposition step of of double Ca-deposition/oxidation in He-flow process. (a) Inner chamber with lid and rod specimen in place. (b) All experimental parts, including granular Ca charge, after use. All parts shown were stainless steel.

inner chamber to serve as a heat sink and to prevent the Ca charge from premature oxidation during the sealing of the quartz tube. The first Ca deposition step in this process involved a heat treatment of 100-150 h at 775-800°C in a muffle furnace. Figures 5a, b and c, respectively, show the inside of the quartz tube, the sample with its assembly, and a close-up of the coated sample following the Ca deposition step in vacuum. Ca-deposited samples were oxidized as described in the He flow process. Development of stable CaO on sample surfaces via double Ca deposition/oxidation in vacuum was again accomplished by repeating the Ca deposition and oxidation steps.

Following each step (Ca1, Ox1, Ca2, Ox2), sample surfaces were examined by SEM to characterize their microstructure. Chemical composition of the surface was determined by EDX and XRD analysis. After exposure to Li at 500, 600, and 700°C, both surfaces and cross-sections of several specimens were analyzed and characterized by the techniques described above

RESULTS AND DISCUSSION

Preliminary work on the development of the He-flow process, and the results from the testing and characterization of several V-4Cr-4Ti coupons coated with CaO were presented in earlier reports.[2-5] It was reported that CaO coatings on V-4Cr-4Ti coupon samples remained intact after exposure to Li for 68 h at 500°C.[1,5] The structural integrity of the CaO coating on each sample before and after exposure to Li was confirmed by examination and characterization of its surface and cross-sectional area by SEM for microstructure and SEM/EDX for elemental analysis of the surface and depth profile of the cross-sectional area. It was also reported that the electrical resistance, measured external to Li, of these coated samples was high and was in excess of the design requirements for a fusion device.

(a) **(b)** **(C)**

Fig. 5. Photographs of experimental setup after Ca-deposition step in double Ca-deposition/oxidation in vacuum. (a) quartz outer chamber. (Dark layer inside is Ca deposit.); (b) inner chamber with portion of quartz tube that contans some used Ca charge, and rod specimen with a bolt/nut assembly that held it in place inside inner chamber; (c) close-up of Ca-coated rod specimen. Except for quartz tube, all parts were stainless steel.

.During the present reporting period, several V-4Cr-4Ti specimens in the form of 1-mm-thick coupons and 5-mm-diameter rods were coated with CaO by the He-flow process, and exposed to Li for ≈100h at 600 and 700°C. Li used for the 600°C exposure contained ≈10 at.% Ca, and Li used for the 700°C exposure was pure, i.e. contained no added Ca. Specimen surfaces and cross sections were analyzed by SEM/EDX after each step of the process and after exposure to Li. The coating on each sample exposed to Li was also identified by XRD; the results are presented in Table 1. SEM photomicrographs of the tip, middle, and top portions of the rod sample after exposure to Li (w/10 at.%Ca) at 600°C are shown in Fig. 6. Cross-sectional area of the coupon sample exposed to Li at 600°C and that for the rod sample exposed to pure Li at 700°C are shown Fig. 7. X-ray diffraction analysis results are presented in Fig. 8 for the surfaces of rod and tab samples exposed for ≈100 h to Li that contained 10 at% Ca. Figure 9 shows XRD patterns obtained from various locations along the length of a 70-mm-long rod specimen after exposure to pure Li for ≈106 h at 700°C, along with those from the rod specimen given in Fig. 8.

The results show that CaO coating on both the rod and coupon specimens was intact after exposure to Li-10 at.% Ca for ≈100-h at 600°C. This was confirmed by SEM/XRD elemental analysis of each sample surface before and after Li exposure (see Table 1), and by XRD analysis after exposure to Li, which indicated the presence of CaV_2O_5 in the coating on these samples (see Fig. 8). Both samples were electrically insulating at room temperature before and after the exposure to Li. The 70-mm-long rod specimen that was exposed to pure Li at 700°C exhibited similar surface coating and electrically insulating characteristics at room temperature before exposure to Li. This sample was exposed to pure Li (i.e., Li with no Ca), for ≈100 h at 700°C. After the exposure, the sample exhibited no measurable electrical conductivity at room temperature. However, elemental

	Process Step[a]	T (°C)	Time (h)	Ca-Range[b] (Area) (at.%)	Ca_{min} (Spot)[b] (at.%)	O_2-Range[b] (Area) (at.%)	V-Range (Area)[b] (at.%)	CaO Thickness[c] (µm)	Phases identified by XRD[d]
4S14 coupon	Ca	737	125	30 - 50	25	30 - 60	1 - 25		
	Ox	700	135	20 - 30	1	15 - 55	25 - 65		
	Ca	735	125	65 - 78	50	22 - 48	0 - 1		
	Ox	700	164	50 - 55	45	40 - 50	0 - 5		
	Li(w/Ca)	600	100	40 - 45	37	50 - 59	0 - 5	13 - 20	CaO, CaV_2O_5
44Rod2 rod	Ca	790	141	30 - 70	1	20 - 50	1 - 72		
	Ox	600	48						
		700	165	10 - 30	3	42 - 50	30 - 51		
	Ca	775	125	60 - 69	50	30 - 36	0 - 2		
	Ox	700	200						
	Li	700	106	1 - 5		20 - 70	10 - 58	2 - 5	CaO, CaV_2O_5, V
44Rod3 rod	Ca	795	130	20 - 80	9	26 - 41	0 - 30		
	Ox	700	174	20 - 50	1	13 - 50	0 - 80		
	Ca	780	125	25 - 60	25	28 - 58	0 - 30		
	Ox	700	200						
	Li(w/Ca)	600	100	30 - 52	30	39 - 60	0 - 18	10 - 15	CaO, CaV_2O_5

Table 1. Experimental conditions and results of coupon and rod samples coated with CaO by the process of double Ca-deposition/oxidation in He-flow

[a] Steps in development of CaO coating by double Ca-deposition/oxidation process and subsequent exposure to Li; Ca and Ox indicate Ca-deposition and oxidation steps, respectively; Li (w/Ca) and Li indicate exposure of specimens to Li-10 at.% Ca and to pure Li, respectively.

[b] Obtained from EDX analysis of areas or spots on specimen surfaces.

[c] Obtained from measurement of scale thickness in SEM photomicrographs of specimen cross sections.

[d] Determined from the patterns obtained from XRD analysis of sample surfaces.

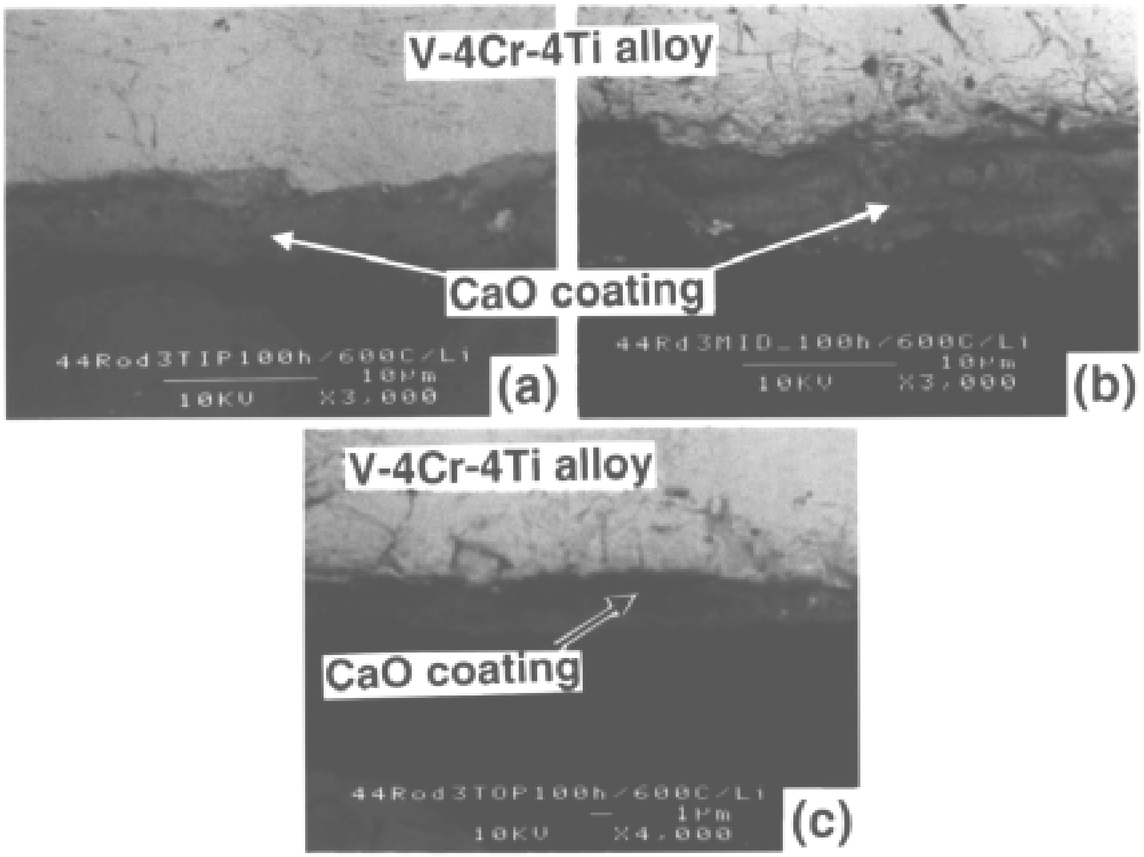

Fig. 6. SEM photomicrographs showing cross sections of (a) tip, (b) middle, and (c) top portions of 70-mm-long V-4Cr-4Ti rod specimen after exposure to Li-10 at.% Ca at 600^{o}C for ≈100 h. Specimen was coated with CaO by process of double Ca-deposition/oxidation in He flow.

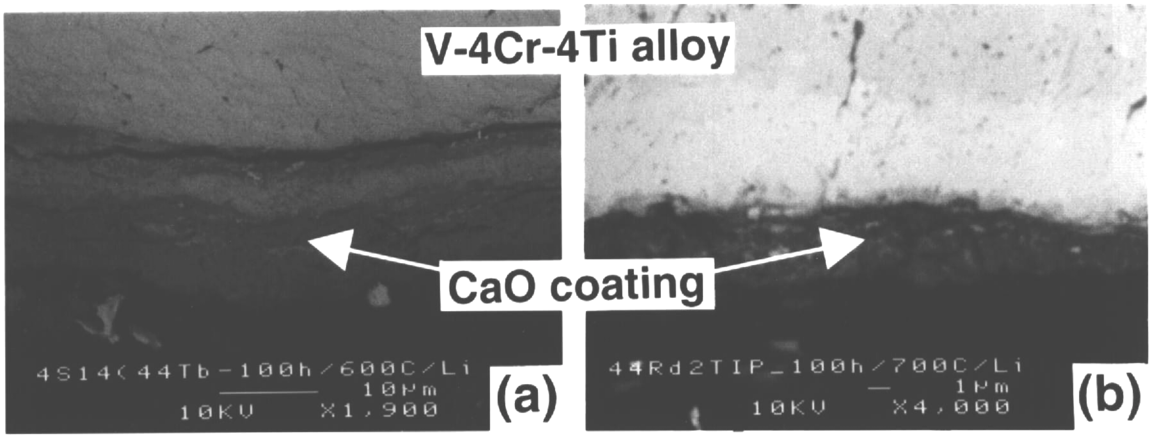

Fig. 7. SEM photomicrographs showing cross-sectional areas of V-4Cr-4Ti alloy specimens after exposure to liquid Li. (a) tab specimen exposed to Li-10 at.% Ca at 600°C for ≈100 h; (b) rod specimen exposed to pure Li at 700°C for ≈106 h. Both specimens were coated with CaO by double Ca-deposition/oxidation in He-flow process.

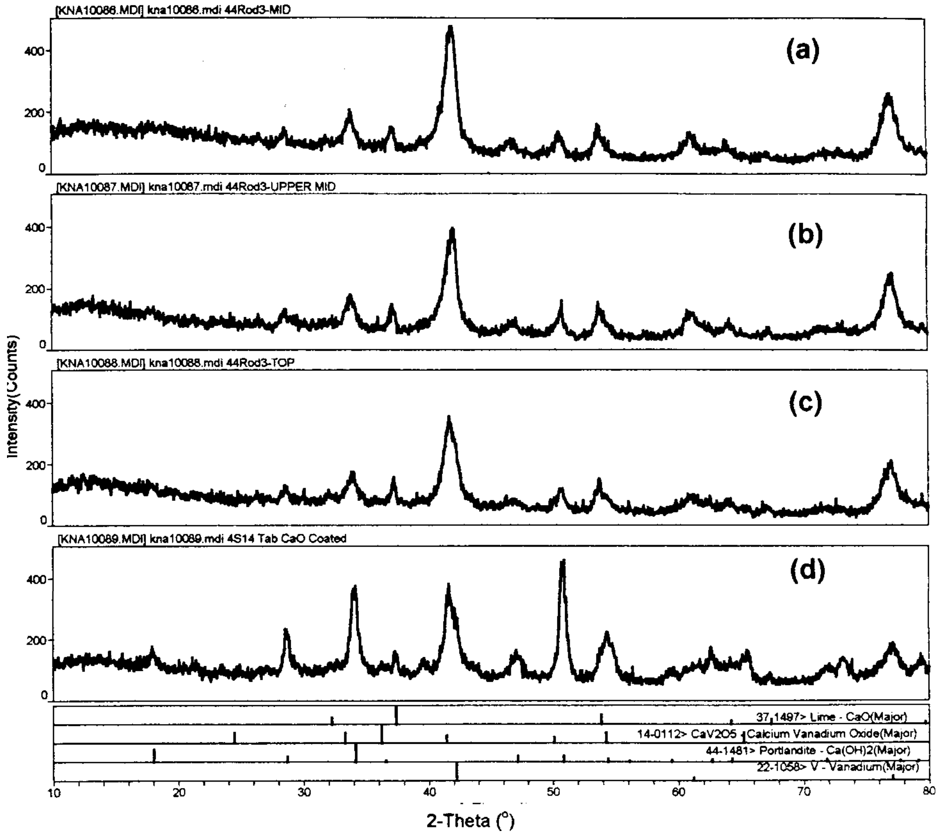

Fig. 8. X-ray diffraction patterns for surfaces of V-4Cr-4Ti samples after ≈100 h exposure to Li at 600°C. (a) Middle of rod, (b) upper-middle of rod, (c) top of rod, and (d) coupon.

analysis by SEM/XRD showed very little Ca on its surface (see Table 1), and the thickness of the coating was appreciably thinner than that of the others (see Figs. 6 and 7). X-ray diffraction analysis of the surface indicates the presence of various phases, including CaO, CaV_2O_5, and V. These results indicate that Ca dissolved in Li may be an important consideration for the stability of electrically insulating CaO coating in liquid Li.

The goal of another series of studies initiated during the current reporting period is to develop the vacuum process described earlier in an effort to obtain a thicker coating by volatilizing a larger amount of Ca in vacuum. Also being investigated is the effect that O-precharging of the specimens exerts on the coating thickness, integrity, and stability in liquid Li. Most of the specimens from these experiments are in various stages of the double Ca-deposition/oxidation process. However, some of the preliminary results are provided in Table 2 and Fig. 10. Results indicate that either the He-flow or vacuum process may be used to coat V-4Cr-4Ti alloy with Ca, the vacuum system yielding a little higher amount of Ca and less oxygen. Also, there is a strong indication that O-precharging can lead to a measurably more uniform Ca concentration than the other two processes. Further results from these experiments will be provided in future reports.

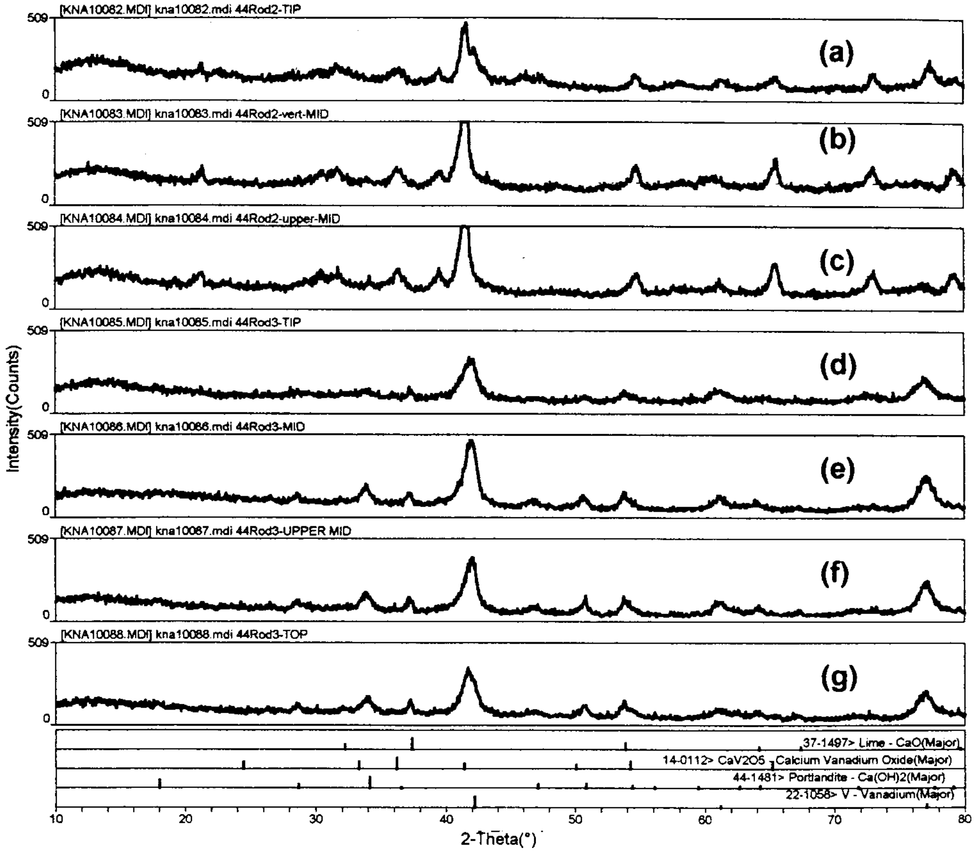

Fig. 9. X-ray diffraction patterns for surfaces at various locations along the length of 70-mm long V-4Cr-4Ti rod. (a)–(c): Rod after 106 h exposure to pure Li at 700^{o}C and (d)–(g): Rod after ≈100 h exposure to Li-10 at.% Ca at 600^{o}C.

REFERENCES

1. K. Natesan, C. B. Reed, M. Uz, J. H. Park, and D. L. Smith, "Electrically Insulating Coatings for V-Li Self-Cooled Blanket in a Fusion System," Argonne National Laboratory Report ANL/TD/TM00-10, May 2000.
2. K. Natesan, Z. Zeng, W. E. Ruther, M. Uz, and D. L. Smith, "Development of Electrically Insulating CaO Coatings," Fusion Reactor Materials Progress Report for the Period Ending June 30, 2000, Argonne National Laboratory, DOE/ER-0313/28, p. 30, September 2000.
3. K. Natesan, C. B. Reed, M. Uz, and D. L. Rink, "Development of Electrically Insulating CaO Coatings," Fusion Reactor Materials Progress Report for the Period Ending June 30, 1998, Argonne National Laboratory, DOE/ER-0313/24, p. 82, September 1998.
4. K. Natesan, M. Uz, and S. Weider, "Development of Electrically Insulating CaO Coatings," Fusion Reactor Materials Progress Report for the Period Ending December 31, 1998, Argonne National Laboratory, DOE/ER-0313/25, p. 69, April 1999.
5. K. Natesan, M. Uz, and S. Weider, "Development of Electrically Insulating CaO Coatings," Fusion Reactor Materials Progress Report for the Period Ending June 30, 1999, Argonne National Laboratory, DOE/ER-0313/26, p. 57, September 1999.

Table 2. Experimental conditions and Ca, O and V contents of V-4Cr-4Ti coupons after first Ca deposition step of double Ca-deposition/oxidation in He-flow and in vacuum processes.

Sample ID and pretreatment	Process Environment	T (^{o}C)	T (h)	Ca-Range[a] (Area) (at.%)	Ca_{min}[a] (Spot) (at.%)	O_2-Range[a] (Area) (at.%)	V-Range[a] (Area) (at.%)
44-7 Pre-ox.[b]	Vacuum	775	120	60 - 90	50	1 - 50	0.5 - 2
44-31 As-is[c]	Vacuum	780	165	27 - 40	5	10 - 50	1 - 70
44-11 As-is[c]	He-flow	800	166	34 - 78	4	20 - 50	1 - 52

[a] Obtained from energy-dispersive x-ray analysis of areas or spots on sample surfaces.

[b] Coupon preoxidized for 200 h at 600°C in $5x10^{-4}$ torr O_2.

[c] Coupons with no pre-treatment of surfaces.

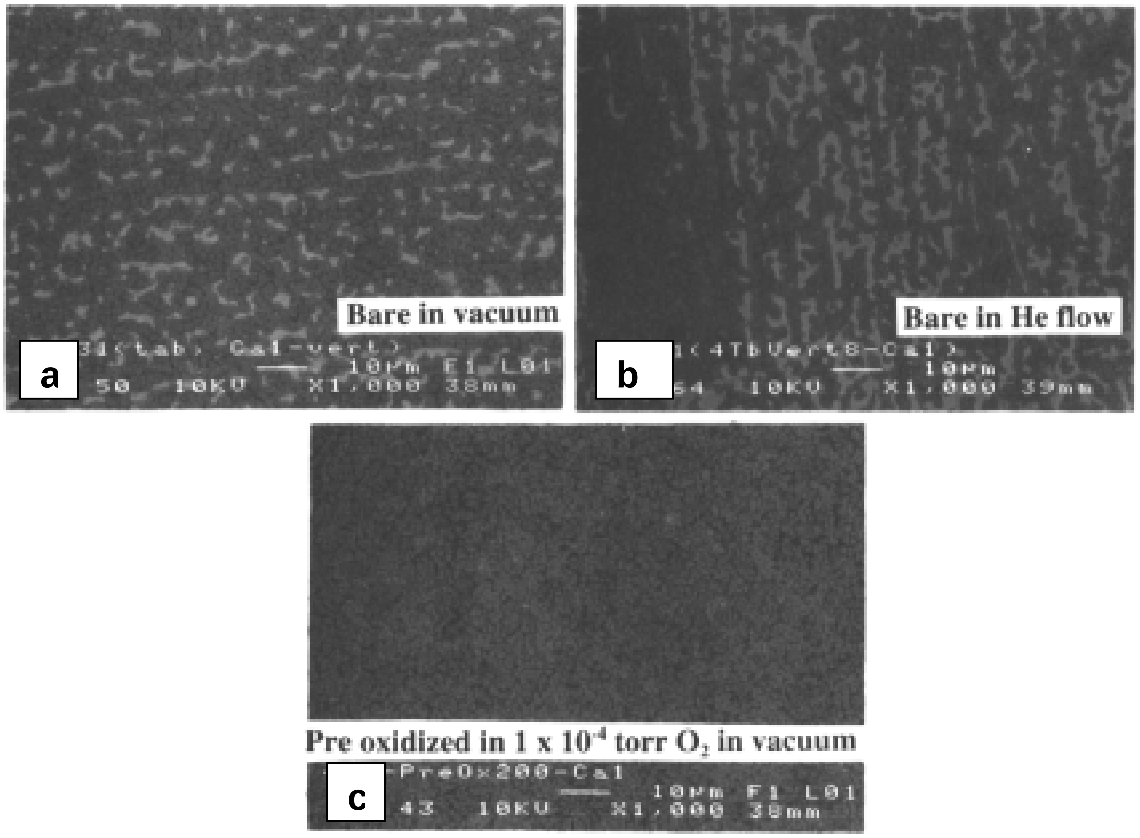

Fig. 10. SEM photomicrographs of surfaces of tab specimens after single Ca-deposition step. (a) tab with no pretreatment after Ca-deposition in vacuum; (b) tab with no pretreatment after Ca-deposition in He flow; (c) tab with O-precharge in $5x10^{-4}$ torr O_2 environment, and subsequently exposed for Ca-deposition in vacuum.

STRUCTURAL ANALYSIS OF PLATE-SHAPED PRECIPITATES IN NEUTRON IRRADIATED V-4Cr-4Ti

- D.T. Hoelzer and S.J Zinkle (Oak Ridge National Laboratory)

OBJECTIVE

To investigate the mechanisms of migration, segregation, and precipitation of the interstitial elements (C, O, N) in vanadium alloys during thermomechanical treatments, welding, neutron irradiation, and exposure to oxidizing environments.

SUMMARY

Neutron irradiation of V-4Cr-4Ti at ~510°C and dose of ~4 dpa resulted in the formation of a relatively high number density of plate shaped precipitates on $\{100\}_{bcc}$ habit planes. The TEM analysis showed that their average size was ~24 nm (+/- 12 nm) in diameter and ~1-3 nm in thickness. Diffuse streaking from the precipitates was observed to lie parallel to $<100>_{bcc}$ directions and centered at $^3/_4$<200> positions in electron diffraction patterns. Based on an orientation relationship observed between the precipitates and bcc matrix and a tilting experiment on one plate variant, the structural analysis indicated that the crystal structure of the plates was consistent with the fcc structure, which is the same for the golobular-shaped Ti-(OCN) phase. The analysis also showed that diffuse scattering observed at $^2/_3$<222> positions in electron diffraction patterns is not caused by the plate shaped phase.

PROGRESS AND STATUS

Introduction

The results obtained in this study were from a V-4Cr-4Ti alloy that was incorporated in the varying temperature irradiation experiment (HFIR 13J) performed under the framework of the Japan-USA Program of Irradiation Tests for Fusion Research (JUPITER) [1-3]. This experiment was designed to study the effects of temperature variation on the microstructure and mechanical properties of candidate fusion reactor structural materials.

Several recent studies have shown that Ti-rich precipitates form with a plate shaped morphology in vanadium alloys containing Ti. This result has been observed for a variety of experimental conditions that include, (1) annealing at 500°C in a low oxygen pressure environment followed by annealing at 950°C [4], (5) post gas tungsten arc weld heat treatment at 950°C [5], and (6) neutron irradiation at low doses and temperatures >315°C (HFBR) [6], 18 dpa and 600°C (DHCE) [7], 4dpa and ~390° (EBR-II X530) [8], 13-27dpa and 430-600°C (FFTF-DHCE) [8], and 14-40dpa and ~400-600°C (FFTF/MOTA) [9,10]. It is reasonable to assert based on these studies that the precipitates form on {100} planes in the bcc matrix [6], are associated with diffuse streaks in electron diffraction patterns such as a radial streak in the $<100>_{bcc}$ direction at ~$^3/_4$<200> position and possibly a tangential streak at ~$^2/_3$<222> position [7], and are Ti-rich containing interstitial solute atoms [4-6]. However, there still exists considerable uncertainty about the crystal structure, composition, and morphology of these precipitates, especially at particle sizes in the nanometer range. For example, nano-size precipitates were observed in neutron irradiated V-(4-5)Cr-(4-5)Ti at 400°C that were determined by PEELS to be Ti-rich, but the structure could not be unambiguously identified nor could the diffuse streaks observed at $^3/_4$<200> and $^2/_3$<222> be assigned to one or two types of precipitates [11]. Therefore, the purpose of this study is to develop a better understanding of the structure and crystallography of the plate shaped precipitates that form in vanadium alloys containing Ti, such as V-4Cr-4Ti.

Experimental Procedure

Details of the JUPITER HFIR 13J variable temperature experiment have been published [1-3]. The TEM results of this study were from the V-4Cr-4Ti (Wah Chang heat #832665) that was neutron irradiated at an average temperature of 510°C (+/- 10°C) and dose of ~4 dpa.

Results

The microstructure of the neutron irradiated V-4Cr-4Ti alloy consisted of the bcc V-rich matrix phase, an inhomogeneous distribution of prior globular-shaped Ti-OCN particles, and a homogeneous distribution of small plate-shaped precipitates with a relatively high number density of $\sim 4.2\times10^{21}/m^3$. The plate-shaped precipitates were associated with diffuse electron scattering that was observed as streaks lying parallel to $<100>_{bcc}$ in selected area electron diffraction (SAED) patterns. Figure 1 shows the bright field (BF) and dark field (DF) micrographs of the precipitates. The inset in Figure 1b shows the diffuse streak (marked by the arrow head) that was used to form the DF image. For these micrographs, the sample was oriented between the $[001]_{bcc}$ and $[011]_{bcc}$ zone axes and the diffuse streak associated with the plates was observed near $^3/_4$<200> position. The analysis of the plates showed them to have an average diameter of 24 nm (+/- 12 nm) and a thickness typically less than 2-3 nm.

Figure 2 shows the plate-shaped precipitates with the thin foil specimen oriented along the $[001]_{bcc}$ zone axis. At this orientation, two rotational variants of the plates are observed edge on and appear as rods in the projected image of Figure 2a. Both plate variants contain an $\{001\}_{bcc}$ habit plane. The SAED pattern shown in Figure 2b was obtained by tilting slightly off the precise $[001]_{bcc}$ zone axis in order to emphasize the diffuse streaking pattern from a single plate variant, i.e. the plate lying parallel to $(100)_{bcc}$ in Figure 2a. This slight tilting resulted in a symmetrical pattern of diffuse streaks with each lying parallel to the <100> directions. Along with the streak marked $^3/_4$<200>, a similar streak exists closer to the 110 reflection and another one is superimposed on the 020 reflection.

Focusing on the $(100)_{bcc}$ plate variant, SAED patterns were then obtained at the [011] and [111] zone axes and are shown in Figure 3. This was accomplished by tilting the thin foil specimen normal to the $<100>_{bcc}$ diffuse streaks, i.e. using $g=200_{bcc}$, from B=[001] to B=[011] (45° tilt) and then from B=[011] to B=[111] (~35° tilt). A systematic row of diffuse streaks associated with the

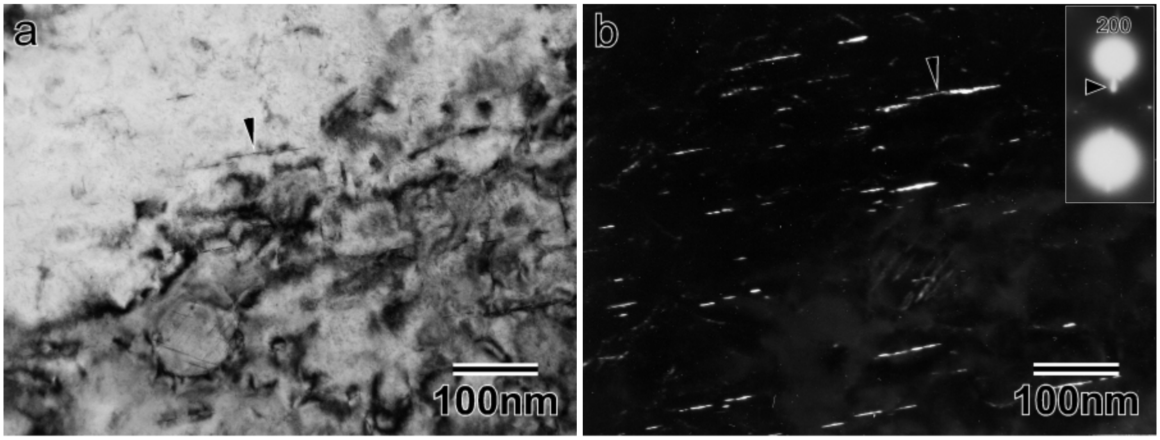

Figure 1. TEM micrographs showing the plate shaped precipitates that formed in the neutron irradiated V-4Cr-4Ti. (a) bright field and (b) dark field using diffuse streak at g = $^3/_4$<200>.

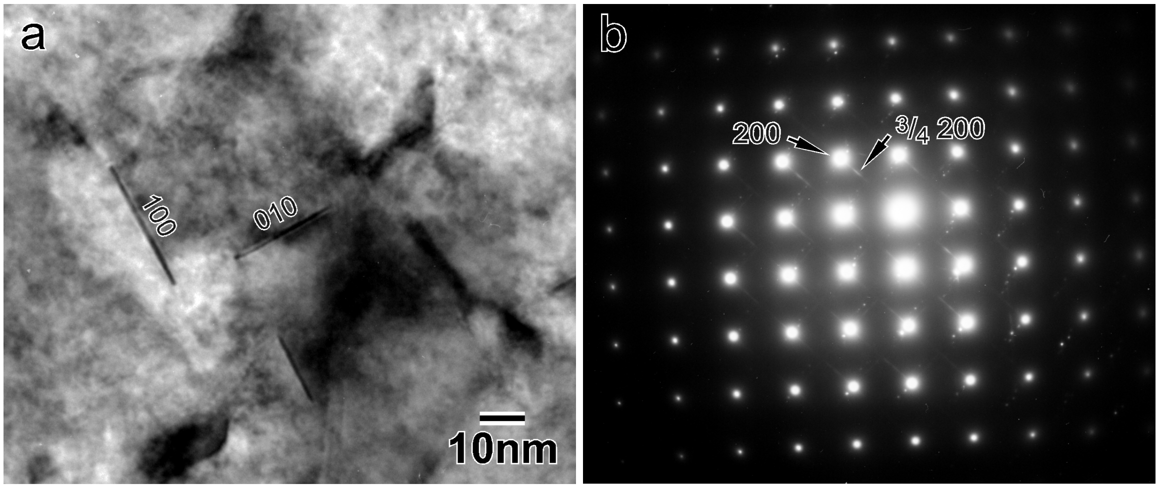

Figure 2. (a) TEM bright field micrograph showing two plate variants with (100) and (010) habit planes and (b) SAED pattern showing the diffuse streaking pattern for the (100) plate variant at the slightly tilted off axis $[001]_{bcc}$ zone axis.

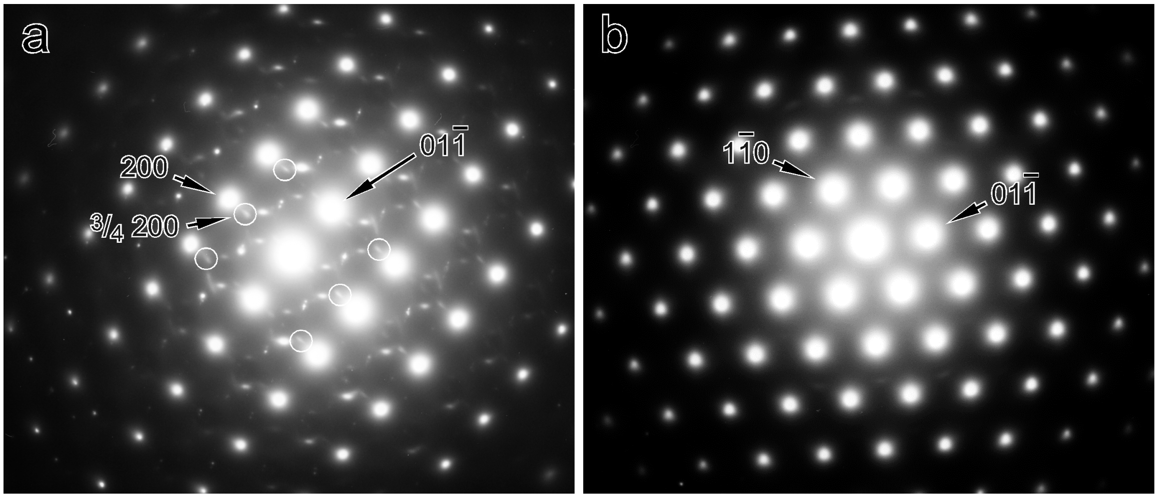

Figure 3. SAED patterns showing the diffuse streaking pattern for the (100) plate variant that was observed at (a) the $[011]_{bcc}$ zone axis and (b) the $[111]_{bcc}$ zone axis.

(100) plate variant are observed at the $[011]_{bcc}$ zone axis as shown in Figure 3a. These streaks are enclosed in circles. Additional diffuse scattering signals are also observed at the $[011]_{bcc}$ zone axis including the diffuse arcs at ~$^{2}/_{3}$<222>. However, tilting to the $[111]_{bcc}$ zone axis along $g=01\bar{1}$ resulted in no apparent visible diffuse streaks as shown in Figure 3b.

Discussion

The results showed that neutron irradiation at ~510°C and dose of ~4 dpa resulted in the formation of a relatively high number density of plate shaped precipitates. Although no compositional data was obtained at the time of this report, the observation of diffuse streaks in electron diffraction patterns and the $\{100\}_{bcc}$ habit plane indicate that these precipitates are consistent with Ti-rich plates reported from previous studies [5,6]. In a recent study [12], a similar morphology and crystallography was observed for plates that formed in oxygen doped V-4Cr-4Ti annealed at 950°C [4] and analysis by EELS and EDS showed them to be Ti-rich containing varying levels of C, O and N. The same type of compositional analysis will be performed on the plates observed in the neutron irradiated specimen.

The crystal structure of the plate shaped phase was investigated by analyzing electron diffraction patterns recorded in the tilting experiment on one plate variant and comparing them with simulated diffraction patterns. The SAED pattern shown in Figure 1b indicates that an orientation relationship (OR) exists between the plate shaped phase and the bcc matrix. Since the intensity profile causing the diffuse streak is due to the phase shape factor, a maximum occurs near the center of the streak. The location of the intensity maximum was used for calculating the d-spacings, which are listed in Table 1 for several <100> streaks at the $[001]_{bcc}$ zone axis. The streak that lies normal to $g=020_{bcc}$ is superimposed on the 020_{bcc} reflection and can be confirmed by constructing a line that connects the center of streaks located near 200_{bcc} and $1\bar{1}1_{bcc}$, which intersects the 020_{bcc}. A reasonable correlation with the fcc crystal structure was then made based on self-consistencies in the measured d-spacings, interplanar angles, and structure factor considerations, i.e. using the (hkl) ratio method. Thus, the OR shown in Figure 1b was indexed as the $[011]_{fcc}$ zone axis for the precipitates. From this result, the OR was consistent with $[001]_m$ // $[011]_p$ and $(200)_m$ // $(200)_p$, where the subscript m is for matrix and p is for precipitate. This OR is the same as the Baker-Nutting OR [13] and has been observed for TiO precipitates in V-Ti alloys [14]. Finally, the lattice parameter of the fcc structure was calculated from the (hkl) assignments of the measured d-spacings and was found to be **a**=0.419 (+/- 0.010 nm).

Simulated electron diffraction patterns were generated using DiffractII v1.2a (1990) in order to understand the diffuse streaking patterns recorded at $[001]_{bcc}$ and $[011]_{bcc}$ zone axes for the single plate variant used in the tilting experiment. Input crystallographic parameters were based on the lattice parameter calculated for the bcc matrix and fcc precipitate phase and the OR observed at the $[001]_{bcc}$ zone axis. Figure 4 shows the results of the simulation taking into account two rotational plate variants, i.e. the plates observed on (100) and (010) habits in Figure 2a, and the plate shape factor. Figure 4a shows that the simulation accurately predicts the location of the intensity maxima, assuming a spherical shape, and also the direction of the intensity profile, or streak, when the plate shape factor is applied to the two plate variants at the [001] zone axis. At the $[011]_{bcc}$ zone axis shown in Figure 4b, a systematic row of streaks appear in the <100> direction at ~$^3/_4$<2xx>, where x=0,1,2..n, and another row of streaks intersect the matrix reflections at x00, where x=0,2,4,..even. Indexing these streaks is consistent with the $[010]_{fcc}$ zone axis for the (100) plate variant used in the tilting experiment. The (010) plate variant lies 45° to the $[011]_{bcc}$ zone axis and does not contribute to diffuse streak patterns in the SAED pattern (Figure 3a). However, it is possible that rel-rods caused by the plate shape factor may extend from higher order Laue zones and intersect the Ewald sphere. This possibility as well as double diffraction effects may account for the extra diffuse scattering phenomena that was observed at the $[011]_{bcc}$ zone axis. Finally, the simulated pattern observed in Figure 4c indicates that the

Table 1. Structural analysis of the plate shaped precipitates.

Number	<100> Streak	d-spacing (+/- 0.002 nm)	(hkl) (fcc basis)	Ratio (Number reference)	
1	near 111	0.242	111	1.180 ($^1/_2$)	1.592 ($^1/_3$)
2	near 200	0.205	200	1.349 ($^2/_3$)	---
3	superimposed on 020	0.152	220	---	---

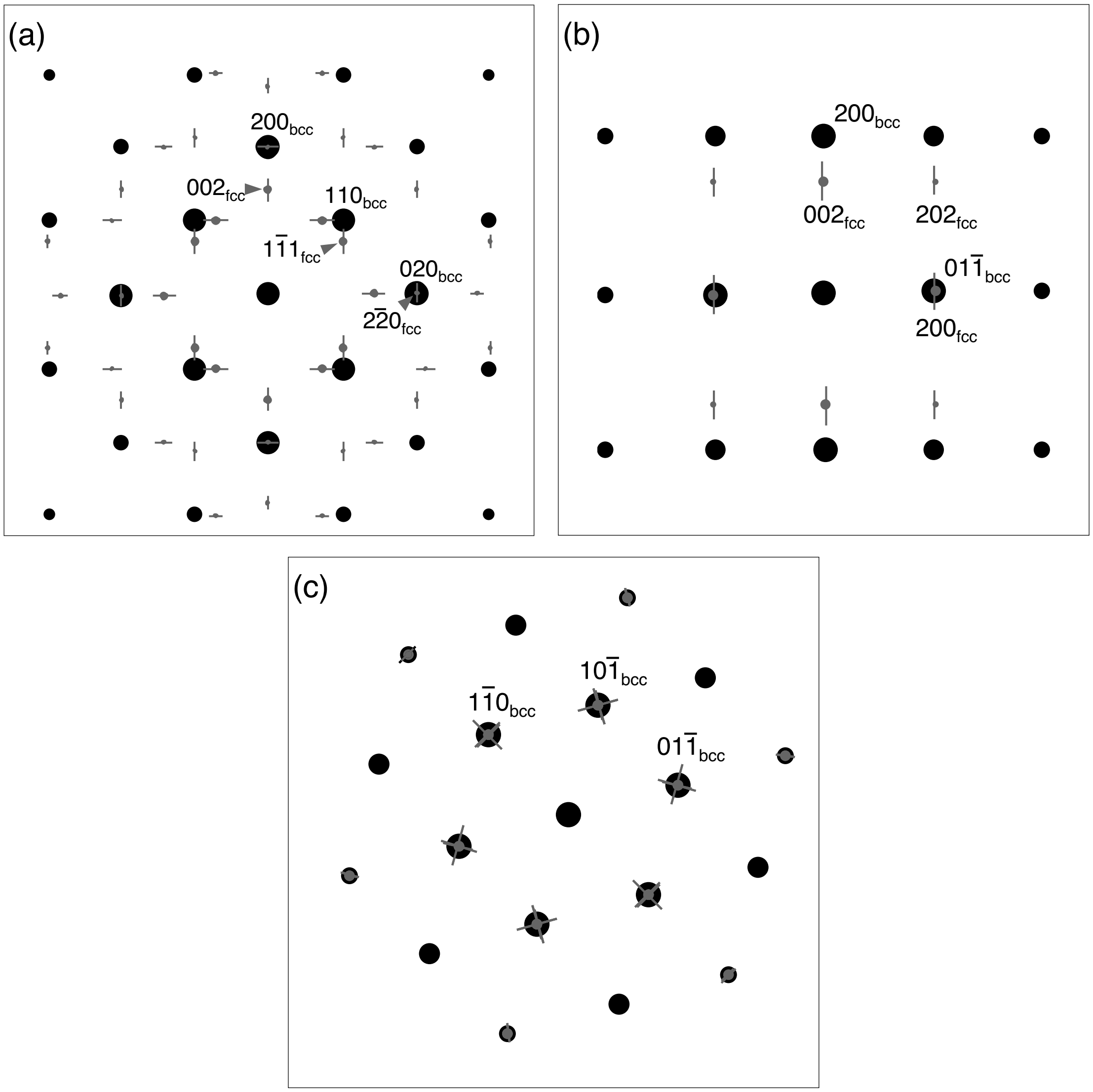

Figure 4. Simulated electron diffraction patterns showing the diffuse scattering patterns of the (100) and (010) plate variants at: (a) B=[001]$_{bcc}$, (b) B=[011]$_{bcc}$, and (c) B=[111]$_{bcc}$ zone axes.

streaks from both plate variants are superimposed on matrix reflections and that this explains why no diffuse scattering was observed at the [111]$_{bcc}$ zone axis in Figure 3c. From the OR, there are no low indice zone axes of the fcc phase for any rotational plate variant that coincide with the [111]$_{bcc}$ zone axis. Thus, the agreement between SAED and simulated patterns is consistent with the fcc structure for the plate shaped precipitates, which is the same structure as the Ti-rich (OCN) phase [15].

The simulated electron patterns showed that there was no relationship between the Ti-rich plate shaped phase and the diffuse streaks, or arcs, that occur at the ~$^2/_3$<222> position. These diffuse arcs have typically been observed at the <011>$_{bcc}$ zone axis [6,7] and are observed in the [011]$_{bcc}$ zone axis of the SAED pattern shown in Figure 3a. This conclusion was based on investigating the diffuse scattering behavior from all three rotational {100} plate variants at the $[011]_{bcc}$ zone axis and changing the foil thickness as well as plate thickness in order to account for the diffuse arcs. No combination of parameters or variants could simulate the $^2/_3$<222> diffuse arcs. Thus, it is concluded based on these results that the diffuse scattering at $^2/_3$<222> is due to a different phase than the Ti-rich plate shaped phase. A similar conclusion was also obtained from the TEM analysis of the defect structures in neutron irradiated V-4Cr-4Ti at a dose of 19dpa and ~323°C (BOR-60 FUSION experiment); diffuse arcs at $^2/_3$<222> positions were observed but diffuse streaks at $^3/_4$<200> positions were not observed in SAED patterns [16]. Preliminary results indicate that the diffuse arcs at $^2/_3$<222> positions are due to surface contamination that occurs during thin foil preparation.

The results of this and other previous studies indicate that Ti-rich plates form in V-based alloys containing Ti in both neutron irradiated and unirradiated thermally aged conditions with no significant differences in structure and crystallography. However, differences in the experimental conditions could affect the formation temperature of the Ti-rich plates. The rate limiting parameter for precipitation under normal unirradiated conditions is the diffusion of solute Ti atoms. Since long-range diffusion of solute Ti atoms does not occur below 500°C in unirradiated V-alloys [17], this result implies that the Ti-rich plates will form only at temperatures higher than 500°C or after very long time at temperatures slightly above 500°C in the unirradiated condition. Alternatively, solute Ti atoms could interact with point defects generated during neutron irradiation, enhancing their diffusion rate and subsequently the precipitation of plates at temperatures below 500°C or above this temperature in shorter time. This mechanism appears to be consistent with experimental results; the precipitation of Ti-rich plates occurs at temperatures in the range from ~315°C to above 600°C in neutron irradiation studies [6-10,18] and at temperatures usually >600°C in unirradiated thermal aging studies [4,5,12,14]. The lower temperature limit and minimum time at temperature for precipitation of the Ti-rich plates have not been established in unirradiated annealing studies.

REFERENCES

1. A.L. Qualls and T. Muroga, J. Nuclear Materials, **258-263**, (1998), p. 407.
2. S.J. Zinkle, “Summary of the U.S. Specimen Matrix for the HFIR 13J Varying Temperature Irradiation Capsule,” Fusion Materials Semiannual Progress Report, DOE/ER-0313/23, December 1997, p. 352.
3. A.L. Qualls, “Summary of the Operation of the Varying Temperature Experiment,” Fusion Materials Semiannual Progress Report, DOE/ER-0313/28, June 2000, p. 266.
4. B.A. Pint, P.M. Rice, L.D. Chitwood, J.H. DeVan, and J.R. DiStefano, “Microstructural Characterization of External and Internal Oxide Products on V-4Cr-4Ti,” Fusion Materials Semiannual Progress Report, DOE/ER-0313/24, June 1998, p. 77.
5. M.L. Grossbeck, J.F. King, D.J. Alexander, P.M. Rice, and G.M. Goodwin, J. Nuclear Materials, **258-263**, (1998), p. 1369.
6. P.M. Rice and S.J. Zinkle, J. Nuclear Materials, **258-263**, (1998), p. 1414.
7. D.S. Gelles and H.M. Chung, “Microstructural Examination of Irradiated Vanadium Alloys,” Fusion Materials Semiannual Progress Report, DOE/ER-0313/21, December 1996, p. 79.
8. H.M. Chung, J.Gazda, and D.L. Smith, “Irradiation-Induced Precipitation and Mechanical Properties of Vanadium Alloys at <430°C,” Fusion Materials Semiannual Progress Report, DOE/ER-0313/24, June 1998, p. 49.
9. S. Ohnuki, D.S. Gelles, B.A. Loomis, F.A. Garner, and H. Takahashi, J. Nuclear Materials, **179-181**, (1991), p. 775.
10. M. Satou, K. Abe, H. Kyano, and H. Takahashi, J. Nuclear Materials, **191-194**, (1992), p. 956.

11. D.S. Gelles, P.M. Rice, S.J. Zinkle, and H.M Chung, J. Nuclear Materials, **258-263**, (1998), p. 1380.
12. J. Bentley and B. Pint, "Analytical Electron Microscopy of V-4%Ti-4%Cr Alloys, to be published in the proceedings of the Microscopy Society of America, (2001).
13. J.W. Edington, in "Practical Electron Microscopy in Materials Science," N.V. Philips' Gloeilampenfabrieken, Eindhoven, 1975.
14. K.H. Kramer, J. Less-Common Metals, **21**, (1970), p. 365
15. D.T. Hoelzer, "Structural Analysis of Ti-oxycarbonitrides in V-Cr-Ti Base Alloys," Fusion Materials Semiannual Progress Report, DOE/ER-0313/25, December 1998, p. 59.
16. D.T. Hoelzer, Unpublished results, (2000).
17. R.E. Gold, D.L. Harrod, R.L. Ammon, R.W. Buckman, Jr., and R.C. Svedberg, in Technical Assessment of Vanadium-Base Alloys for Fusion Reactor Applications, Final Report prepared by Westinghouse Electric Corp. under Contract EG-77-C-02-4540 for the Department of Energy, Office of Fusion Energy, (1978).
18. R. Carlander, S.D. Harkness, and A.T. Santhanam, "Effects of Radiation on Substructure and Swelling Behavior of Vanadium Alloys," ASTM STP 529, 1973, p. 399.

HELIUM ANALYSIS FROM THE DHCE-1 SIMULATION EXPERIMENT -

D. L. Smith (Argonne National Laboratory)

Objective

The objective of this task is to provide an evaluation of the Proof-of-Principle Dynamic Helium Charging Experiment (DHCE-1). The current effort is focused on an analytical analysis of the helium generated in the vanadium alloys to compare with the measured helium concentrations.

Summary

A detailed calculation of the predicted helium generation rates in unalloyed vanadium and the reference V-4Cr-4Ti alloy irradiated in the DHCE-1 Proof-of-Principle experiment has been performed with the available data base on fundamental properties. Results of these detailed calculations indicate that the experimentally measured helium concentrations are in good agreement with the calculated values. Approximately 90% of the measured values are within a factor of 0.5 to 1.5 of the calculated values, which is quite good agreement. The validity of the experiment is further verified by a comparison of the experimental results from the other alloys included in the experiment with calculated correlation factors for each of the seven capsules. This paper presents a summary of the comparison of the results from the detailed calculations with experimental helium concentrations in the vanadium alloys in the DHCE-1 proof-of-principle experiment.

Introduction

A Dynamic Helium Charging Experiment (DHCE) was developed as a unique method for investigating the effects of fusion relevant helium generation rates on the properties of vanadium alloys irradiated in a fission reactor neutron spectrum [1]. The helium transmutation rate in candidate vanadium alloys at the first wall of deuterium-tritium fusion system from the high-energy neutrons is about 4 appm He/dpa (atomic parts per million helium for a neutron damage level of one atomic displacement per atom of the alloy). This value corresponds to a value of less than 0.02 appm He/dpa in a typical fast-fission reactor neutron spectrum. The effect of this high helium transmutation rate produced by high-energy fusion neutrons remains as the key issue regarding the performance limits of candidate structural materials for the fusion first-wall applications. Since we do not have a high flux 14 MeV neutron source for materials testing of the simultaneous effects of helium and neutron damage on the properties of materials for fusion applications, we must rely on simulation experiments, theory and modeling to evaluate these effects. The DHCE with vanadium alloys provides a unique method for providing insight and understanding of the effects of fusion-relevant helium generation on neutron irradiated materials. Features of the DHCE include:

- Close simulation to fusion neutron spectrum irradiation effects involving simultaneous helium production with neutron damage.
- Nearly constant He/dpa generation.
- He/dpa rates projected for a fusion environment can be obtained.
- Applicable to a range of He/dpa, fluence, temperature, and alloy composition variables.
- Applicable to existing heats of vanadium alloys; does not require preparation of special small heats.

A proof-of-principle (POP) experiment (DHCE-1) with a range of vanadium alloy compositions was conducted as part of the US/Japan (Monbusho) collaboration on fusion materials research. The DHCE-1 succeeded in demonstrating that the technique can achieve elevated He/dpa ratios in vanadium alloys for a range of conditions. Experimental measurements of the helium concentrations in the various alloys indicated that the helium generation rates from the DHCE ranged from ~10-1000 times the helium transmutation rates for pure alloys in the fission neutron spectrum. The ideal enhancement to reach the fusion-relevant value is a factor of ~200. For many of the specimens the enhancement factor was ~40, which was less than desired amount but a large enhancement compared to the helium transmutation rate in a fission neutron spectrum.

A detailed calculation of the predicted helium generation rates in unalloyed vanadium and the reference V-4Cr-4Ti alloy has been performed with the available database on fundamental properties. Results of these detailed calculations indicate that approximately 90% of the experimentally measured helium concentrations are within a factor of 0.5 to 1.5 of the calculated values, which is quite good agreement. The validity of the experiment is further verified by a comparison of the experimental results from the other alloys included in the experiment with calculated correlation factors for each capsule. This paper presents a summary of the comparison of the results from the detailed calculations with experimental helium concentrations in the vanadium alloys in the DHCE-1 proof-of-principle experiment.

Calculation of Helium in V-4Cr-4Ti and Vanadium

A detailed calculation of the predicted helium concentrations in unalloyed vanadium and the reference V-4Cr-4Ti alloys included in the DHCE-1 proof-of-principle experiment has been performed [1, 2]. The calculations include the helium generated during the irradiation cycle, helium generated during the reactor down time, and helium generated after termination of the irradiation but before the test specimens were retrieved and analyzed. The helium generation in the vanadium includes both generation from the tritium precharge as well as from tritium generated from ^{6}Li reactions during the irradiation. Helium loss due to burnout and reductions due to tritium leakage are also included in the calculation. Specific experimental parameters for each irradiation capsule are included in the calculation. Parameters for each capsule of the DHCE-1 are given in Table 1.

Helium in the vanadium is generated by the decay of tritium in the vanadium. The two sources of tritium are a precharge of tritium in a “mother alloy” contained in each capsule and from tritium generated from ^{6}Li during the irradiation. For the conditions of the DHCE-1, most of the tritium originates from the precharge. Varying amounts of tritium were precharged in the various capsules in an attempt to account for variations associated with the different experimental temperatures and to accommodate uncertainties in the database at the time. Variations in ^{6}Li were introduced as an experimental variable with higher enrichment at the higher temperatures to partially makeup for tritium losses by permeation through the capsule walls. A key feature of the experimental approach is not to inject tritium into the test specimens until the neutron damage is initiated. The tritium remains in the “mother alloy” until the capsule is heated upon insertion and startup of the reactor. The tritium rapidly redistributes upon heating such that tritium decay to helium is initiated at the same time as the neutron damage begins.

The redistribution of tritium to the vanadium alloy test specimens is dependent on the tritium precharge, the masses of lithium and vanadium in the capsules and the distribution coefficient of tritium between lithium and the vanadium alloys. The tritium distribution coefficient is dependent on the temperature and the alloy composition as will be discussed later. The tritium precharge and the masses of lithium and vanadium in each capsule are indicated in Table 1.

The distribution coefficient for tritium between lithium and vanadium is obtained from the hydrogen solubility expressed by the Sieverts' constants. The Sieverts' constants defined by Veleckis et al [3] for hydrogen in lithium, which differ slightly from the values used originally, are recommended as the most reliable. The Sieverts' constant for hydrogen in lithium as a function of temperature is given by

$$\ln K_{S(Li)} = -6.498 + \frac{6182}{T} \quad , \quad \text{atom fraction/atm}^{0.5} \qquad (1)$$

The Sieverts' constants for vanadium obtained from a compilation of hydrogen solubility measurements is given by

$$\ln K_{S(V)} = -7.510 + \frac{3980}{T} \quad , \quad \text{atom fraction/atm}^{0.5} \qquad (2)$$

Table 1. DHCE-1 Test parameters and ^{3}He analyses of vanadium and V-4Cr-4Ti alloy.

Capsule ID	**4D1**	**4D2**	**5 E2**	**5D1**	**5 E1**	**5C1**	**5C2**
Irradiation Temperature, C	430	430	430	500	500	600	600
Lithium Mass, g	0.765	0.765	0.67	0.938	0.952	0.808	0.955
Li(6) Fraction, %	5.0	4.5	1.0	6.5	1.0	8.0	8.0
Total Specimen Mass, g	5.86	5.38	5.38	5.77	5.82	5.82	5.95
Plenum Volume, ml	2.85	2.93	3.11	2.53	2.49	2.77	2.47
Distribution Coeff, Ka	56.9	56.9	56.9	40.3	40.3	27.1	27.1
Tritium Precharge, Ci	99	70	26	74	57	16	18
Precharge Tritium, appm in Li	30200	21350	9055	18400	13970	4620	4398
Calculated He-3 in V-4Cr-4Ti, appm							
Tritium leakage from TZM capsule	10.8	10.9	5.7	14.6	10.2	6.7	6.6
Tritium leakage from Mo capsule	10.8	10.9	5.7	14.6	10.2	4.1	4.0
Measured He-3 in V-4Cr-4Ti, appm	11.6	9.9	2.5	14.0	5.5	7.9	6.8
	9.9	20.9	2.5	14.1	5.6	8.0	74.0
Calculated He-3 in vanadium, appm							
Tritium leakage from TZM capsule	10.1	10.2	5.4	12.8	9.0	5.6	5.5
Tritium leakage from Mo capsule	10.1	10.2	5.4	12.8	9.0	3.4	3.3
Measured He-3 in vanadium, appm	8.8	15.2	2.5	31.6	12.3		10.4

Recent results on the Sieverts' constant for the V-4Cr-4Ti alloy [4] are given by

$$\ln K_{S(V44)} = -6.725 + \frac{3500}{T} \quad , \quad \text{atom fraction/atm}^{0.5} \qquad (3)$$

Based on these equations the distribution coefficients for hydrogen between lithium and vanadium and V-4Cr-4Ti expressed in atom fraction of hydrogen are given by

$$\ln K_A\,(H_{Li}/H_V) = 1.002 + \frac{2202}{T} \quad , \quad \text{atom fraction} \qquad (4)$$

$$\ln K_A\,(H_{Li}/H_{V44}) = 0.227 + \frac{2682}{T} \quad , \quad \text{atom fraction} \qquad (5)$$

The distribution coefficients for hydrogen in the Li/V and Li/V-4Cr-4Ti systems are plotted as a function of temperature in Figure 1.

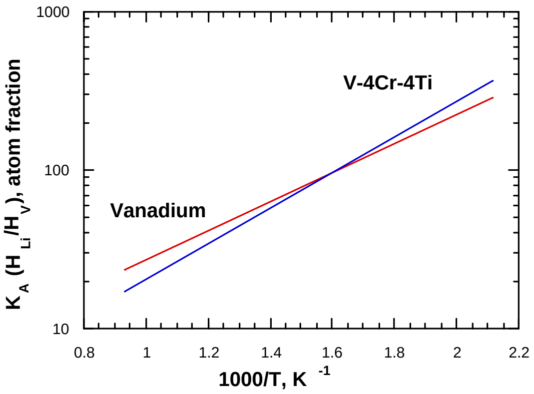

Figure 1. Distribution coefficient for hydrogen for the lithium Vanadium and Lithium V-4Cr-4T systems.

These hydrogen distribution coefficients are valid for hydrogen concentrations up to the saturation value for LiH formation in equilibrium with hydrogen in solution in lithium. The saturation value of hydrogen in lithium for LiH formation is given as a function of temperature by

$$\ln N_{LiH} = 3.769 + \frac{5472}{T} \quad , \quad \text{mole-fraction} \qquad (6)$$

The helium generated in the V-4Cr-4Ti and unalloyed vanadium is calculated for each capsule in the DHCE-1 based on the experimental parameters given in Tables 1 and 2.

Table 2. Experimental parameters of DHCE-1.

Irradiation Time	203 days at Irradiation Temperature
Off cycle Time	92 days at 365°C
Time after reactor shutdown	300 days at 200°C
Time until specimens analyzed	90-180 days at RT

This detailed calculation for helium generation in the V-4Cr 4Ti alloy and vanadium specimens in DHCE –1 includes the following:

- He generated from tritium precharge during irradiation at temperature
- He generated from tritium produced from ^{6}Li during irradiation
- He loss due to burn-out during irradiation
- He generated during the off-cycle of the reactor
- He generated after reactor shutdown before removal of subassembly from reactor
- Reduction in He generation as a result of tritium loss due to permeation through the capsule wall.
-

Based on previous experience with hydrogen, the tritium redistributes rapidly between the vanadium alloy specimens and lithium after a change in temperature. Results of the calculated ^{3}He concentrations in vanadium and V-4Cr-4Ti are given for each capsule in Table 1. These results are plotted in Figs. 2 and 3 for the V-4Cr-4Ti alloy and vanadium, respectively. With few exceptions, the results of the experimentally determined ^{3}He concentrations are in quite good agreement with the calculated values that account for the parameter variations in the experiment. In all cases (capsules), most of the ^{3}He in the vanadium specimens is generated from tritium from the precharge. Most of the ^{3}He (~ 86%) is generated in the specimens during the irradiation. Only about 13% is generated during the off-cycle time since the tritium tends to redistribute to the lithium at the lower temperature (365^{o}C). Only about 1% of the ^{3}He is generated after the reactor shutdown and before the specimens were analyzed even through this was a relatively long time (several months). This again is due to the tritium distribution at low temperatures. Since the ^{6}Li content was varied for each capsule, the ^{3}He generated from tritium produced from ^{6}Li varied considerably. Higher ^{6}Li concentrations were used in the 600^{o}C capsules in an attempt to partially balance the higher tritium leakage. Indeed, the ^{3}He generated from the ^{6}Li produced tritium varied from ~2 to 20% of the total. The ^{3}He burn-out varies as the concentration of ^{3}He increases but is a relatively small fraction (<10%). The tritium leakage is negligible for the two lower temperatures 430 and 500^{o}C, but could result in a maximum reduction of about 30% at 600^{o}C. The worse case scenario is based on calculated permeation rates for molybdenum. Recent results by Altunoglu and Braithwaite [5] indicate that the diffusivity of hydrogen in TZM alloy (used for the DHCE-1 capsules) is considerably less than that for molybdenum. They also indicate significant reductions in the diffusivity of hydrogen in TZM with lower hydrogen pressures. The actual permeation rates for the TZM capsules may also be reduced by a thin oxide film which is characteristic of the capsule surfaces. The tritium loss by permeation remains as the largest uncertainty at temperatures of 600^{o}C and above. However, the calculated ^{3}He concentrations tend to support the possibility that tritium permeation rates based on molybdenum data may over predict the tritium losses. All experimental values are within a factor of two of the calculated values except for one analysis (74 appm ^{3}He) of V-4Cr-4Ti in capsule 5C2 at 600^{o}C. This is good agreement for a proof-of-principle experiment of this complexity. It certainly appears that the one alloy specimen from 5C2 must have gotten mixed up during one of the many handling procedures. As discussed later, the ^{3}He concentrations in several other alloy specimens analyzed at the same time had ^{3}He concentrations as high or higher than the specimen in question.

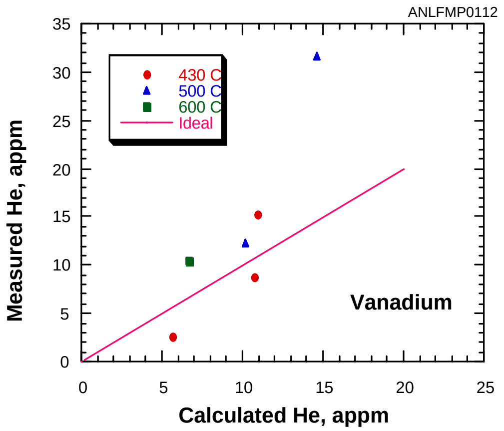

Figure 2. Measured vs. calculated ^{3}He concentrations in vanadium irradiated in the DHCE-1.

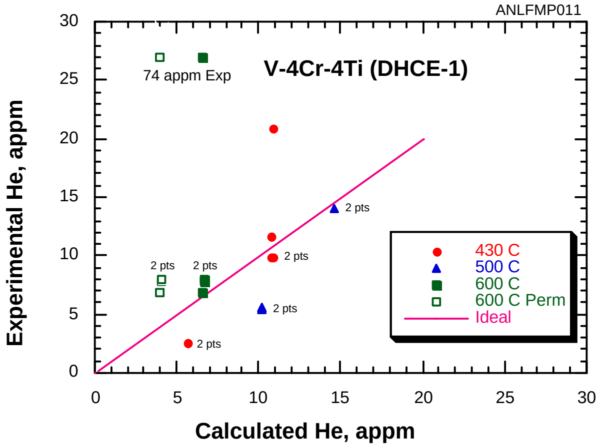

Figure 3. Measured vs. calculated ^{3}He concentrations in vanadium irradiated in the DHCE-1.

Correlation of Experimental Results

In addition to the vanadium and the V-4Cr-4Ti alloy discussed above, the ^{3}He content was measured for nine other vanadium alloys irradiated in the same seven capsules. These alloys consisted primarily of binary alloys of vanadium with ~5% alloying additions of interest for fundamental studies. Results of the experimental analyses are summarized in Table 3. It is apparent from these results that three of the alloys, viz., V-1Si, V-5Fe, and V-5Cr-5Ti (Si, Al, Y), exhibited much higher ^{3}He contents than the other alloys. These differences are attributed primarily to differences in the hydrogen distribution coefficients between lithium and these alloys. Since we do not have well defined Sieverts' constants for hydrogen in these alloys, we cannot calculate the ^{3}He concentrations accurately. However, a correlation of the results from these alloys with the results from the vanadium and V-4Cr-4Ti alloy are given at the bottom of Table 5. The ratios of the measured ^{3}He concentrations for the other alloys to these normalized concentrations of helium in vanadium and V-4Cr-4Ti alloy for each capsule were calculated (see Table 3). The ratios for each alloy are averaged to provide a measure of the hydrogen distribution for each alloy compared to the normalized distribution for the vanadium and V-4Cr-4Ti alloy. For example, the average ^{3}He concentration of the V-1Si alloy is 8.9 times the reference value (average of vanadium and V-4Cr-4Ti), that of the V-5Fe is a factor of 9.6 higher, and that of V-5Nb is lower by a factor of 0.87. For the total 48 analyses presented in Table 3, only 5 analyses (including the 74 appm ^{3}He for V-4Cr-4Ti in capsule 5C2) vary outside the range 0.5 – 1.5 of the average for each alloy composition. Figure 4 is a plot of the normalized concentrations for each alloy (measured ^{3}He concentration divided by the normalized ^{3}He concentration for the vanadium and V-4Cr-4Ti alloy) as a function of the calculated ^{3}He concentration for the V-4Cr-4Ti alloy in each capsule. The line represents an ideal correlation.

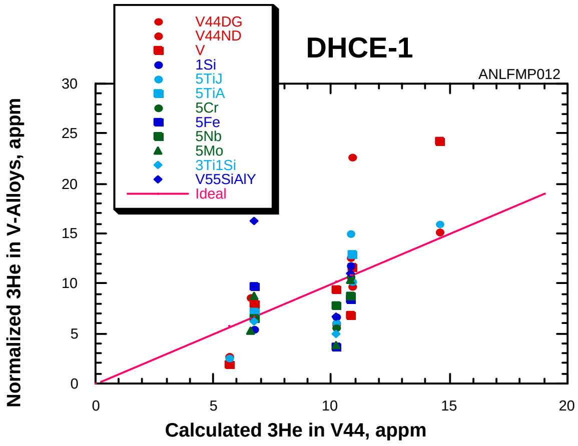

Figure 4. Normalized ^{3}He concentrations in Twelve Vanadium alloys at a function of the calculated ^{3}.

This figure indicates that results from all alloys provide a reasonably good correlation with the calculated values for V-4Cr-4Ti. Further, these results show some consistent patterns. For example, all alloys in capsule 5E2 indicated measured ^{3}He concentrations lower than predicted. This would indicate that the tritium in this capsule was slightly lower than expected. The results from all alloys in capsule 5E1 indicate similar behavior. The results from the other five capsules are in good agreement with the ideal correlation. As indicated earlier, only five analyses show substantial deviations from the ideal correlations and three of these analyses differ only by about a factor of two.

Conclusions

Results of a detailed calculation for the ^{3}He generation in vanadium and V-4Cr-4Ti alloy irradiated in the DHCE-1 experiment show good agreement with the measured ^{3}He concentrations except for one analysis, which is most likely, the result of a mix-up in specimens during handling. The detailed analysis includes variations in temperature, tritium precharge, ^{6}Li enrichment, masses of V-alloys and lithium, variations in reactor operating cycle, post irradiation effects, ^{3}He burn-out, and tritium leakage from the capsules. Correlations of measured ^{3}He concentrations from all alloys analyzed indicate consistent results for all but five of the 48 specimens analyzed. These correlations indicated that the tritium in two of the seven capsules was slightly lower than expected. Tritium leakage through the TZM capsule remains as the largest uncertainty at the higher temperatures (600°C and above), but the leakage rate may be lower than originally assumed.

The results of these analyses and the consistency of the experimental results support the position that the DHCE-1 successfully demonstrated that this method can be used to investigate effects of fusion relevant helium generation rates with fission reactor irradiations of vanadium alloys. The average ^{3}He generated in the vanadium alloy specimens was about 40 times the He transmutation rate in vanadium alloys exposed to a typical fast fission neutron spectrum.

References

1. D. L. Smith, et al., J. Nuclear Material 155-157 (1988) 1359.
2. H. M. Chung, B. A. Loomis and D. L. Smith, J. Nuclear Materials 233-237 (1996) 466.
3. E. Veleckis, R. M. Yonco, and V. A. Maroni, “The Current Status of Fusion Reactor Blanket Thermodynamics”, IAEA Report IAEA-SM-236/56 (1986) p. 3.
4. D. L. Smith, R. E. Buxbaum and C. B. Reed, “Hydrogen Solubility in Vanadium Alloys and Lithium Alloys”, US DOE Report, DOE/ER – 0313/28 (2000) p. 8.

Table 3. Measured and calculated ^{3}He concentrations in vanadium alloys irradiated in

Capsule		4D1	4D2	5E2	5D1	5E1	5C2	5C1	Avg Factor	
V	Measured He-3, appm	8.83	15.2	2.54	31.6	12.3	10.4			
	Normalization Factor	0.87	1.01	1.01	1.59	1.58	1.81		1.3	
	Normalized He-3, appm	6.79	11.69	1.95	24.31	9.46	8.00			
V-1Si	Measured He-3, appm	105				59.9	48.8			
	Normalization Factor	10.39	0.00	0.00	0.00	7.68	8.51		8.9	
	Normalized He-3, appm	11.80	0.00	0.00	0.00	6.73	5.48			
V-5Ti	Measured He-3, appm	18.0	12.2	3.05	19.2	7.19	8.10			
	Normalized Factor	1.78	0.81	1.21	0.97	0.92	1.41		1.2	
	Normalized He-3, appm	15.00	10.17	2.54	16.00	5.99	6.75			
V-5Ti(BL-47)	Measured He-3, appm		15.5				8.59			
	Normalized Factor	0.00	1.03	0.00	0.00	0.00	1.50		1.2	
	Normalized He-3, appm	0.00	12.92	0.00	0.00	0.00	7.16			
V-5Cr	Measured He-3, appm	6.45				3.35	26.3			
	Normalized Factor	0.64	0.00	0.00	0.00	0.43	4.59		0.6	
	Normalized He-3, appm	10.75	0.00	0.00	0.00	5.58	43.83			
V-5Fe	Measured He-3, appm	80.6				34.9	93.4			
	Normalized Factor	7.97	0.00	0.00	0.00	4.47	16.29		9.6	
	Normalized He-3, appm	8.40	0.00	0.00	0.00	3.64	9.73			
V-5Nb	Measured He-3, appm	7.65				6.78	5.70			
	Normalized Factor	0.76	0.00	0.00	0.00	0.87	0.99		0.87	
	Normalized He-3, appm	8.79	0.00	0.00	0.00	7.79	6.55			
V-5Mo	Measured He-3, appm	9.81				3.56	8.22			
	Normalized Factor	0.97	0.00	0.00	0.00	0.46	1.43		0.94	
	Normalized He-3, appm	10.44	0.00	0.00	0.00	3.79	8.74			
V-5Mo	Measured He-3, appm						5.02			
	Normalized Factor	0.00	0.00	0.00	0.00	0.00	0.88		0.94	
	Normalized He-3, appm	0.00	0.00	0.00	0.00	0.00	5.34			
V-3Ti-1Si	Measured He-3, appm	34.7				5.02	6.25			
	Normalized Factor	3.43	0.00	0.00	0.00	0.64	1.09		1.0	
	Normalized He-3, appm	34.70	0.00	0.00	0.00	5.02	6.25			
V5Cr5TiSiAlY	Measured He-3, appm	177				108	260			
	Normalized Factor	17.51	0.00	0.00	0.00	13.85	45.35		16	
	Normalized He-3, appm	11.06	0.00	0.00	0.00	6.75	16.25			
V4Cr4Ti	Measured He-3, appm	11.6	9.0	2.5	14.0	5.5	6.8	8.0		
	Normalized Factor	1.15	0.60	0.99	0.70	0.71	1.19		0.92	0
	Normalized He-3, appm	12.61	9.78	2.72	15.22	5.98	7.39	8.7		
V4Cr4Ti	Measured He-3, appm	9.9	20.9	2.5	14	5.6	74	7.9		
	Normalized Factor	0.98	1.39	0.99	0.70	0.72	12.91		0.92	-1.1734
	Normalized He-3, appm	10.76	22.72	2.72	15.22	6.09	80.43	8.6		
Avg V/V44	Measured He-3, appm	10.11	15.03	2.51	19.87	7.80	5.73			
Calc He in V44	appm He-3	10.8	10.9	5.7	14.6	10.2	6.7	6.6		

QUANTITATIVE OXYGEN ANALYSES FOR V-4Cr-4Ti ALLOYS

Y. Yan, D.P. McGann, D.L. Smith and H. Tsai (Argonne National Laboratory)

OBJECTIVE

The objective of this task is to perform quantitative oxygen analyses on V-4Cr-4Ti alloys from ANL's 832665 heat, the General Atomics (GA)'s 832864 heat and Japan's NIFS-1 heat, and to evaluate the effects of oxygen content on the mechanical properties of V-4Cr-4Ti alloys.

SUMMARY

A quantitative oxygen analysis has been performed for V-4Cr-4Ti alloys. The oxygen concentration is about 210 wppm for Japan's NIFS-1 heat, 324 wppm for ANL’s 832665 heat, and 385 wppm for the GA’s 832864 heat. Our experiment indicates that, after cutting, the oxygen analysis specimen should be pickled to remove the surface oxide.

EXPERIMENTAL PROCEDURE

Three V-4Cr-4Ti alloys: the heat 832665, the heat 832864 and the NIFS-1 heat from ~4-mm plate were cut into small pieces (weight: ~0.3 g) using a wet diamond saw. Specimen temperature was kept low with cutting water to reduce the oxidation produced during the specimen cutting. Before the cutting, the V-4Cr-4Ti plates from the heat 832665 and GA heat were annealed in a high vacuum (better then 3 x 10^{-7} torr) at 1000°C for 1 hour. After cutting, the original oxide patina on the surface was removed using pickling solution (40 ml HF, 40 ml HNO_3, 120 ml lactic acid, 100 ml distilled water). The specimens were rinsed thoroughly with the pickling solution for ~2 minutes. An ultrasonic cleaner with Acetone and then Ethanol was used for ~5 minutes to clean possible dusts/liquids attached on the specimens that were induced during sample preparation.

Oxygen analyses were performed by using a LECO oxygen determinator at Argonne National laboratory. The determinator is located in a glove box, and can be used to both irradiated and unirradiated specimens. According to the operation procedure, the determinator had been calibrated for the oxygen by a standard sample before the analysis was performed.

RESULTS

Pre-peak from the Surface Oxide

To evaluate the effect from the surface oxide, the oxygen analysis was performed on specimens from the heat 832665 under different sample preparation conditions: 1) as-cut specimens (no pickling); 2) after cutting, clean the specimens with Acetone/Ethanol in an ultrasonic cleaner; 3) after cutting, perform pickling and then cleaning the specimens with Acetone/Ethanol in an ultrasonic cleaner.

It has been found that, for the as-cut specimens of the heat 832665, there is a pre-peak of the oxygen (see Fig. 1), and the oxygen concentration is also higher than that in the specimens that were cleaned by Acetone/Ethanol in an ultrasonic cleaner. This indicates that there was some contamination on the specimen surface before ultrasonic cleaning. Our tests also showed that, after pickling and Acetone/Ethanol cleaning, the oxygen concentration is lower than both the as-cut and the as-cleaned samples. No pre-peak of the oxygen was observed in the pickled and then Acetone/Ethanol cleaned sample (see Fig. 2). Detailed analyses indicated that the total oxygen contribution from the surface contamination on the specimens induced during sample preparation could be as high as 20-30% of the total, depending on the sample preparation. Thus it is necessary to perform pickling and Acetone/Ethanol cleaning before the oxygen test is performed.

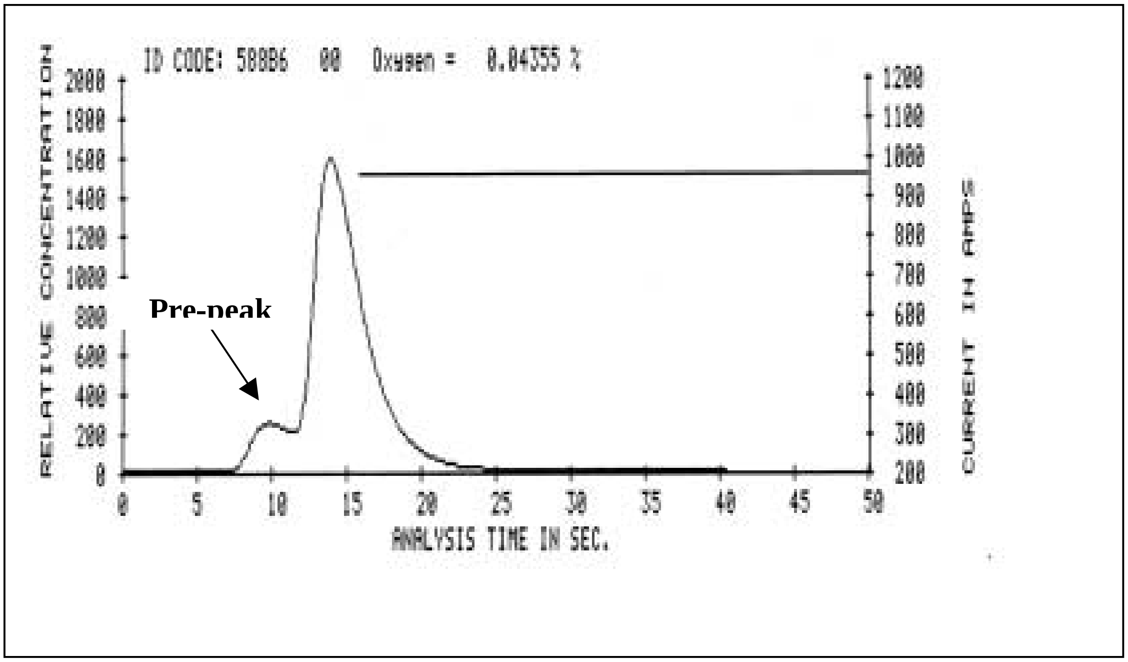

Fig. 1. Oxygen analysis for the as-cut specimen of the heat 832665.

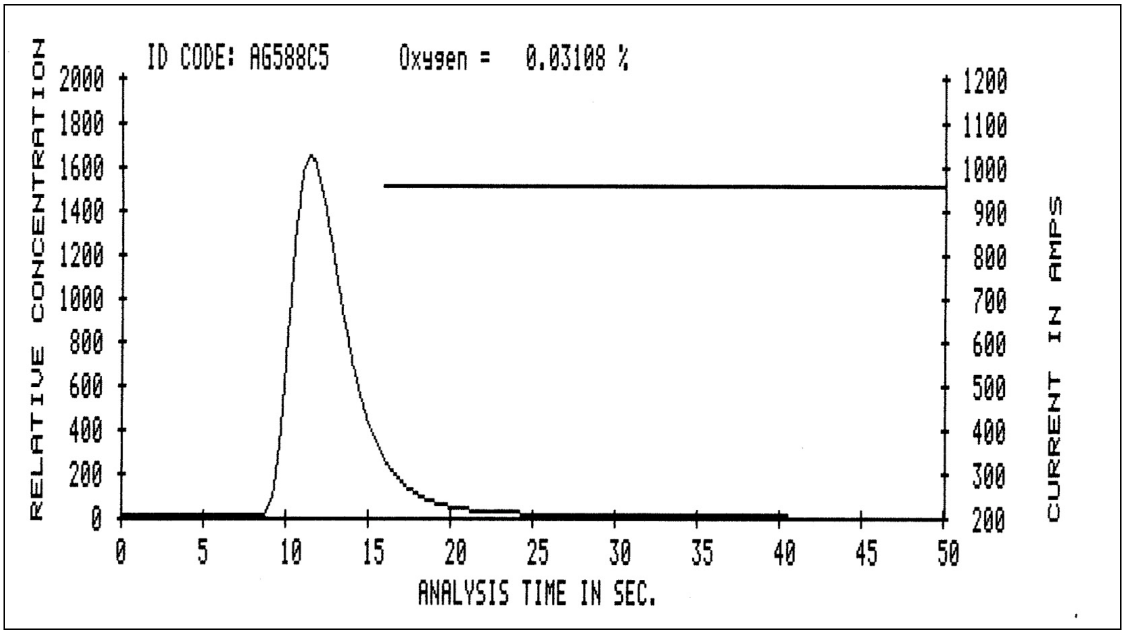

Fig. 2. Oxygen analysis for a specimen of the heat 832665. The specimen was pickled, and then cleaned by using Acetone/Ethanol.

ANL vs. Teledyne Results of Oxygen Analysis on V-4Cr-4Ti from the Heat 832665

To obtain a good statistical result, multi-tests were conducted for the V-4Cr-4Ti alloys from the different heats. The results of oxygen analysis on the 4-mm thick plate from heat 832665 are given in Table 1. The chemical analysis for oxygen determined by Teledyne Wah Chang on the ingot is included in the table for comparison. Our analyses indicated that the O content for the 832665 is about 324 ppm with a standard deviation ~3.4%, which is consistent with the Teledyne's result 310 ppm for the alloy ingot.

Table 1. Oxygen analysis on V-4Cr-4Ti from the heat 832665 (annealed plate)

ANL Data (4-mm plate)			TWC Data (ingot)		
Specimen ID	Weight (g)	Oxygen (%)	Specimen ID	Weight (g)	Oxygen (%)
588C5	0.3750	0.0311	1	N/A	0.0280
588C6	0.4232	0.0332	2	N/A	0.0360
588C7	0.2281	0.0315	3	N/A	0.0290
588C8	0.3303	0.0337			
Average		**0.0324**	**Average**		**0.0310**

ANL Results of Oxygen Analysis on V-4Cr-4Ti from the NIFS-1 heat and the GA heat 832864

Table 2 summarizes our results of oxygen analyses on V-4Cr-4Ti alloys from Japan's NIFS-1 heat, the GA's 832864 heat, and ANL's 832665 heat. It was found that the oxygen content of the Japanese heat NIFS-1 is lower than the heat 832665 and GA heat, and the GA heat has the highest oxygen content among these three heats in the ~4-mm plate. This consistent set of oxygen analyses can be used to evaluate the effects of oxygen on the differences in the Charpy impact and tensile properties of the V-4Cr-4Ti alloys. The ductile-to-brittle-transition temperature (DBTT) for all three heats of this alloy annealed at 1000°C is below - 190°C, indicating that the variations in the oxygen content at these levels has little effect on the impact properties [1, 2].

Table 2. ANL result of oxygen analysis on V-4Cr-4Ti alloy specimens

Heat	**Average Oxygen (%)**
NIFS-1	0.0210
GA	0.0385
832665	0.0324

FUTURE ACTIVITIES

The fracture surface of selected specimens after the impact test will be examined by scanning electron microscopy to delineate the fracture mode. Microstructure characterization on these three heats is underway and will be reported in the future.

REFERENCES

1. Y. Yan, H. Tsai, A. D. Storey, D.L. Smith, and Z. Xu, Microstructural characterization and impact properties of V-4Cr-4Ti Laser Weldments**,** Fusion Materials Semiannual Progress Report DOE/ER-0313/28, June 2000.
2. Y. Yan, H. Tsai, D.P. McGann, and D.L. Smith, Impact Properties of V-4Cr-4Ti alloy from the GA's 832864 heat, (this progress report).

UNIAXIAL CREEP BEHAVIOR OF V-4Cr-4Ti Alloy*

K. Natesan, W. K. Soppet, and D. L. Rink (Argonne National Laboratory)

OBJECTIVE

The objectives of the creep test program are to (a) to establish time/temperature relationships for creep properties, such as creep rupture strength, 1% creep in 10,000 hr, onset of third-stage creep, etc., all of which are key parameters in designing structural components for service at elevated temperatures; (b) provide a basis to establish the upper-use temperature associated with creep limits for application of V-base alloys; and (c) evaluate the influence of variations in the concentrations of substitutional and interstitial elements on the creep properties of fusion-reactor-relevant V-base alloys.

SUMMARY

A systematic study is currently being conducted at Argonne National Laboratory (ANL) to evaluate the uniaxial creep behavior of V-Cr-Ti alloys as a function of temperature in the range of 650-800°C and at applied stress levels in the range of 75-380 MPa. At present, the principal effort has focused on the V-4Cr-4Ti alloy of Heat 832665; however, another heat of a similar alloy from General Atomics (GA) will also be used in the study. During this reporting period, additional creep tests were conducted at 700 and 800°C at lower stress levels than in earlier tests. In addition, the tested specimens are examined for O contamination, if any, by vacuum fusion analysis of the tested specimens and by micro hardness measurements of specimen cross-sections. The test results indicate that in the temperature range of 650-800°C, creep deformation follows a power-law creep with stress exponents indicative of a dislocation-climb-controlled process.

INTRODUCTION

Refractory alloys based on V-Cr-Ti are being considered for use in first-wall structures in advanced blanket concepts that involve liquid Li as a coolant and breeding material. Furthermore, advanced concepts that involve He as a coolant also require structural alloys such as V-Cr-Ti, which can withstand thermal loading at high temperature. It is important that for advanced fusion systems, design concepts establish the upper temperature limits for structural components based on various design criteria. At temperatures above 600°C, the time-dependent creep properties of V alloys must be considered when evaluating performance limits.

The long-term creep properties of the V-base alloys will be influenced by the time-dependent nucleation and growth of precipitates that include nonmetallic elements such as O, N, and C. Several of our microstructural studies of V-base alloys have identified precipitates such as face-centered-cubic Ti(O, N, C) with variable O, N, and C ratios. To correlate microstructural development with creep properties, it is essential to establish the time-dependent evolution of type, number, and location of precipitates in V-base alloys. Moreover, development of several of these precipitates can be influenced by the exposure environment during creep testing. Over the long term, creep data are needed for environments with a wide range of chemistries and that encompass high vacuum to low partial pressures of O and H, as well as He of various purities.

SCOPE OF WORK

In the near term, the program will experimentally evaluate uniaxial creep properties of V-Cr-Ti materials in high-vacuum environments at temperatures of 650-800°C, with emphasis on baseline creep behavior of the alloys and correlations between microstructures and properties. Another aspect of the program will be creep

---

*This work has been supported by the U.S. Department of Energy, Office of Fusion Science, under Contract W-31-109-Eng-38.

tests on heats of V-base alloys that represent a range of variations in the concentrations of both substitutional and interstitial elements, in order to provide an understanding of the effects of these variables on creep behavior.

EXPERIMENTAL PROGRAM

The effort is focused on the ANL-procured large heat of nominal composition V-4Cr-4Ti and on the GA heat of a similar composition.[1-3] Flat creep specimens (1 mm in thickness) and specimens with cylindrical cross sections (2.5 mm diameter), were used in the initial phase of the program.[3] All specimens were fabricated according to ASTM Standard E8-96a with the gauge length oriented parallel to the rolling direction. Tests were conducted on specimens annealed at 1000°C for 1 h in vacuum.

During this reporting period, several tests were continued at 700 and 800°C. The specimens were wrapped in Ti foil to minimize contamination of the sample, especially by O. The creep-test procedure is in accordance with ASTM E139-96. Four ATS model 2140 uniaxial direct constant-load creep-test machines have been allocated for this program and test details are given in Ref. 3. The test program is aimed at obtaining the steady-state creep rate, onset of tertiary creep, rupture strain, rupture life, and times for accumulation of 1 and 2% strain. At least four stress levels are planned at each temperature to obtain sufficient data to develop Larson-Miller correlations between time, temperature, and applied stress. The information will be used to assess the upper-use temperature for the material, based on appropriate design criteria and as a basis for alloy improvement.

RESULTS

During this period, several additional creep tests were conducted at 700 and 800°C. Furthermore, two tests were completed at 700°C to complement and compare the data generated in the biaxial creep test program at 700°C conducted at Pacific Northwest National Laboratory (PNNL).[4] Creep strain/time plots were reported earlier for several specimens that we tested in vacuum at 650, 700, 725, and 800°C.[3] The data showed that the primary creep period is negligible in all tests, and the secondary (or linear) creep portion of the curve is small. The curves showed an accelerating creep behavior over the range of the present tests, especially at 725 and 800°C. A linear least-squares analysis function is used to provide a consistent method to extract minimum creep rate, onset of tertiary creep, and creep strain at the onset of tertiary creep.[3] Table 1 provides an update of the creep data obtained in the ANL test program. Figure 1 shows the variation of time to rupture and minimum creep rate as a function of applied stress for the alloy tested at 650, 700, 725, and 800°C. An examination of the results showed that in the temperature range of 650-800°C, the creep deformation follows a power-law creep with stress exponents indicative of a dislocation-climb-controlled process.

To determine the extent of O contamination, if any, in the creep specimen, cross sections of the tested specimen were mounted and polished, after which Vickers hardness measurements were made along the thickness direction; the results were reported earlier.[2-3] In general, hardness values ranged from 145 to 195, and variation was negligible within a given specimen, indicating that the contamination is minimal over the range of the current study. Examination of the fracture surfaces of tested specimens showed a ductile mode of fracture in all specimens. The specimens tested at 800°C showed rupture strains of 30-61%, and thinning of the cross section in the fracture zone was significant.

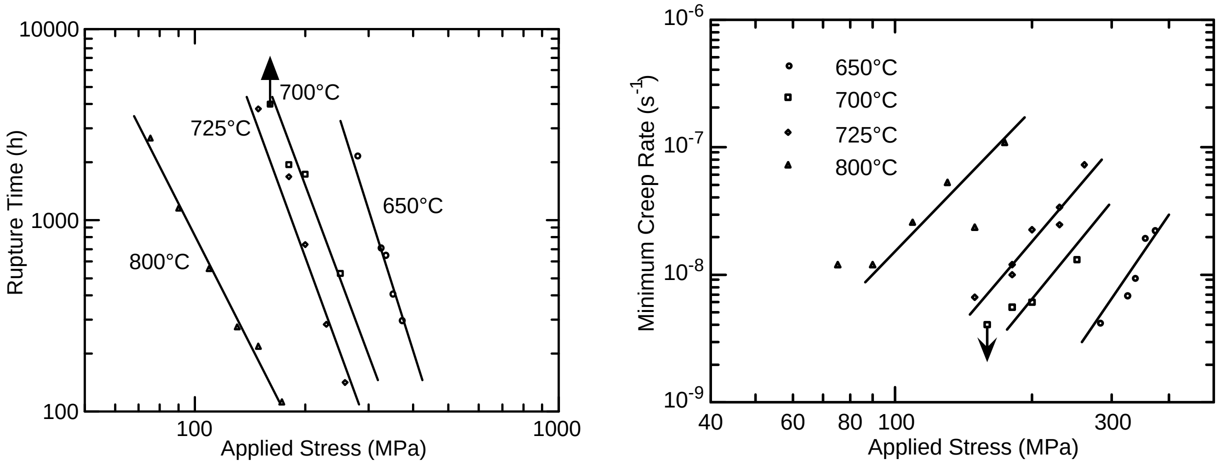

Fig. 1. Variation of rupture time (left) and minimum creep rate (right) as a function of applied stress for V-4Cr-4Ti alloy creep tested at 650-800°C.

Table 1. Creep test data obtained for V-4Cr-4Ti alloy at 650-800°C

Temperature (°C)	Applied stress (MPa)	Time to rupture (h)	Rupture strain	Minimum creep rate (s^{-1})	Time-to-onset of tertiary (h)	Strain-to-onset of tertiary	Time for 1% strain (h)	Time for 2% strain (h)
650	370	300	0.18	2.2×10^{-8}	160	0.021	41	156
	350	415	0.14	2.0×10^{-8}	252	0.023	76	212
	335	661	0.15	9.3×10^{-9}	325	0.017	118	400
	322	719	0.16	7.0×10^{-9}	440	0.029	-	-
	280	2176	0.18	4.2×10^{-9}	1250	0.024	360	1025
700	250	530	0.27	1.3×10^{-8}	250	0.016	120	282
	200	1715	0.28	6.1×10^{-9}	325	0.013	230	510
	180	1959	0.30	5.6×10^{-9}	525	0.014	300	650
	180[a,b]	>3800	>0.04	1.1×10^{-9}	1050	0.007	1300	2300
	160[c]	>4000	>0.04	$<4.0 \times 10^{-9}$	-	-	-	-
725	260	139	0.17	7.2×10^{-8}	75	0.024	20	63
	230	280	0.25	3.3×10^{-8}	106	0.024	58	130
	230[b]	215	0.23	2.4×10^{-8}	105	0.014	61	127
	200	737	0.27	2.2×10^{-8}	265	0.023	78	220
	180	1701	0.32	1.0×10^{-8}	530	0.029	50	315
	180[b]	2281	0.43	1.2×10^{-8}	475	0.024	140	379
	150	3783	0.38	6.6×10^{-9}	270	0.012	211	458
800	174	112	0.30	1.1×10^{-7}	45	0.023	14	38
	150	215	0.46	2.3×10^{-8}	85	0.011	77	115
	130	275	0.61	5.3×10^{-8}	45	0.013	37	59
	110	559	0.46	2.6×10^{-8}	67	0.012	61	101
	90	1147	0.55	1.2×10^{-8}	150	0.075	-	-
	75	2691	0.45	1.2×10^{-8}	200	0.014	120	270
	75[b,c]	>3525	>0.09	2.7×10^{-9}	925	0.014	475	1200

[a] In progress.

[b] Round cross-section specimen.

[c] Terminated before failure.

REFERENCES

1. K. Natesan, W. K. Soppet, and D. L. Rink, Uniaxial Creep Behavior of V-Cr-Ti Alloys, Semiann. Progress Report for Period Ending June 30, 1999, DOE/ER-0313/26, Sept. 1999, p. 20.
2. K. Natesan, W. K. Soppet, and D. L. Rink, Uniaxial Creep Behavior of V-Cr-Ti Alloys, Semiann. Progress Report for Period Ending December 31, 1999, DOE/ER-0313/27, March 2000, p. 17.
3. K. Natesan, W. K. Soppet, and D. L. Rink, Uniaxial Creep Behavior of V-Cr-Ti Alloys, Semiann. Progress Report for Period Ending June 30, 2000, DOE/ER-0313/28, Sept. 2000, p. 39.
4. R. J. Kurtz and M. L. Hamilton, Biaxial Thermal Creep of V-4Cr-4Ti at 700 and 800°C, ibid, p. 3.

CHARACTERIZATION AND IMPACT PROPERTIES OF V-4Cr-4Ti LASER WELDMENTS*

Y. Yan, D.L. Smith, Z. Xu, and H. Tsai, (Argonne National Laboratory) and T. Nagasaka and T. Muroga
(National Institute of Fusion Science, Japan)

OBJECTIVE

The objective of this task is to assess the quality of laser welds on various heats of V-4Cr-4Ti alloys and to evaluate the effects of alloy chemistry and microstructure and the effects of weld parameters on the mechanical properties of weldments. In addition, modifications of the alloy microstructure induced by the laser beam provides a sensitive method for evaluating the effects of microstructural and compositional variations on the mechanical properties of these alloys. This effort includes evaluation of methods for controlling the atmospheric contamination of during welding. This activity involves joint work conducted as part of the US/Japan(Monbusho) collaboration.

SUMMARY

The effects of alloy chemistry and microstructure on the Charpy-impact properties of laser weldments of three heats of V-4Cr-4Ti alloy were investigated. The impact properties of all three heats indicate similar behavior with a DBTT of approximately -200°C based on one-third size Charpy specimens in the annealed condition. However, The Charpy impact properties of the weldments, which have a significantly different microstructure, indicate significantly different DBTT's for the three heats. Laser welds or bead-on-plate microstructures obtained with the laser beam provide a unique method for investigating the effects of microsturctural and trace element concentrations on the properties of these alloys. Chemical analyses for several trace elements have been performed on the three heats in an attempt to determine which elements affect the mechanical properties. Further research is in progress to investigate the sensitivity of the V-4Cr-4Ti alloy system to minor variations in trace element concentrations and microstructural variations produced by varying the heat treatment.

EXPERIMENTAL PROCEDURE

A specific objective of this activity is to evaluate the effects of alloy chemistry variations in the various heats on V-4Cr-4Ti alloys on the properties of laser weldments and of variations in the microstructure produced by the laser beam. The starting material for this series of tests was obtained from the 500 kg heat #832665 of V-4Cr-4Ti alloy produced in the US by TWC for ANL, the 1200 kg heat #832864 produced by TWC for GA, and a 30 kg heat of V-4Cr-4Ti alloy produced in Japan for NIFS. Material used for this series of tests was in the form of ~4-mm thick plate annealed at 1000 or 1050°C for 1-2 hr. Chemical analyses were performed on the 4-mm plate and compared with analyses supplied by the vendor. All samples were chemically pickled to remove any surface contamination before sending for analysis. Laser welding was performed on a Nd:YAG laser welding facility [1]. The laser weldment was produced by butt-welding of two annealed plates of ~4-mm thickness. Direction of the weld travel was perpendicular to the rolling direction of the plate. Details of the welding procedure are given in Ref. 1.

An electric discharge machine was used to cut all of the Charpy-impact specimens. The specimens were 1/3-size, i.e., 3.3 mm thick x 3.3 mm wide x 25.4 mm long, with a 30°, 0.61-mm-deep, 0.08-mm-root-radius V notch. The base metal specimens were machined from an annealed plate. Notch orientation (i.e., crack propagation direction) was perpendicular to the final rolling direction and into the thickness of the plate. The weld specimens were prepared with the V-notch in the weldment in the thickness direction, as shown in Fig. 1.

Charpy tests were conducted with a Dynatup drop-weight tester. The tester was verified before these tests by using a 1/3-size high-energy ferritic steel calibration specimen supplied by Oak Ridge National Laboratory. The calibration showed good agreement (within 1%) between the ANL measured absorbed energy and the published ORNL data [2].

RESULTS

Chemical Analysis

Chemical analysis for selected elements have been performed for the ~4-mm plate used for the welding and the Charpy impact testing. The results of these analyses are presented in Table 1 along with analyses of the ingot materials for each heat. In general, the analyses for the plate material are in good agreement with results from the ingot analyses. The oxygen analyses indicate that contamination of the alloys during the many rolling and annealing steps to the 4-mm plate was negligible. The most notable differences in the impurity concentrations measured are the higher Si content of 832665, the lower Al and Fe contents in NIFS-1, the high Mo content of 832665, and the low Nb content of NIFS-1. The oxygen concentrations in the ~4-mm plate are highest for the 832864 and lowest for NIFS-1; however, these are not large differences.

Table 1. Chemical Analysis of V-4Cr-4Ti Heats

Element	Heat #832665		Heat #832864		Heat NIFS-1		
	Nominal Ingot (wppm)	Base Weld Plate (wppm)	Nominal Ingot (wppm)	Base Weld Plate (wppm)	Ingot 31kg Japan (wppm)	Nominal 6.6mm Plate Japan (wppm)	Base 4.0mm Plate ANL (wppm)
O	310	324*	397	385	181	181	210**
N	85		130	65	103	88	
C	80		37		56	67	
Si	780	570	273	<100	200	200	<100
Al	160	250	193	208	100	100	81
Fe	220	190	227	125	200	200	37
Mo	320	300	<50	30	<100	<100	16
Nb	<60	80	106	114	<100	<100	0.6
Cu		7		6			6
Ni		9		7			<5

*Avg. 4 analyses **Avg. 5 analyses

Oxygen analyses were also performed on selected laser weldments to determine the extent of any oxygen contamination during the laser welding. Results of the oxygen analyses for the weld material are compared with the values for the annealed plate materials in Table 2. In all three materials the oxygen pick-up in the weld region was quite small demonstrating that the inert gas purge system used on the laser welder provided adequate environmental control. This type of environmental control provides high flexibility for laser welding of large components and for field welding.

Table 2. Oxygen Analysis of Laser Weld Joints of V-4Cr-4Ti Alloys

Specimen Number	Oxygen, wppm Weld	 Base Metal
832665/ID303/300A	236	324
832665/ID#052500A	313	324
Nifs-1/ID#J031300/JP-B-1	286	210
832864/ID#1019001	469	385

Impact Properties of V-alloy Weldments

The Charpy impact properties of the laser weldments provide a sensitive indication of the effects of chemistry and microstructure on the properties of the vanadium alloys. The Charpy impact properties for the three heats of V-4Cr-4Ti alloys have been measured. The impact properties for the 832665 and NIFS-1 heat are presented in Fig. 1. The Charpy impact properties for 832864, which are presented in a related paper for this Semiannual report period [1], are similar to those for the 832665 heat. The DBTT of the weldments based on the one-third size Charpy specimens are slightly below room temperature, approximately 0°C for both US heats (832665 and 832864). The DBTT of the NIFS-1 heat is below -175°C, which is nearly the same as that of the base material for all three heats.

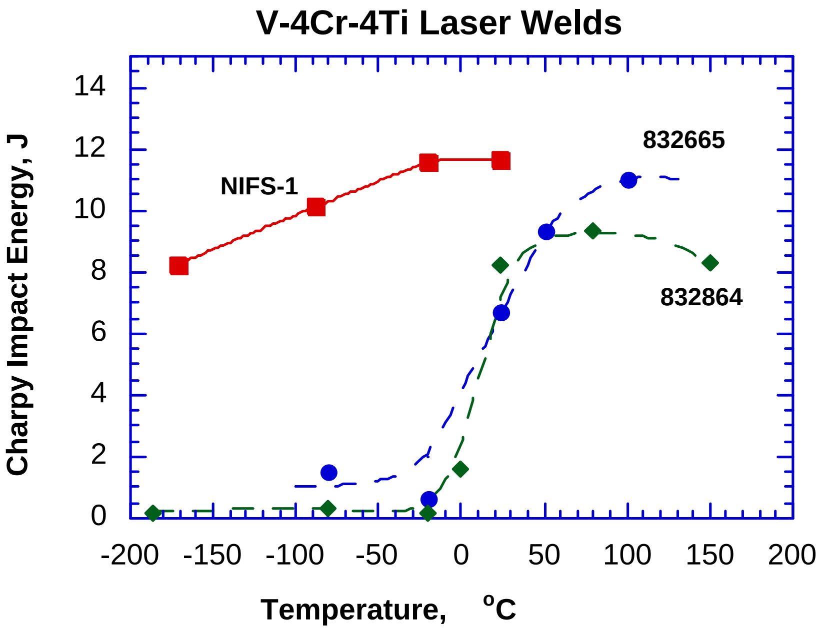

Fig. 1. Charpy Impact properties of Laser weldments of V-4Cr-4Ti alloys

An objective of this task is to determine the basis for the significant difference between the DBTT for the 832665 and 832864 heats compared to that for the NIFS-1 heat. The oxygen content of the NIFS heat is lower than that of the other heats; however, the oxygen content of the 832864 heat differs from that of the 832665 heat by about the same amount as the difference between the NIFS-1 heat and the 832665 heat. As indicated above, the Al, Fe and Nb are all significantly lower in the NIFS-1 heat and; therefore, could contribute to the difference in the impact properties. The Si and Mo contents are significantly higher in the 832665, but the DBTT is similar to that of the 832864 heat, which would indicate that these elements are not the primary contributor to the difference in impact properties. These data would suggest that either the Al, Fe or Nb may be the major contributor to the differences in the impact properties unless some other trace element not included in these analyses is responsible.

Clearly, evaluation of the laser weldments appears to provide a sensitive technique for evaluation of the effects of trace element and/or microstructure on the properties of candidate vanadium alloys. A similar approach using the laser beam as a means of producing various thermo-mechanical treatments of the microstructure provides a unique method for investigating the effects of composition and microstructure on the properties of vanadium alloys. Further investigations using these approaches will be conducted.

References

[1] Y. Yan, et al., Impact Properties of V-4Cr-4Ti Laser Weldments from the GA (832864) Heat (this progress report)

MICROSTRUCTURAL EXAMINATION OF IRRADIATED V-4CR-4TI PRESSURIZED CREEP TUBES - D. S. Gelles (Pacific Northwest National Laboratory)*

OBJECTIVE

The objective of this effort is to provide further understanding of processes controlling irradiation creep in vanadium alloys.

SUMMARY

Three pressurized tubes of V-4Cr-4Ti have been examined to determine microstructural development due to irradiation creep following irradiation in ATR at 300ºC.

PROGRESS AND STATUS

Introduction

Application of vanadium alloys such as V-4Cr-4Ti for fusion requires understanding of irradiation creep response in order to optimize reactor design. A number of experiments are underway in order to provide that data,[1] but the nature of irradiation creep experiments limits the number of data points that can be accumulated. Generally, this is done by irradiating pressurized tubes and determining the change in tube diameter as a function of irradiation dose. However, recent experiments do not allow reirradiation of specimens and therefore a diameter change measurement includes effects of primary creep, steady state creep, and perhaps, tertiary creep, as well as effects of swelling and densification due to precipitation. It is therefore beneficial to characterize the microstructure and to measure densification and swelling response in order to better assess pressurized tube response. This report is intended to provide microstructural examinations of pressurized tubes of V-4Cr-4Ti heat 832665 following irradiation in the Advanced Test Reactor (ATR), Idaho Falls, at ~300ºC to ~5 dpa. The creep response of pressurized tubes in the ATR experiment is shown in Figure 1. In order to optimize microstructural information obtained from this study, specimens irradiated at the higher temperature were selected for examination. The present study continues work on similar tubes following thermal creep deformation.[2]

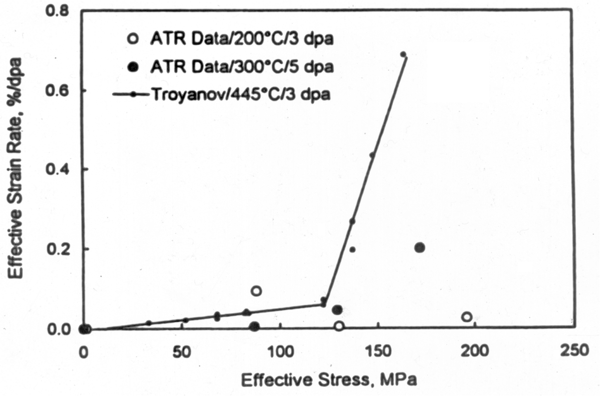

Figure 1. Effective strain rate for ATR irradiated specimens in comparison with torsional creep tests by Troyanov.[1]

Experimental Procedure

Details for the pressurized tubes examined in this study are provided in Table 1. Ring sections of tubing were sectioned and punched to produce 3 mm curved disks. Disks were thinned by grinding but evidence of the curvature was retained in order to be able to orient the microstructure relative to the stress state. Disks were then electropolished

---

[*] Pacific Northwest National Laboratory (PNNL) is operated for the U.S. Department of Energy by Battelle Memorial Institute under contract DE-AC06-76RLO-1830.

at low temperature using standard techniques to produce thin foils. Each disk was mounted in the microscope so that images could be related to the tube orientation and therefore the state of stress could be related to the microstructure. Dislocation imaging involved procedures that allowed identification of all $\frac{a}{2}$<111> Burgers vectors present.

Table 1. Conditions for specimens examined.

ID	Hoop Stress (MPa)	Temp. (ºC)	Dose	Strain (%)
A1	0	286	4.3 dpa*	0.11
A10	87	302	4.6 dpa*	0.10
A7	129	300	4.7 dpa*	0.28

* 133 EFPD or 3192 h

Results

The microstructure of the unstressed condition A1 is shown in Figure 2. This figure and the two that follow have been prepared to allow identification of all $\frac{a}{2}$<111> Burgers vectors present, so three views of the same area are given, one in 01$\bar{1}$ contrast and one in 200 contrast both taken near a (011) orientation and the third in $\bar{1}$01 contrast taken after a large tilt of the foil. A large TiO_2 particle is located on the lower right in order to reveal any changes in behavior near such particles.

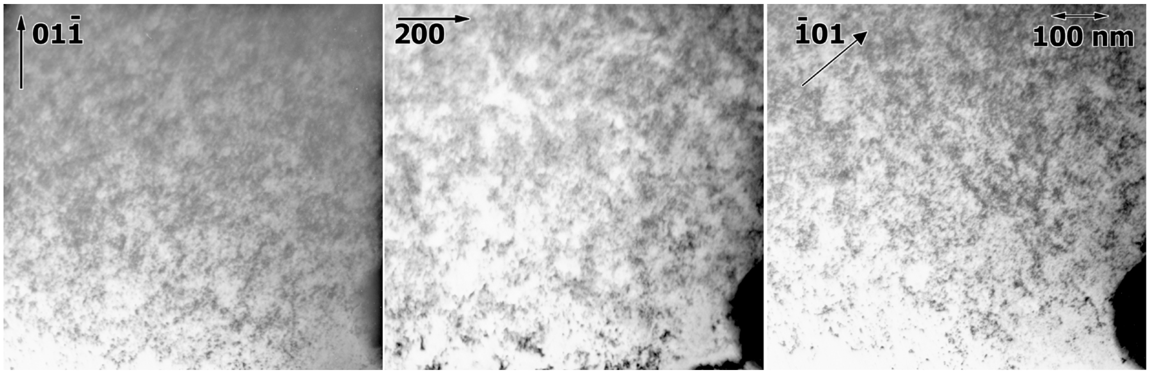

Figure 2. Condition A1 at 300ºC, 0 MPa to 4.3 dpa and 0.11% strain.

Similar images are also provided for conditions A10 and A7 in Figures 3 and 4, respectively. Examination and comparison of Figures 2, 3 and 4 reveals that dislocation images are difficult to identify due to extensive precipitation that is present. Diffraction only revealed additional intensity in the vicinity of ⅔ <222>. The dislocations appear to be only of type $\frac{a}{2}$<111>, based on imaging under 200 strain contrast, as is usually the case in vanadium alloys. No evidence for void swelling could be identified.

In the course of examination of condition A7, it became apparent that several examples of grain boundary migration could be identified. Two examples are provided in Figure 5. In the first case, the boundary has moved but was pinned by a large TiO_2 particle, so migration probably is on the

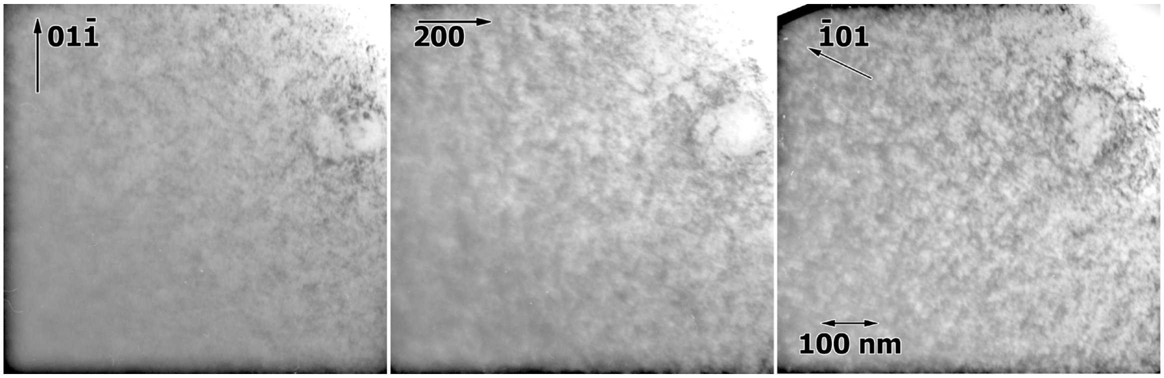

Figure 3. Condition A10 at 300ºC, 87 MPa to 4.6 dpa and 0.10% strain.

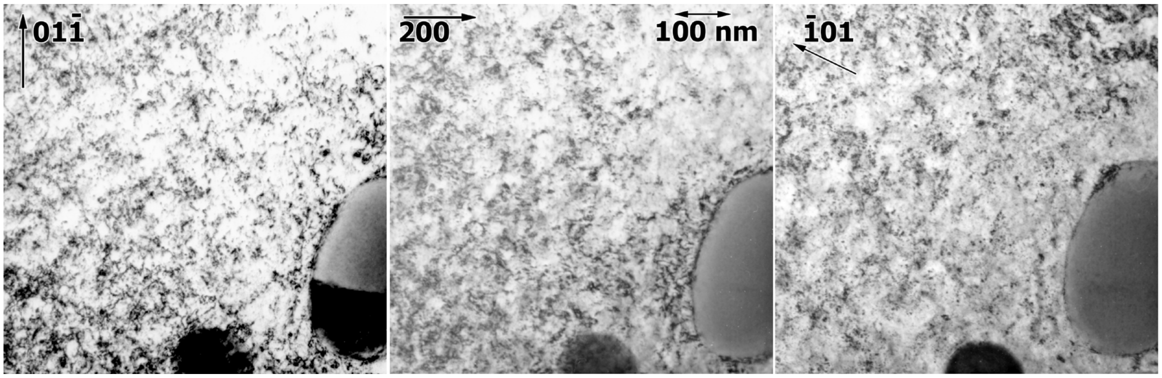

Figure 4. Condition A7 at 300ºC, 129 MPa to 4.7 dpa and 0.28% strain.

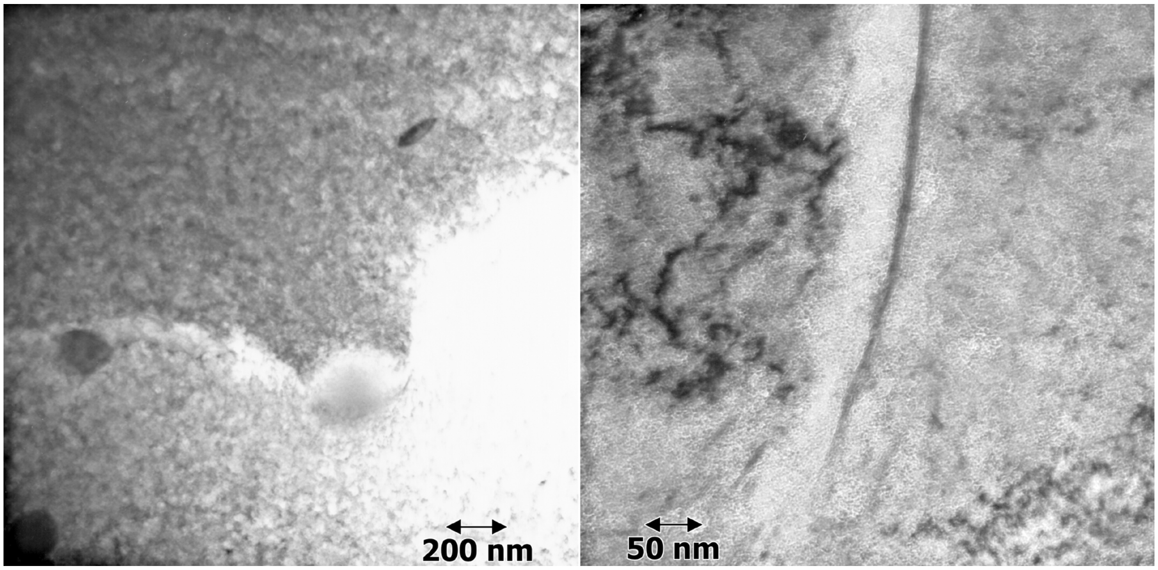

Figure 5. Examples of grain boundary migration in condition A7 at 300ºC, 129 MPa to 4.3 dpa.

order of 800 nm, or close to 1 µm. In the second case, the boundary has polished differently than the surrounding matrix with what appears to be a denuded zone (without precipitation, perhaps) adjacent. Specimen A7 was further examined using field emission gun analytical electron microscopy in order to identify chemistry changes near migrating boundaries. Results are given in Figure 6 showing plots of composition as a function of position across the boundary. A digital image is inset for each plot in order to show the positions of the points analyzed. Scan “gb 1” indicates enhancement of Cr at the boundary and depletion to the right with accompanying enhancement of Si at the boundary. Scans “gb 6” and “gb 7” of the same boundary but at different locations confirm Cr enrichment at the boundary. Scan “gb 3 repeat” demonstrates extremely high Si levels. Therefore, enrichment due to Cr and Si is indicated in coordination with grain boundary migration but Ti shows negligible evidence of enrichment.

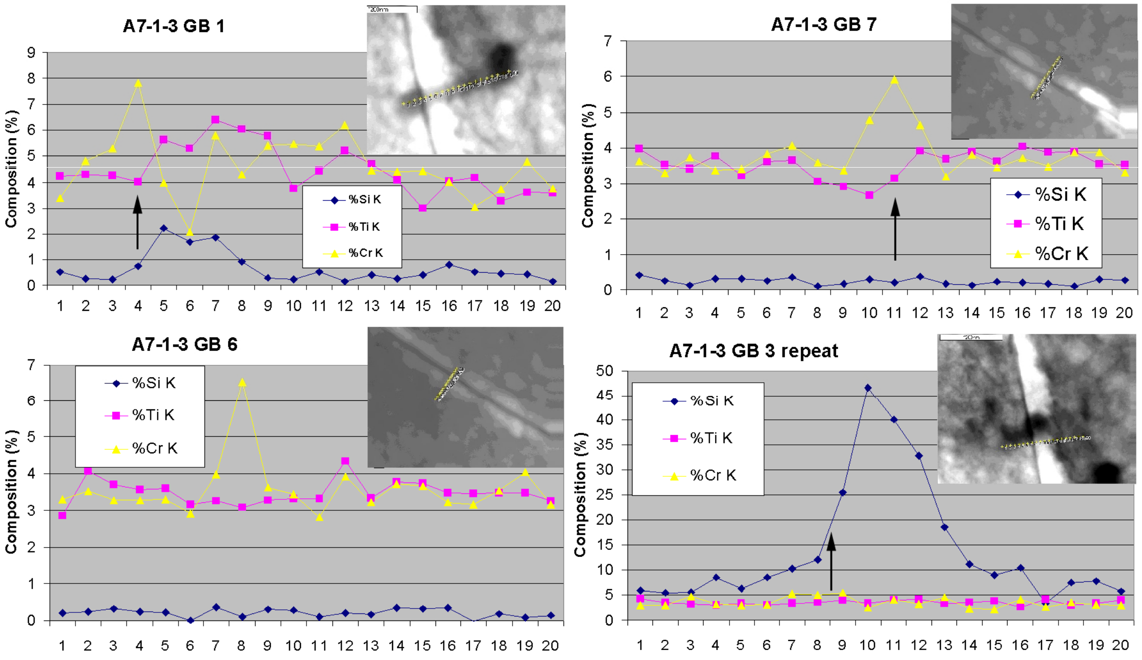

Figure 6. Grain boundary composition profiles in condition A7 at 300ºC, 129 MPa to 4.3 dpa.

Discussion

The results of microstructural examinations of irradiated V-4Cr-4Ti pressurized tubes may be summarized as follows:

> Extensive fine precipitation was found with diffraction intensity at ⅔ <222>. Precipitates may be nucleating near dislocation structure.
>
> The dislocation structure consisted of perfect dislocation line segments with few loops identified.
>
> Stress appears to encourage grain boundary migration

Evidence for segregation of Cr to boundaries and Si behind boundaries was found to accompany grain boundary migration.

Therefore, irradiation creep of V-4Cr-4Ti is probably controlled by climb of $\frac{a}{2}$<111> dislocations. Grain boundary migration is observed, probably enhanced by stress, but it is not anticipated that grain boundary sliding plays an important role in deformation. As with unstressed conditions, precipitation at low temperatures is extensive, obscuring other microstructural features and leading to irradiation hardening. Identification of the precipitate remains poorly defined. No evidence for non-steady state creep could be found.

It can be noted that this work was hindered by poor foil preparation leading to examinations of thicker specimens than optimum (see for example Figure 3) with a resultant need for digital dodging of the image. Dodging remnants appear at the edge of each image and are retained to emphasize that extensive dodging was used.

Conclusions

Irradiation creep at 300ºC is associated with dislocation development and may be affected by precipitation. Stress appears to encourage grain boundary migration during irradiation creep. Segregation of Cr to boundaries and Si behind boundaries was found to accompany the grain boundary migration.

FUTURE WORK

This work will be continued when more specimens are available for testing. Specimens irradiated in HFIR at 500°C would be appropriate.

ACKNOWLEDGEMENTS

This work would not have been possible without the cooperation and participation of H. Tsai and coworkers at the Argonne National Laboratory.

REFERENCES

[1] H. Tsai, H. Matsui, M. C. Billone, R. V. Strain and D. L. Smith, J. Nucl. Mater. 258-63 (1998) 1471.

[2] D. S. Gelles, M. L. Hamilton and R. J. Kurtz, DOE/ER-0313/26 (1999) 11.

IMPACT PROPERTIES OF V-4Cr-4Ti LASER WELDMENTS FROM THE GA'S HEAT

Y. Yan, H. Tsai, A. D. Storey, D.L. Smith, and Z. Xu (Argonne National Laboratory)

OBJECTIVE

The objective of this task is to assess the quality of both the base metal and the laser weld on V-4Cr-4Ti alloys from the General Atomics (GA)'s heat (832864) and to evaluate the effects of the oxygen content on the impact properties of V-4Cr-4Ti alloys.

SUMMARY

Charpy-impact properties of laser weldments of GA heat 832864 V-4Cr-4Ti alloy were investigated. Impact testing was performed with annealed specimens of the both base metal and the laser weldment in as-machined (by electric discharge machining with water as the flushing fluid) condition. The ductile-to-brittle-transition temperature (DBTT) for the base metal is below –187°C and for the laser weld is about 0°C. Additional microstructure characterization on the laser weld is underway.

BACKGROUND

Laser welding offers potential advantages for welding vanadium alloys, including increased flexibility for field and large component welding with acceptable atmospheric control. A pulsed Nd:YAG laser with a fiber optic delivery system is used to conduct a systematic investigation of the weld parameters and environmental control requirements for obtaining high-integrity laser welds of vanadium alloys. The current effort is focused on evaluation of laser welds on ≈4-mm-thick plate of V-4Cr-4Ti alloys. The post-weld characterization includes Charpy-impact testing and microstructural characterization of the welds.

EXPERIMENTAL PROCEDURE

Fabrication of Charpy Specimens

The starting material for this series of tests was obtained from GA heat V-4Cr-4Ti alloy, which was annealed in a high vacuum (better then 3 x 10^{-7} torr) at 1000°C for 1 hour. Laser welding was performed on a Nd:YAG laser welding facility [1, 2]. The laser weldment was produced by butt welding of two annealed plates of ~4.8 mm thickness. Direction of the weld travel was perpendicular to the rolling direction of the plate. Details of the welding procedure are given in Ref. 2.

An electric discharge machine was used to cut all of the Charpy-impact specimens. The specimens were 1/3-size, i.e., 3.3 mm thick x 3.3 mm wide x 25.4 mm long, with a 30°, 0.61-mm-deep, 0.08-mm-root-radius V notch. Notch orientation (i.e., crack propagation direction) was perpendicular to the final rolling direction and into the thickness of the plate. The weld specimens were prepared with the V-notch in the weldment in the thickness direction, as shown in Fig. 1. The specimens were not exposed to other hydrogenous materials (cleaning fluids, etc.) after they were cut.

Impact Testing

In addition to the weld specimens, several base alloy specimens were tested as a comparison. Under standard test procedures, specimens were cut from cold-worked material and then annealed before testing. In addition to the annealing, this procedure would remove any hydrogen that might have been picked up during machining. For investigation of the weld properties, it was necessary to weld annealed material and then machine the specimens.

Charpy tests were conducted with a Dynatup drop-weight tester. The tester was verified before these tests by using a 1/3-size high-energy ferritic steel calibration specimen supplied by Oak Ridge National Laboratory. The calibration showed good agreement (within 1%) between the ANL measured absorbed energy and the published ORNL data [3].

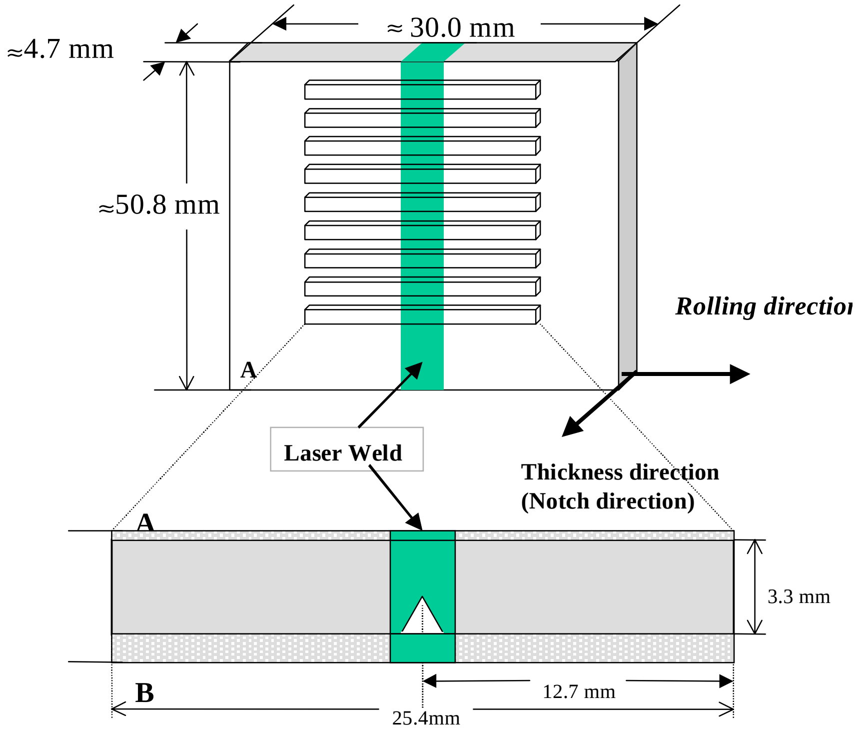

Figure 1. Schematic illustration of the fabrication of Charpy specimens.

Specimen temperature during impact testing was measured with a thermocouple that was spot-welded to the end of the specimen. For tests in which temperatures were above ambient, a hot-air blower provided the heating; for tests in which temperatures were below ambient, argon gas prechilled with a mixture of dry ice, acetone, and liquid nitrogen provided the cooling. In both cases, the specimens were held at the test temperature for a significant period for the temperature to stabilize before the test. Five specimens, three for the base metal and two for the laser weld, were degassed for hydrogen before the impact tests.

RESULTS

Eleven Charpy-impact tests, four for the base metal and seven for the laser weld for GA heat 832864, have been completed this period. The initial series of impact tests was conducted on base alloy specimens to establish the baseline for the weld specimens. Hydrogen-degassed (at 400°C for 1 hr) specimens have been evaluated and reported in previous report [1], thus all impact tests in this report were performed on the nondegassed specimens of GA heat.

Specimens from the base metal and weldments for heats 832864 and 832665 of V-4Cr-4Ti alloys have been tested and the results are included in Figs. 2 and 3. The DBTT of the as-machined base metal from GA heat is below –187°C (see Fig. 2), similar to the DBTT for the H-degassed base metal from the heat 832665. The oxygen content (385ppm) of heat 832864 (4.7mm sheet) is slightly higher than that (324ppm) of the heat 832665 (4.0 mm sheet). Thus our primary results indicate that there is not much difference in the DBTT of the two heats even though there are some differences in the oxygen content [4] and the microstructure [1].

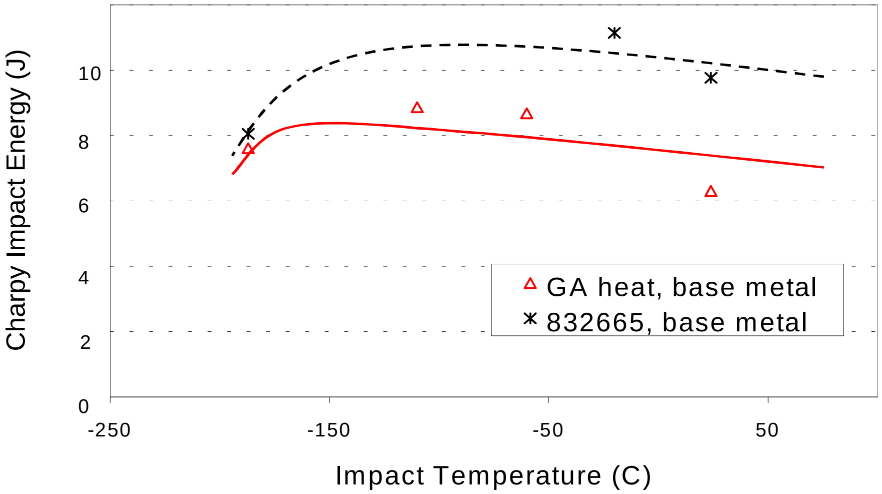

Fig. 2. Charpy-impact data for base metal specimens from GA heat (in as-machined condition) and the heat 832665 V-4Cr-4Ti (hydrogen-degassed at 400°C for 1 hr) showing ductile behavior.

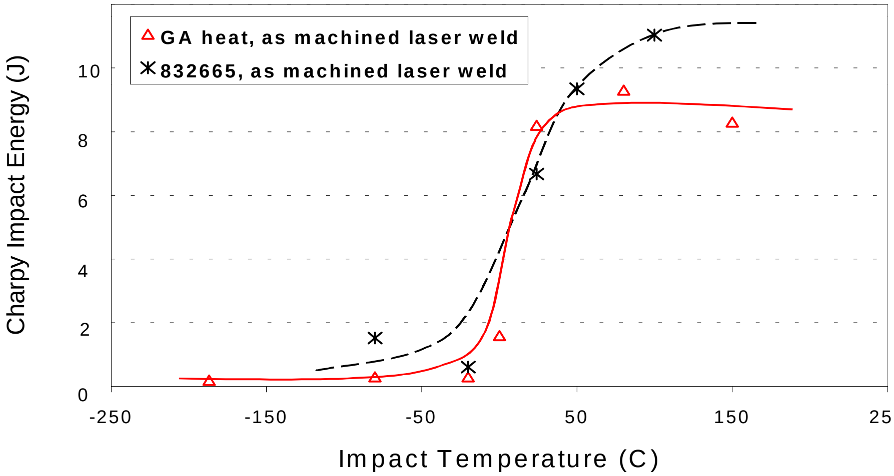

Fig. 3. Charpy-impact data for as machined laser weldment specimens from GA heat (101900I) and the heat 832665 (031300B) V-4Cr-4Ti alloys showing ductile behavior.

Impact tests on the as-machined laser welds indicated that the DBTT of the weld specimens from GA heat is ≈0°C, which is similar to the DBTT of the weld specimens from the heat 832665 (see Fig. 3). Oxygen analyses and chemical analysis are being performed on the weldments to determine the extent of oxygen pickup during the welding and to evaluate effects of oxygen concentration and other impurities on the properties. Further investigations are in progress to determine these various effects on the laser welds.

FUTURE ACTIVITIES

The fracture surface of selected specimens will be examined by scanning electron microscopy to delineate the fracture mode. Oxygen analyses and chemical analyses on the weldments are underway and will be reported in the future.

REFERENCES

[1] Y. Yan, H. Tsai, A. D. Storey, D.L. Smith, and Z. Xu, Microstructural characterization and impact properties of V-4Cr-4Ti Laser Weldments, Fusion Materials Semiannual Progress Report DOE/ER-0313/28, June 2000.

[2] Z. Xu, D.L. Smith, Y. Yan, and C.B. Reed, Laser welding of V-4Cr-4Ti alloy, Fusion Materials Semiannual Progress Report DOE/ER-0313/28, June 2000.

[3] D. J. Alexander, W. R. Corwin, and T. D. Owings, “The Production of Calibration Specimens for Impact Testing of Subsize Charpy Specimens,” ASTM STP 1248, p. 32.

[4] Y. Yan, H. Tsai, D.P. McGann, and D.L. Smith, Quantitative Oxygen AnalysEs for V-4Cr-4Ti Alloys (this progress report).

SUMMARY REPORT ON THE US/JAPAN JUPITER COLLABORATION INTEGRATED FOCUS ON FUNDAMENTAL STUDIES - VANADIUM INITIATIVE

– H.L. Heinisch (Pacific Northwest National Laboratory*) and N. Sekimura (University of Tokyo)

OBJECTIVE

The objective of the Integrated Focus on Fundamental Studies, Vanadium Initiative (IFFS-VI) was to foster direct collaborations, integration of efforts, and joint utilization of resources by the US and Japan under the JUPITER Fusion Materials Collaboration agreement. The basic concept of IFFS-VI was to integrate theory, modeling and experiments, as well as the efforts of Japanese and US participants, toward a common focus on a specific technological problem in Fusion Materials research.

SUMMARY

IFFS-VI was initiated by the participants in the JUPITER Workshop on Theory and Modeling for Fusion Materials held October 30, 1997, during ICFRM-8 in Sendai, Japan. The original initiative is described, participants and collaborations are identified, and progress is summarized.

PROGRESS AND STATUS

Introduction

At the JUPITER Workshop on Theory and Modeling for Fusion Materials held October 30, 1997, in Sendai, the IFFS-VI program was devised and embraced by both sides of the JUPITER collaboration as a means of focusing our individual and joint efforts on the fundamental aspects of radiation effects in fusion materials. IFFS-VI was a program of theory, modeling, simulation and experiments focused on the specific problem of understanding and predicting the effects of temperature variation during fission reactor irradiation on the microstructure development and property changes of V-4Cr-4Ti. This problem was chosen because it aimed our theory and modeling programs at the prime candidate material that has received the least attention in that regard so far. However, it was not our intention that activities under IFFS-VI would preclude further work on advancing the fundamental understanding of irradiation effects in general.

The primary temperature variation experiments to be performed had been planned as a major JUPITER irradiation in HFIR before IFFS-VI was started. They were to provide experimental information on defect accumulation and property changes under well-controlled and monitored conditions. The temperature variation experiments were envisioned as a good comparative data base against which to evaluate the theories and models in V alloys, as well as in general. V-4Cr-4Ti, other V alloys of interest and some pure metals were among the materials included in the experiments. Separate low-dose irradiations were performed in the JMTR reactor and with heavy ions in Japan.

IFFS-VI was expected to continue throughout the remainder of the JUPITER collaboration and become a strong basis upon which to build future Japan/US collaborations on theory, modeling and experiments.

---

* Pacific Northwest National Laboratory is operated for the U.S. Department of Energy by Battelle Memorial Institute under contract DE-AC06-76RLO 1830.

IFFS-VI Tasks

The IFFS-VI theory and modeling tasks fall into the broad categories of Interatomic Potentials, Defect Properties, Cascade Generation, Annealing Simulation and Comparison with Experiments. A more detailed breakdown of the tasks outlined in Sendai is indicated below. It was never anticipated that sufficient resources would exist for the completion of all the tasks during the JUPITER collaboration. However, the task lists serves as an important instrument for focussing and integrating the activities of both sides. The experimental tasks associated with the neutron irradiations in HFIR and JMTR were planned and performed independent of IFFS-VI.

1. Interatomic Potentials

   a) Design and evaluate interatomic potentials for V, Ti, Cr and their interactions among themselves and with He (and O?).

   b) Evaluate applicability and feasibility of Tight Binding molecular dynamics (MD) for defect simulations.

2. Defect Properties

   a.) Calculate properties of defects in vanadium

      i.) Formation energies, binding energies
         Vacancy clusters, loops ,SFT, voids
         SIA clusters, loops
      ii.) Migration energies, diffusivities
         Vacancies, vacancy clusters
         SIAs, SIA clusters, SIA loops

   b.) Determine alloy and impurity properties

      i.) Binding energies of Ti atoms to point defects and clusters
      ii.) Binding energies of Cr atoms to point defects and clusters

   c.) Simulate defect interactions

      i.) V point defect – dislocation interactions
      ii.) Loop – dislocation interactions
      iii.) Role of Ti, Cr near dislocations
      iv.) Oxide precipitate formation

   d.) Evaluate helium interactions

      i.) He diffusivity in V
      ii.) He binding energies to defects, impurities
      iii.) He at grain boundaries

3.. Cascade Generation

   a.) Create data base of cascades in vanadium for relevant recoil energy spectra
   b.) Examine effects of Ti and Cr alloying elements on defect production

c.) Examine effects of cascade overlap

4. Monte Carlo and Analytical Simulations of Microstructural Evolution

    a.) Determine the fractions of surviving defects for individual cascades as a function of temperature and energy

    b.) Simulate damage accumulation in bulk as a function of temperature and recoil spectrum

    c.) Determine the effects of temperature variation on damage accumulation

    d.) Examine the role of grain boundaries on damage accumulation and He accumulation

5. Comparison with Experiments

The Varying Temperature Irradiation Experiment in HFIR will subject test specimens to cyclic changes in temperature during irradiation. Each cycle will consist of 0.05 dpa at a lower temperature, followed by 0.45 dpa at a higher temperature. Ten temperature cycles are planned for each of two low-high temperature pairs (200-350 C and 300-500 C). TEM specimens and mini-tensile, -Charpy and -bend bar specimens will be irradiated. Materials include ferritic and austenitic steels, refractory alloys, copper alloys and vanadium alloys. The vanadium alloys include pure vanadium, binary and ternary alloys, as well as the V-4Cr-4Ti alloy that is the subject of IFFS-VI. Pure Fe, Cu, Mo and W are also included in the experiment matrix.

Prior to obtaining the results from repeated cycles in HFIR, several irradiations will be carried out in JMTR for conditions identical to one cycle of the HFIR Varying Temperature Irradiation Experiment.

Some irradiation effects data for vanadium, V-4Cr-4Ti and other vanadium alloys already exists, although effects of temperature variation are not included.

IFFS-VI Strategy

It was envisioned that most of the IFFS-VI tasks could be worked on simultaneously and at various levels of physical realism until all the pieces could be fit together with the requisite level of physical reality. It was also expected that many of the developments in theory and modeling of irradiation effects that have been ongoing for many years are directly relevant to IFFS-VI without being developed specifically for V-4Cr-4Ti or pure V or even bcc metals and alloys, especially the development of models over multi-scales dealing with defect accumulation, microstructure evolution and mechanical property changes. These models are being developed in a general way and can be made specific to V-4Cr-4Ti when the necessary fundamental information for that material is available from first principles calculations, MD simulations, etc.

IFFS-VI Progress in Theory, Modeling and Experiments

Only a small fraction of the items on the daunting list of tasks above has been completed, but, given the unofficial nature of the Theory and Modeling Tasks under JUPITER and the limited resources available, IFFS-VI should be considered a success. Several direct collaborations of US and Japanese participants were initiated or sustained in response to the IFFS-VI program. Tools have been developed to investigate issues specific to vanadium as well as to extend our basic knowledge of radiation effects in metals and alloys. Perhaps IFFS-VI even influenced individual program goals and priorities. Specific details of the technical accomplishments under IFFS-VI can be found in the publications listed below.

A progress report on the first year of IFFS-VI was published in the *Fusion Materials Semiannual Progress Report for the Period Ending December 31, 1998* (DOE/ER-0313/25, 1999, p. 254). Progress on IFFS-VI was also reviewed at two JUPITER Collaboration Workshops on Theory and Modeling, held following the ICFRM-9, October 10-15, 1999 in Colorado Springs, and following the Materials Research Society Fall Meeting in Boston, December 1, 2000.

Progress on the Experiments

The Varying Temperature Irradiation Experiment in HFIR ended May 16, 1999, after eight of the planned ten cycles had been completed. A total dose of 4 dpa in the vanadium alloys was achieved. Post-irradiation examination of the specimens began in late 2000.

Lower dose irradiations were also carried out in JMTR under conditions similar to those of the HFIR Varying Temperature Irradiation Experiment but with significantly shorter temperature variation cycles. Ion irradiations with stepwise temperature variation have also been performed. Post-irradiation examination of many specimens has been completed.

IFFS-VI PUBLICATIONS

Below is a list of publications on fundamental studies of radiation damage relevant to IFFS-VI objectives (theory and modeling of damage production, damage accumulation and microstructure evolution; effects of temperature variation; irradiation experiments on vanadium and vanadium alloys and experiments on temperature variation under irradiation) involving US and Japanese JUPITER participants that have been published or submitted during the IFFS-VI program. The list of 36 papers is probably not exhaustive, but it represents well the studies performed in the three categories into which it is organized: Atomistic, Analytical and Experimental studies. Papers listed in **bold** type explicitly involve vanadium or vanadium alloys. Seven of the papers involve direct collaboration of Japanese and US investigators, as indicated by their authorship.

ATOMISTIC

E. Alonso, M. J. Caturla, T. Diaz de la Rubia and J. M. Perlado, Simulation of damage production and accumulation in vanadium, J. Nucl. Mater. 276 (2000) 221.

K. Morishita and T. Diaz de la Rubia, "A Molecular Dynamics Simulation Study of Displacement Cascades in Vanadium", J. Nucl. Mater. 271&272 (1999) 35.

K. Morishita, T. Diaz de la Rubia and A. Kimura, Mobility of self-interstitial atom clusters in vanadium, tantalum and copper, COSIRES

2000, USA, July, 2000, to be published in Nuclear Instruments and Methods in Physics Research B.

T. Morioka, K. Morishita and N. Sekimura, Monte-Carlo Simulation of point-defect behavior in cascades, Nucl. Inst. and Methods B 153 (1999) 130.

Y. Shimomura, I. Mukouda, K. Sugio and P. Zhao, Atomistic processes of damage evolution in neutron-irradiated Cu and Ni at high temperature, Rad. Effects and Defects in Solids, 148 (1999) 127.

Y. Shimomura, I. Mukouda and K. Sugio, Computer simulation on the void formation in neutron-irradiated Cu and Ni at high temperature, J. Nucl. Mater. 271&272 (1999) 225.

M. J. Caturla, N. Soneda, E. Alonso. B. D. Wirth, T. Diaz de la Rubia and J. M. Perlado, Comparative study of irradiation damage accumulation in Cu and Fe, J. Nucl. Mater. 276 (2000) 13.

R. Stoller, The role of cascade energy and temperature in primary defect formation in iron, J. Nucl. Mater. 276 (2000), 22.

Dislocation loop structure, energy and mobility of self-interstitial atom clusters in BCC iron, B. D. Wirth, G. R. Odette, D. Maroudas and G. E. Lucas, J. Nucl. Mater. 276 (2000) 33.

E. Kuramoto, Computer simulation of fundamental behaviors of interstitial clusters in Fe and Ni, J. Nucl. Mater. 276 (2000) 143.

Q. Xu, H. L. Heinisch and T. Yoshiie, Effects of temperature variation during neutron irradiation on defect accumulation in copper, J. Nucl. Mater. 283-287 (2000) 297.

H. L. Heinisch, B. N. Singh and S. I. Golubov, The effects of one-dimensional glide on the reaction kinetics of interstitial clusters, J. Nucl. Mater. 283-287 (2000) 737.

K. Morishita, T. Diaz de la Rubia, E. Alonso, N. Sekimura and N. Yoshida, A molecular dynamics simulation study of small cluster formation and migration in metals, 283-287 (2000) 753.

ANALYTICAL

E. Donahue, G. R. Odette and G. E. Lucas, On the mechanisms and mechanics of fracture toughness of V-4Cr-4Ti alloy, J. Nucl. Mater. 283-287 (2002) 518.

E. Donahue, G. R. Odette and G. E. Lucas, A physically based constitutive model for a V-4Cr-4Ti alloy, J. Nucl. Mater. 283-287 (2000) 637.

S. Sharafat and N. M. Ghoniem, Comparison of a microstructure evolution model with experiments on irradiated vanadium, J. Nucl. Mater. 283-287 (2000) 789.

N. M. Ghoniem, L. Sun, Fast sum method for the elastic field of 3-D dislocation ensembles, Phys. Rev. B, 60 (1999) 128 .

N. M. Ghoniem, B. N. Singh, L. Z. Sun and T. Diaz de la Rubia, Interaction and accumulation of glissile defect clusters near dislocations, J. Nucl. Mater. 276 (2000) 166.

Y.Katoh, R. E. Stoller, T.Muroga and A.Kohyama, Simulating the influence of radiation temperature variations on microstructural evolution, J. Nucl. Mater. 283-287 (2000) 313.

M. Ando, Y. Katoh, H. Tanigawa and A. Kohyama, The contribution of various defects to irradiation-induced hardening in austenitic model alloy, J. Nucl. Mater. 283-287 (2000) 423.

N. M. Ghoniem, L. Z. Sun, And B. N. Singh , 3-D dislocation dynamics study of plastic instability in irradiated copper," J. Nucl. Mater., 283-287 (2000) 741.

N. M. Ghoniem, S.- H. Tong, and L. Z. Sun, Parametric dislocation dynamics: a thermodynamics-based approach to investigations of mesoscopic plastic deformation, Phys. Rev. B, 61 (2000) 913.

N. M. Ghoniem, Computational methods for mesoscopic, inhomogeneous plastic deformation, Proc. First Latin American Symposium on Materials Instabilities, Valpareso, Chile, Kluwer Publication, 2000.

N. M. Ghoniem, S.- H. Tong, B. N. Singh, and L. Z. Sun, On dislocation interaction with radiation- induced defect clusters and plastic flow localization in FCC metals, Phil. Mag., submitted (2001).

J. M. Huang and N. M. Ghoniem, The dynamics of dislocation interaction with sessile self-interstitial atom (sia) defect cluster atmospheres, accepted for publication, J. Comp. Mat. Science, (2001).

L. Z. Sun, N. M. Ghoniem, Z. Q. Wang, Analytical and numerical determination of the elastic interaction energy between glissile dislocations and stacking fault tetrahedra in FCC metals, accepted for publication, J. Mat. Sci. & Engr., (2001).

EXPERIMENTAL

N. Nita, T. Iwai, K, Fukumoto and H. Matsui, Effects of temperature change on the mechanical properties and microstructural evolution of vanadium alloys under ion irradiation, J. Nucl. Mater. 283-287 (2000) 60

N. Sekimura, T. Iwai, Y. Arai, S. Yonamine, A. Naito, Y., Miwa, and S. Hamada, Synergistic effects of hydrogen and helium on microstructural evolution in vanadium alloys by triple ion beam irradiation, J. Nucl. Mater. 283-287 (2000) 224.

H. Watanabe, T, Arinaga, K. Ochiai, T. Muroga and N. Yoshida, Microstructure of vanadium alloys during ion irradiation with stepwise change of temperature, J. Nucl. Mater. 283-287 (2000) 286.

K.-i. Fukumoto, H. Matsui, H. Tsai and D. L. Smith, Mechanical behavior and microstructural evolution of vanadium alloys irradiated in ATR-A1, J. Nucl. Mater. 283-287 (2000) 492.

K.-i. Fukumoto, H. Matsui, Y. Candra, K. Takahashi, H. Sasanuma, S. Nagata, and K. Takahiro, Radiation induced precipitation in V-(Cr,Fe)-Ti alloys irradiated at low temperature with low dose during neutron or ion irradiation, J. Nucl. Mater. 283-287 (2000) 535

D. T. Hoelzer, M. K. West, S. J. Zinkle and A. F. Rowcliffe, Solute interactions in pure vanadium and V-4TCr-Ti alloy, J. Nucl. Mater. 283-287 (2000) 616.

T. Nagasaka , H. Takahashi , T. Muroga, T. Tanabe (c) and H. Matsui, Recovery and recrystallization behavior of vanadium at controlled various nitrogen and oxygen levels, J. Nucl. Mater. 283-287 (2000) 816.

T. Hayashi, K. Fukumoto and H. Matsui, Study of point defect behaviors in vanadium and its alloys by using HVEM, J. Nucl. Mater. 283-287 (2000) 868.

D. T. Hoelzer, S. J. Zinkle, and A. F. Rowcliffe, The defect microstructure of V-4Cr-4Ti alloy following neutron irradiation at 323°C, Symposium R on Microstructural Processes in Irradiated Materials, 2000 MRS Fall Meeting, Boston, Nov. 27 - Dec. 1, 2000.

M. Satou, Radiation hardening of vanadium alloys, Symposium R on Microstructural Processes in Irradiated Materials, 2000 MRS Fall Meeting, Boston, Nov. 27 - Dec. 1, 2000.

T.Okita, T. Kamada and N. Sekimura, Effects of dose rate on microstructural evolution and swelling under neutron irradiation, J. Nucl. Mater. 283-287 (2000) 220.

FUTURE WORK

With the completion of the JUPITER Collaboration March 31, 2001, IFFS-VI will be officially terminated, but the overall concept of the IFFS-VI approach and the progress and cooperative efforts in theory, modeling and fundamental experiments that resulted from it will be carried on within the next collaboration.

2.0 SILICON CARBIDE COMPOSITE MATERIALS

EFFECT OF HEAT TREATMENT ON SILICON CARBIDE BASED JOINING MATERIALS FOR FUSION ENERGY

- C. A. Lewinsohn and R. H. Jones (Pacific Northwest National Laboratory)*, T. Nozawa, M. Kotani, H. Kishimoto, Y. Katoh and A. Kohyama (Kyoto University, Japan).

OBJECTIVE

Reliable and practical joining techniques are required to enable the use of silicon carbide composites (SiC/SiC) in fusion energy systems. Based on criteria relevant to fusion applications, silicon carbide (SiC) has been selected as a promising joint material [1]. The objective of this work is to evaluate the thermal stability and mechanical properties of joints consisting of silicon carbide based materials between silicon carbide substrates.

SUMMARY

Two general approaches to obtaining silicon carbide-based joint materials were used. The first method relies on reactions between silicon and carbon to form silicon carbide, or to bond silicon carbide powders together. The second method consists of pyrolysing a polycarbosilane polymer to yield an amorphous, covalently bonded material. In order to assess the long-term durability of the joint materials, various heat treatments were performed and the effects on the mechanical properties of the joints were measured. Although the joints derived from the polycarbosilane polymer were not the strongest, the value of strength measured was not affected by heat treatment. On the other hand, the value of the strength of the reaction-based joints was affected by heat treatment, indicating the presence of residual stresses or unreacted material subsequent to processing. Further investigation of reaction-based joining should consist of detailed microscopic studies; however, continued study of joints derived from polymers is also warranted.

PROGRESS AND STATUS

Introduction

A limitation of SiC/SiC composite materials is that they can only be produced in limited sizes and shapes. Therefore, to fabricate a complete fusion energy system a method of joining SiC/SiC components is required. In fusion energy systems utilizing silicon carbide first-wall materials it would be undesirable to use a joining technique that introduces dissimilar materials at the inner face of the first wall. In addition, to avoid poisoning the plasma, the first wall must be hermetic. Therefore, two attractive methods of joining silicon carbide with other forms of silicon carbide have been developed: reaction bonding [2-5], and preceramic polymer adhesives [6-13]. In this report, recent results regarding the effect of heat treatment on both types of joint will be presented. The results will be incorporated with earlier ones, for completeness.

Experimental Technique

Based upon recent promising reports [9], allyl-hydridopolycarbosilane (aHPCS) was selected as a polymeric precursor to obtain SiC based joints. To evaluate the suitability of joints formed by aHPCS, butt-joined, flexural specimens for four point bend testing were fabricated from plates of monolithic, chemically vapor deposited (CVD) silicon carbide (Morton

---

*Pacific Northwest National Laboratory (PNNL) is operated for the U.S. Department of Energy by Battelle Memorial Institute under contract DE-AC06-76RLO-1830.

Advanced Materials, Woburn, MA) and joined by Starfire Systems, Inc. (Watervliet, NY), developers of the aHPCS polymer. Two plates of CVD silicon carbide, approximately 4 mm-thick, were cut into 25 mm-long by 30 mm-wide pieces. The polymer was applied to the 30 x 4 mm faces and held in a special fixture. The material was cured and pyrolysed by Starfire Systems, Inc. The pyrolysis temperature was 850˚C. The joined materials were sent to Chand Inc. (Worcester, MA), for additional machining into mechanical test specimens.

Plates of monolithic silicon carbide (Hexoloy SA, Carborundum Co., Niagara, NY) were joined using the ARCjoinT technique at NASA Glenn Research Center [3-5]. Two plates of monolithic silicon carbide, approximately 4 mm thick, were cut into 25 mm-long by 30 mm-wide pieces. A carbonaceous mixture was applied to the ends of the plates that were to be joined and this was cured at 110-120°C for 10 to 20 minutes. Subsequently, a slurry of pure silicon powder was applied to the surface of the joint region and heated up to 1425°C for 5-10 minutes. Capillary forces drew the molten silicon into the joint region where it reacted with the carbon to form silicon carbide. The resulting joint material consisted of silicon carbide with controllable amounts of silicon and other phases as determined by the composition of the raw materials and infiltrant. Since all of the silicon carbide in the resulting material is formed by reaction of the liquid silicon with the carbonaceous preform, this method will be referred to as reaction forming (RF).

A limited number of joints between pieces of silicon carbide composite material were also fabricated. This composite was reinforced with Hi-Nicalon fibers (Nippon Carbon Co., Tokyo, Japan) that had been coated with a 1 μm-thick layer of carbon prior to matrix infiltration via chemical vapor infiltration. In addition, an approximately 2 μm-thick layer of silicon carbide was deposited on the outside of the composite to inhibit oxidation at high-temperatures.

Plates of monolithic silicon carbide (Hexoloy SA, Carborundum Co., Niagara, NY) were also joined using a reaction bonding technique. One or two layers of SiC and C powders held in tape form by organic binding agents were placed between two plates of monolithic silicon carbide that was cut into 25 mm-long by 30 mm-wide pieces. The plates were held in a proprietary fixturing and heating apparatus capable of rapid heating and cooling (Busek Co. Inc., Natick, MA). The specimens were heated to 1425°C for 10 to 30 minutes, under applied pressure ranging from $6.90 – 9.65 \times 10^5$ Pa. In this process existing silicon carbide powders are bonded to each other by silicon carbide formed by reaction of the liquid silicon with the carbon powders. Therefore, this latter technique is referred to as reaction bonding (RB). Both latter methods, however, fall into the general class referred to as reaction based.

The plates that were joined using the methods described above were cut into bars that were approximately 44 x 4 x 4 mm. The bars were cut so that the joint was at the middle of the bar and the plane of joining was aligned so that it was parallel to the applied load. Several of the bars were heat treated for 100 h, at 1100°C, in a vacuum furnace or in flowing, gettered argon. Some bars were heat treated, in a cyclic manner, between 200˚ and 1100˚C, for 10 cycles. The bars were heated and cooled at 20˚C/min, in vacuum or flowing argon, and held at 1100˚C for 10 h. Other bars were heat treated, in vacuum, in a cyclic manner between 250˚ and 1100˚ C. The specimens were heated at 425˚C/min and held at 1100˚C for 15 min and cooled at a rate of approximately 142˚C/min. Twenty-five cycles were performed.

Mechanical tests were performed by four-point loading of the bars described above. This configuration subjects the specimens to a constant bending moment in the region between the two inner load points. This test, therefore, is a measure of the flexural strength of the joint. Other tests were performed using asymmetrical four-point loading. This test, as described by Unal [14], subjects the specimens to a constant, through-thickness shear stress in the middle of the specimen. This test, therefore, is a measure of the shear properties of the joint material. Flexural loading was obtained by applying a compressive force on the fixtures using a rigid, mechanical test frame.

Results

The room temperature strength values of all the materials have been reported earlier [15,16]. The values of strength measured varied from 50 – 200 MPa (see Table I). The strength of heat treated specimens, normalised by the average strength value of untreated specimens, is shown in Figure 1. From the data, it is seen that the effect of the 100 h heat treatment, at 1100°C, in argon, on the value of the strength of the joints derived from aHPCS was small. On the other hand, the value of the strength of joints made from reaction-bonded material increased, and that of reaction formed material decreased. These latter results indicate that either residual stresses were present in the specimens tested at room temperature, or microstructural development occurred during the heat treatments. Since the strength of reaction-bonded material was higher when measured at 1100˚C [15], it is likely that some of the increased strength may be due to the relief of residual stress. Detailed microscopic investigations are required to determine the precise mechanisms for the observed behavior.

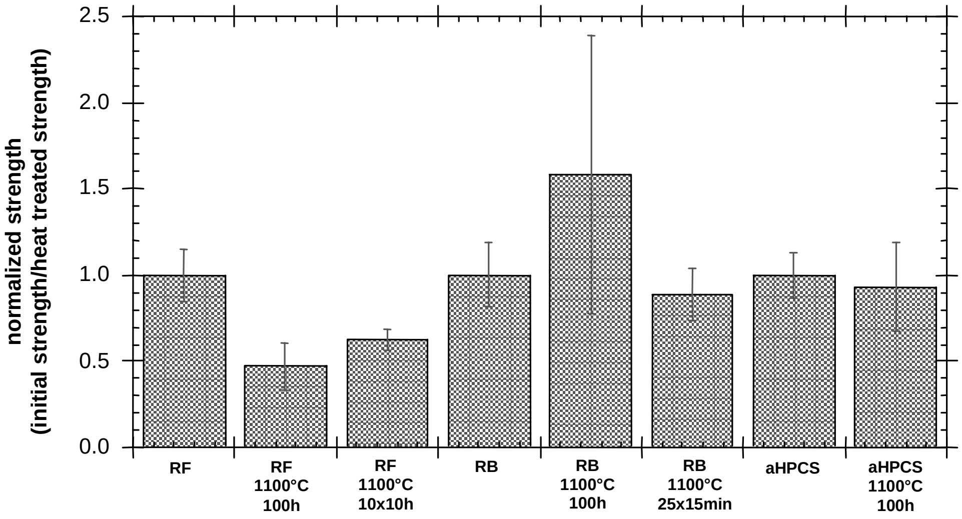

Figure 1. A comparison of room temperature strength after heat treatment, normalised by the strength, for reaction formed (RF), reaction bonded (RB), and polymer derived (aHPCS) joints.

Although the strength values for joints derived from aHPCS were not strongly affected by heat treatment, there is concern that the amorphous nanostructure of these materials is not stable under irradiation. Microcracking was observed on the fracture surfaces of tested specimens. It is well known that silicon carbide based fibers, derived from preceramic polymer materials, undergo shrinkage during irradiation. The material, however, can be processed at relatively low temperatures, which minimizes the potential for degradation of the fibers in composites. Reaction-based joining, however, requires processing above the melting temperature of the particular silicon alloy chosen. Pure silicon melts at 1410˚C. In addition, the influence of excess silicon, prevalent in all reaction-based SiC materials, during irradiation is unknown. Therefore, joints derived from polymer materials deserve further study.

Table I Experimental Results

Joint Material	Substrate	Treatment	Test Method*	Average Strength (MPa)	Std. Deviation (MPa)
Reaction-formed SiC	Sintered SiC	untreated	4PBS	53.4	6.0
Reaction-formed SiC	SiC_f/SiC_m	untreated	4PBS	78.0	8.0
Reaction-formed SiC	SiC_f/SiC_m	untreated	AFPB	32.0	4.9
Reaction-formed SiC	SiC_f/SiC_m	1100˚C,100 h, inert gas	AFPB	15.0	4.4
Reaction-formed SiC	SiC_f/SiC_m	RT-1100˚C, 10 x, 10 h hold	AFPB	20.0	1.9
Reaction-bonded$^{\#}$	Sintered SiC	untreated	4PBS	134	25.4
Reaction-bonded$^{\#}$	Sintered SiC	untreated, tested at 1100˚C, air	4PBS	247	85
Reaction-bonded$^{\#}$	Sintered SiC	1100˚C,100 h, inert gas	4PBS	212	108
Reaction-bonded$^{\#}$	Sintered SiC	250-1100˚C, 25 x, 15 min hold	4PBS	119	20
aHPCS	CVD SiC	untreated	4PBS	85.0	11.0
aHPCS	CVD SiC	1100˚C,100 h, inert gas	4PBS	79.0	21.0

All tests conducted at room temperature, unless otherwise noted.
*4PBS = 1/4, four-point bend strength; AFPB = asymmetric four point bend strength.
$^{\#}$ derived from the tape cast material.

Conclusions

The effects of heat treatments on the strength of silicon carbide-based joints obtained from two general methods were investigated. The strength of joints derived from a polymer precursor were unaffected by heat treatment. On the other hand, heat treatment degraded the strength of reaction formed joints and enhanced that of reaction bonded joints. Polymer derived joints can be fabricated at temperatures that are not expected to degrade the properties of SiC/SiC, yet issues of microcracking must be addressed. On the other hand, reaction-based joining is also an attractive method, but the effect of irradiation on residual silicon must be investigated.

FUTURE WORK

Efforts will be made to optimize processing conditions used for obtaining joints via polymer based methods, such that bending strengths greater than 150 MPa will be obtained. Furthermore, attempts will be made to obtain specimens of reaction-based material with controlled amounts of excess silicon, in order to study the effect of residual silicon on mechanical properties. In addition, efforts will be made to measure the strength of promising joint materials at elevated temperatures.

REFERENCES

[1] C. A. Lewinsohn, R. H. Jones, "A Review of Joining Techniques for SiC_f/SiC_m Composites for First Wall Applications," Fusion Materials Semiannual Progress Report for the Period Ending June 30, 1998, DOE/ER.

[2] B. H. Rabin, and G. A. Moore, "Joining of SiC-Based Ceramics by Reaction Bonding Methods," J. Mat. Synth. & Proc., **1** [3], 195-201 (1993).

[3] M. Singh, "A Reaction Forming Method for Joining of Silicon Carbide-Based Ceramics," Scripta Mater., **37** [8], 1151-1154 (1997).

[4] M. Singh, S. C. Farmer, and J. D. Kiser, "Joining of Silicon Carbide-Based Ceramics by Reaction Forming Approach," Cer. Eng. Sci. Proc. 18 [3], 161-166 (1997).

[5] M. Singh, "Joining of Sintered Silicon Carbide Ceramics For High Temperature Applications," J. Mat. Sci. Lett, in press.

[6] R. Riedel, L. Ruswich, L. An, and R. Raj, "Amorphous Silicoboron Carbonitride Ceramic with Very High Viscosity at Temperatures above 1500°C," J. Am. Ceram. Soc., **81** [12], 3341-3344 (1998).

[7] S. Yajima, K. Okamura, T. Shishido, Y. Hasegawa, and T. Matsuzawa, "Joining of SiC to SiC Using Polyborosiloxane," Am. Ceram. Soc. Bull., **60**, 253, (1981).

[8] A. Donato, P. Colombo, and M. O. Abadirashid, "Joining of SiC to SiC using a preceramic Polymer," pp. 471-476 in High-Temperature Ceramic -Matrix Composites I, A. G. Evans and R. Naslain (eds.), Ceram. Trans., **57**, The American Ceramic Society, Westerville, Ohio, USA, 1995.

[9] W. J. Sherwood, C. K. Whitmarsh, J. M Jacobs, and L. V. Interrante, "Joining Ceramic Composites Using Active Metal/HCPS Preceramic Polymer Slurries," Cer. Eng. Sci. Proc., **18**, 177-184 (1997).

[10] O. Unal, I. E. Anderson, M. Nostrati, S. Ijadi-Maghsoodi, T. J. Barton, and F. C. Laabs, "Mechanical Properties and Microstructure of a Novel SiC/SiC Joint," pp. 185-194 in Ceramic Joining, I.E. Reimanis, C. H. Henager, Jr., and A. P. Tomsia (Eds.), Ceramic Transactions, vol. 77, The American Ceramic Society, Westerville, Ohio, USA, 1997.

[11] P. Colombo, "Joining Ceramics Using Preceramic Polymers," in Interfacial Science in Ceramic Joining, NATO Advanced Research Workshop, Bled, Slovenia, November 12-15, 1997.

[12] P. Colombo, V. Sglavo, E. Pippel, and J. Woltersdorf, "Joining of Reaction-Bonded Silicon Carbide Using a Preceramic Polymer," J. Mat. Sci., **33**, 2409-2416 (1998).

[13] E. Pippel, J. Woltersdorf, P. Colombo, and A. Donato, "Structure and Composition of Interlayers in Joints Between SiC Bodies," J. Eur. Ceram. Soc., **17**, 1259-1265 (1997).

[14] O. Unal, I. E. Anderson, and S. I. Maghsoodi, “A Test Method to Measure Shear Strength of Ceramic Joints at High Temperatures,” J. Am. Ceram. Soc., **80** [5], 1281-1284 (1997).

[15] C. A. Lewinsohn, R. H. Jones, M. Singh, H. Serizawa, Y. Katoh, and A. Kohyama, “Reaction Based SiC Materials for Joining Silicon Carbide Composites for Fusion Energy,” Fusion Materials Semiannual Progress Report for the Period Ending December 31, 1999, DOE/ER.

[16] C. A. Lewinsohn, R. H. Jones, T. Nozawa, M. Kotani, Y. Katoh, and A. Kohyama, “Polymer Derived SiC Materials for Joining Silicon Carbide Composites for Fusion Energy,” Fusion Materials Semiannual Progress Report for the Period Ending June 30, 2000, DOE/ER.

MECHANICAL PROPERTIES OF HELIUM IMPLANTED SILICON CARBIDE – L. L. Snead (Oak Ridge National Laboratory), R. Scholz (JRC Ispra), A. Frias Rebelo (Whereabouts Unknown)

Abstract

It has been long apparent that ceramics will undergo significant gas production, transmutation and material "burn-up" under high energy neutron irradiation. For example, the original calculations [1] for pure SiC exposed to 1 MW-a/m^2 of 14.1 MeV monoenergetic neutrons yielded 1596 appm helium, 440 appm hydrogen, 458 appm magnesium, 234 appm beryllium and 72 appm aluminum, as well as some less significant transmutants. Clearly, helium is the largest product and, because of its limited diffusivity in SiC [2-4], may cause significant swelling and/or stress in the material. This paper will give preliminary results of the effect of high levels of helium on the mechanical properties of CVD SiC.

Discussion

There are many possible mechanical property changes possible due to the fast-neutron transmutation of SiC. The production of the metallic impurities may increase creep as they will tend to migrate to grain boundaries and will, in most cases, be above their melting points. Also, the effect of material burn-up needs to be addressed, especially considering more than one percent of the atoms in the material have been displaced or transmuted at 1 MW-a/m^2, possibly leaving behind gas, vacancies or other fugitive elements in their lattice sites. Helium and hydrogen production (and corresponding production of Mg, Al and Be) is also dependent on the neutron energy spectrum. This is demonstrated in Figure 1, which gives the gas production as a function of the distance through the ARIES IV blanket [5]. Also included in this figure is the gas/DPA ratio in the blanket. From these data, it is seen that helium production is approximately 2000 appm at the first wall, (for 1 MW-a/m^2) and drops to less than 20 appm at the end of the blanket region. From inspection of the He/DPA curve of the same figure it is seen that the helium production is quite dependent on the neutron energy ranging from 130 appm/DPA near the first wall to about 30 appm/DPA at the end of the blanket region. Because of the neutron energy dependence of gas production it is useful to compare the helium production to DPA ratio of SiC with that of the metallic systems. Specifically, the He/DPA ratios for type 316 stainless steel is approximately 20 appm/DPA at the first wall and changes by less than a factor of two at the end of the blanket region [6].

There has been limited study of high levels of helium on the mechanical properties of SiC. In these studies [7-9] helium has been uniformly injected into a CVI SiC/Ceramic Grade Nicalon™ fiber composite material. A decrease in bend strength was observed in all cases. However, this degradation (~30-40%) is consistent with what would be expected given the displacment dose associated with the helium implantations.

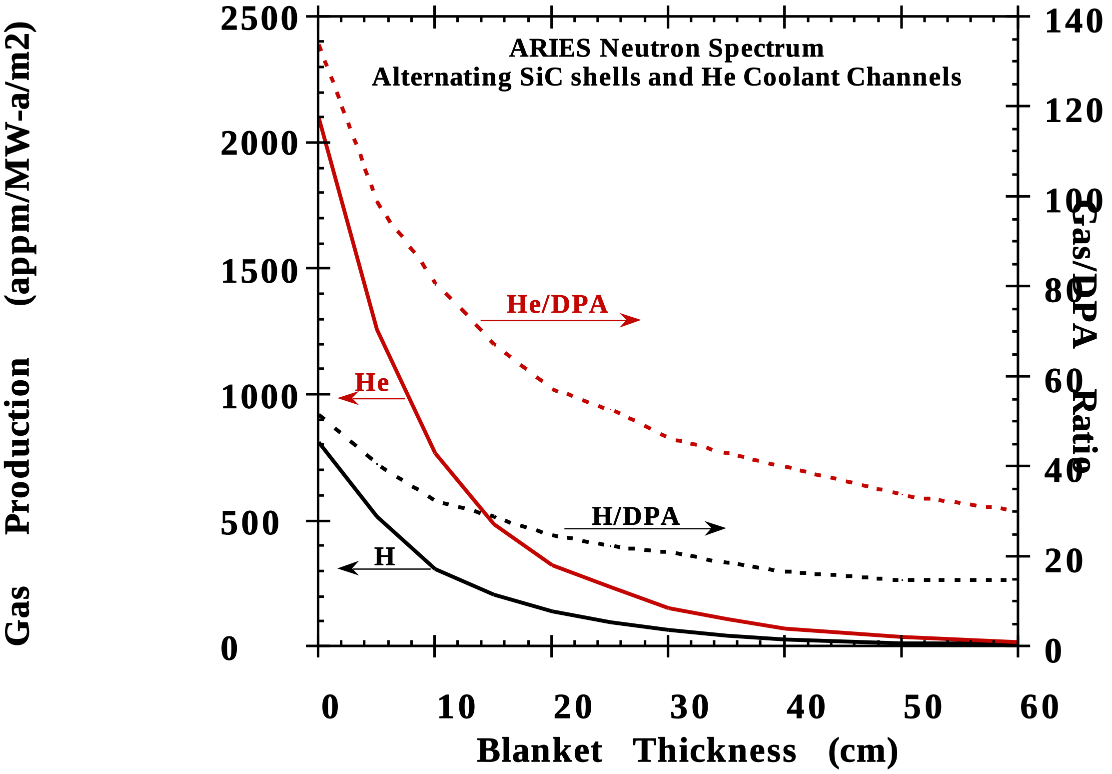

Figure 1: Effect of fusion neutrons on the gaseous production in SiC.

Experimental

Samples of Morton CVD SiC were machined into 1 x 1 x 25 mm bend bars and polished and chamfered on one surface. This middle section of this surface was then implanted uniformly over a depth of 0.46 mm with helium at 600°C using the cyclotron at JRC Ispra. The width of the implantation was 10 mm symmetric about the center of the sample. The helium implantation levels were 100 and 1000 appm. Samples were tested in four-point bending with a load and support span of 10 and 20 mm, respectively. The implanted side was placed in tension. Indentation hardness and toughness were measured using a Bueller Micro-Vickers hardness tester at a load of 500 g. Fracture toughness follows the Evans-Davis Model [10]. Density was measured using a density gradient column technique. Elastic modulus was measured using a Nanoindenter 2™ in the continuous stiffness mode.

Results

Figure 2 shows the Weibull failure probability for the non-irradiated, 100 appm and 1000 appm implanted SiC. It is important to note that the number of tests is limited, and therefore the standard deviation fairly high. However, from the data it is clear that the stress required to break the samples was increased with increasing helium implantation. It is worth noting, however, that due to the swelling of the helium implanted material (~0.5 %) the region to be tested was under compression prior to testing. The effect of this has not been analyzed. From the limited data, the effect of helium on the Weibull modulus can not be determined.

Weibull Analysis of He Implanted CVD SiC

	Mean ± St. Dev. (MPa)	Tests	Weibull Modulus	Size Parameter (MPa)
Non-Implanted	353 ± 72	29	13	368
100 appm	474 ± 127	10	7	508
1000 appm	532 ± 120	9	10	560

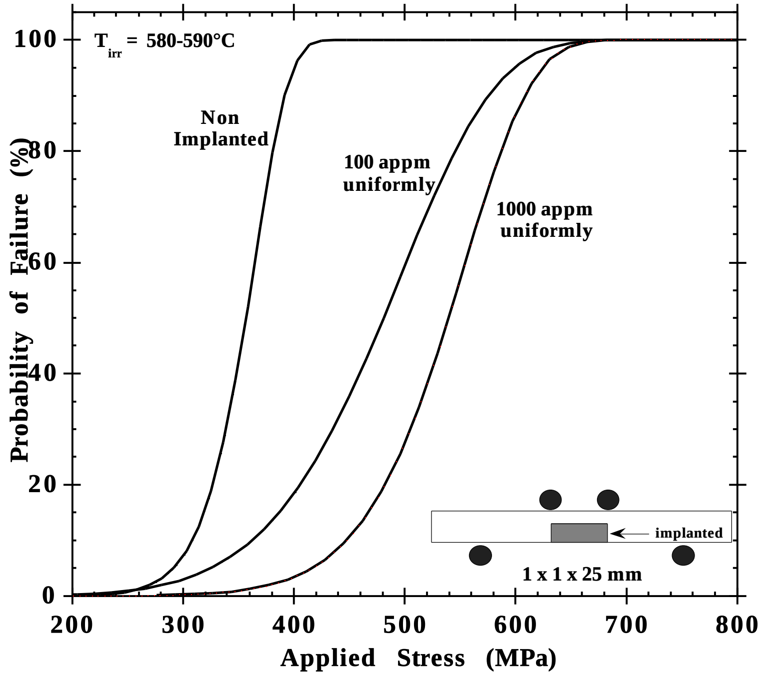

Figure 2: Bend Test resuts for non-implanted and He implanted CVD SiC.

From the data in Table 1 it is seen that there is a trend towards higher strength, higher hardness, and lower indent fracture toughness. The elastic modulus as measured by nanoindentation shows a slight decrease with irradiation.

Table 1: Mechanical Properties of non and He-implanted CVD SiC

Property	Virgin	100 appm	1000 appm
Swell (%)	**0**		**~0.5**
Bend Strength MPa	**353 ± 72**	**474 ± 127**	**532 ± 122**
Indent Fracture Toughness (MPa/m$^{1/2}$)	**1.4**	**1.2**	**0.9**
Vickers Hardness (Kg/m^2)	**2257 ± 103**	**2381 ±120**	**2516 ±180**
Elastic Modulus (GPa)	**527**	**515**	**490**

An interesting observation related to the toughness is the state of the surface following the Vicker's hardness measurement. It appears that the propagation of cracks and spalling of the surface is more pronounced in the as-implanted condition. An example of this can be seen in Figure 3, which shows a non-implanted and 1000 appm helium implanted example. In many cases, the spalling which is evident in the 1000 appm micrograph occurs. This sort of spalling was not seen for the non-implanted samples. Again, it should be noted that there was likely a compressive stress state in the implanted area due to the heterogeneous swelling which may cause or exacerbate spalling. Also of note is that non-implanted data was taken in non-implanted regions of the implanted samples, ruling out material non-uniformity or environmental factors which might cause property variation.

Future Work

The purpose of this work was to provide a baseline for identical materials, both implanted and non-implanted, which were irradiated in the 14J HFIR irradiation experiment. This irradiation provided ~8 dpa at 800°C, yielding a fusion-relevant He/dpa ratioup to 125. Following the post-irradiation examination data should be available on non-irradiated, neutron irradiated, as-implanted, and as-implanted and neutron irradiated specimens. This should allow a clean comparison of the effects of helium and helium + dpa on the mechanical properties of CVD SiC.

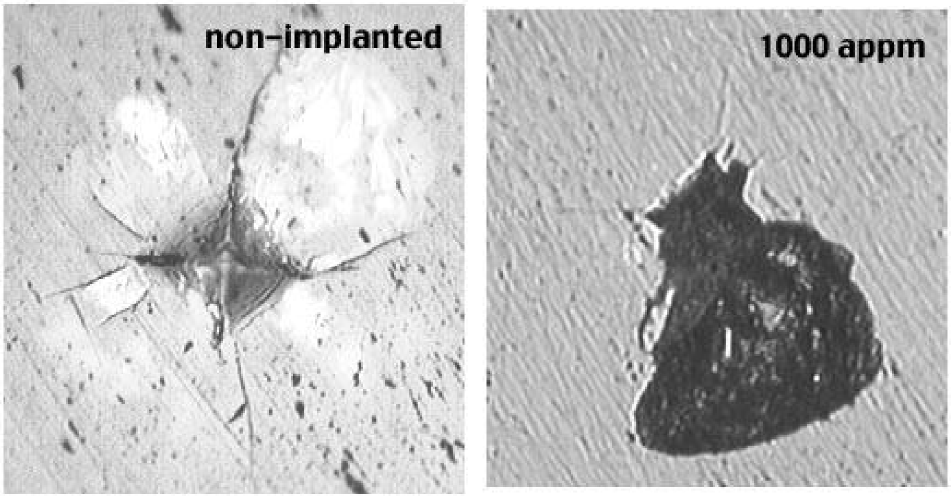

Figure 3: Optical images of Vicker's Indentations.

References

1. Rovner, L.H. and G.R. Hopkins, *Ceramic materials for fusion.* Nucl. Tech., 1976. **29**: p. 274-302.
2. Jung, P., *Diffusion and retention of helium in graphite and silicon carbide.* Journal of Nuclear Materials, 1992. **191-194**: p. 377-381.
3. Causey, R.A., J. Nucl. Mater., 1993. **203**: p. 196-205.
4. Sasaki, K., et al., *Helium release and microstructure of neutron-irradiated SiC ceramics.* Journal of Nuclear Materials, 1991. **179-181**: p. 407-410.
5. El-Guebaly, L., *Personally communicated data.*. 1995.
6. W M Stacey, J., *Fusion*. 1981: John Wiley and Sons.
7. Scholz, H.W., P. Fenici, and A.F. Rebelo. in *Miniturized Specimens for Testing of Irradited Material*. 1995. Juelich.
8. Rebelo, A.J.F., et al., *Comparison of the mechanical beaviour of SiC/SiC composites following neutron irradiation and helium implantation.* Journal of Nuclear Mateerials, 1998.
9. Hasegawa, A., et al., Journal of Nuclear Materials, 1998. **253**: p. 31.
10. Evans, A.G. *Fracture Toughness: The Role of Indentation Techniques*. in *Proceedings of the Eleventh National Symposium on Fracture Mecahnics Part II.* 1979: ASTM, Philadelphia.

TENSILE TESTING OF UNIDIRECTIONAL SILICON CARBIDE COMPOSITES FOR FUTURE IRRADIATION EXPERMENTS

T. Hinoki[1], L.L. Snead[2], E. Lara-Curzio[2], Y. Katoh[1] and A. Kohyama[1]
(1) Institute of Advanced Energy, Kyoto University); (2) Oak Ridge National Laboratory

OBJECTIVE

The objective of this study is, to develop the experimental method of tensile tests of the SiC/SiC composites to be irradiated, and to obtain tensile properties of the unirradiated SiC/SiC composites expected for fusion application.

SUMMARY

The SiC/SiC composites, which have three kinds of unidirectional stoichiometric SiC fibers and various fiber coating, were prepared by I-CVI method for future irradiation experiments. In-plane tensile bars and transthickness tensile specimens were cut from these materials. In-plane tensile tests, transthickness tensile tests and four point bend tests were carried out at ambient temperature. While the specimens, SCS-9A^{TM} fibers were used, showed superior ultimate tensile stress, more than 1 GPa, to the other specimens, proportional limit stress of the specimens, Hi-Nicalon^{TM} type-S fibers were used, was larger than the other specimens. The specimens, Tyranno^{TM} SA fibers were used or multiple SiC fiber coating was applied, showed brittle fracture behavior. Correlation between tensile results and flexural results was discussed. Transthickness tensile tests were unsuccessful because of insufficient bond between fixture and epoxy.

PROGRESS AND STATUS

1. INTRODUCTION

The high temperature mechanical properties and low activation make SiC/SiC composites very attractive as fission and fusion reactor materials [1]. At present, interfacial properties between the fiber and matrix of neutron-irradiated SiC/SiC composites limit mechanical performance [2]. This limitation has been attributed primarily to shrinkage in the SiC-based fibers due to irradiation-assisted oxidation [3], irradiation-induced recrystalization of microcrystalline fibers [4-6], and to large dimensional changes of the carbon [7] coating applied to the fiber. To avoid or at least minimize these radiation effects, the recent trend in SiC fiber development is toward lower oxygen content, reduced free carbon and enhanced crystallinity. Previous work regarding ion-irradiation effect on carbon interphase microstructure indicated that the basal planes of the irradiated graphite-like carbon appear to be chopped into small fragments and consequently amorphous-like structures were observed [8]. The development of more radiation-resistant SiC composites is based on the use of stoichiometric SiC fibers with lower oxygen and SiC-based coating. Recently, stoichiometric SiC fibers have been developed including Hi-Nicalon^{TM} type-S [9], Sylramic^{TM}, Tyranno^{TM} SA [10] and SCS-9A^{TM} [11].

It was difficult to evaluate actual mechanical performance of SiC/SiC composites by flexural tests. Flexural strength includes tensile strength, compression strength and interfacial shear strength. This difficulty attributes to mismatch of tensile strength and compression strength of SiC/SiC composites. To appreciate mechanical performance of SiC/SiC composites, evaluation by tensile tests are desired rather than flexural tests. However tensile testing of SiC/SiC composites is more difficult than the other materials due to limitation of size and difficulty of processing. In this study, tensile tests of the SiC/SiC composites with stoichiometric fibers and various interphase to be irradiated was successfully carried out.

2. EXPERIMENTAL

Materials

The materials used in this study were unidirectional SiC fiber reinforced SiC composites and fabricated by isothermal chemical vapor infiltration (I-CVI) method at Hyper-Therm High-Temperature Composites, Inc. for ORNL/Kyoto University round robin irradiation program. All fibers used were low oxygen stoichiometric SiC fiber, Hi-Nicalon^{TM} type-S, Tyranno^{TM} SA and SCS-9A^{TM}, while SCS-9A^{TM} has a carbon core 33 μm in diameter and outer silicon-rich carbon layers [12]. Fiber properties were reported as shown in Table 1 [9-11]. Fibers were coated with either carbon, multiple SiC or “porous” SiC by CVI prior to matrix deposition. Mixtures of methyltrichlorosilane, argon, methane and hydrogen gases were used to deposit the “porous” SiC coating on fiber. In the multiple SiC interphase, the first SiC layer was deposited followed by a thin,

Table 1: The properties of stoichiometric SiC fibers used in this work

SiC Fiber	C/Si Atomic Ratio	Oxygen Content (wt%)	Tensile Strength (GPa)	Tensile Modulus (GPa)	Elonga-tion (%)	Density (g/cm^3)	Diameter (μm)
Hi-Nicalon Type-S	1.05	0.2	2.6	420	0.6	3.10	12
Tyranno SA	1.08	0.3	2.8	420	0.7	3.02	10
SCS-9A	1.0	0	3.45	307	1.1	2.8	79

interrupted layer of pyrolytic carbon. Four SiC layers were fabricated with interrupted pyrolytic carbon in the multiple SiC coating [13]. Properties of the SiC/SiC composites used are shown in Table 2. SEM images of cross section of the specimens with C fiber coating were shown in Fig. 1, respectively. Fiber coating thickness and fiber volume fraction was estimated from SEM images of cross section. One of the reasons for low fiber volume fraction was extra SiC coating of the SiC/SiC composites as seal coating.

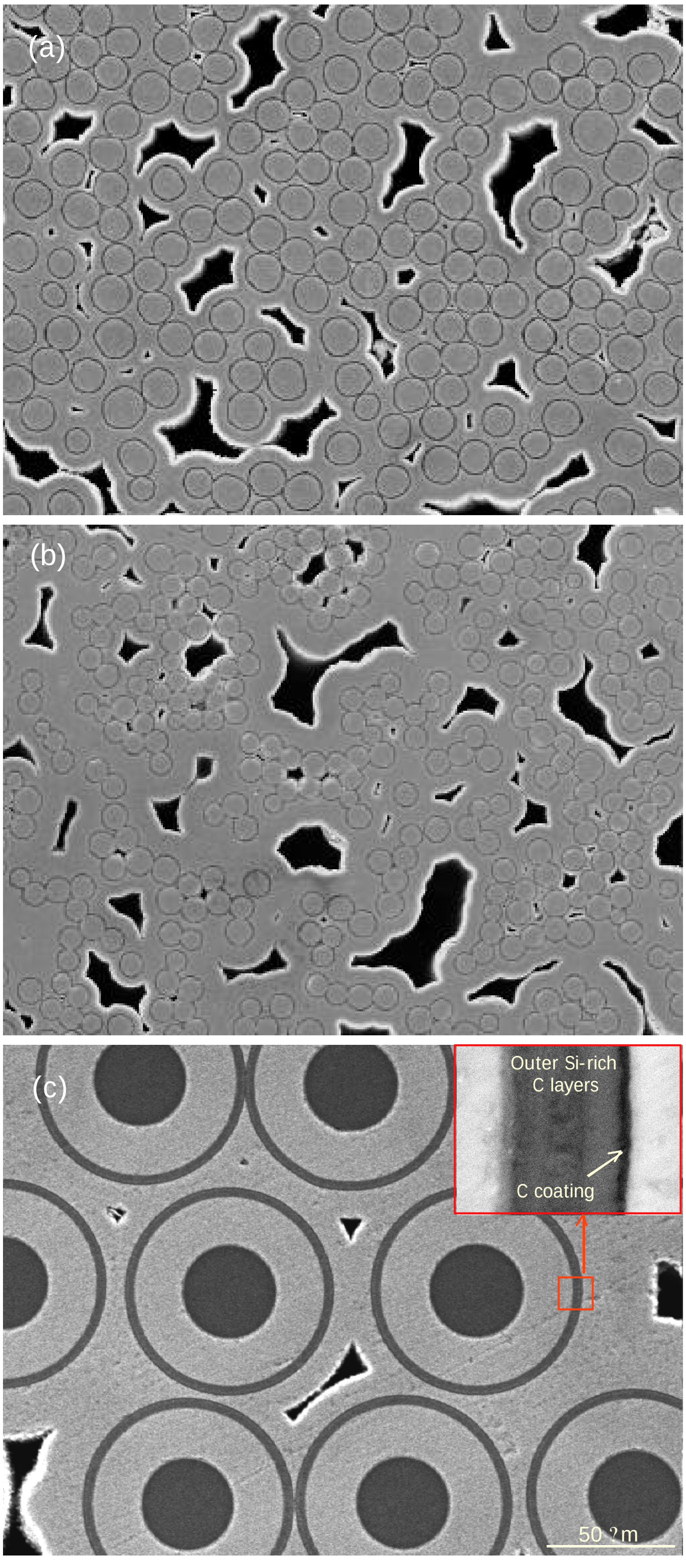

Fig. 1: SEM images of cross section of the specimens with C fiber coating, (a) Hi-Nicalon^{TM} type-S, (b) Tyranno^{TM} SA and (c) SCS-9A^{TM} specimen

Technique

Two kinds of tensile tests were carried out. One was standard tensile test for fiber direction, in-plane tensile test. For this, the specimens with straight-gauge section were prepared. The specimen size was 50^{l} x 4^{w} x 1.5^{t} mm for Hi-Nicalon^{TM} type-S samples and Tyranno^{TM} SA specimens or 50^{l} x 4^{w} x 1.0^{t} mm for SCS-9A^{TM} specimens. These specimens had 18^{l} x 4^{w} x 1.5^{t} mm and 18^{l} x 4^{w} x 1.0^{t} mm gauge size, respectively. Wedge-type grip was used. Aluminum tabs were applied between specimens and grip to adjust the specimens to grip and to promote uniform stress within grip. Aluminum tab surfaces were serrated by a rough file and attached to specimens by the epoxy to prevent slippage between an aluminum tab and a specimen. A specimen with aluminum tabs was fixed in the couple of fixtures with sufficient lateral pressure to prevent slippage between the fixture and a specimen. This specimen with the fixture was fixed to the load train couplers. The load train couplers

Table 2: Properties of the specimens

ID	TST1	TST2	TSM	TSP	SAC	SAM	S9C	S9M	S9P
Fiber	Hi-Nicalon^{TM} Type-S				Tyranno^{TM} SA		SCS-9A^{TM}		
Fiber Coating	C		Multiple SiC	"Porous" SiC	C	Multiple SiC	C	Multiple SiC	"Porous" SiC
Coating Thickness (nm)	520	720	580	380	560	880	330	580	240
Density (g/cm^3)	2.58	2.58	2.65	2.56	2.55	2.53	2.64	2.60	2.56
Vf (%)	29	29	38	26	21	24	32	33	38

was non fixed load train couplers with universal joints, which promote self-alignment of the load train during the movement of crosshead to reduce specimen bend. The fixture and the load train couplers are based on ASTM C1275. A specimen, the fixture and the load train coupler are shown in Fig. 2. The strain was measured by means of the capacitive extensometer (Instron Inc.). Two balanced arms, pivoted in the center, transmit the displacement of the specimen to an outboard capacitive transducer to measure the specimen strain. However the distance of these two arms was 25 mm, while gauge length of the specimens was 18 mm. The supplementary arms to measure this shorter gauge was prepared and fixed to original arms. The capacitive extensometer with the supplementary arms was shown in Fig. 3. All tests were conducted with the cross-head speed of 10 μm/sec at ambient temperature.

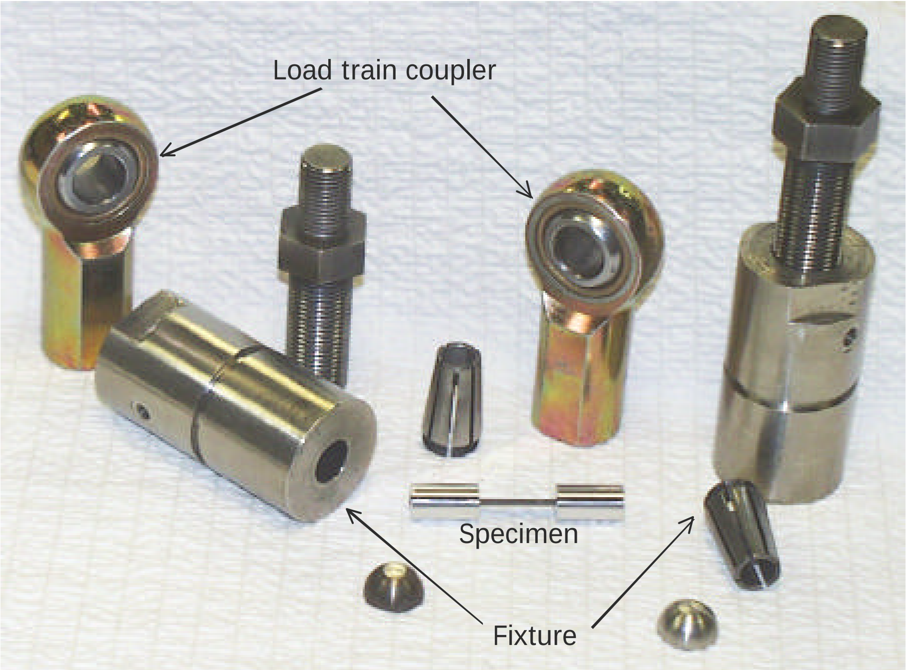

Fig. 2: Specimen, fixture and load train coupler for in-plane tensile test

Four point bend tests were carried out to correlate with tensile properties. The same specimens with in-plane tensile specimens were used. The support span and the load span were 40 mm and 20 mm, respectively. The crosshead speed was 0.021 mm/sec.

Transthickness tensile tests were also carried out to evaluate shear stress of fracture mode I. The specimens, whose size were 5^l x 5^w x 1.5^t mm for Hi-Nicalon^{TM} type-S specimens and Tyranno^{TM} SA specimens or 5^l x 5^w x 1.0^t mm for SCS-9A^{TM} specimens, were prepared. The pair of fixtures, which have 5 mm square face to attach the specimen, were also prepared. The fixture attached to the specimen by the epoxy was connected to the load train couplers, which have universal joints to promote self-alignment of the load train during the movement of crosshead to reduce specimen bend. The specimens, the fixtures and the load train couplers are shown in Fig. 4. All tests were conducted with the cross-head speed of 10 µm/sec at ambient temperature.

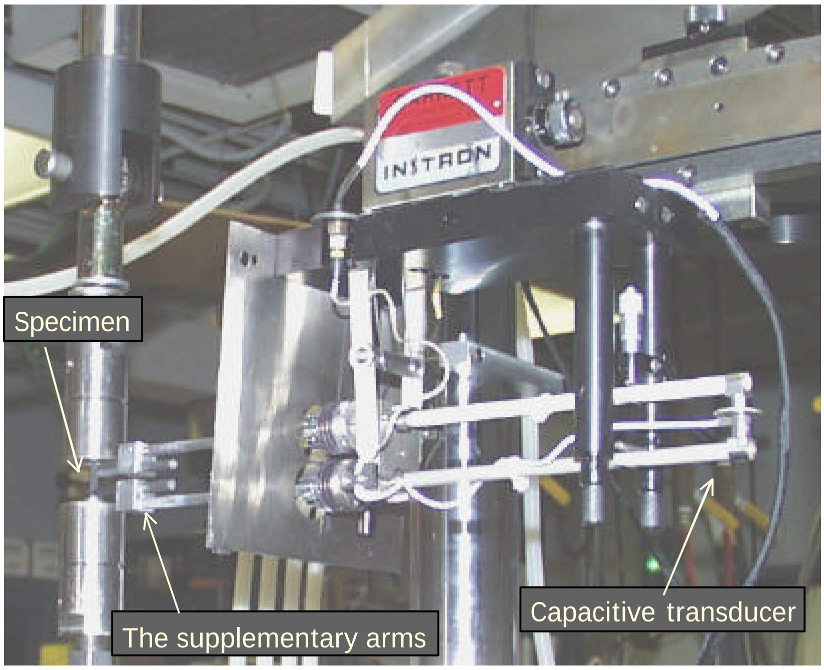

Fig. 3: Capacitive transducer with the supplementary arms

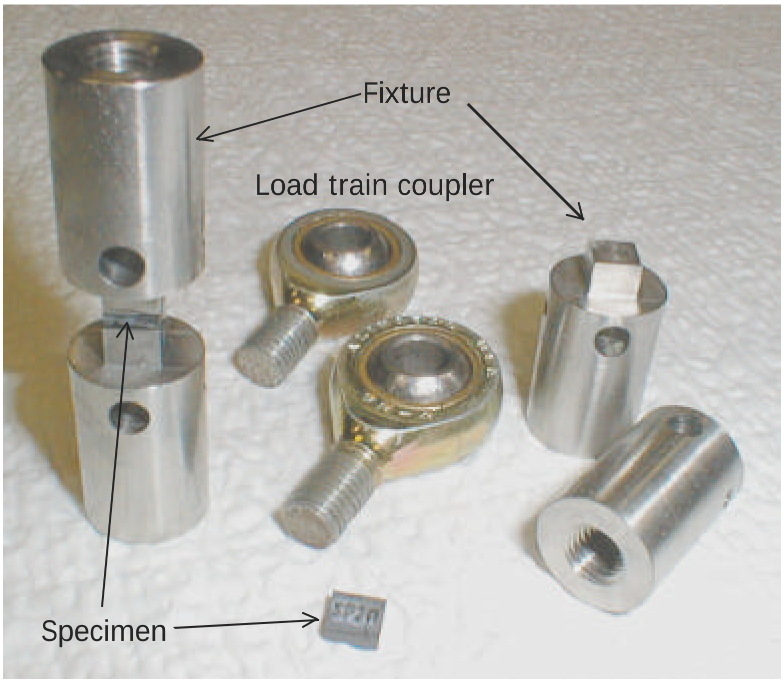

Fig. 4: Specimen, fixture and load train coupler for transthickness tensile test

3. Results

In-plain tensile tests

Stress-strain behavior of three specimens, which have Hi-Nicalon^{TM} type-S, Tyranno^{TM} SA and SCS-9A^{TM}, respectively, and C interphase between fiber and matrix, are shown in Fig. 5. This shows the typical effect of fiber properties on mechanical properties and trend of whole results. SCS-9A^{TM} specimens showed larger average ultimate tensile stress (UTS) and strain than Hi-Nicalon^{TM} type-S specimens and Tyranno^{TM} SA specimens, while proportional limit stress (PLS) of Hi-Nicalon^{TM} type-S

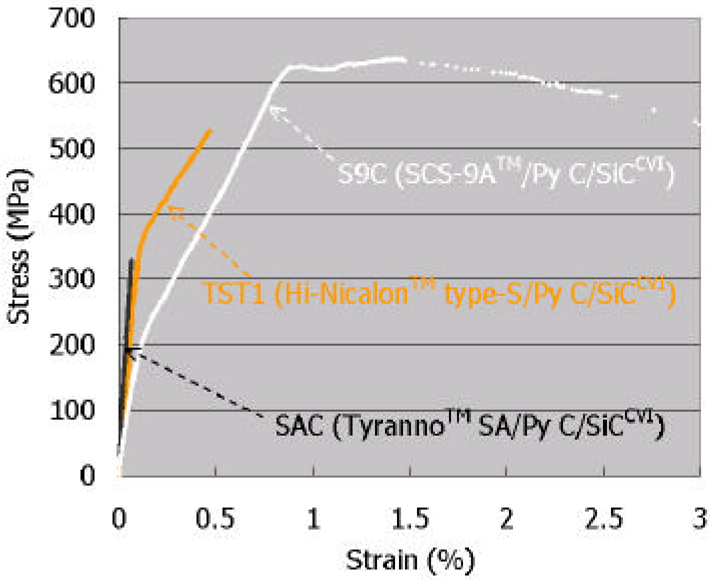

Fig. 5: Effect of fiber properties on strain-stress curve of tensile tests

specimens was largest. PLS was obtained from 0.01 % strain offset. Average modulus of Tyranno™ SA specimens was larger than the others. These tensile properties corresponded to fracture surfaces in Fig. 6. A few mm fiber pullouts are shown in SCS-9A™ specimens fracture surface. TST1 specimens showed fiber pullouts in a little complicated fracture surface compared to SAC specimens. SAC specimens showed very brittle fracture behavior.

Tensile properties and fracture behaviors were affected by fiber coating, respectively. Multiples coating specimens showed smaller UTS than the other coating specimens. PLS and modulus of multiple coating specimens were also smaller in Hi-Nicalon™ type-S specimens and Tyranno™ SA specimens. Multiple SiC coating specimens were brittle compared to the other coating specimens. "Porous" SiC coating specimens of SCS-9A™ specimens showed better tensile properties than C coating specimens, although C coating specimens were better in Hi-Nicalon™ type-S specimens. The results of these tensile tests are summarized in table 3.

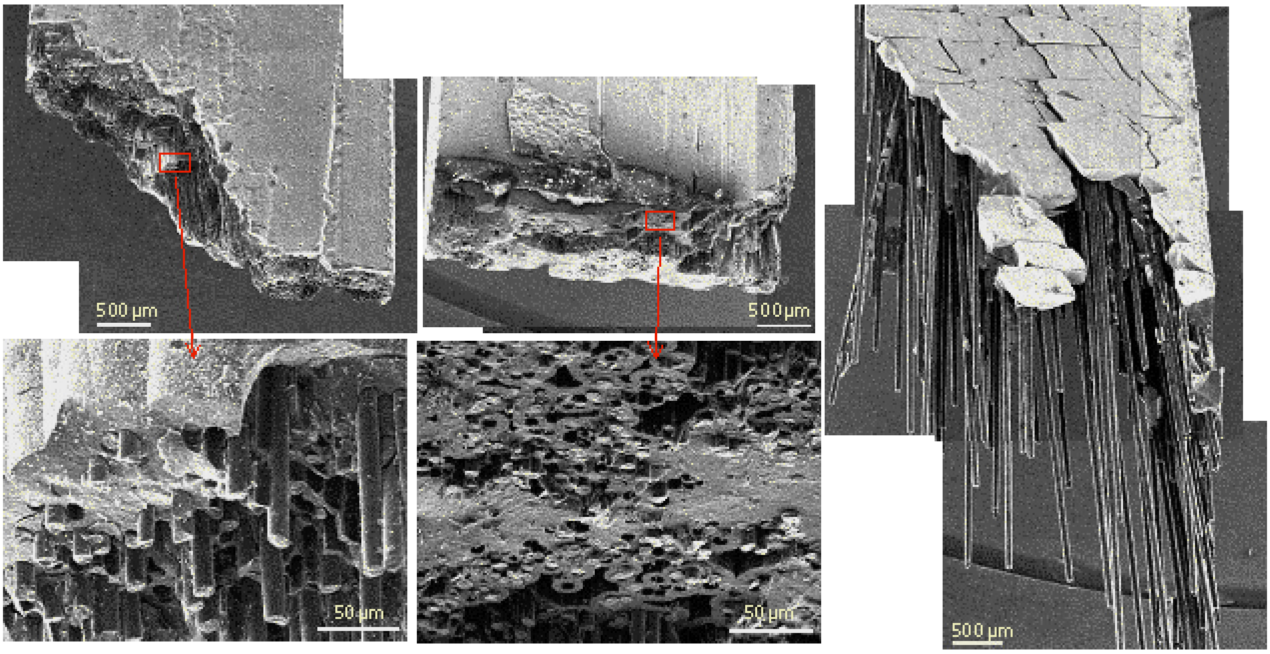

Fig. 6: Effect of fiber properties on fracture surface after tensile tests

Table 3: Summary of mechanical properties

ID	**TST1**	**TST2**	**TSM**	**TSP**	**SAC**	**SAM**	**S9C**	**S9M**	**S9P**
Tensile Modulus (GPa)	336	306	256	307	417	350	203	294	373
Flexural Modulus (GPa)	296	284	237	260	219	205	347	302	350
Tensile PLS (MPa)	339	268	229	276	220	148	166	246	227
Flexural PLS (MPa)	490	533	356	422	214	199	260	321	356
UTS (MPa)	442	319	229	282	220	148	622	562	860
Flexural Strength (MPa)	907	748	757	485	255	199	982	908	959

Four point bend tests

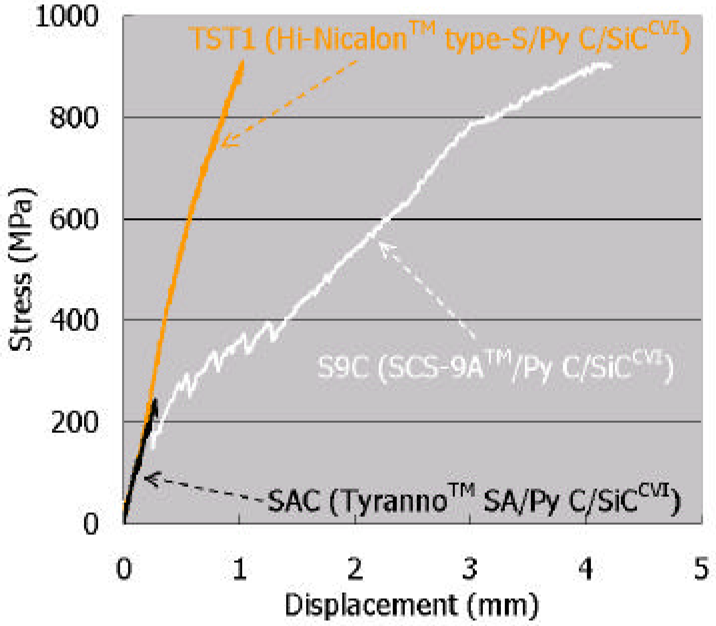

Fig. 7: Effect of fiber properties on flexural

Flexural stress and PLS showed similar trend to tensile results. Flexural curve of three specimens, which have Hi-Nicalon^{TM} type-S, Tyranno^{TM} SA and SCS-9A^{TM}, respectively, and C interphase between fiber and matrix, are shown in Fig. 7. SCS-9A^{TM} specimens showed larger flexural stress and strain than Hi-Nicalon^{TM} type-S specimens and Tyranno^{TM} SA specimens, while PLS of Hi-Nicalon^{TM} type-S specimens was largest. PLS was obtained from 0.01 % strain offset. However modulus of Tyranno^{TM} SA specimens was not largest but smallest. PLS and flexural stress of four point bend tests were larger than PLS and UTS of tensile tests, especially Hi-Nicalon^{TM} type-S specimens.

There was some different effect of fiber coating on mechanical properties between tensile properties and flexural properties. While multiple SiC fiber coating specimens showed inferior tensile properties to the other fiber coating specimens, they showed some superior properties than the other specimens in flexural tests. Flexural strength of C fiber coating specimens was larger than the other coating specimens. The results of these flexural tests are also summarized in table 3.

Transthickness tensile tests

All specimens tested were not broken within specimens, but at interface between a specimen and a fixture as shown in Fig. 8. This is because bond between stainless steel and the epoxy was insufficient. Both specimens and fixtures were cleaned well. However all tests were unsuccessful with maximum stress, about 10 MPa.

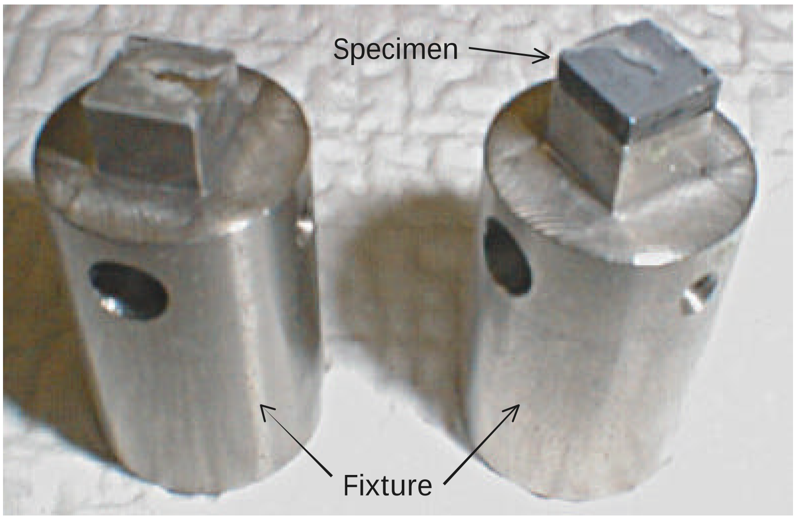

Fig. 8: Specimen and fixture after transthickness tensile test

4. Discussions

Evaluation of Tensile Properties

There was large effect of the fiber on tensile properties. Tyranno^{TM} SA specimens showed very brittle fracture behavior. This is considered that large interfacial shear strength was most of the reasons, while interfacial shear properties were not evaluated yet. Same kind of coating was applied to each fiber. However fiber surface roughness was different, respectively. Interfacial shear properties were different, if a kind of fibers was different. Interfacial coating properties of each fiber should be optimized.

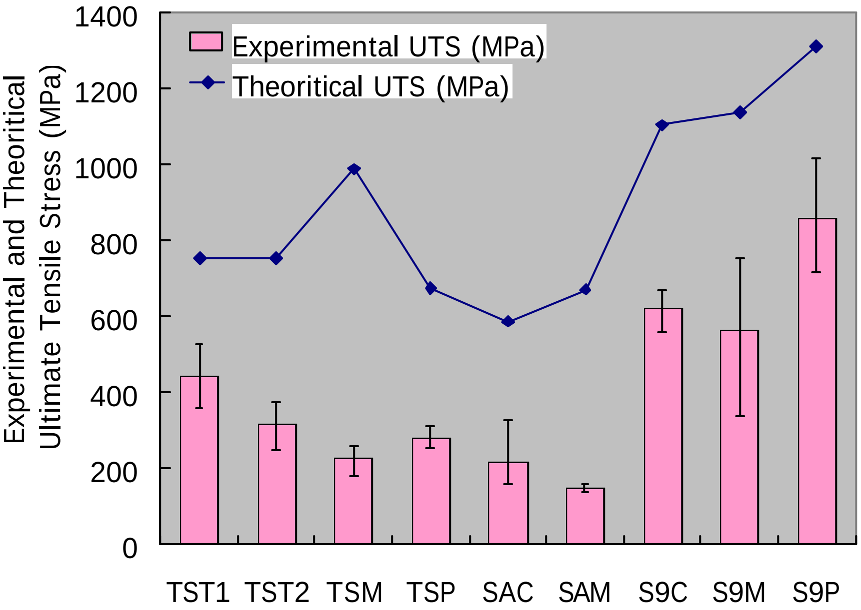

Fig. 9: Comparison of experimental UTS and theoretical UTS

Multiple SiC fiber coating specimens showed relatively brittle fracture behavior. Some papers say that interfacial shear strength of C fiber coating specimens depends on its coating thickness [14,15]. In multiple SiC coating, C coating was just used to interrupt SiC coating and its thickness was very thin. So this interfacial shear strength might be very strong. However the specimens used in this work were for neutron irradiation. This multiple coating specimens are expected to show superior properties under neutron irradiation.

Some reasons were inferred regarding relatively low PLS of SCS-9A^{TM} specimens. If the Poison ratio of the fiber is same and there is a gap of the ratio between the fiber and the matrix, the larger fiber diameter specimens is easier to debond at fiber-matrix interface than the smaller diameter fiber specimens.

It is said that UTS depends on fiber strength [16]. Theoretical UTS was estimated from fiber strength and fiber volume fraction and compared with the experimental results in Fig. 9. Error bars of the experimental UTS show minimum and maximum UTS of the same specimens. Correlation between the experimental and theoretical UTS is obvious, while there is some scatter. To increase fiber volume fraction is very effective to increase UTS.

Correlation between Tensile Properties and Flexural Properties

Correlation of rough trend between tensile and flexural properties was seen. Flexural properties include compression of the specimens. It is said that compressive stress is much larger than tensile stress in SiC/SiC composites. In this study, most of PLS and flexural strength of flexural tests were larger than the results of tensile tests.

Irradiation Experiments

The specimens used in this experiment are supposed to use for irradiation experiments, HFIR 14J, rabbits, JMTR. First specimens is supposed to be irradiated at rabbits from 26 July to 21 August, 2000 at the cycle 381 and from 7 September to 1 October, 2000 at the cycle 382. Table 4 shows material properties and irradiation conditions. Each rabbit contained 4 tensile bars, 6 transthickness specimens and SiC temperature monitor as shown in Fig. 10. The specimens will be irradiated at JMTR 00M-95U. Total dose and temperature expected are 1 dpa and 800 or 1000 °C. In this capsule, in-plane tensile bars, double-notched specimens (DNS) [17] and bend bars will be contained. DNS

Table 4: Material properties and irradiation condition of rabbits cycle 381 and 382

	Fiber	Interphase	Position	Temp. (^{o}C)	Dose (dpa) /cycle	Total dose (dpa)
FUN 1	Hi-Nicalon Type-S	Py C T1	1	380	0.8	0.8
FUN 2	Hi-Nicalon Type-S	Py C T1	1	380	0.8	1.8
FUN 5	Hi-Nicalon Type-S	Py C T2	1	380	0.8	1.8
FUN 17	Tyranno SA	Py C	2	615	1.4	2.8
FUN 21	SCS-9	Py C (1ML SiC)	2	615	1.4	2.8

will be used to evaluate interfacial shear strength.

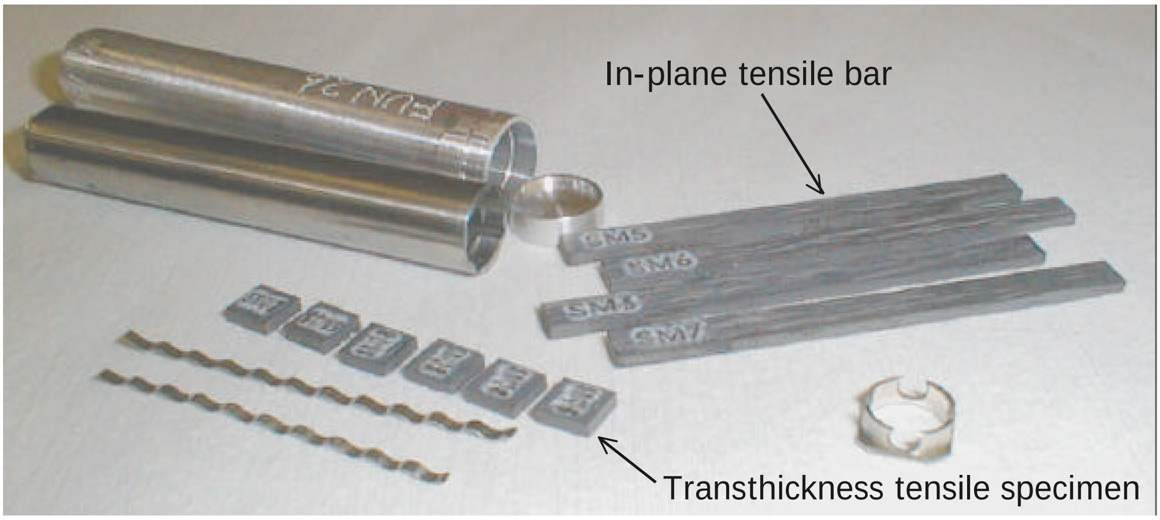

Fig. 10: Rabbit capsule and specimens to be irradiated

CONCLUSIONS

(1) SCS-9A^{TM} specimens showed superior UTS, more than 1 GPa at maximum, to the other fiber specimens. However PLS of Hi-Nicalon^{TM} type-S specimens was larger than one of SCS-9A^{TM} specimens. Tyranno^{TM} SA specimens showed brittle fracture behavior.
(2) Multiple SiC fiber coating specimens were brittle compared with the other fiber coating specimens.
(3) It was obvious that UTS depended on fiber strength and fiber volume fraction.
(4) Corresponding of rough trend between tensile and flexural properties was seen. However there were some differences in the effect of fiber coating on mechanical properties.
(5) Transthickness tensile tests were unsuccessful because of insufficient bond between fixture and epoxy. Modification of fixture surface or fixture material is required.

ACKNOWLEDGE

This work was supported by Japan-USA Program of Irradiation Test for Fusion Research (JUPITER) and by Core Research for Evolutional Science and Technology (CREST) program under the title of "R & D of Environment Conscious Multi-Functional Structural Materials for Advanced Energy Systems".

REFFERENCES

[1] P. Fenici, A.J. Frias Rebelo, R.H. Jones, A. Kohyama and L.L. Snead, J. Nucl. Mater., 258-263

(1998) 215.

[2] L.L. Snead, R.H. Jones, A. Kohyama and P. Fenici, J. Nucl. Mater., 233-237 (1996) 26-36.

[3] L.L. Snead, M.C. Osborne and K.L. More, J. Mater. Res. 10(3) (1995) 736.

[4] A. Hasegawa, G. E. Youngblood and R.H. Jones, J. Nucl. Mater., 231 (1996) 245.

[5] M.C. Osborne, C.R. Hubbard, L.L. Snead and D. Steiner, J. Nucl. Mater., 253 (1998) 67-77.

[6] G.E. Youngblood, R.H. Jones, A. Kohyama and L.L. Snead, J. Nucl. Mater., 258-263 (1998) 1551-1556.

[7] J.H.W. Simmons, Radiation Damage in Graphite, Pergamon Press, (1965).

[8] Y. Katoh, T. Hinoki, A. Kohyama, T. Shibayama and H. Takahashi, Ceram. Eng. Sci. Proc., 20 [4] (1999) 325-332.

[9] M. Takeda, A. Urano, J. Sakamoto and Y. Imai, J. Nucl. Mater., 258-263 (1998) 1594-1599.

[10] T. Ishikawa, Y. Kohtoku, K. Kumagawa, T. Yamamura and T. Nagasawa, Nature, 391 (1998) 773-775.

[11] Internet homepage of Textron systems Inc., http://www.systems.textron.com/scs9.htm.

[12] C.A. Lewinsohn, L.A. Giannuzzi, C.E. Bakis and R.E. Tressler, J. Am. Ceram. Soc., 82 [2] (1999) 407-413.

[13] L.L. Snead, M.C. Osborne, R.A. Lowden, J. Strizak, R.J. Shinavski, K.L. More, W.S. Eatherly, J. Bailey and A.M. Williams, J. Nucl. Mater., 253 (1998) 23-30.

[14] E. Lara-Curzio and M. K. Ferber, Numerical Analysis and Modeling of Composite Materials, Ed. J. W. Bull, Blackie Academic & Professional, 12 (1995) 357-399.

[15] T. Hinoki, W. Zhang, A. Kohyama, S. Sato and T. Noda, J. Nucl. Mater., 258-263 (1998) 1567-1571.

[16] J.P. Piccola, Jr., M.G. Jenkins and E. Lara-Curzio, Thermal and Mechanical Test Methods and Behavior of Continuous-Fiber Ceramic Composites, ASTM STP 1309, Edited by M.G. Jenkins, S.T. Gonczy, E. Lara-Curzio, N.E. Ashbaugh and L.P. Zawada, American Society for Testing and Materials, (1997) 3-15.

[17] E. Lara-Curzio and M. K. Ferber, Thermal and Mechanical Test Methods and Behavior of Continuous-Fiber Ceramic Composites, ASTM STP 1309, Edited by M.G. Jenkins, S.T. Gonczy, E. Lara-Curzio, N.E. Ashbaugh and L.P. Zawada, American Society for Testing and Materials, (1997) 31-48.

3.0 FERRITIC/MARTENSITIC STEELS

SUMMARY OF IEA WORKSHOP/WORKING GROUP MEETING ON FERRITIC/MARTENSITIC STEELS FOR FUSION—R. L. Klueh (Oak Ridge National Laboratory)

OBJECTIVE

The objective of this report is to describe the working group meeting and workshop held to review planned and completed work that is being undertaken to prove the feasibility of using ferritic/martensitic steels for fusion applications.

SUMMARY

The International Energy Agency (IEA) Working Group on Ferritic/Martensitic Steels for Fusion held a workshop in Tokyo, Japan, 2-3 November 2000. Participants came from Europe, Russia, the United States, and Japan to review the progress of the collaboration on reduced-activation ferritic/martensitic steels and the development of plans for future collaboration. At this workshop, data that have been obtained during the collaboration were reviewed, and it was generally agreed that the testing phase for the IEA heats of steel obtained for this collaboration is near completion. A database has been established on the completed work, and that database is available to the international community. Based partially on the work performed in this collaboration, the European Union has developed specifications for a new reduced-activation steel, EUROFER 97, which has been produced and is now being evaluated. The other material of interest at this workshop was oxide dispersion-strengthened (ODS) steel, which was the subject of presentations from Europe, Japan, and the United States. The consensus is that selective utilization of these steels offers the possibility of a ferritic martensitic steel that will allow higher operating temperatures for a fusion device, although it is recognized that ODS steels are still in the early stage of development.

PROGRESS AND STATUS

Introduction

The IEA Working Group on Ferritic/Martensitic Steels for Fusion under the auspices of the IEA Executive Committee for the Implementing Agreement on Fusion Materials conducted a workshop at Tokyo, Japan, 2-3 November 2000. Researchers from the European Union (6) the United States (8), Switzerland (2), Russia (2), and Japan (23) participated. The purpose of the Working Group is the establishment and coordination of an international collaborative test program to determine the feasibility of using ferritic/martensitic steels for fusion.

This workshop was the eleventh meeting of the Working Group, which was formed as a result of a workshop on ferritic/martensitic steels in Tokyo in October 1992. At the first meeting following the Tokyo workshop, the Working Group developed specifications for large heats of reduced-activation steels and outlined a collaborative research program. Two 5-ton heats of the IEA-modified F82H steel and two 1-ton heats of JLF-1 steel were subsequently produced, fabricated into plates, and distributed to the participants of the collaboration. Weldments were also produced and distributed. Subsequent meetings have been used to plan a test program and to coordinate the acquisition of the data needed to prove feasibility for the steels for fusion applications.

Research and Development Activities

The following is a brief description of the information presented at the Tokyo workshop. Copies of viewgraphs and other information presented at the workshop are available.

RAF/M Development Programs

This session reviewed the programs of the European Union, Japan, Russia, and the United States.

B. van der Schaaf presented the materials development program of the European Union, which is presently in the second year of a four-year program. The program is focused on building a breeding blanket, which means design data, licensing, codes, database, etc., are important. The majority of the work is on the reduced-activation EUROFER 97, on which a range of studies is underway; these studies include: metallurgical characterization, mechanical properties of base metal and welds, irradiation effects, aging effects, dissimilar metal welds, and compatibility. Irradiations up to 30 dpa and 450ºC are to be carried out. Compatibility studies in both water and Pb17Li are planned. In parallel with the studies on the conventional steels, work will also be pursued on ODS steels using the EUROFER 97 alloy to produce the metal powder from which the ODS alloy will be produced.

V. Chernov presented the Russian materials program. The objective of the program is an understanding of the irradiation behavior of ferritic/martensitic steels. To that end, a 5-year irradiation program is planned for the BN-600 reactor. Work will concentrate on 12Cr conventional and reduced-activation steels. Irradiations are planned at 400-600ºC and 35-85 dpa. The 12Cr steels were chosen because of their better heat resistance.

The U. S. program, which was presented by R. L. Klueh, has as its objective the widening of the temperature operating window for the ferritic/martensitic steels. At the low-temperature side, emphasis is on understanding the phenomena and mechanisms of fracture with studies of microstructure-property relationships, specimen size effects, crack geometry effects, etc. Understanding helium effects is extremely important. At the high-temperature side, alloy development, including the development of dispersion-strengthened steels will be pursued.

For the Japanese program discussed by S. Jitsukawa, the primary target of the program is the development of ferritic/martensitic steels with improved properties at elevated temperature. These studies, which involve Japanese national institutes, universities, and industry, are of importance because reduced-activation ferritic/martensitic steel has been selected as the candidate material for a blanket structure of a prototype reactor. Development of ODS steels is also a part of the program. The Japanese program is carried out in conjunction with a blanket design concept and the service conditions projected for an operating machine. Design studies of prototype reactors with ferritic/martensitic steels have been and are being conducted. In the future, blanket test modules using these materials are planned.

The final paper of this session was by T. Hatano, who discussed the conceptual design of a DEMO blanket that has been developed by JAERI. Any such fusion plant must be competitive with other power-generation systems and must predict the technological requirements for a commercial reactor. To meet such objectives, a system with high thermal efficiency is required, and the result was a blanket designed to be cooled with supercritical water with a first wall temperature above 600ºC. This would probably mean that conventional ferritic/martensitic steels could not be used, and ODS steels would have to be developed if a ferritic steel is to operate at such a temperature.

Baseline Properties

K. Shiba discussed the status of the database (unirradiated) on mechanical properties of the IEA heats of F82H and JLF-1 steels developed primarily by the IEA collaboration. Large amounts of tensile, creep, and impact data have been obtained. Fracture toughness, fatigue, and thermal fatigue data have also been determined, and the mechanical properties of welds and welded joints have been measured. The round robin test results indicated reasonable agreement between the IEA parties participating in the testing. A recommendation from the testing program is the use of a rolling temperature <1050ºC, which will produce a smaller and more favorable prior austenite grain size.

Aging studies of F82H at 500-650ºC have demonstrated the propensity of the steel to form Laves phase, which lowers the impact toughness.

A. Mӧslang presented data generated at Karlsruhe on the isothermal strain-controlled low-cycle fatigue and thermal fatigue properties on several steels, including F82H, OPTIFER, MANET, and EUROFER 97. A large number of results for these steels was presented. Among those results, it was observed that MANET II displayed an order of magnitude better thermal fatigue strength (200-600ºC) than OPTIFER and F82H. The reason for this is probably the higher strength of the MANET. For the thermal creep, the effect of hold time and the temperature window (upper and lower temperatures) has a large effect on the properties. Because of the large effect of the test conditions, care needs to be exercised in the selection of conditions to arrive at a manageable testing schedule.

N. Baluc discussed the constitutive behavior of ferritic/martensitic steels and, in particular, F82H. This behavior is determined up to the uniform strain with tensile tests over a broad range of temperatures (-196 to 450ºC) and strain rates supplemented with strain-rate jump, relaxation, and Cottrell-Stokes (reversibility of the flow stress with temperature) experiments. The constitutive relations were then based on a dislocation mechanics model that is based on the decomposition of thermal and athermal components of the yield stress and strain-hardening components.

Irradiation Effects on Mechanical Properties and Microstructure

The radiation effects studies in the Japanese program were presented by K. Shiba, Y. Kohno, A. Kohyama, and T. Sawai. Shiba reviewed the irradiation studies of F82H. A wide-range of tensile and Charpy results have been generated, including studies to determine a helium effect. Kohno detailed the irradiation studies of the impact behavior of JLF-1 and F82H to 60 dpa at 365-425ºC in EBR-II and FFTF. Kohyama discussed the university results, primarily fatigue and tensile behavior. Sawai discussed recent microstructure studies on irradiated F82H.

F. Tavassoli, using the European properties database developed for ITER as an example, discussed the development of a design database for reduced-activation ferritic/martensitic steels. This database was started by collecting and analyzing the data on modified 9Cr-1Mo steel, after which it was extended to F82H steel and the data that have been generated in the IEA collaboration. In the future, collection of data on F82H will continue, and data collection on EUROFER will begin. The importance of fully traceable material (i.e., fabrication history, thermomechanical treatments, test conditions and procedures, irradiation conditions, etc.) was emphasized.

B. van der Schaaf discussed an irradiation program on electron beam and TIG weldments being carried out at Petten. KLST impact specimens taken from various positions of the welds were irradiated at a nominal 300ºC to about 2.5 dpa. Differences in properties with position in the weld were demonstrated, with the bottom material having the lowest DBTT, the top the highest. Similar effects were observed before and after neutron irradiation. Certain of the weldments had DBTT values over 200ºC after irradiation.

R. L. Klueh described preliminary fracture toughness results for F82H steel before and after irradiation to about 3.8 dpa at 220-280ºC and 310-405ºC. Embrittlement occurred for the lower temperature irradiation, with only small changes occurring at the higher temperatures. In the second part of Klueh's presentation, microstructural observations and tensile and creep properties of two Fe-12Cr ODS steels were described. An Fe-Cr-W-Ti-Y_2O_3 steel showed excellent creep and tensile properties. Dual-beam ion irradiations of the ODS steels indicated the effect of particle size and particle number density on the distribution of the helium in the microstructure.

Advanced Alloys

In fracture toughness studies of the commercial ODS ferritic steel MA 957 discussed by G. R. Odette, it was found that the properties were very anisotropic, as determined by the fabrication process (extrusion), the inclusion content, and geometry. Remarkably high fracture toughness was found in the L-R (longitudinal-radial direction of the extruded rod) direction where a transition temperature of -40ºC was measured. This compared to very poor properties in the other two perpendicular directions. The properties in these directions were hindered by elongated Al_2O_3 inclusions.

M. Toloczko reported on the irradiation creep of pressurized tubes drilled from extruded rods of the commercial ODS ferritic steel MA 957 irradiated to 110 dpa in FFTF at 400-600ºC and compared the results to those on HT9 irradiated similarly. MA 957 steel had equal or slightly better irradiation creep resistance than HT9, with the difference improving with increasing temperature, indicating the effectiveness of the Y_2O_3 dispersion on the creep strength.

Initial results of the European Union program to produce an ODS steel based on a matrix of the EUROFER 97 composition with about 0.25% Y_2O_3 were reviewed by F. Tavassolli. Billets of 400 g and 5 kg were produced by a combination of mechanical alloying and the hot isostatic pressing (HIP) process at 1020ºC and 1000 bars for 2 h. Results indicated a higher strength at 600ºC than the EUROFER 97 produced by conventional techniques.

S. Ukai presented results on a ferritic and martensitic ODS steel developed at JNC, on a martensitic ODS steel based on JLF-1 developed by MONBUSHO, and on a series of martensitic steels based on F82H being developed by JAERI. He remarked on the positive effect of Ti in the JNC steels. The JNC ferritic and martensitic steels had similar internal creep strength, although the martensitic alloy had a slightly higher ultimate tensile strength at 700ºC in tensile tests on rings in the hoop direction. The MONBUSHO and JAERI ODS steel programs are in the early stages of development. Researchers in the MONBUSHO program at Kyoto university produced a steel using JLF-1 powder and 0.3% Y_2O_3, and they are in the process of determining the optimum heat treatment and mechanical properties. The JAERI program with F82H powder and a Y_2O_3 oxide dispersion is in the process of determining the optimum composition.

Activities on RAF Development

K. Ehrlich reported on the European effort to develop EUROFER 97. He explained the rationale for the higher chromium and tantalum and lower tungsten and boron contents in the EUROFER 97 compared to previous steels, particularly the F82H steel. A large-scale (3.5 ton) heat of EUROFER 97 has been produced, and preliminary results show good behavior (physical metallurgy, transformation behavior, hardenability, and mechanical properties—tensile, impact, and creep) relative to previous grades of reduced-activation steel. Preliminary results were also presented on ODS steels with 0.3 and 0.5 % Y_2O_3 produced by the HIP process using EUROFER 97 powder. The tensile strength of the ODS steels was higher than for the EUROFER 97 produced by the conventional process with no apparent sacrifice in tensile ductility.

Work was reported by R. L. Klueh on the effect of Cr, W, Ta, and B on the properties of 5-9Cr-WV steels containing 0.25% V and 0.1% C. Tungsten had little effect on strength but had a positive effect on DBTT. Tantalum improved the strength and the DBTT, but doubling Ta from 0.1 to 0.2 had no effect. Boron had little effect on strength and a negative effect on DBTT of 5 and 7% Cr steels, but it had a positive effect on 9% Cr steel. For 5, 7, and 9Cr-2WVTa steels, the 5 and 9Cr steels had the best strength, and the 5Cr steel had the best Charpy properties.

V. Chernov presented work on the 12 Cr reduced-activation steels developed in Russia. Two industrial-size heats have been manufactured, and their initial microstructures and mechanical properties have been determined. These steels contained about 20% delta-ferrite, but it was concluded that this amount should not adversely affect the properties. In the future, they will seek to make steels without delta-ferrite. The new steels will be included in the future irradiation experiments that were discussed in an earlier presentation.

A. Kimura described work on JLF-1 reduced-activation steels without and with 1.5% Ni and showed that irradiation of the steels in ATR and JMTR produced a larger hardening in the nickel-containing steel. He also presented work for TEM specimens of helium-injected steel tested in a small-punch test. No effect of hardening due to helium could be detected, and no change in fracture mode of the helium-containing specimens tested at low temperatures was observed. TEM studies on JLF-1 after irradiation (425-600ºC) and thermal aging (375-600ºC) were presented that demonstrated the formation of Laves phase under the test conditions. A (Ti,Ta)-rich precipitate also formed during irradiation.

M. Victoria showed results from pure iron and F82H irradiated with neutrons in an experimental reactor and with 600 keV protons in the PIRX facility at PSI. The displacement damage in the neutron-irradiated iron produced a cavity structure. When helium was generated in the proton irradiation for irradiation doses similar to the neutron irradiation, a similar cavity structure was produced. Therefore, the fact that helium does not produce hardening, as observed in numerous experiments, is explained, because the helium is distributed in the pre-existing cavities (those produced by displacement damage). Cavity structures similar to those observed in the iron were also observed in F82H after irradiation, indicating a similar explanation applies to the more complicated alloy. This observation of a lack of hardening caused by helium in the steels complicates any explanation of the increase in DBTT of these steels that has been attributed to helium.

G. R. Odette reported on progress in master curve development for BCC alloys. The use of the master curve is part of a larger effort that has the objective to eventually use small test specimens to obtain data that can be used in the structural analysis of a design and to set operating limits for the structure. To reach this goal, a science- and engineering-based process is proposed that involves the use of constitutive models developed from microstructure-property relationships to produce micromechanical-based local fracture models that can be applied to small specimens used to measure mechanical properties. Examples of the use of the procedure for unirradiated and irradiated materials were presented.

N. Yamamoto reported on load-controlled in-situ fatigue tests of F82H irradiated by 17 MeV protons at 60ºC and 1×10^{-7} dpa/s. Fatigue life was enhanced under irradiation that was explained by the radiation-induced point defects that are continuously produced during the fatigue process. F82H was also implanted by alpha-particles with 1000 appm helium at 550ºC, after which creep-rupture tests were made at 550ºC. No indication of helium embrittlement was observed in terms of the rupture time and ductility, and there was no indication of a change in fracture mode.

V. Chernov discussed corrosion of Armco iron by lead that contained oxygen. An oxygen effect was established in terms of the oxide phases that form. A model was developed to explain the observations. The model involves the cyclical formation and dissolution of the various oxides on the iron surface.

Other Presentations

Three presentations not on the agenda were made during one of the discussion sessions.

A Kohyama presented work by H. Sakasegawa et al. on the microstructure-mechanical properties correlations for high-temperature properties of JLF-1 with 2% W and the JLF-1 composition but with higher tungsten concentrations (2.5, 3.0, and 3.5% W were examined). Increasing tungsten to above 2% is considered a possible way to produce a steel for use at higher temperatures than is possible for a steel with 2% W. Increasing the tungsten to 3.5% increased the tensile and creep strength and lowered the impact toughness. For long-time creep-rupture tests, TEM indicated that the increased tungsten increased the amount of Laves phase that formed and caused the elimination of M_6C from the microstructure compared to the JLF-1 with 2% W. Although the amount of tungsten in solution was greater in a 3% W steel than a 2% W steel before test, there was little difference after a 650 or 700ºC creep-rupture test.

D. S. Gelles described the use of isotopic tailoring with ^{54}Fe to study hydrogen and helium effects. When ^{54}Fe is irradiated in HFIR, both helium and hydrogen is produced, and this is a possible way to conduct a single-variable irradiation experiment on the effect of these gases on mechanical properties. A small number of TEM disks have been irradiated, and a technique was developed that made it possible to obtain not only microstructural information, but also mechanical property data with a shear punch test from a single specimen. In principle, the use of ^{54}Fe appears to be the ideal technique for studying helium effects, the only problem being the high cost of the isotope (about $20,000/g).

T. Hirose presented data on the fatigue of JLF-1 and F82H at ambient temperature obtained using 25.4-mm-long miniature hourglass specimens and a laser extensometer. No effect of specimen size was observed when compared to full-size (100-mm long) specimens. Cyclic softening occurred up to failure; the failure appeared to start with a crack that initiated at a prior austenite grain boundary. Transmission electron microscopy of specimens from the vicinity of the fracture surface indicated a polygonization-like structure replacing the tempered martensite structure during the test.

A presentation on results of irradiation experiments of ferritic/martensitic steels by V. K. Shamardin indicated that a large amount of data have been generated in Russian irradiation experiments in the BOR-60 reactor over the range 335-390ºC up to a maximum damage dose of about 50 dpa. Irradiations have been made on 9Cr-1WVTa steel with 0.1% C and a 12Cr-2WVTiB steel with 0.15% C. The results are important because the experiments have considered the effect of composition, processing, microstructure, etc., and the results need to be considered as further alloy development proceeds.

Discussion Sessions

Discussion sessions were held on the following topics: (1) Summary of Round-Robin Tests and Future Collaboration, (2) Irradiation Effects, and (3) Improvement of the Alloy.

The testing of the IEA heats of F82H and JLF-1 and the round-robin testing that was part of the overall testing has produced a large amount of data. A database has been established by JAERI, and there was a discussion about the need to document the data. Specimen types and sizes were also discussed. The type of specimen used for fatigue tests was thought to be most important, as there appears to be discrepancies on data obtained on hourglass and parallel-side specimens.

The still unanswered question of helium effects hangs over the ferritic/martensitic steels. Simulation techniques (implantation, ^{54}Fe, Ni, and B doping) with their inherent uncertainties are the only methods presently available for such studies, and there are proposals for future work to try and use these techniques constructively. This uncertainty with helium makes the need for a 14 MeV neutron source urgent for the fusion program.

Alloy development for fusion has now moved beyond the F82H and JLF-1 used in the IEA collaboration, as the Europeans and Japanese have determined compositions and processing schedules for the 7-9 Cr class of steel, and large heats are being procured for characterization and development of an engineering database. The area of interest for future development is the ODS steels. The general approach in Europe is to use the EUROFER 97 composition for the matrix and Y_2O_3 for the dispersion to produce a martensitic ODS steel. Similar approaches are being used in Japan with the F82H and JLF-1. In the United States, both ferritic and martensitic ODS steels will be investigated. There is a need to explore a collaborative approach in this endeavor.

Action Items

The following action items were proposed:

1. Produce a report documenting the data collected in the collaborative work on the IEA heats of steel.
2. A meeting will be organized for around February 2001 to discuss a collaboration on ODS steels.
3. A large heat of the new European reduced-activation steel, EUROFER 2001 will be produced. Any of the IEA participants that wish to obtain material to incorporate in their test program should inform B. van der Schaaf of their needs (how much and what type of geometry).

No time or place for the next workshop was determined. It would be possible to hold a workshop in conjunction with ICFRM-10, but the need for a workshop in addition to the ICFRM-10, where much of the new work on ferritic/martensitic steels would be expected to be discussed, needs to be determined.

RECENT RESULTS FOR THE FERRITICS ISOTOPIC TAILORING (FIST) EXPERIMENT - D. S. Gelles, M. L. Hamilton, B. M. Oliver and L. R. Greenwood (Pacific Northwest National Laboratory),[*] S. Ohnuki (University of Hokkaido, Japan), K. Shiba (JAERI Tokai, Japan), Y. Kohno (Muroran Institute of Technology, Japan), A. Kohyama (Kyoto University, Japan) and J. P. Robertson (Oak Ridge National Laboratory)

OBJECTIVE

The objective of this effort is to quantify transmutation-induced irradiation hardening response in isotopically tailored ferritic alloys following irradiation at 300, 400 and 500°C in order to better understand behavior in this alloy class.

SUMMARY

The results of shear punch testing, microstructural examination, and hydrogen and helium analyses performed on irradiated isotopically tailored alloys are reported for specimens irradiated in the HFIR JP20 experiment.

PROGRESS AND STATUS

Introduction

Post-irradiation deformation response, microstructural change, and transmutation induced gas generation of hydrogen and helium has been reported based on measurements of two specimen conditions of an isotopically tailored alloy containing ^{54}Fe addition to the F82H composition in order to study hydrogen and helium embrittlement in single variable experiments.[1,2] Those results were shown to indicate that transmutation-induced hydrogen may play an important role in irradiation embrittlement.[3] Recently, three more isotopically tailored specimen conditions irradiated in the HFIR JP20 experiment in positions 6, 9 and 7 corresponding to ~8 dpa at 300, 400 and 500ºC were made available for examination. This report is intended to provide post-irradiation deformation response base on the shear punch technique, microstructural examination and transmutation induced gas content for these three conditions.

Experimental Procedures

Two transmission electron microscopy (TEM) disks of ^{54}Fe isotopically tailored F82H were obtained from each of the HFIR JP20 experiment positions 6, 9 and 7. The experimental design of the JP20 experiment is described in reference 4, specimen loading is documented in reference 5 and irradiation history and neutron dosimetry can be found in reference 6. The corresponding specimen identification codes are: C601 and C602 for position 6 at 300ºC, C605 and C606 for position 9 at 400ºC, and C609 and C610 for position 7 at 500ºC. One disk for each condition was tested by shear punching and then prepared as a thin foil using the central 1 mm disk created during shear punch testing as described previously.[1,2] The outer ring that remained was then sectioned and used for hydrogen and helium analyses using procedures described previously.[7]

---

[*] Pacific Northwest National Laboratory (PNNL) is operated for the U.S. Department of Energy by Battelle Memorial Institute under contract DE-AC06-76RLO-1830.

Results

Results of shear punch testing are provided in Table 1 and the test curves are shown in Figure 1. Table 1 and Figure 1 include results from previous tests. From these results, it can be shown that irradiation at 500°C produces only slightly higher hardening than in the unirradiated condition whereas irradiation at 300 and 400°C produces similar levels of hardening, intermediate between that due to irradiation at 250°C to 2.4 dpa and irradiation at 300°C to 34 dpa.

Table 1. Results of shear punch testing at room temperature.

ID	MATERIAL	CONDITION	τ_{ys}	τ_{ms}
A943-5	F82H IEA	Unirradiated	340,345,350	458,469,473
F191-3	F82H STD	Unirradiated	325,350,360	476,482,492
C103	F82H STD	300°C, 34 dpa	580	609
FN91-3	F82H ^{54}Fe	Unirradiated	390,400,406	519,520,522
FN51-2	F82H ^{54}Fe	250°C, 2.3 dpa	500,520	602,608
C601	F82H ^{54}Fe	300°C, 7.3 dpa	575	655
C605	F82H ^{54}Fe	400°C, 7.3 dpa	595	660
C609	F82H ^{54}Fe	500°C, 7.5 dpa	400	540
C603	F82H ^{54}Fe	300°C, 34 dpa	600	738
C203	F82H B-F82H	300°C, 34 dpa	470	656

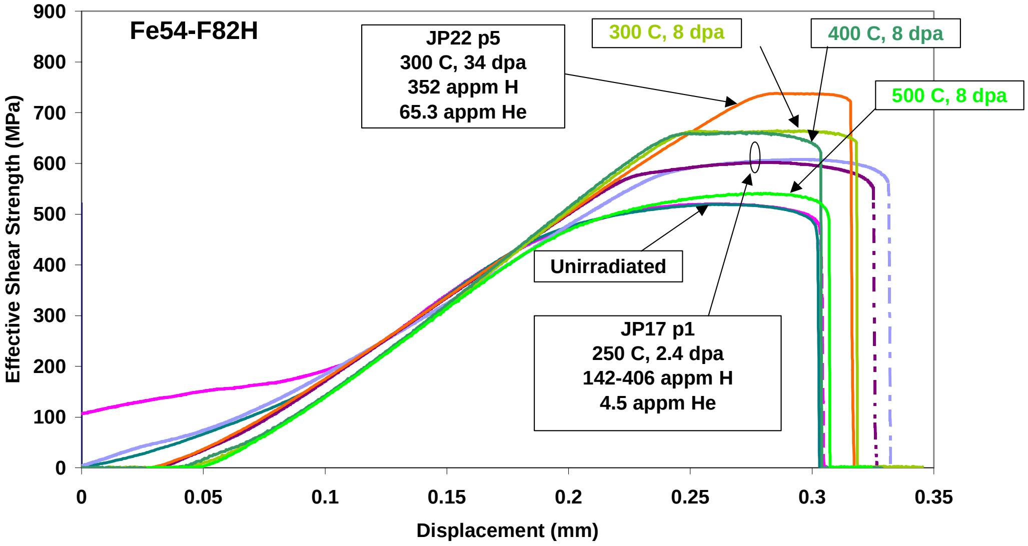

Figure 1. Shear punch test traces for FIST specimens containing ^{54}Fe.

Helium concentrations have been measured for specimens C601, C605 and C609 and the results are provided in Table 2 along with results from previous FIST measurements. Hydrogen concentrations were also measured and the results are provided in Table 3 along with previous results. Helium levels for the three conditions are found to be similar indicating that changes in irradiation temperature did not affect helium retention. Hydrogen levels varied with temperature, the highest levels found after irradiation at 400°C, with lower hydrogen following irradiation at 300°C and the lowest following irradiation at 500°C.

Table 2. Helium concentrations in FIST samples.

Sample	Material	Irradiation Conditions	Mass[a] (mg)	Measured ^{4}He (10^{14} atoms)	Helium Concentration (appm)[b] Measured	Average[c]
FN51-2	F82H+^{54}Fe	JP17/250°C	1.073	0.5278	4.550	4.52
			1.603	0.7765	4.481	±0.05
C103	F82H+^{n}Fe	JP22/300°C	1.567	3.684	21.89	21.8
			1.892	4.407	21.69	±0.1
C203	F82H+^{10}B	JP22/300°C	0.851	29.81	325.9	320
			1.864	63.05	314.7	±8
C603	F82H+^{54}Fe	JP22/300°C	1.047	7.348	64.92	64.8
			1.711	11.96	64.66	±0.2
C601	F82H+^{54}Fe	JP22/300°C	1.042	1.179	10.47	10.4
			1.342	1.507	10.39	±0.1
C605	F82H+^{54}Fe	JP22/400°C	0.626	0.6937	10.25	10.2
			1.246	1.372	10.19	±0.1
C609	F82H+^{54}Fe	JP22/500°C	0.459	0.5625	11.34	11.2
			1.090	1.308	11.10	±0.2

[a] Mass of specimen for analysis. Mass uncertainty is ±0.002 mg.

[b] Helium concentration in atomic parts per million (10^{-6} atom fraction) with respect to the total number of atoms in the specimen.

[c] Mean and standard deviation (1σ) of duplicate analyses.

Microstructural examinations have been performed on each of the conditions available. Examples of these microstructures at low magnification are provided in Figure 2, with one example following irradiation at 300°C, two examples following irradiation at 400°C and one example following irradiation at 500°C. All show typical martensite lath structure decorated with $M_{23}C_6$ carbide. Of particular note are the voids showing at low density following irradiation at 400°C (and therefore two examples are given). Also, it is possible but difficult to quantify, that following irradiation at 500°C precipitate decoration of lath boundaries is more complete.

Table 3. Hydrogen concentrations in FIST samples.

ID	Material	Irradiation Conditions	Mass[a] (mg)	Measured Hydrogen (10^{15} at)	Hydrogen Concentration (appm)[c] Measured	Corrected[b]	Avg[d]
FN92	F82H+^{54}Fe	Unirradiated	2.112	1.16	51	-	44
			2.916	1.34	43	-	±6
			2.699	1.29	44	-	
			1.081	0.875	37	-	
FN51-1	F82H+^{54}Fe	JP17/250°C	2.523	15.1	554	510	406
			3.228	8.92	256	212	±151
			0.840	5.29	583	539	
			1.551	6.78	405	361	
FN51-2	F82H+^{54}Fe	JP17/250°C	2.834	3.82	125	81	142
			3.276	8.70	246	202	±86
C603	F82H+^{54}Fe	JP22/300°C	0.723	3.10	398	354	352
			0.924	4.24	425	381	±21
			1.038	4.33	386	342	
			1.221	4.96	376	332	
C601	F82H+^{54}Fe	JP22/300°C	1.734	17.9	954	910	845
			2.082	18.5	824	780	±92
C605	F82H+^{54}Fe	JP22/400°C	1.819	26.7	1360	1316	1280
			2.208	30.7	1287	1243	±52
C609	F82H+^{54}Fe	JP22/500°C	1.915	15.4	746	702	630
			2.549	16.6	601	557	±103

[a] Mass of specimen for analysis. Mass uncertainty is ±0.002 mg.
[b] Corrected for hydrogen measured in unirradiated control material, FN92.
[c] Hydrogen concentration in atomic parts per million (10^{-6} atom fraction) with respect to the total number of atoms in the specimen.
[d] Mean and standard deviation (1σ) of replicate (corrected) analyses.

The dislocation and bubble structures were studied in greater detail by examining these microstructures in dark field under dislocation contrast. Examples are provided in Figure 3 comparing a region of interest for each condition under g=01$\bar{1}$ and 200 dark field along with a bright field image, for C601 and C605 in void contrast and for C609 in dislocation contrast. Figure 3 shows that the dislocation structure changes with irradiation temperature, loop size increasing and density decreasing with increasing temperature. However, other differences can be identified. For example, a<100> Burgers vectors predominate following irradiation at 400°C, but are not present following irradiation at 500°C and may not be present following irradiation at 300°C. This is demonstrated most straightforwardly in Figure 3e) where horizontal features (perpendicular to the operating 200 diffraction vector) are of Burgers vector a[100] whereas all other dislocation line segments (in weaker contrast) are of type $\frac{a}{2}$<111>. Also of note are smaller equiaxed features in Figures 3a and b) about 5 nm in diameter. These may be small loops or gas bubbles, but because they are not visible in Figure 3c), it is expected that they are due to precipitation, possible α‘ or carbide. Finally, bubbles on the order of 5 nm in diameter may be seen in Figure 3c) but the density is apparently low.

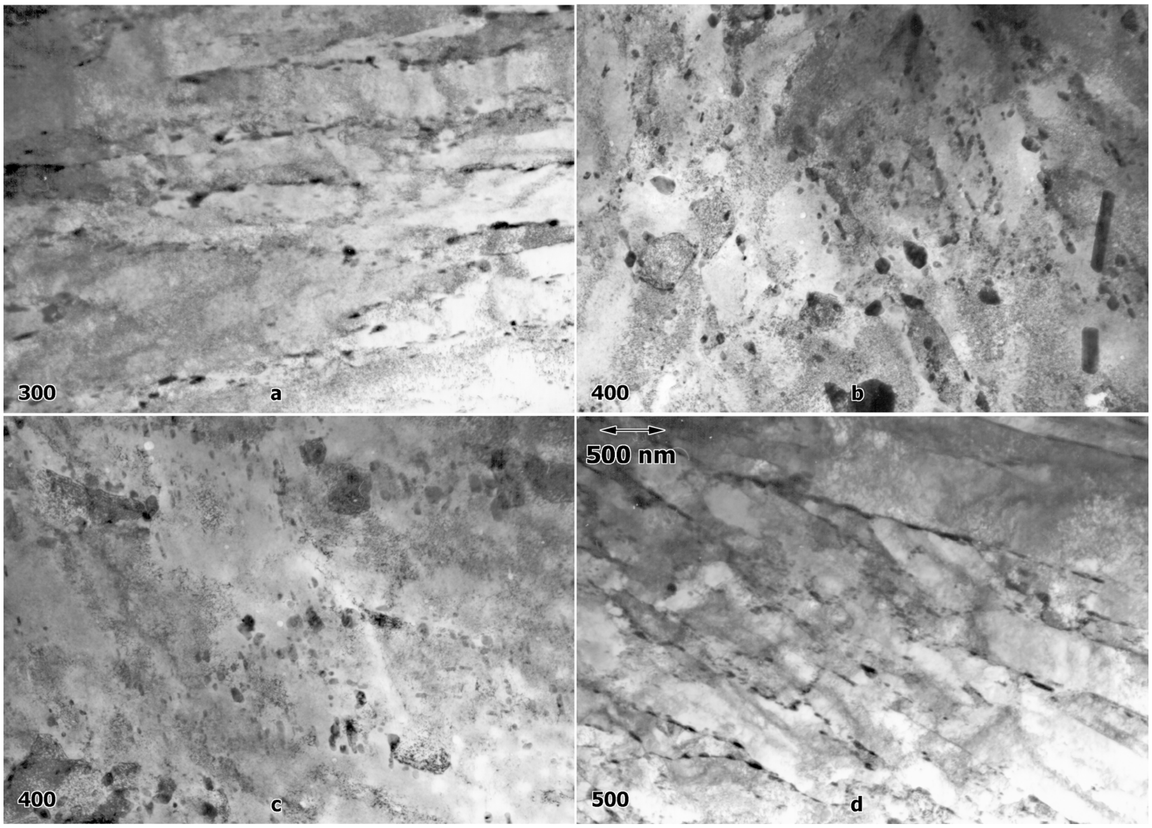

Figure 2. Low magnification examples of microstructures in C601 a), C605 b) and c), and C609 d) .

Discussion

Irradiation hardening response is plotted as a function of dose and temperature for effective shear yield and maximum strength, respectively, in Figures 4 through 7. Data from samples C601, C605 and C609 is labeled 300 C, 400 C and 500 C, respectively. Behavior of strength as a function of dose in Figures 4 and 6 follows expected behavior for 300 and 400°C but strength following irradiation at 500°C is much lower. This is further demonstrated in Figures 5 and 7. Therefore, it is reasonable to directly compare response following irradiation at 250, 300 and 400°C. Note that this response is typical of irradiation hardening without the influence of transmutation-induced gases.

In order to identify effects of He and H produced by transmutation during irradiation, it is best to plot hardening behavior as a function of He and H as shown previously.[8] Therefore, the change in effective shear strength is shown plotted as a function of He and H content in Figure 8. Figure 8 includes previous results as well as results for conditions C601, C605 and C609. From Figure 8, several conclusions can be drawn. Strength changes found previously as a function of He are similar to that in Figure 8, except for results at 500°C. Therefore, conclusions drawn previously may still apply: that it is possible that there is no effect of He on yield response whereas a bi-linear response can be identified for the maximum strength if one excludes results at 500°C. Bi-linear response is indicated because zero hardening is imposed for zero He. Results as a function of H must be interpreted differently. Data for C601, C605 and C609 give very different irradiation hardening behavior as a function of H compared to response found previously, with no straightforward correlation evident.

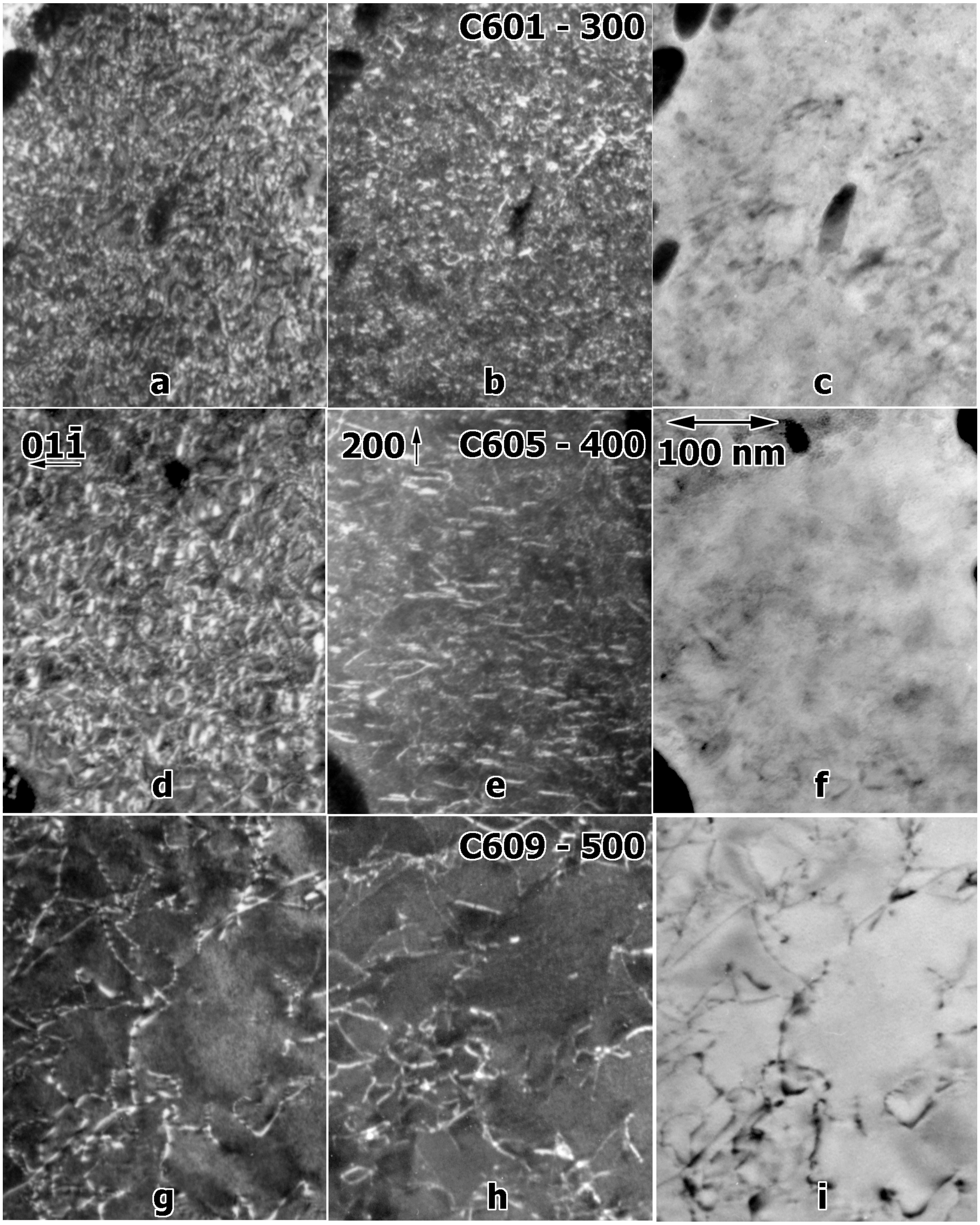

Figure 3. Dislocation structure in conditions C601, C605 and C609 shown in $\bar{g} = 01\bar{1}$, 200 and bright field contrast, respectively.

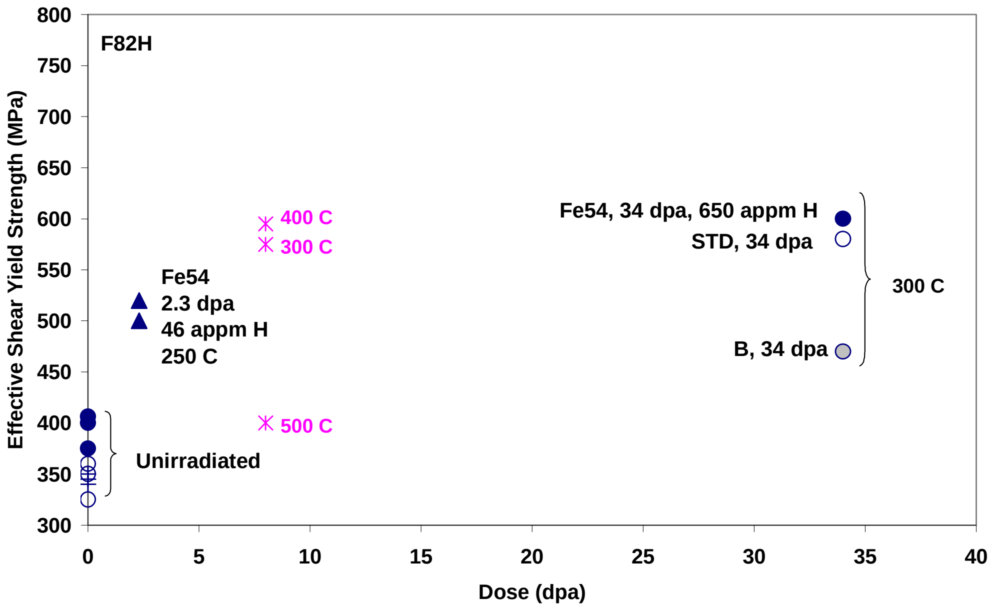

Figure 4. Effective Shear Yield Strength as a function of dose for isotopically tailored F82H.

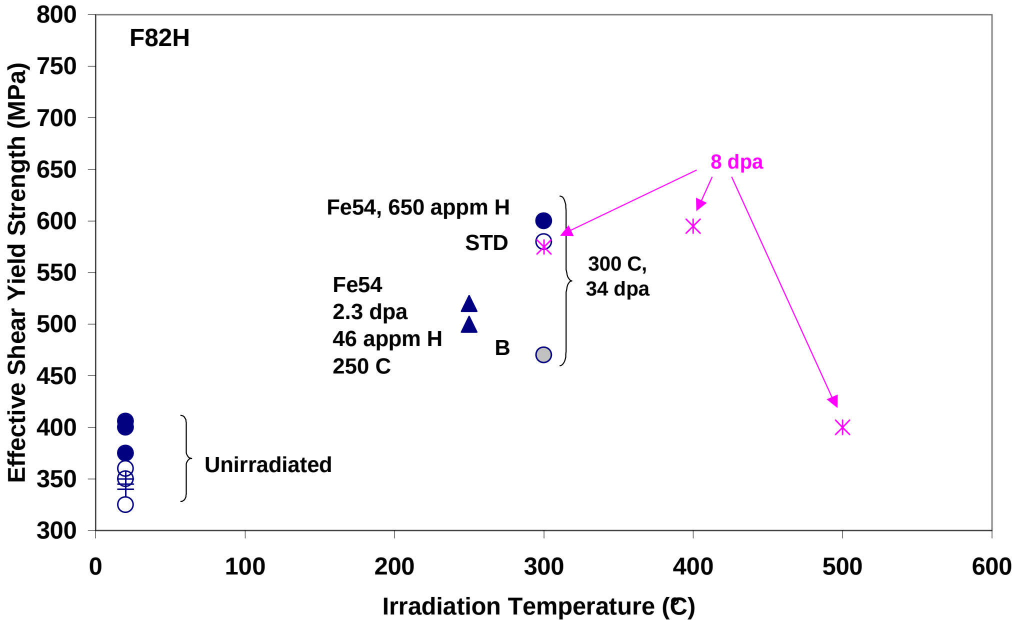

Figure 5. Effective Shear Yield Strength as a function of temperature for isotopically tailored F82H.

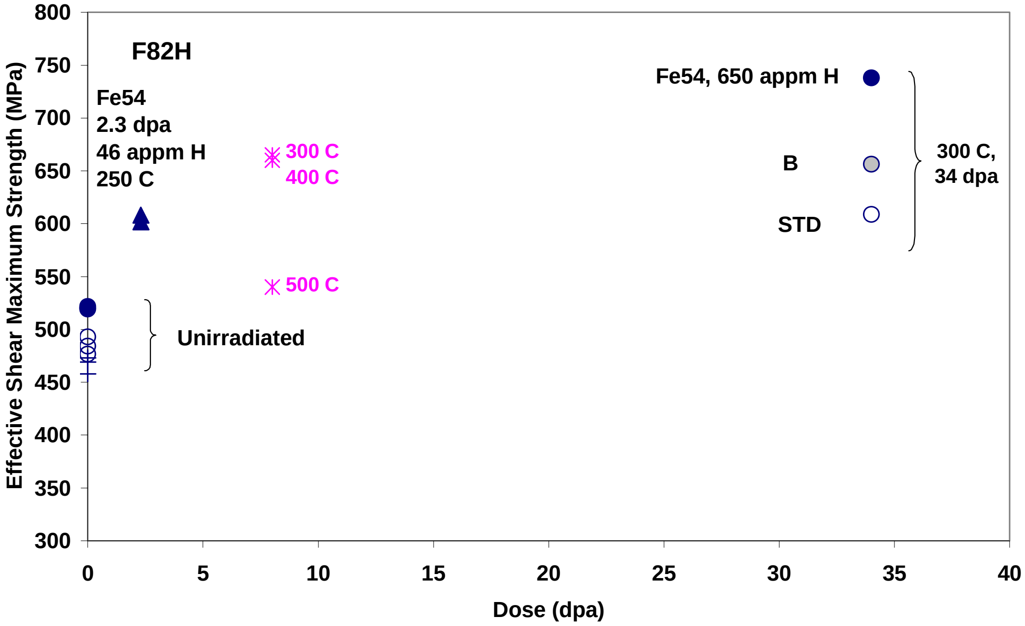

Figure 6. Effective Shear Maximum Strength as a function of dose for isotopically tailored F82H.

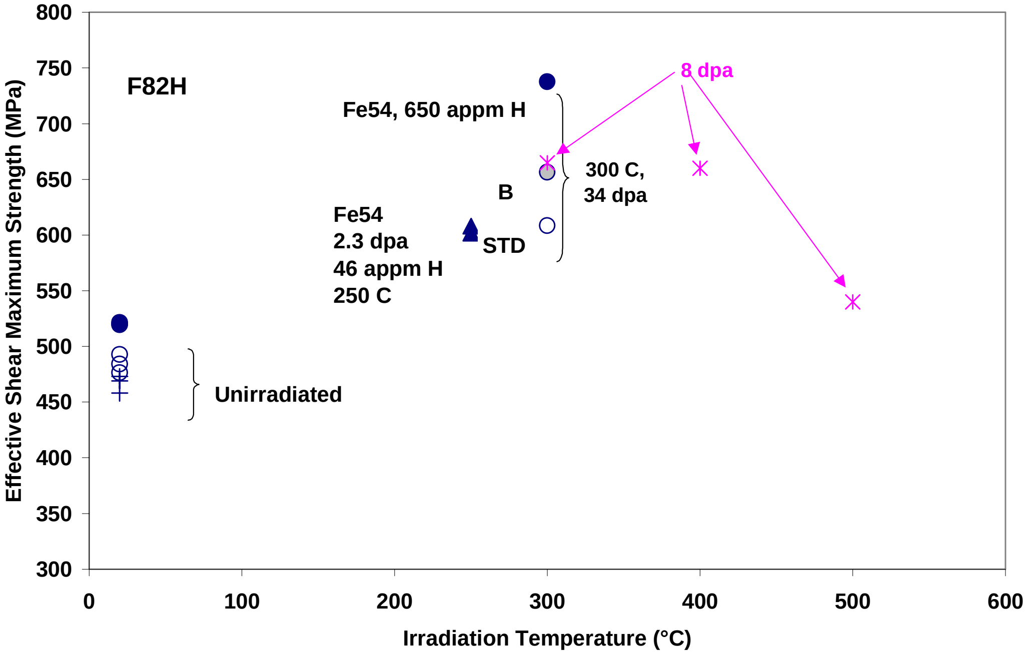

Figure 7. Effective Shear Maximum Strength as a function of temperature for isotopically tailored F82H.

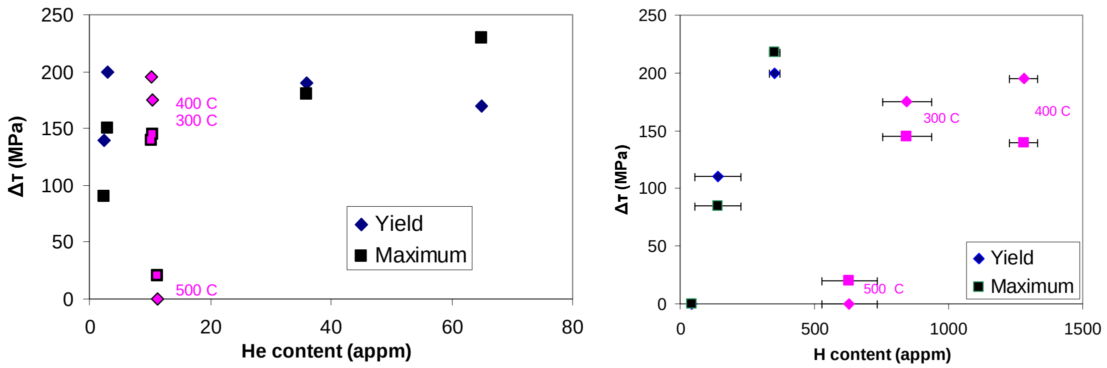

Figure 8. Change in τ_{ys} and τ_{ms} due to irradiation as a function of a) He content and b) H content for FIST alloys.

It must be noted that the measurements of helium in specimens C601, C605 and C609 fit predicted behavior whereas measurements for H are considerably higher than expected. This is demonstrated in Figure 9 a) and b) showing He and H measured levels in comparison with prediction. The He measurements agree with calculations that take into account increased helium production from both 54Fe and transmutation to 55Fe (Reference 7), as shown in Figure 9a. Calculations for H, which also take into account the Fe isotopic cross sections and transmutation are compared with the data in Figure 9b. Most of the H measurements are higher than predicted, although an earlier measurement at a higher dose is considerably below the calculated value. The earlier data was interpreted to indicated that H can be lost during irradiation whereas the present data indicated that not only is H not lost, it can be generated at higher than expected rates.

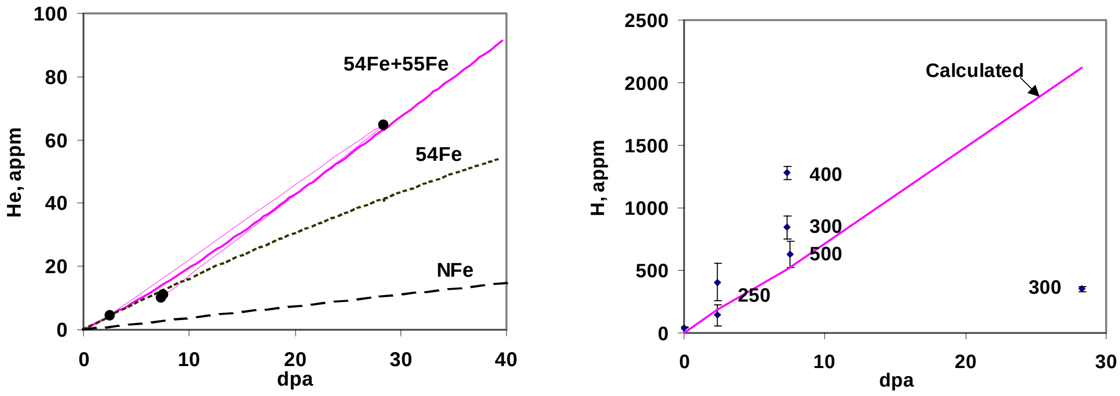

Figure 9. Helium and hydrogen production in ^{54}Fe isotopically tailored F82H, measurement verses prediction.

Only one of the two specimens available for examination has been used. Therefore, consideration is being given to using the remaining specimens for remeasurement of H. Also, this work would be enhanced greatly if control conditions (those without ^{54}Fe) were available. Then it should be possible to objectively account for effects of transmutation-induced He and H. Unfortunately, it has not yet been possible to obtain such control conditions.

Conclusions

Three conditions of isotopically tailored F82H irradiated in the HFIR JP20 experiment have been tested, examined by TEM, and analyzed for He and H content in order to quantify irradiation hardening due to transmutation-induced helium and hydrogen.

> Hardening due to irradiation is found following irradiation at 300 and 400°C, that is intermediate between that at lower and higher dose, but hardening is negligible following irradiation at 500°C.
>
> Microstructural examinations show typical behavior of irradiation as a function of irradiation temperature, with moderate swelling after 400°C irradiation but few bubbles after irradiation at 300°C.
>
> Correlations of change in hardening with He and H content show little indication of transmutation-induced hardening, but measured H levels do not agree with predictions and therefore H production and analysis requires further study.

FUTURE WORK

Uses for the duplicate unused specimens from this study will be considered. Availability of other specimens pertinent to this work will be sought. A more complete test is being considered for future HFIR irradiation.

REFERENCES

[1] M. L. Hamilton, D. S. Gelles, S. Ohnuki, K. Shiba, Y. Kohno, and A. Kohyama, DOE/ER-0313/25 (1999) 136.
[2] D. S. Gelles, S. Ohnuki, K. Shiba, Y. Kohno, A. Kohyama, J. P. Robertson, and M. L. Hamilton, DOE/ER-0313/25 (1999) 143.
[3] S. Ohnuki, Y. Kohno, A. Kohyama, K. Shiba, D. S. Gelles, M. L. Hamilton, and J. P. Robertson, presented at ICFRM-9 in Colorado Springs October 1999, paper 7.04.
[4] J. E. Pawel, and R. L. Senn, DOE/ER-0313/12 (1992) 15.
[5] J. E. Pawel, A. W. Longest, R. L. Senn, K. Shiba, D. W. Weatherly, and R. G. Sitterson, DOE/ER-0313/15 (1994) 3.
[6] L. R. Greenwood and C. A. Baldwin, DOE/ER-0313/18 (1998) 305.
[7] L. R. Greenwood, B. M. Oliver, S. Ohnuki, K. Shiba, Y. Kohno, A. Kohyama, J. P. Robertson, J. W. Meadows and D. S. Gelles, J. Nucl. Mater. 283-287 (2000) 1438.
[8] D. S. Gelles, M. L. Hamilton, B. M. Oliver, and L. R. Greenwood, DOE/ER-0313/27 (2000) 149.

SHEAR PUNCH PROPERTIES OF LOW ACTIVATION FERRITIC STEELS FOLLOWING IRRADIATION IN ORR

- R. M. Ermi, M. L. Hamilton, and D. S. Gelles (Pacific Northwest National Laboratory) and A. M. Ermi (COGEMA Engineering Corporation, Richland, WA)

OBJECTIVE

The objective of this effort is to determine the irradiation induced hardening response in low activation ferritic steels following irradiation at temperatures of 400°C and below in order to better understand behavior in this alloy class at low irradiation temperatures.

SUMMARY

Shear punch post-irradiation test results are reported for a series of low activation steels containing Mn following irradiation in the Oak Ridge Reactor at 330 and 400°C to ~10 dpa. Alloy compositions included 2Cr, 9Cr and 12Cr steels with V to 1.5% and W to 1.0%. Comparison of results with tensile test results showed good correlations with previously observed trends except where disks were improperly manufactured because they were too thin or because engraving was faulty.

PROGRESS AND STATUS

Introduction

The post-irradiation tensile test response has been reported for a series of reduced activation alloys containing manganese following irradiation in the Oak Ridge Reactor (ORR) at 60, 200, 330, and 400°C to ~10 dpa.[1] The alloys include 2% Cr alloys with V additions, and 9% and 12% Cr alloys containing Mn with V and W additions (Table 1). Companion transmission electron microscopy (TEM) specimens were included in that irradiation experiment at 330 and 400°C in order to provide microstructural information. Recent improvements in specimen preparation technique now allow preparation of transparent foils from 1 mm diameter disks.[2] Smaller samples reduce magnetic and radioactivity effects allowing, for example, more effective identification of precipitate phases. Therefore, the standard 3 mm diameter TEM disks had to be reduced to 1 mm and it was expedient to obtain shear punch information in the process. This report therefore provides shear punch data for the TEM specimens contained in the ORR test.

Experimental Procedure

Compositions and identification codes for specimens irradiated in the ORR-MFE 6J and 7J tests are provided in Table 1. Table 1 includes identification code information for corresponding tensile specimens. Specimens were of standard TEM geometry, 3 mm in diameter x 0.20 mm. Shear punch tests were performed at room temperature using standard techniques.[3] The 6J test accumulated a midplane fluence of 2.4 x 10^{22} n/cm^2 (total) or 8.8 x 10^{21} n/cm^2 (E>0.1 MeV) and the 7J test accumulated a fluence of 2.7x 10^{22} n/cm^2 (total) or 9.5 x 10^{21} n/cm^2 (E>0.1 MeV).[4,5] This corresponds to damage levels of 6.6 - 6.8 and 7.1 - 7.3 dpa, respectively, variations corresponding to lower or higher chromium levels. Predicted helium levels are 2.1 to 2.3 appm for both tests, with variations due to higher or lower chromium levels, respectively.

Table 1. Identification codes (TEM / Tensile) and compositions for TEM specimens irradiated in the ORR-MFE 6J and 7J tests.[1]

ID code	Heat # or alloy name	Composition (w/o)					
		Cr	V	W	Mo	C	Mn
P3/TE	V02262	2.25	0.5			0.1	
P5/TZ	UC-19	2.25	1.5		0.2	0.1	0.3
RB/TR	V02268	9	0.3	1.0		0.1	2.5
P6/TM	V02264	9	0.5			0.1	
P9/TP	V02266	9	0.5			0.1	2.0
P7/TN	V02265	9	1.3			0.2	1.0
RE/TU	V02269	12	0.3	1.0		0.1	6.5
RA/TL	V02267	12	1.0			0.1	6.5

Results

The shear punch results are given in Table 2 along with corresponding tensile results. These results can be compared by plotting tensile yield strength against effective shear yield stress and ultimate tensile strength against effective shear maximum stress, as shown in Figures 1 and 2. Both plots include a trend line at a slope of 2 and a separation between the 330 and 400 C data points. Figures 1 and 2 indicate that the correlation found previously at a slope of ~2 applies to these data sets, but several data points deviate significantly from the trend line.

Discussion

A review of experimental details showed that all points that deviated significantly from the trend lines in Figures 1 and 2 corresponded to defective TEM disks. Either they were thinner than 0.006” (0.15 mm) [P3LH and P9LH] whereas TEM disks were intended to be 0.008” (0.20 mm) thick, or engraving codes were not located properly [P5LB was engraved at the center and P7LH was engraved on both sides]. Disks are oriented with engraving codes up and away from the punch to avoid stress risers in regions under tension. Engraving problems consistently raised shear strength values about 100 MPa from the trend line whereas disks with reduced thickness gave inconsistent behavior, sometimes higher and sometimes lower than the trend line. Standard procedures require die tolerances be related to specimen thickness, but a fixed die tolerance was used for this work. However, a recent study has shown that the mechanical properties obtained from the shear punch test are relatively insensitive to specimen thickness over the range of thicknesses covered in the present study.[6] Therefore, the inconsistent mechanical properties obtained from thin specimens is not understood. But it can be concluded that shear punch tests on irradiated low activation alloys can be expected to give consistent estimates of strength provided disks are not undersized in thickness and engraving codes do not interfere with testing.

Conclusions

A series of low activation alloys that were irradiated as TEM disks in the ORR have been tested by shear punching and the values obtained have been compared with tensile tests on companion specimens irradiated under identical conditions.

Comparison of shear punch and tensile behavior is found to be consistent with previous trends except when specimens are too thin or when engraving codes are improperly positioned. Therefore, it should be possible to assess strength increases due to irradiation of low activation alloys using shear punch procedures providing disks are carefully manufactured.

Table 2. Shear punch and uniaxial tensile test results on low activation steel specimens following irradiation in ORR.

ID TEM/Tensile	Dose (dpa)	Irr Temp (°C)	Test Temp (°C)	Effect.Yield Shear (MPa)	Effect.Max. Shear (MPa)	YS (MPa)	UTS (MPa)	UE (%)	TE (%)
P3LB/TE11	7.1	330	22	680	888	1367	1412	0.8	5.8
P3LH/TE13	7.1	400	22	320	462	1198	1230	0.8	6.9
P4LB/	7.1	330	22	580	694				
P4LH/	7.1	400	22	405	506				
P5LB/TZ11	7.1	340	22	650	717	1014	1014	0	0
P5LH/TZ15	7.1	400	22	305	423	661	700	1.4	8.6
RBLB/TR11	7.2	330	22	480	567	885	893	0.4	8.4
RBLH/TR15	7.2	400	22	260	458	576	673	6.2	16.6
P6LB/TM11	7.2	330	22	480	620	879	883	0.3	9.6
P7LB/TN11	7.2	330	22	500	613	917	933	0.6	8.9
P7LH/TN13	7.2	400	22	410	555	504	618	7.4	20.1
P9LB/TP11	7.2	330	22	430	537	960	971	0.5	8.1
P9LH/TP13	7.2	400	22	400	546	565	643	5.1	17.8
RELB/TU11	7.3	330	22	530	650	1009	1066	1.4	7.8
RELH/TU15	7.3	400	22	420	581	755	888	5	10.2
RALB/TL11	7.2	330	22	480	587	970	1004	3	10.8
RALH/TL13	7.3	400	22	400	553	719	846	7.1	15.3

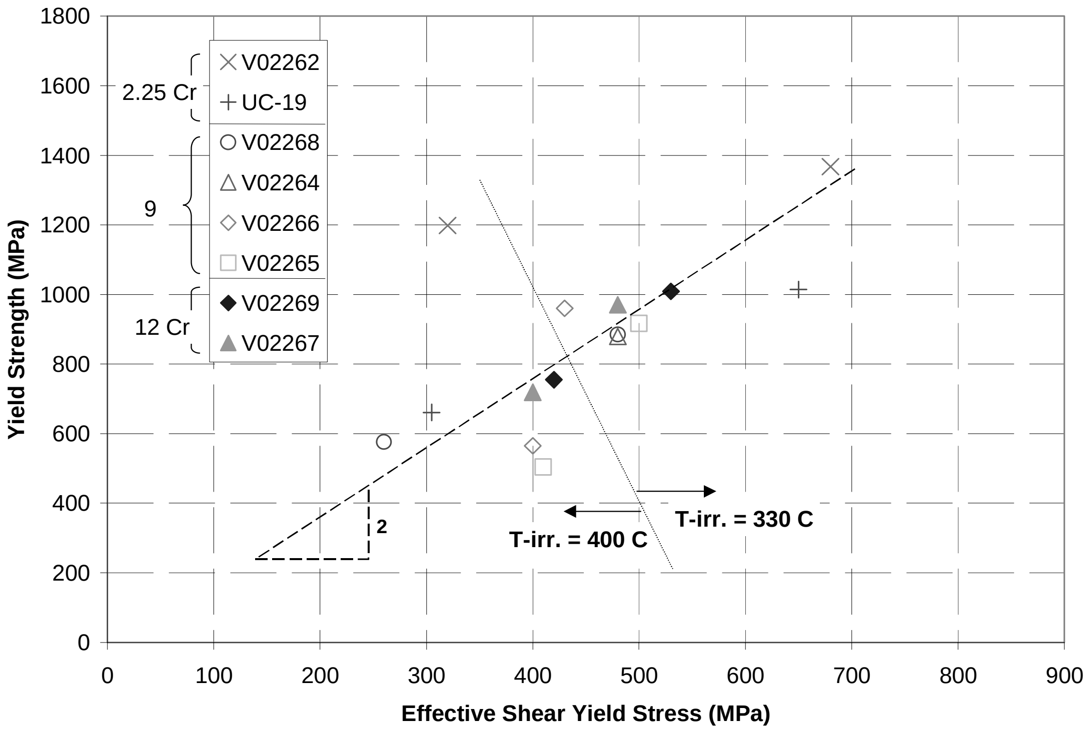

Figure 1. Comparison of tensile yield strength and effective shear yield stress.

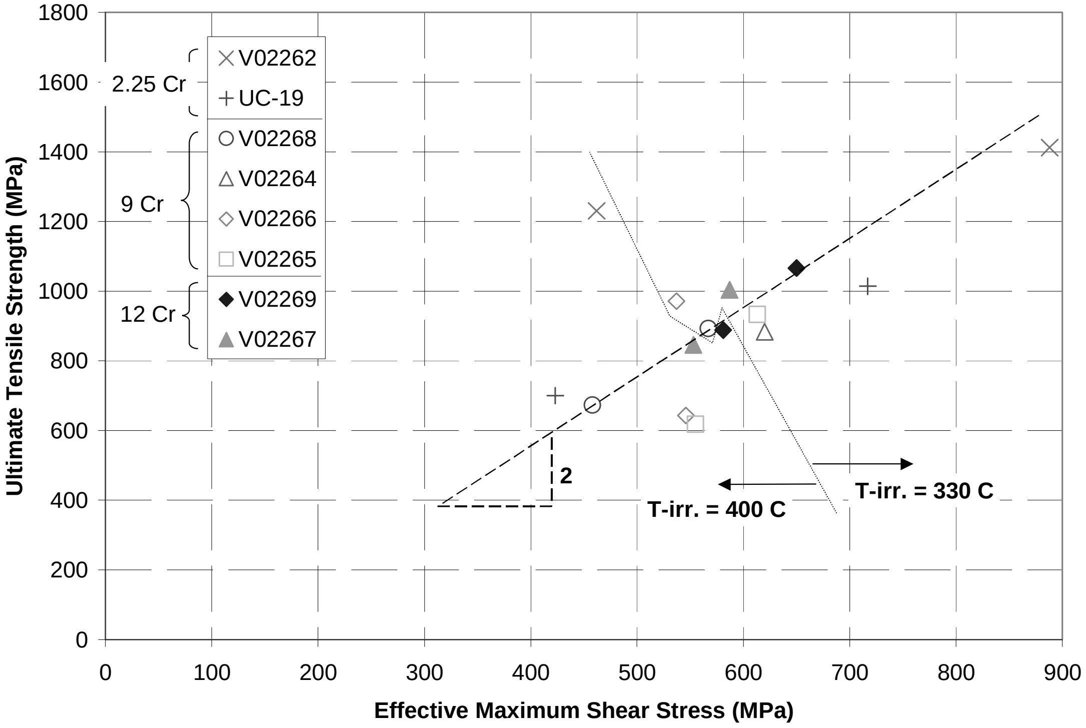

Figure 2. Comparison of ultimate tensile strength and effective maximum shear stress.

FUTURE WORK

TEM specimens 1 mm in diameter will be thinned and examined. The effort is then expected to shift to acquisition and testing of the ORR specimens further irradiated in HFIR.

REFERENCES

[1] M. L. Hamilton and D. S. Gelles, DOE/ER-0313/26 (1999) 102.

[2] S. Ohnuki, K. Shiba, Y. Kohno, A. Kohyama, J. P. Robertson, M. L. Hamilton and D. S. Gelles in Microstructural Processes in Irradiated Materials, MRS Symposium Proceedings Volume 540 (1999) 603.

[3] M. L. Hamilton, D. S. Gelles, S. Ohnuki, K. Shiba, Y. Kohno, and A. Kohyama, DOE/ER-0313/25 (1999) 136.

[4] L. R. Greenwood, DOE/ER-0313/6 (1989) 23.

[5] L. R. Greenwood, DOE/ER-0313/8 (1990) 34.

[6] M. B. Toloczko, Y. Yokokura, K. Abe, M. I. Hamilton, F. A. Garner and R. J. Kurtz, Fourth Symposium on Small Specimen Test Techniques, ASTM STP 1418, to be published.

LONG-TERM HIGH TEMPERATURE OXIDATION BEHAVIOR OF ODS FERRITICS -- B. A. Pint (Oak Ridge National Laboratory)

OBJECTIVE

The objective of these experiments was to examine the long-term, high temperature (700°-1100°C) oxidation behavior of oxide dispersion strengthened (ODS) Fe-(12-13)wt%Cr alloys. These alloys are being considered for both fusion and fossil energy applications. By adding an oxide dispersion, the creep strength of ferritic alloys is significantly increased, allowing increased reactor operating temperature. However, the corrosion resistance of these materials have not been studied in fusion-relavent environments such as He and water-containing gases. The initial testing has focused on oxidation in air and air with 10% water vapor to obtain baseline reaction rates.

SUMMARY

Four ODS ferritic compositions were tested for up to 10,000h at 700°-1100°C. At 700°-800°C in air, the reaction rates were very low for all of the alloys. At 900°C, the addition of Y_2O_3, compared to Al_2O_3, showed a distinct benefit in improving the oxidation resistance, due to a reactive element effect. The absence of Ti and W in one alloy appeared to result in a thinner reaction product after oxidation at 800°C. One composition was tested in 10% water vapor at 900°C and at 1000°C and 1100°C in air. Under these higher temperature conditions, there was a significant increase in the rates of oxidation. With only 13-14at%Cr in these alloys, their corrosion-limited operating temperature is less than 1000°C.

PROGRESS AND STATUS

Experimental Procedure

The chemical compositions of the four test materials are given in Table I. Alloys FCW-Y and FCW-Al were supplied by Sumitomo Corp. and contain dispersions of Y_2O_3 and Al_2O_3 respectively. Alloys FC-Y and FCW-YT were supplied by Kobe Steel and contained dispersions of Y_2O_3 and Y_2O_3-TiO_2 respectively. Coupons with 3-5cm^2 of surface area were made of each composition and polished to a 0.3µm finish. Prior to oxidation, the specimens were cleaned in acetone and methanol. Oxidation experiments in air were conducted with specimens in individual annealed alumina crucibles with lids. This allows any spalled or evaporated oxide to be collected in the crucible in order to measure a total mass change.[1] Oxidation kinetic data in air were generated by weighing every 100h (1000°-1100°C) or 500h (700°-900°C) to totals of 1000-10000h using a Mettler model AG245 balance. Oxidation exposures in air with 10%H_2O were conducted by flowing the gas through a closed alumina tube that was inside a resistively-heated horizontal tube furnace. Distilled water was atomized into the flowing gas stream above its condensation temperature and heated to the reaction temperature within the alumina tube. Water was collected and measured after flowing through the tube to calibrate the amount of injected water. Specimens were held in slots in an alumina boat in the furnace hot zone. After these exposures, selected specimens were examined in plan-view by SEM and/or Cu-plated and sectioned for metallographic analysis.

Table I. Chemical compositions of the ferritic ODS alloys in atomic percent. Some of the nominal values (marked NOM)) have been confirmed experimentally (EXP) by induction coupled plasma analysis and combustion analysis.

	FCW-Y (EXP)	FC-Y (NOM)	FCW-YT (NOM)	FCW-Al (EXP)
Fe	83.1	86.9	85	80.6
Cr	14.2	12.8	13	14.3
W	0.9		0.9	0.9
Y	0.12	0.12	0.13	<0.01
Ti	0.37		0.47	0.01
Al	0.03			3.3
Si	0.10			<0.10
Ni	0.03			0.06
Mn	0.03			0.01
O	0.76			0.73
N	0.07			0.06
C	0.23			0.05
S (ppm)	114			129

Results and Discussion

Reaction Kinetics

Figure 1 shows the mass changes for the various alloys at 700° and 800°C during 500h cycles in air. These data were used to calculate parabolic rate constants, Table II. At 700°C, FC-Y and

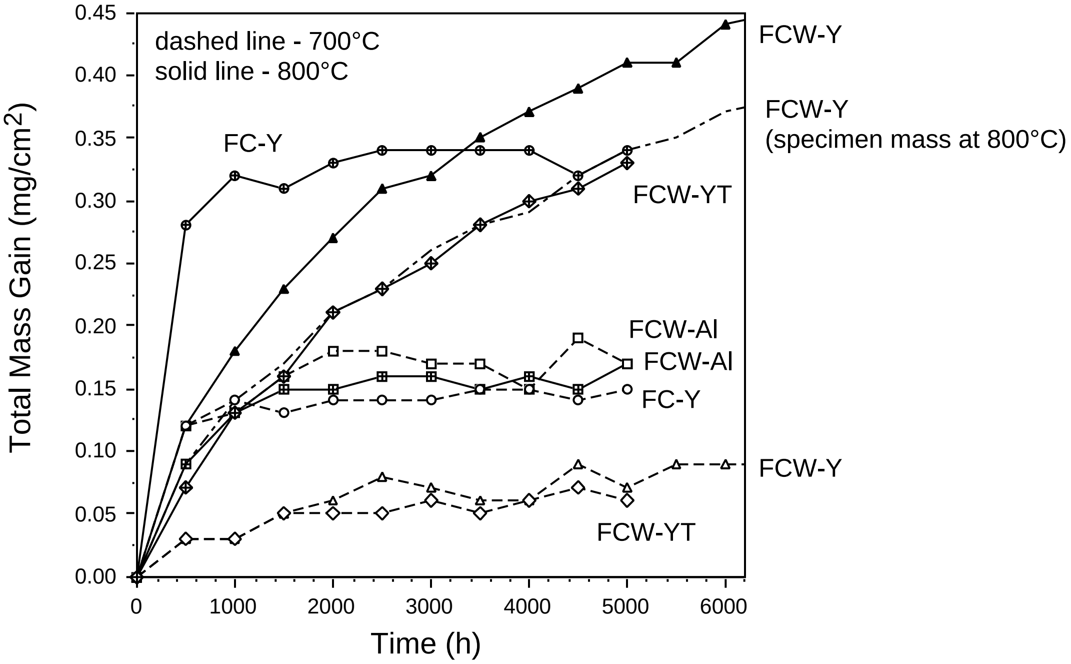

Figure 1. Total mass gains measured during 500h cycles in air at 700°C (dashed lines) and 800°C (solid lines) for the ODS ferritic alloys.

Table II. Parabolic rate constants (g^2/cm^4s) calculated from the oxidation data in air

	700°C	800°C	900°C	1000°C
FCW-Y	1.9×10^{-16}	7.1×10^{-15}	6.3×10^{-14}	2.1×10^{-10}
FC-Y	1.2	0.24		
FCW-YT	2.2	8.0	4.6×10^{-14}	
FCW-Al	2.8	0.75	2.8×10^{-12}	

FCW-Al initially showed higher mass gains but subsequently showed similar mass gain rates as the other alloys, Table II. These two alloys (FC-Y and FCW-Al) also behaved differently at 800°C. FC-Y showed a very high initial mass gain followed by little additional mass gain. FCW-Al showed the lowest mass gain of any of the alloys at 800°C. This was likely due to the Al addition (3.3at%) being able to slow the rate of Cr_2O_3 formation or possibly the formation of an Al_2O_3 protective layer which has a slower rate of growth than Cr_2O_3. Low levels of Al have previously been reported to improve oxidation resistance in Cr_2O_3-forming alloys.[2] However, it was reported that higher Al levels (>4at%) were required to form a continuos Al_2O_3 layer on Fe-Cr-Al alloys.[3] Nevertheless, ODS alloys contain numerous dislocations and sub-grain boundaries which could allow faster Al diffusion along defect pathways and result in a stronger Al effect than that observed in wrought alloys.

Both the total and specimen mass gains for FCW-Y at 800°C are shown in Figure 1. The difference between the two numbers is attributed to the evaporation of CrO_3 from the specimen as the inside of the crucible turned green but no spalled oxide was found in the bottom of the crucible. The other alloys did not exhibit as much evaporation and thus showed somewhat lower total mass gains. When the oxide scale evaporates, higher rates are expected as the diffusion distance through the oxide does not increase as it would for a more stable oxide.

Figure 2 shows the oxidation data obtained at 900°C. For these alloys with relatively low Cr levels, this is a very high test temperature. As the reaction rate increases with temperature, the metal can become severely depleted in Cr resulting in rapid or breakaway oxidation of the base metal (Fe). In air, FCW-Y and FCW-YT performed well, with similar reaction rates, Table II. However, FCW-Al showed a very high reaction rate during the first 500h in air and subsequently went into breakaway oxidation during the next cycle. This behavior was attributed to the absence of Y in this material. Since the specimen of FCW-Al was 1.4mm thick and thus had a larger reservoir of Cr than the 1mm thick FCW-Y specimen, FCW-Al should have exhibited a longer life. It is well known that an addition of Y reduces the growth rate of Cr_2O_3 by a factor of 10-100 at this temperature.[2,4-5] The faster growing scale on FCW-Al (compare the mass gain after one cycle to FCW-Y) consumed more Cr in this alloy and likely caused depletion near the metal-scale interface. No scale spallation was measured after one cycle but any cracking of the scale could could have caused the rapid reoxidation during the next cycle, sending the alloy into breakaway oxidation.

The addition of water vapor in 100h cycles showed a significant effect on the performance of FCW-Y at 900°C, Figure 2. Large mass losses were attributed to evaporation of CrO_3 which is accelerated by the presence of water vapor. This suggests that further testing will be required if these alloys will experience exposure to water-containing environments in service, even at lower

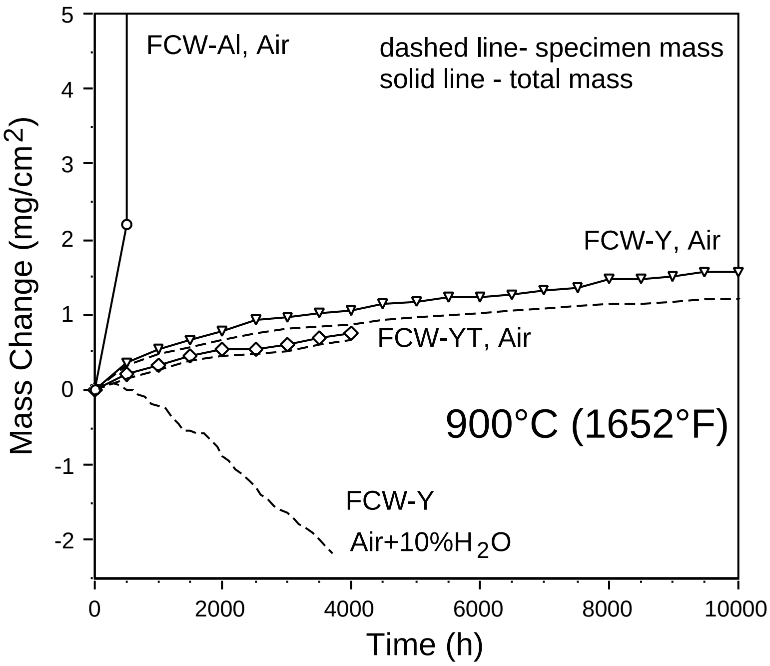

Figure 2. Total (solid lines) and specimen (dashed lines) mass gains measured at 900°C in air and air with 10% water vapor. The addition of water vapor to the test resulted in mass losses for FCW-Y compared to exposure in air.

temperatures. Accelerated pressures and higher flow rates will further increase this problem.

FCW-Y also was exposed in 100h crucible tests at 1000°C and 1100°C in air. A significant increase in the oxidation rate between 900° and 1000°C indicated that the alloy was not forming a protective external scale at 1000°C, Table II. At 1100°C, the alloy was fully consumed after 100h. Thus, the maximum operating temperature for this class of alloys in air appears to be <1000°C.

Characterization

Metallographic cross-sections of the scales formed on FCW-Y are shown in Figure 3. The thicknesses of the oxide corresponded well with the mass gains in Figures 1 and 2. At the higher temperatures, the metal-scale interface appeared to roughen, possibly due to growth stresses in the oxide. Also, there appeared to be a significant increase in the amount of internal oxide with increasing temperature. The internal oxide was likely rich in Cr which further depletes the Cr reservoir in the metal. There appeared to be pores in the scale formed at 900°C (Figure 3c); however, these could have been caused by pullouts of fine grains during polishing.

Figure 4 shows the scales formed on FC-Y and FCW-YT after exposures at 700° and 800°C. The scale on FC-Y after 5000h at 700°C showed some Fe-rich nodule formation, arrows in Figure 4a. This is consistent with the high initial mass gain for this alloy, Figure 1. The fact that the mass gain did not increase as rapidly after the first 500h suggests that the nodules did not continue to grow during exposure. The reason for nodule formation may be inhomogeneities in the alloy composition (areas of low Cr) or due to the slightly lower overall Cr content in this alloy, Table I.

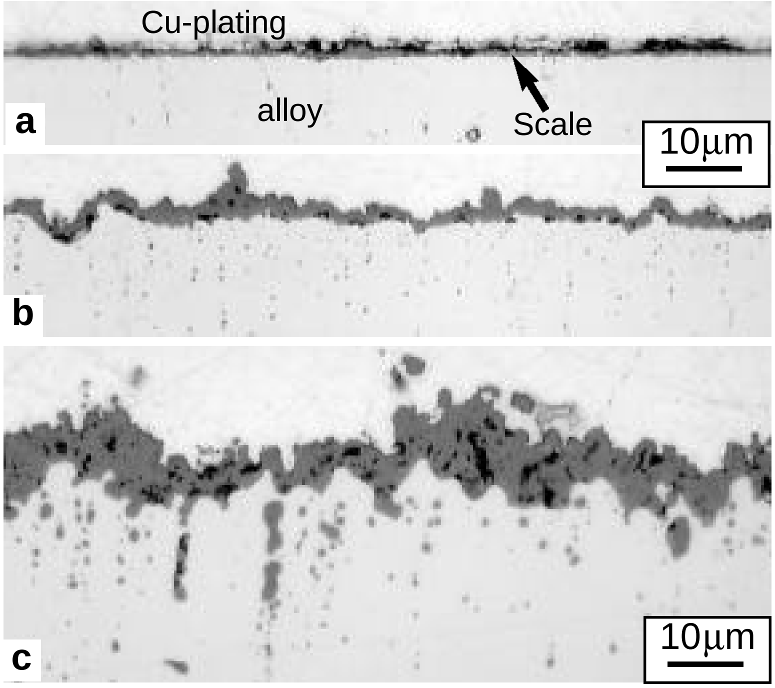

Figure 3. Light microscopy of polished sections of FCW-Y after 10,000h exposures in air at (a) 700°C, (b) 800°C and (c) 900°C.

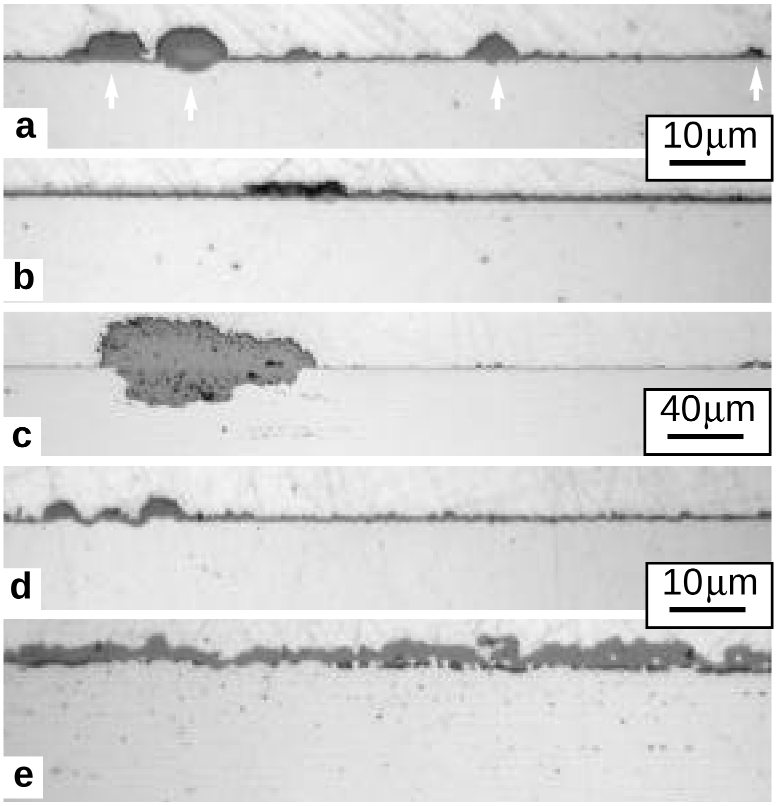

Figure 4. Light microscopy of polished sections of FC-Y (a,c,d) and FCW-YT (b,e) after 5000h exposures in air at (a,b) 700°C and (c,d,e) 800°C. Arrows in (a) mark Fe-rich oxide nodules.

Similar behavior was observed at 800°C, where some very large nodules formed, Figure 4c, which again corresponded with the high initial mass gain, Figure 1. Away from the nodules, the scale was very thin (Figure 4d) compared to that formed on FCW-Y (Figure 3b) and FCW-YT (Figure 4e). The thinner scale resulted in a lower parabolic rate constant (which does not include the transient nodule formation), Table II. The reason for the thinner scale may be the absence of Ti in this alloy. The incorporation of Ti in the scale may accelerate the growth of the scale as Ti has been shown to dope the Cr_2O_3 grains as well as to segregate to the grain boundaries.[5] While Ti is added for mechanical properties,[6] it may have a slightly negative effect on the oxidation resistance. This alloy also does not contain W, but this refractory metal is not likely to have a major effect on oxidation resistance.

Compared to FCW-Y, the scale on FCW-YT appeared somewhat different as the oxidation faces were aligned differently to the extrusion direction. The large faces of the FCW-Y coupon were normal to the extrusion direction while those on FCW-YT was parallel to it. The oxide particles in the metal reflect this difference. This may be why the scale was somewhat flatter on FCW-YT, Figure 4e. However, this section was after 5000h while that for FCW-Y (Figure 3b) was after 10000h. For FCW-YT at 800°C, the interface appeared to be somewhat rough with possibly a sub-layer (darker areas adjacent to the substrate) present. This will be examined by microprobe analysis. Previous TEM work on FCW-Y showed the presence of a thin ($<0.5\mu m$) silica-layer at the Cr_2O_3 -metal interface.[7] This layer is believed to have a strong influence on the reaction kinetics. However, this layer is not easily observed by light microscopy or SEM. In general, FCW-Y and FCW-YT had similar compositions and similar oxidation behavior.

REFERENCES

1. B. A. Pint, P. F. Tortorelli and I. G. Wright, in M. Schütze and W. J. Quadakkers eds., Cyclic Oxidation of High Temperature Materials, The Institute of Materials, London, 1999, p.111.
2. P. Y. Hou and J. Stringer, Mater. Sci. Eng. A202 (1995) 1.
3. M. Lambertin and G. Beranger, in W. Embury ed., High Temperature Oxidation and Sulfidation Processes, Canadian Institute of Metals, Ottawa, 1990, p.93.
4. A. Strawbridge and P. Y. Hou, Mater. High Temp. 12 (1994) 177.
5. B. A. Pint, Oxid. Met. 45 (1996) 1.
6. S. Ukai, M. Harada, H. Okada, M. Inoue, S. Nomura, S. Shikakura, K. Asabe, T. Nishida, and M. Fujiwara, J. Nucl. Mater. 204 (1993) 65.
7. D. T. Hoelzer, B. A. Pint and I. G. Wright, J. Nucl. Mater. 283-287 (2000) 1306.

4.0 COPPER ALLOYS

No contributions.

5.0 BCC REFRACTORY METALS AND ALLOYS

IMPROVEMENTS IN THE DUCTILITY OF MOLYBDENUM WELDMENTS BY ALLOYING ADDITIONS OF Zr, B and C — M. K. Miller, E. A. Kenik, K. F. Russell (Oak Ridge National Laboratory) and A. J. Bryhan (Applied Materials, Santa Clara, CA)

Objective

The aim of this project is to perform a microstructural characterization of zirconium-, boron- and carbon-doped molybdenum weldments to understand the dramatic improvement in ductility over conventional molybdenum alloys.

Summary

A significant improvement in the ductility of molybdenum weldments has been achieved through the addition of zirconium, aluminum, carbon and boron at the parts per million level. A ductility of 20% has been obtained in gas-tungsten arc weldments in 6.35-mm-thick plate. This improvement over molybdenum's traditional 3% ductility has been achieved by improving the normally low fracture stress of grain boundaries. Atom probe tomography has revealed segregation of zirconium, boron and carbon to and the depletion of oxygen at the grain boundaries in the base metal and the heat affected zone.

Introduction

Molybdenum-based alloys possess a unique combination of physical properties including high strength at elevated temperatures, high thermal conductivity, low coefficient of thermal expansion, and excellent performance in neutron flux environments. Therefore, molybdenum alloys are potential candidates for applications in fusion reactors. However, the low ductility of welds (typically 3%) has limited their applications. The lack of ductility has been especially apparent for welds made in thick material where triaxial constraint predominates. Bryhan has shown that controlled additions of substitutional and interstitial alloying elements can provide almost 20% elongation from gas-tungsten arc (GTA) welds in 6.35-mm-thick material.[1]

Experimental

The composition of the molybdenum alloy used in this investigation as determined by glow discharge mass spectrometry is given in Table 1. The alloy was vacuum arc-cast with a zirconium addition intended to getter the oxygen and nitrogen impurities together with parts per million additions of carbon and boron intended to strengthen the grain boundaries. The 4-pass welding process was performed on 0.25 inch (6.35 mm) plate in a controlled atmosphere chamber where the oxygen, nitrogen and water vapour impurity levels were each less than 10 wppm. The welding filler metal was molybdenum containing 20, 30, or 47 wt. % rhenium.

Table 1. Composition of the molybdenum alloy used in this study as determined by glow discharge mass spectrometry.

Element	wppm	appm
Zirconium	1500	1600
Carbon	12	96
Boron	6	53
Oxygen	42	250
Nitrogen	26	178
Iron	6	10
Silicon	3	10
Molybdenum	Balance	Balance

The distributions of the alloying additions in the microstructure of the base metal and the heat affected zone were characterized by a combination of field ion microscopy (FIM) and atom probe tomography (APT).[2] Microstructural characterizations were performed in the Oak Ridge National Laboratory (ORNL) energy-compensated atom probe and the ORNL energy-compensated three-dimensional atom probe.[2] No prior examination or pre-selection of the field ion specimens in the transmission electron microscope was performed in order to eliminate any possibility of carbon contamination during specimen preparation and characterization. Field ion images were recorded with the use of helium as the imaging gas and with a specimen temperature of 30-50K. Atom probe analyses were performed with a specimen temperature of 50K, a pulse repetition rate of 1500 Hz and a pulse fraction of 20% of the standing voltage.

Results and Discussion

Mechanical Properties

Tensile tests[1] were performed at room temperature at strain rates between 8.3×10^{-3} and 12.5×10^{-6} s^{-1} in stroke control and the results are summarized in Table 2. Strain was measured over two weldment regions to measure strain localization: 25 mm centered over the weld and 8.5 mm over one heat-affected zone. Tests were performed at a standard strain rate of 8.3×10^{-4} s^{-1} and also at faster and slower rates to determine the effect of strain rate. The maximum observed elongation, pertinent to typical engineering use, was 19.5%. Even at 8.3×10^{-3} s^{-1}, useful ductility (>10%) was apparent in the material welded with Mo-30 wt% Re filler alloy.

Table 2. Room temperature tensile test results for GTA-welded molybdenum alloy with three different Mo-Re filler alloys.[1]

Filler metal (wt. %)	Strain rate in 25mm s^{-1}	Range of elongation in gauge length, %		Yield stress, MPa	Ultimate tensile stress, MPa	Number of tests
		25 mm	8.4 mm			
Mo-20% Re	$8.3x10^{-4}$	8.2-15.2	10.4-14.0	428	524	6
	$8.3x10^{-5}$	11.0	6.0	392	470	1
Mo-30% Re	$8.3x10^{-3}$	10.0-12.6	7.9-11.6	537	583	2
	$8.3x10^{-4}$	19.5	>15.0[1]	481	544	1
	$1.25x10^{-6}$	22.6	>15.0[1]	267	457	1
Mo-47% Re	$1.25x10^{-6}$	10-26	8->15.0[1]	250	484	3

[1] 15.0% maximum measurement with the extensometer.

Fracture was found to occur in either the heat-affected zone or the weld zone, as shown in optical micrographs in Fig. 1 and in the scanning electron micrographs taken with backscattered electrons in Fig. 2. The lighter contrast in the backscattered image in the weld region is due to the presence of rhenium from the filler material. Some porosity was observed in the weld region, particularly close to the edge of the weld next to the heat affected zone. The fracture mode was transgranular cleavage with only small regions of intergranular fracture, as shown in Fig. 3. This observation is in contrast to the intergranular fracture typical of welds in commercial grade molybdenum alloys and indicates that the grain boundaries are not preferentially embrittled. This change of fracture mode suggests that the alloying additions increased the grain boundary fracture stress above the yield stress.

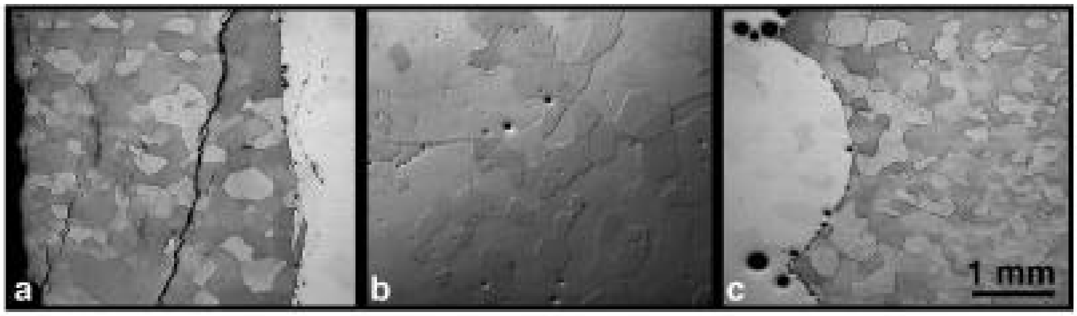

Fig. 1. Optical micrographs of a) and c) heat affected zones and b) weld region.

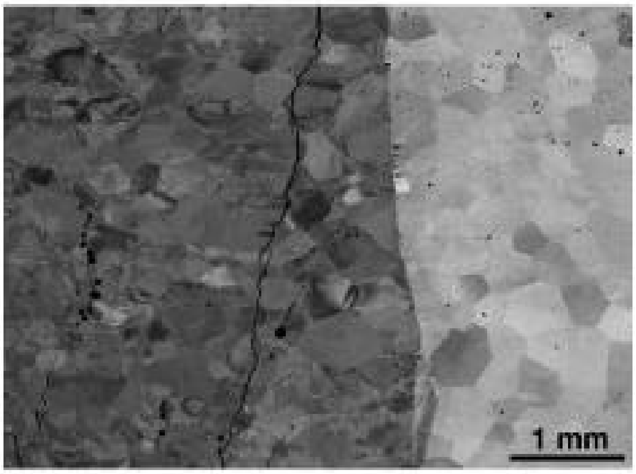

Fig. 2. Backscattered electron micrograph of the heat affected zone (dark region on left hand side) and the weld (lighter region).

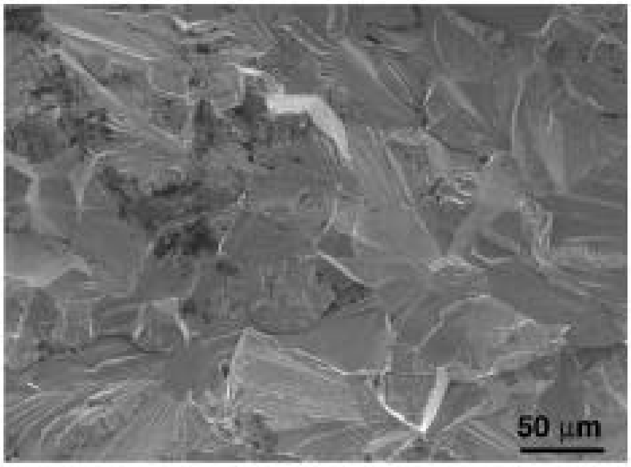

Fig. 3. Fracture surface of the molybdenum tensile specimen showing the transgranular mode of failure.

Microstructural Characterization

Extensive field evaporation studies of the matrix revealed no intragranular precipitates. The matrix compositions were measured in the three-dimensional atom probe and were found to be consistent with the alloy composition. These matrix measurements together with the extensive field evaporation studies of the matrix indicate that no significant loss of the solute additions occurred to precipitation of carbides or borides.

Field ion micrographs of grain boundaries in the base metal and the heat affected zones are shown in Fig. 4. In addition to the typical zone contrast exhibited by molybdenum alloys,[2] both

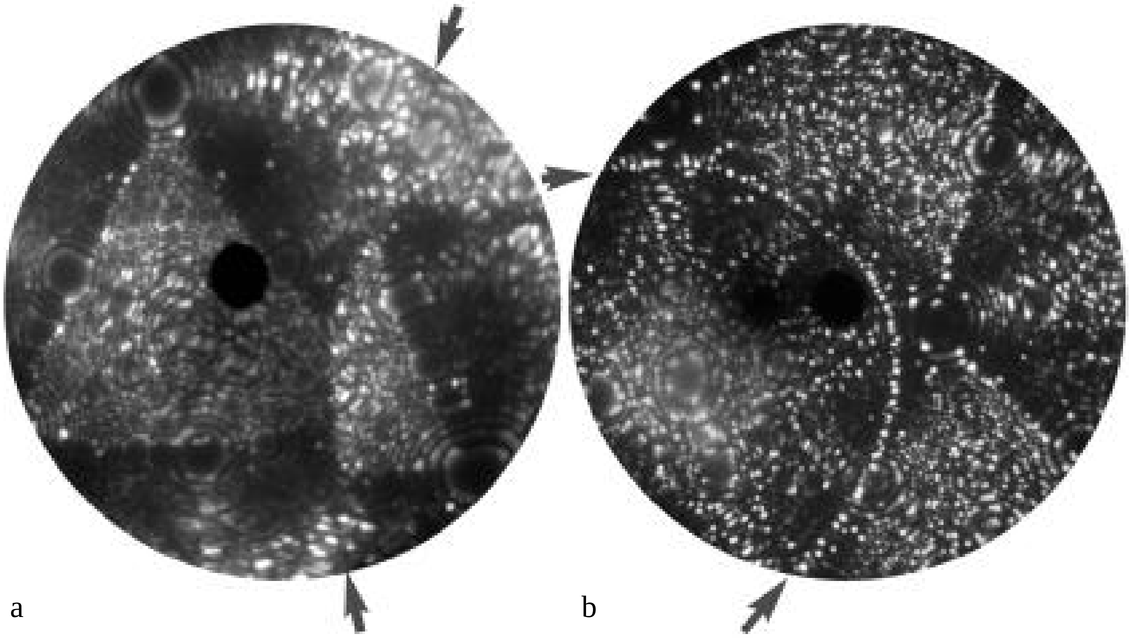

Fig. 4. Field ion micrographs of grain boundaries in a) the base metal and b) the heat affected zone. Solute decoration is apparent at both grain boundaries.

materials exhibited some bright spot decoration at the grain boundaries. These bright spots are indicative of solute segregation.[2] Comparison of the predicted low temperature evaporation field of molybdenum (41 Vnm^{-1}) with the other solutes suggests that the bright spots (i.e., atoms that are more resistant to field evaporation) are boron (64 Vnm^{-1}) or carbon (103 Vnm^{-1}) atoms rather than zirconium (28 Vnm^{-1}) atoms.[3] The level of segregation appeared to be significantly higher in the heat affected zone.

The identity of the solute species responsible for these bright spots was determined by atom probe tomography.[2] Atom maps of regions of specimens that contained grain boundaries in the base metal and the heat affected zone are shown in Fig. 5. In these atom maps, each sphere represents the position of an atom in the volume of analysis. The molybdenum atoms have been omitted for clarity. It is evident that significant segregation of zirconium, carbon and boron to the grain boundary has occurred in the base metal. In addition, the oxygen level at the grain boundary was significantly reduced from the matrix level. The boron segregation was found to be significantly more prevalent in the head affected zone.

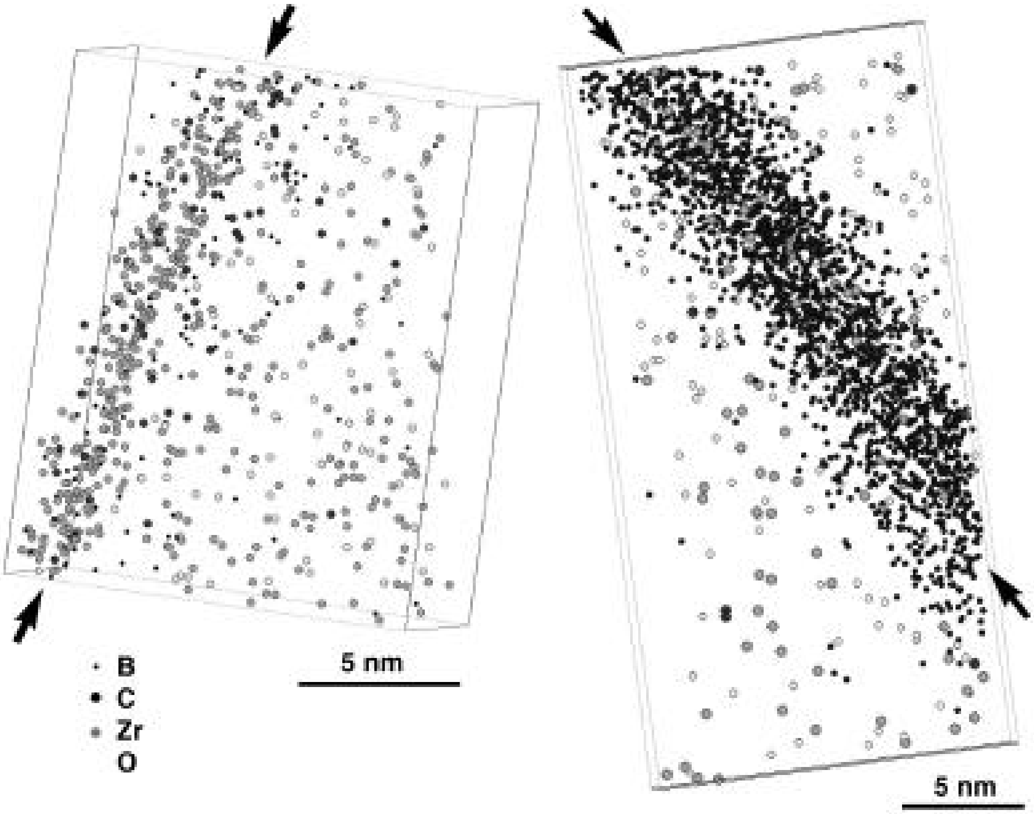

Fig. 5. Atom maps of grain boundaries in a) the base metal and b) the heat affected zone. The molybdenum atoms have been omitted for clarity.

The Gibbsian interfacial excesses of the solutes at these grain boundaries were determined by selected volume analyses of the grain boundary and matrix regions[2] and the results are given in Table 3. The boron excess at the grain boundary in the heat affected zone was two orders of magnitude higher than in the base metal, whereas the zirconium and carbon excesses were substantially less enriched. The oxygen level at the grain boundary in the heat affected zone was found to be very slightly enriched compared to the matrix whereas in the base metal, the oxygen level was significantly reduced. A previous image atom probe study of a grain boundary in molybdenum revealed significant enrichment of oxygen.[4]

These atom probe tomography results have demonstrated that oxygen segregation to the grain boundaries does not occur in this zirconium-, boron- and carbon-doped molybdenum alloy and may be inhibited due to the presence of zirconium, carbon and boron at the grain boundary. Intergranular failure is thereby inhibited through the significant reduction of the oxygen level at the grain boundary.

Table 3. Gibbsian interface excesses of solute at the grain boundary in the base metal and heat affected zone. Errors are based on counting statistics of the number of atoms detected.

Element	Gibbsian Interfacial Excess Atoms m^{-2}	
	Base Metal	Heat Affected Zone
Zirconium	$7.6 \pm 0.6 \times 10^{13}$	$1.4 \pm 0.4 \times 10^{13}$
Carbon	$1.1 \pm 0.3 \times 10^{13}$	$9.9 \pm 9.9 \times 10^{11}$
Boron	$7.3 \pm 2.7 \times 10^{12}$	$9.9 \pm 0.2 \times 10^{14}$
Oxygen	$-3.9 \pm 0.6 \times 10^{12}$	$1.1 \pm 0.4 \times 10^{13}$

Acknowledgements

Research at the Oak Ridge National Laboratory SHaRE User Facility was sponsored by the Division of Materials Sciences and Engineering, U.S. Department of Energy, under contract number DE-AC05-00OR22725 with UT-Battelle, LLC.

References

1. A. J. Bryhan, Joining of Molybdenum Base Metals and Factors Which Influence Ductility, WRC Bulletin 312, Feb. 1986, ISSN 0043-2326.
2. M. K. Miller, Atom Probe Tomography: Analysis at the Atomic Level, Kluwer Academic/Plenum Press, 2000, New York, NY.
3. T. T. Tsong, Surf. Sci., 70 (1978) 211.
4. A. R. Waugh and M. J. Southon, Surf. Sci., 68 (1977) 79.

6.0 AUSTENITIC STAINLESS STEELS

VOID SWELLING AT LOW DISPLACEMENT RATES IN ANNEALED X18H10T STAINLESS STEEL AT 4 to 56 DPA AND 280-332°C

– F. A. Garner (Pacific Northwest National Laboratory)*, S. I. Porollo, A. N. Vorobjev, Yu. V. Konobeev, and A. M. Dvoriashin (Institute of Physics and Power Engineering, Russia)

ABSTRACT

Various components of pressurized water power reactors (PWRs) and some proposed fusion devices such as ITER will operate at lower temperatures and displacement rates than are encountered in many test reactors such as EBR-II, FFTF and HFIR. The question arises if the presence and magnitude of void swelling can be predicted for such irradiation environments. Data on Russian steel can be used to address part of this question. In reactor applications where Western countries typically use annealed AISI 304 stainless steel, it is the Russian practice to use annealed X18H10T, a titanium-stabilized 18Cr-10Ni stainless steel analogous to AISI 321. Using a flow restrictor component from the low-flux breeder zone of the BN-350 reactor in Kazakhstan, it was possible to examine the behavior of void swelling at relatively low temperatures and low displacement rates after 12 years of irradiation. The temperature of this component ranged from 270-340°C with a peak dose rate of 1.6 x 10^{-7} dpa/sec and a peak dose of 56 dpa. Careful sectioning of the component has yielded a large number of microscopy specimens over a ITER-relevant range of temperatures and displacement rates. Microstructural data are presented and show that void swelling at 10 to 50 dpa persists down to ~306°C for dose rates on the order of 1 x 10^{-7} dpa/sec.

Introduction

In some fusion devices such as ITER, the anticipated operating temperatures will be below the inlet temperatures of most current test reactors. The atomic displacement rates may also be much lower than found in many test reactors used in the fusion materials program. It is possible to get some idea of the anticipated swelling behavior under these conditions for fusion applications from ongoing studies in Russia directed toward the possibility of void swelling in pressurized water reactors (PWRs).

It has been predicted that void-swelling and the associated void-induced embrittlement are likely to occur in the AISI 304L and 316L steels that are used in PWR baffle-former assemblies, especially toward the end of the reactor lifetime [1-3]. These steels will receive neutron exposures producing 8 to 100 dpa (displacements per atom) at a maximum displacement rate of ~2 dpa/year over a 40-year lifetime. Temperatures will range from

---

* Pacific Northwest National Laboratory (PNNL) is operated for the U.S. Department of Energy by Battelle Memorial Institute under contract DE-AC06-76RLO- 1830.

~300 to ~400°C, with the highest temperatures developing in positions closest to the core and at the highest neutron fluxes and gamma-heating rates. In such water-moderated reactors the local generation rates of helium and hydrogen in austenitic steels in the baffle-former assembly are comparable to those generated by fusion spectra [1].

Most of the baffle-former structure, however, will experience lower than maximum temperatures, lower dpa rates and thereby lower dpa levels. It is particularly fortunate that the positions experiencing the highest temperatures and highest dpa levels do not exactly coincide, since swelling of 300 series steels in the operational range of interest increases strongly with increases in both variables [4].

Unfortunately, of all easily purchased and widely used stainless steels, AISI 304 is the most swelling-prone steel available, especially when in the annealed, low-carbon condition [5]. This proclivity towards early swelling is primarily a consequence of its low nickel level and moderately high chromium content [4]. Cold-worked 316 is known to resist the onset of swelling much longer than does annealed 304L stainless steel [6,7]. It is also well known that all stainless steels eventually swell at comparable rates, however, but resist the onset of swelling differently, dependent on alloy composition, thermo-mechanical starting state, irradiation conditions, and neutron spectra. The latter determines the generation rates of helium and hydrogen, which can stabilize void nuclei [1].

Evaluation of the potential swelling behavior under ITER-relevant conditions is limited by several factors. First, essentially all data on AISI 304 and 304L were generated in the EBR-II fast reactor, which had an inlet temperature of 370°C, precluding the availability of data in the 300-370°C range that is experienced by most of the baffle-former assembly.

Second, the data on swelling of AISI 304 were generated under conditions of relatively high displacement rate and relatively low levels of helium generation compared to conditions found in PWRs [1]. Both of these factors are known to influence the duration of the incubation and transient regimes of swelling [4].

Data on steels irradiated in Russian and Kazakhstan reactors have previously been used to assess the potential of void swelling at PWR-relevant dpa rates and dpa levels in the temperature range below 370°C. These data show that the Russian steels used in nuclear service exhibit void swelling at lower-than-anticipated dpa levels and irradiation temperatures [8-11], and to increase in swelling with decreasing dpa rate [12].

In order to estimate the lowest temperature at which swelling of AISI 304L might occur at ITER and PWR-relevant dpa rates, an experiment is being conducted on 12X18H10T in the annealed condition. This material was irradiated in the low flux reflector region of the BN-

350 fast reactor, located in Kazakhstan. This steel is similar to AISI 321 and is used in a wide variety of reactors of Russian design for applications where AISI 304 would be used in Western PWRs. In this experiment, however, the helium and hydrogen generation rates were significantly lower than that found in PWRs. Thus, in this case the potentially synergistic effects of dpa rate and gas generation rates can be avoided, with dpa rate effects being dominant.

Experimental Details

This steel has a composition of Fe-18.5Cr-9.5Ni-1.5Mn-0.7Si-0.65Ti-(<0.12C) in wt. %. The composition was confirmed using a "Kamebax" x-ray analyzer in scanning mode on an irradiated specimen.

The examined component was a hexagonal tube with a "flat-to-flat" distance of 96 mm and with a central hole of 65 mm in diameter. The total length of the component, including its upper and lower end units, is 3.44 m, equal to the length of driver fuel and breeder subassemblies. The component served as a flow restrictor to the sodium coolant in the reflector region.

The component was irradiated in the breeder zone of the BN-350 reactor at a radial distance of 94.5 cm from the core axis during 1939 effective power days of irradiation, beginning from November 1972 up to June 1984. At the core midplane cross-section of the component the calculated peak fluence of neutrons is 3.3×10^{23} n/cm^2 (E>0 MeV) or 1.6×10^{23} n/cm^2 (E>0.1 MeV). These peak fluences correspond to a damage dose of 56 dpa (NRT). The corresponding peak dpa rate was 1.56×10^{-7} dpa/sec. On the opposite side of the component the dpa level fell to 22 dpa at the core midplane.

Axial profiles of irradiation temperature at inner and outer surfaces of the component at the minimal radial distance from the core axis are shown in Figure 1. For opposite flats the temperatures are lower by 1-4°C. Across the central hole the temperature varies ±3°C. The irradiation temperature at the internal surface of the component in the core midplane cross-section varies along its perimeter from 299 to 302°C and the temperature at the outer surface varies from 313 to 317°C, so that the temperature decrease through the component wall is ~15°C. The irradiation temperatures depend on the reactor power level and the quoted values were averaged over the entire period of irradiation to determine the nominal temperatures, which are considered to be accurate to ±5°C over the irradiation lifetime.

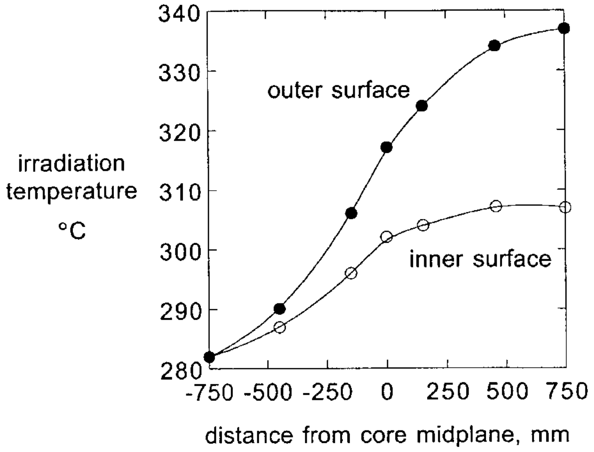

Figure 1. Temperature profiles for the inner and outer surfaces of the flow restrictor component at the position nearest to the core central axis.

Various axial portions of this component have been mechanically sliced to yield 0.4 mm thick plates. These plates were in turn sliced to produce 12 x 4 x 0.5 mm strips at twelve radial positions around the circumference of the component as shown in Figure 2. Microscopy disks of 3 mm diameter were then punched from the strips and thinned to 0.1-0.2 mm using sandpaper grinding. These disks were then thinned electrochemically and examined by electron microscopy at 100 keV. This work is still in progress but nearing completion.

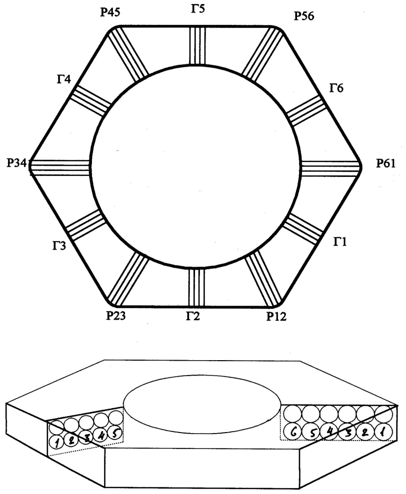

Figure 2. Diagram showing cutting location of microscopy disks for the section taken at the mid-core axial position. The core center lies along the line defined from P34 to P61. The

highest neutron exposure occurred at P61. P and Γ are derived from the Russian terms for corner and flat, respectively.

TABLE I Distribution of Normalized Neutron Fluences and Displacement Dose in Core Midplane Cross-section of the Flow Restrictor Component

Neutron Fluence Relative to Position P61	Point Number							
	P61	Γ1	Γ2	Γ3	P34	Γ4	Γ5	Γ6
E>0 MeV	1.0	0.93	0.69	0.56	0.50	0.56	0.68	0.92
E>0.1 MeV	1.0	0.91	0.60	0.47	0.42	0.47	0.59	0.90
dpa	1.0	0.90	0.57	0.44	0.39	0.44	0.56	0.89

The relative distribution of the total neutron fluence and damage dose for the core midplane cross-section of the component are given in Table I, and the positions of the microscopy specimens are shown in Figure 2. The maximum neutron fluences for E>0 and E>0.1 MeV in the core midplane position are equal to 3.3 x 10^{23} n/cm^2 and 1.6 x 10^{23} n/cm^2, respectively. This fluence corresponds to a displacement dose of 56 dpa. The neutron spectrum in this region of the reflector is relatively soft with only 3.5 dpa produced by 10^{22} n/cm^2 (E>0.1 MeV)

Results

As shown in Figure 3, voids were observed at temperatures as low as 306°C and 25.7 dpa in the slice taken at the core midplane. In the slice taken at 590 mm above the core midplane, swelling was observed as low as 308°C and 10 dpa. Thus, voids probably form at even lower dpa levels in the region just above 300°C, but cannot be observed within the limited slicing matrix employed in this experiment. It should be noted, however, that swelling does not occur below 300°C, at least for doses below ~40 dpa.

While the swelling levels are not large (<0.3%), the appearance of voids at these low temperatures was previously unexpected. The void densities are in the 10^{14}-10^{15} cm^{-3} range with mean diameters of 5 to 9 nm, except at the slices obtained at the higher elevations, where the temperature is higher and the mean diameters are >100 nm.

Typical microstructures are shown in Figures 4 and 5, showing the disappearance of voids at between 313 and 305°C at doses of 30-33 dpa. In addition to voids, the microstructures of all specimens contained dispersions of small G-phase precipitates and also plate-like defects. These are shown in Figures 6 and 7. The plate-like defects are dislocation loops viewed edge-on.

Discussion

The swelling levels reached in this experiment are not very large in the temperature range studied, but swelling of stainless steels are known to exhibit long periods of transient swelling at low rates before the onset of accelerated swelling [4]. In a paper by Porollo and coworkers [13], it is shown that at temperatures in the range 330-342°C the end of the transient regime of both this steel and another steel is on the order of 60 dpa at higher dpa rates, with a swelling rate on the order of ~1%/dpa thereafter. Therefore, it is prudent to assume that a linear extrapolation of the data in this report to higher dpa levels will not yield a correct estimate of swelling.

Another feature of these data is that irradiation temperature appears to be a more important variable than the displacement level in the low temperature regime. Otherwise one would expect the data shown in Figure 3 to tend to show more swelling at lower temperatures as the dpa level increased, rather than to stop swelling at ~300ºC at all doses. This perception is biased, however, by the direct coupling of dpa and dpa rate in these data, such that swelling decreases with dpa rate but increases with dpa level.

Since the composition of this Russian steel is somewhat different from that of AISI 304L, especially in their titanium and carbon contents, one cannot use these data to predict the swelling of AISI 304L. However, based on these results and those of the experiments cited earlier, it is reasonable to expect that swelling of 304L and 316 stainless steels can occur to temperatures approaching 300°C for displacement rates on the order of ~10^{-7} dpa/sec.

It is known that the swelling of 304 and 304L stainless steels at 370-390°C are sensitive to displacement rate, however, with swelling increasing as the displacement rate decreases [13-17]. If this sensitivity also applies at temperatures below 370°C, it is not unreasonable to expect that swelling of AISI 304L will also extend down to ~300°C.

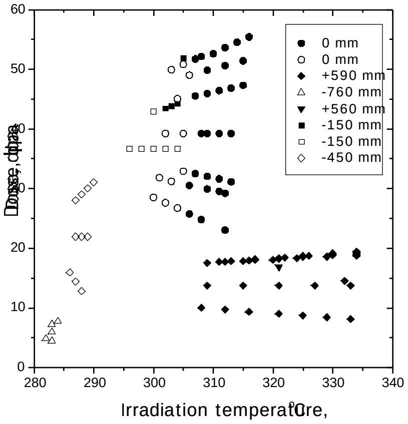

Figure 3. Dose-temperature map of void observations in annealed X18H10T austenitic stainless steel after irradiation in the BN-350 reactor near the core midplane. Elevations where slices were cut are indicated by shape of symbol. Irradiation conditions for midplane flats Γ2 and Γ5 are identical, yielding an overlap of some data, since the microstructures were essentially similar. Solid symbols indicate voids observed; open symbols indicate no voids found.

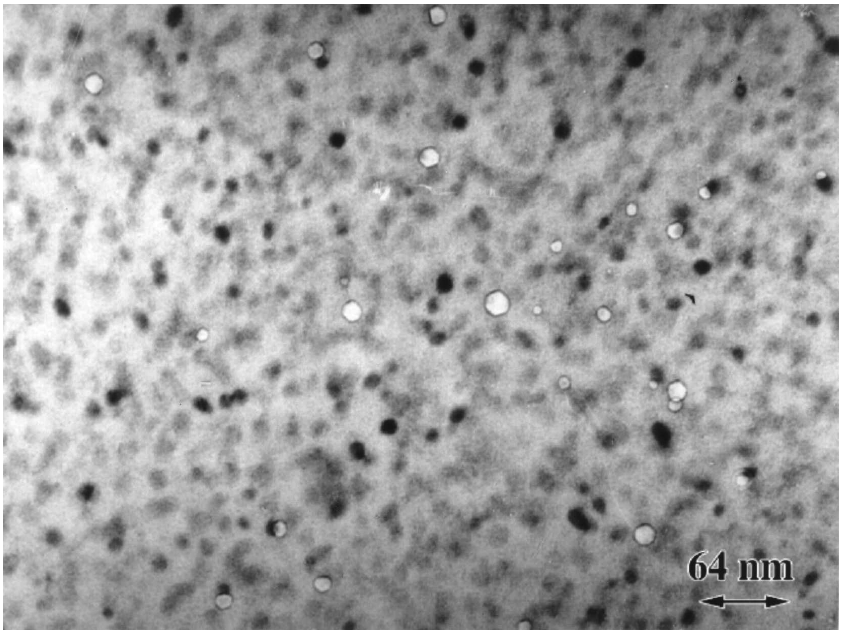

Figure 4. Microstructure of neutron irradiated 12X18H10T at 313°C and 30.2 dpa showing void and precipitate formation. Swelling of 0.05% was produced at 0.84 x 10^{-7} dpa/sec.

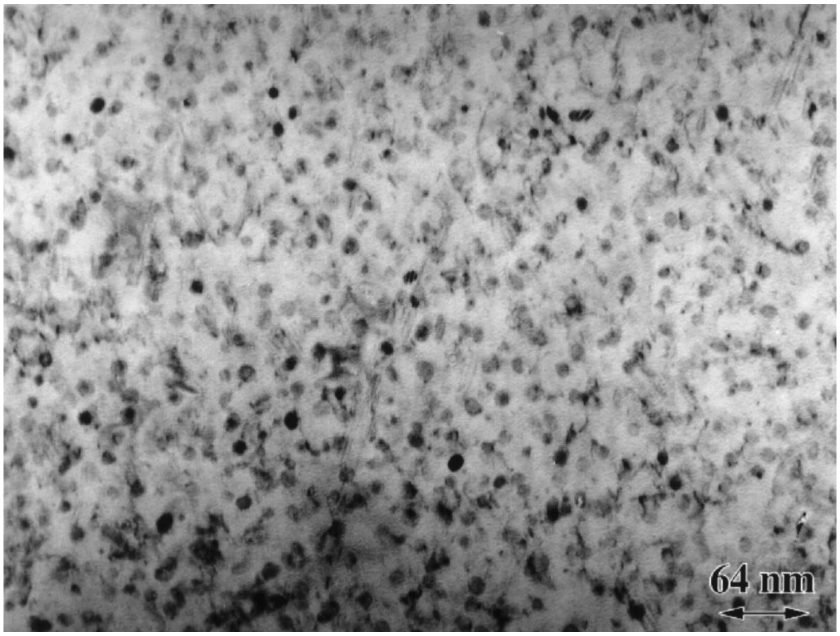

Figure 5. Microstructure at 305°C and 33.0 dpa showing precipitates but no voids at 0.92 x 10^{-7} dpa/sec.

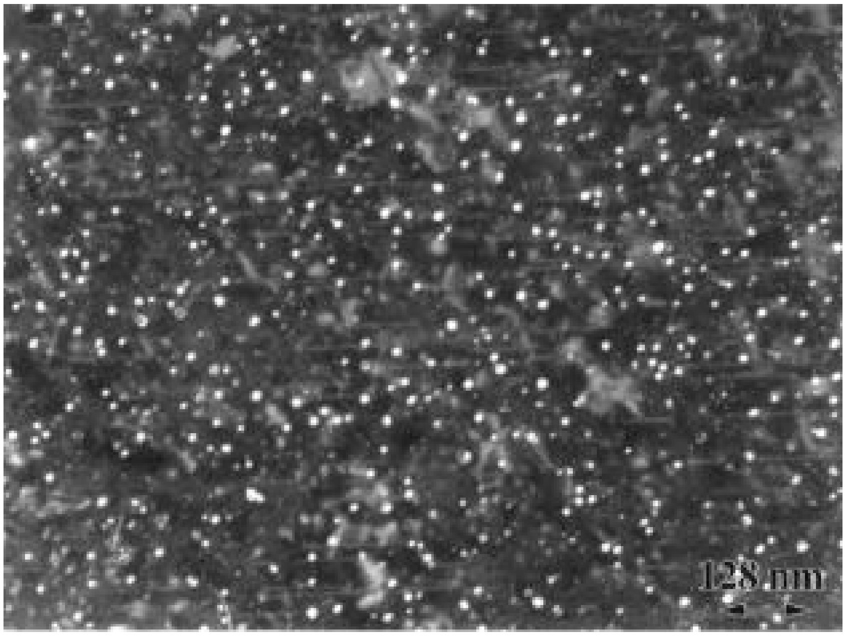

Figure 6. Dark-field micrograph showing G-phase precipitates at 309°C and 31.9 dpa.

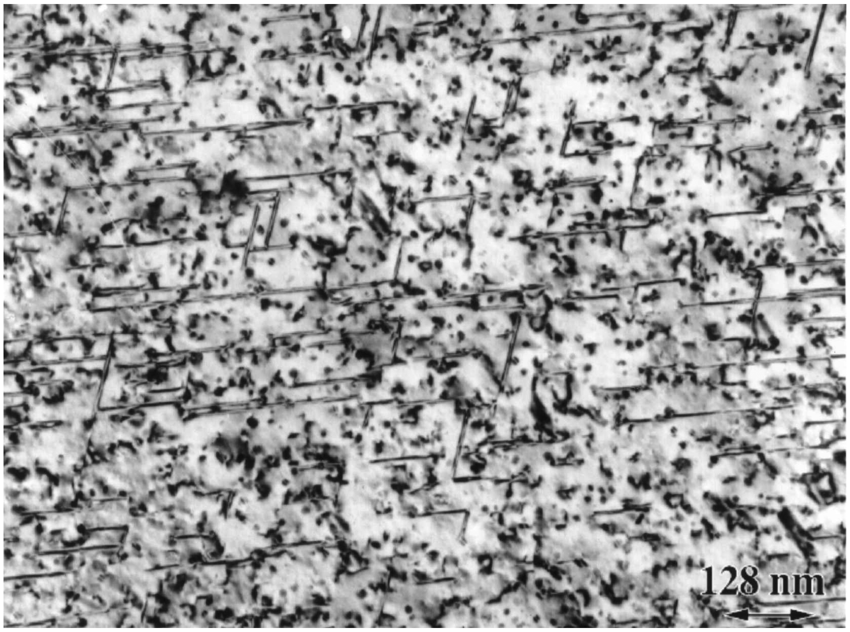

Figure 7. Bright field micrograph of specimen in Figure 6, imaged to show dislocations, precipitates, and a few very small voids, producing ~0.02% swelling at 0.89 x 10 $^{-7}$ dpa/sec

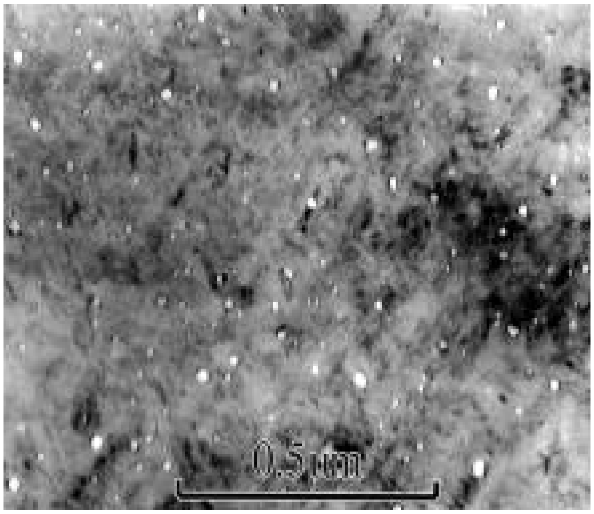

Figure 8. Swelling at ~0.2% observed in annealed 12X18H10T stainless steel at 16.8 dpa and 321°C after irradiation at ~4 x 10^{-8} dpa/sec in the BN-350 fast reactor [8].

One issue not addressed in this report is the possible acceleration of swelling due to higher levels of both helium and hydrogen found in PWR and fusion neutron spectra. In this study voids were found at 25-35 dpa, but in PWR reactor spectra and other even more thermalized spectra, voids appear to form in stainless steels at 1-10 dpa [8, 18-20]. Several recent studies have shown that hydrogen, probably in molecular form, appears to collect in and pressurize voids nucleated by helium [18,21]. It has been proposed that helium-assisted storage of hydrogen will accelerate the onset of void swelling [22].

Conclusions

Until recently it was thought that austenitic stainless steels would not exhibit void swelling at ITER and PWR-relevant temperatures and displacement rates. It has been shown, however, that void swelling in annealed X18H10T appears to develop at temperatures as low as 306°C when irradiated in a Kazakhstan fast reactor at ITER and PWR-relevant damage rates on the order of 1×10^{-7} dpa/sec. This indicates the possibility that similar swelling can occur in 300 series stainless steels in ITER and other fusion devices.

ACKNOWLEDGEMENTS

This research was supported by the Civilian Research and Development Foundation under Grant RE2-123, and both the Office of Basic Energy Science and the Office of Fusion Energy of the U.S. Department of Energy.

REFERENCES

[1] F. A. Garner, L. R. Greenwood, and D. L. Harrod, Sixth International Symposium on Environmental Degradation of Materials in Nuclear Power Systems - Water Reactors, (The Minerals, Metals, and Materials Society, 1993), 783-790.

[2] F. A. Garner, Transactions of the American Nuclear Society, 71 (1994),190-191.

[3] F. A. Garner and M. B. Toloczko, J. Nucl. Mater. 251 (1997), 252-261.

[4] F. A. Garner, "Irradiation Performance of Cladding and Structural Steels in Liquid Metal Reactors", Materials Science and Technology: A Comprehensive Treatment, Volume 10A, (VCH Publishers, 1994), 419-543.

[5] F. A. Garner and D. L. Porter, in Proc. Conf. on Dimensional Stability and Mechanical Behavior of Irradiated Metals and Alloys, BNES, (Brighton, England, 1984), 41-44.

[6] B. R. Siedel and R. E. Einziger, in Proc. Inter. Conf. on Radiation Effects in Breeder Reactor Materials, (AIME, 1977), 625-644.

[7] G. L. Hofman, Nuclear Technology, 47 (1980), 7-22.

[8] F. A. Garner, M. B. Toloczko, S. I. Porollo, A. N. Vorobjev, A. M. Dvoriashin and Yu. V. Konobeev, in Eighth Inter. Symp. on Environmental Degradation of Materials in Nuclear Power Systems - Water Reactors, August 10-14, 1997, Amelia Island, Florida, vol. 2 (1997), 839-845.

[9] S. I. Porollo, A. N. Vorobjev, Yu. V. Konobeev, A. M. Dvoriashin, and F. A. Garner, in Proc. Fourth Inter. Symp. on Contribution of Materials Investigation to the Resolution of Problems Encountered in Pressurized Water Reactors, Fontevraud, France, vol. 1 (1998), 271-280.

[10] F. A. Garner, S. I. Porollo, A. N. Vorobjev, Yu. V. Konobeev, A. M. Dvoriashin, V. M. Krigan, N. I. Budylkin, and E. G. Mironova, in Proc. Fourth Inter. Symp. on "Contribution of Materials Investigation to the Resolution of Problems Encountered in Pressurized Water Reactors", Fontevraud, France, vol. 1 (1998), 249-260.

[11] S. I. Porollo, A. N. Vorobjev, Yu. V. Konobeev, A. M. Dvoriashin, V. M. Krigan, N. I. Budylkin, E. G. Mironova, and F. A. Garner, J. Nuclear Materials, 258-263 (1998), 1613-1617.

[12] V. S. Neustroev, V. K. Shamardin, Z. E. Ostrovsky, A. M. Pecherin, and F. A. Garner, in Proc. Fourth Inter. Symp. on "Contribution of Materials Investigation to the Resolution of Problems Encountered in Pressurized Water Reactors, Fontrevaud, France, vol. 1 (1998), 261-269.

[13] S. I. Porollo, A. M. Dvoriashin, A. N. Vorobjev, V. M Krigan, Yu. V. Konobeev, F. A. Garner, N.I. Budylkin, and E.G. Mironova in Ninth International Symposium on Environmental Degradation of Materials in Nuclear Power Systems – Water Reactors, The Minerals, Metals and Materials Society (TMS) 1999, 1061-1067.

[14] D. L. Porter and G. L. Hudman, Transactions of American Nuclear Society (1980), 230-231.

[15] D. L. Porter and F. A. Garner, in Proc. Effects of Radiation on Materials: Twelfth Inter. Symp., ASTM STP 870, (1985), 212-220.

[16] D. L. Porter, G. D. Hudman, and F. A. Garner, J. Nuclear Materials, 179-181 (1991), 581-584.

[17] G. M. Bond, F. A. Garner, M. L. Hamilton, B. H. Sencer, T. R. Allen, and D. L. Porter, in Ninth International Symposium on Environmental Degradation of Materials in

Nuclear Power Systems – Water Reactors, The Minerals, Metals and Materials Society (TMS) 1999, 1045-1050.

[18] T. R. Allen, J. I. Cole, H. Tsai, S. Ukai, S. Mizuta and T. Yoshitake, in Ninth International Symposium on Environmental Degradation of Materials in Nuclear Power Systems – Water Reactors, The Minerals, Metals and Materials Society (TMS) 1999, 1035-1042

[19] B. A. Gurovich, V. N. Bespalov, Ya. I. Shtrombakh, M. S. Astrahantsev, and F. A. Garner, manuscript in preparation.

[20] P. Spellward, J. Walmsley, and R. Scowen, in Proc. Eighth Inter. Symp. on Environmental Degradation of Materials in Nuclear Power Systems - Water Reactors, August 10-14, Amelia Island, Florida (1997), vol. 2, 734-742.

[21] S. B. Fisher, V. M. Callen, and P. K. Rose, in Effects of Radiation on Materials: 15th Inter. Symp., ASTM STP 1125, (1992), 667-688.

[22] F. A. Garner, B. M. Oliver, L. R. Greenwood and M. L. Grossbeck, manuscript in preparation for J. Nucl. Mater.

[23] F. A. Garner and L. R. Greenwood, J. Nuclear Materials, 233-237 (1996), 1530-1534.

7.0 INSULATING CERAMICS AND OPTICAL MATERIALS

MICROSTRUCTURE OF SWIFT HEAVY ION IRRADIATED SiC, Si_3N_4 AND AlN –

S.J. Zinkle, J.W. Jones (Oak Ridge National Laboratory) and V.A. Skuratov (Flerov Laboratory, Dubna, RF)

OBJECTIVE

The objective of this report is to determine the threshold ionizing radiation stopping powers for creation of displacement damage in ceramics of interest for fusion applications.

SUMMARY

Cross-section transmission electron microscopy was used to investigate the microstructure of single crystal silicon carbide and polycrystalline silicon nitride and aluminum nitride following room temperature irradiation with either 245 MeV Kr or 710 MeV Bi ions. The fluences ranged from $1x10^{12}/cm^2$ (single track regime) to $1x10^{13}/cm^2$. Ion track formation was observed in the Bi ion-irradiated Si_3N_4 specimen in regions where the electronic stopping power exceeded a critical value of ~15 keV/nm (depths <24 µm). Ion track formation was not observed at any depth in 245 MeV Kr ion-irradiated Si_3N_4, in which the maximum electronic stopping power was 14.5 keV/nm. There was no evidence for track formation in either SiC or AlN irradiated with 710 MeV Bi ions, which indicates that the threshold electronic stopping power for track formation in these two ceramics is >34 keV/nm. The high resistance of SiC and AlN to track formation may be due to their high thermal conductivity, but further study is needed to quantitatively evaluate the suitability of the various track formation models.

PROGRESS AND STATUS

INTRODUCTION

Previous studies have shown that discontinuous track formation in ceramic insulators can be produced by swift heavy ions with electronic stopping powers $(dE/dx)_e$ above ~5 to 8 keV/nm, and continuous cylindrical tracks are typically observed for $(dE/dx)_e \geq 15$ to 20 keV/nm [1]. These electronic stopping power thresholds for track formation are only slightly above the calculated electronic stopping powers associated with primary recoil atoms damage in ceramics in a fusion reactor environment. The physical mechanism(s) responsible for track formation in radiolysis-resistant solids are still under debate (e.g., thermal spike vs. Coulomb explosion models). Therefore, additional data on a wide range of materials are needed to investigate material parameters such as the effect of band gap energy and thermal conductivity on track radius, etc. As noted previously [2], it is possible that densely ionizing recoil atoms can create irradiated microstructures that are not achievable with conventional (elastic collision) irradiations. Therefore, materials which exhibit good radiation resistance under elastic collision damage conditions (e.g., $MgAl_2O_4$) may not necessarily exhibit similar radiation damage resistance under energetic recoil ion conditions [2]. This observation needs to be considered for the investigation of candidate in-vessel ceramic insulators for fusion reactors, due to the relatively high recoil ion energy for DT fusion neutrons.

Most previous swift heavy ion studies on ceramics have focussed on oxide insulators. Very little information is known about the behavior of carbides such as SiC [3-5], and even less is known about the behavior of nitride insulators such as AlN and Si_3N_4.

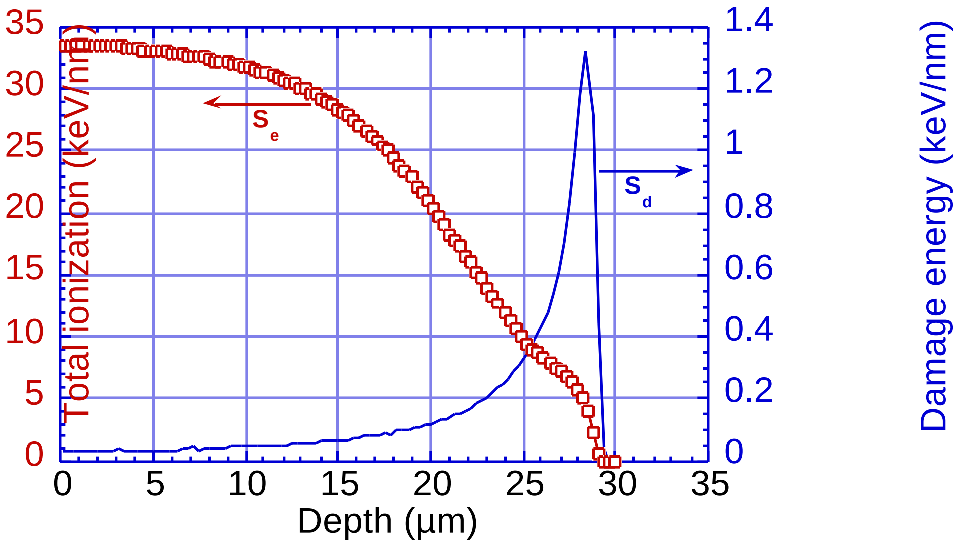

Fig. 1. Calculated damage energy (portion of nuclear stopping power that produces elastic collisions) and electronic stopping power (S_e) for 710 MeV Bi ions in Si_3N_4.

Table 1. Summary of room temperature properties of the investigated SiC, AlN and Si_3N_4 ceramics [7,8].

Material	Crystal structure	Lattice parameters	Density (g/cm^3)	Thermal conductivity (W/m-K)	Band gap (eV)	Ionicity	Sublimation temperature (K)
SiC (Cree)	Hexagonal (6H polytype)	a=0.308 nm c=1.512 nm c/a=4.91	3.21	350	3.0	0.12	2250
AlN (Tokuyama Shapal SH15)	Hexagonal (wurtzite)	a=0.311 nm c=0.498 nm c/a=1.60	3.31	177	6.2	0.40	2790
β-Si_3N_4 (Kyocera SN733)	Hexagonal ($P6_3$ space group)	a=0.760 nm c=0.290 nm c/a=0.290	3.21	29	~8	0.28	2151

EXPERIMENTAL PROCEDURE

Single crystal SiC (Cree) and polycrystalline specimens of AlN (Tokuyama Shapal grade SH15) and Si_3N_4 (Kyocera SN733, hot isostatically pressed) were irradiated at room temperature with either 245 MeV Kr or 710 MeV Bi ions at the Dubna U-400 cyclotron facility. The ion fluences ranged from $1x10^{12}$ ions/cm^2 (isolated track regime) to $1x10^{13}$/cm^2. The electronic stopping power (S_e) and displacement damage profiles were calculated using the TRIM2000 program [6]. Figure 1 shows the calculated results for 710 MeV Bi ions in Si_3N_4. The maximum displacement damage due to elastic collisions occurs at a depth of ~28 µm, and amounts to ~0.013 displacements per atom (dpa) for a fluence of $1x10^{13}$/cm^2, assuming a sublattice-averaged displacement energy of 40 eV. Similar profiles were calculated for Bi ions in SiC and AlN. Table 1 summarizes some of the room temperature physical parameters for the three ceramics.

Following irradiation, cross-section TEM specimens were prepared by gluing the irradiated disks to polished unirradiated disks, sectioning, grinding to 0.1 mm, dimpling to 20 µm, and then dual-gun ion beam thinning at ~80 K with 6 keV Ar ions until perforation occurred near the interface. The specimen surfaces were cleaned using 3 keV Ar ions at an angle of 11˚. The AlN and Si_3N_4 specimens were coated with a thin (~5 nm) layer of carbon prior to examination. The specimens were examined using conventional bright-field and dark-field imaging techniques in a Philips CM-30 microscope operating at 300 kV.

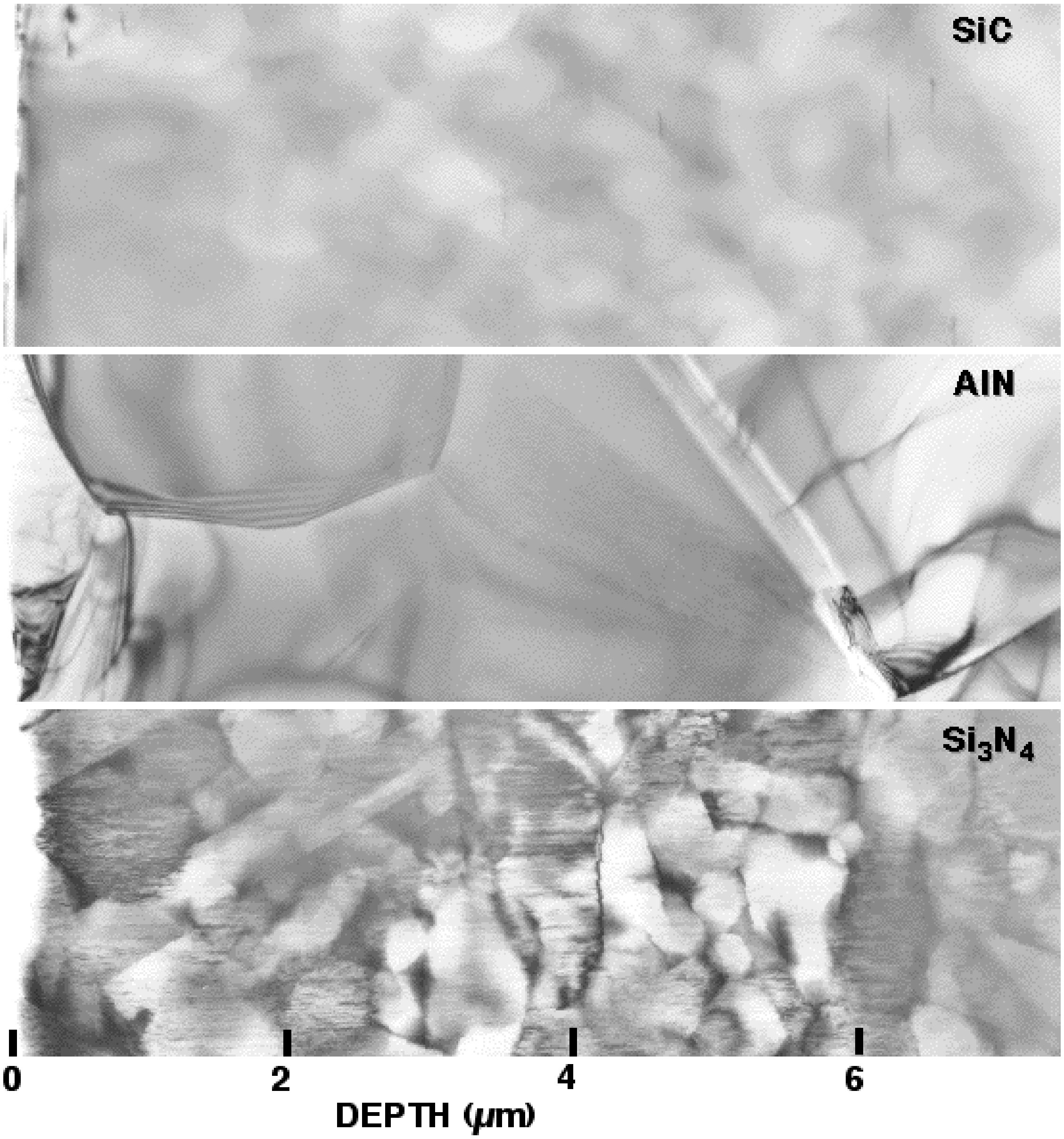

Fig. 2. Comparison of the low-magnification microstructures of SiC, AlN and Si_3N_4 irradiated with 710 MeV Bi ions.

RESULTS

Figure 2 compares the low-magnification bright-field cross-section microstructures of SiC, AlN and Si_3N_4 irradiated with 710 MeV Bi ions. The ion fluences were $1x10^{13}/cm^2$ for SiC and AlN, and $3x10^{12}/cm^2$ for Si_3N_4. Ion tracks were visible in the Si_3N_4 specimen even at low magnification. Conversely, ion tracks were not visible in the SiC and AlN specimens at any location along the ion beam path (bright field and dark field imaging up to 300 kx). The ion tracks in the Si_3N_4 specimen were visible from the irradiated surface to a depth of ~23 µm. This implies that the threshold electronic stopping power for track formation in Si_3N_4 is ~15 keV/nm for Bi ions.

Figure 3 shows a higher magnification view of the microstructure of the Si_3N_4 specimen irradiated with 710 MeV Bi ions to a fluence of $3x10^{12}/cm^2$. The ion track diameter was ~4.5 nm. A diffuse halo was observable in diffraction patterns taken from the ion track region of the specimen. Faint ion tracks could be imaged by centered dark field techniques, using the halo pattern. This implies that the center of the ion track is amorphous in the Si_3N_4 specimens irradiated with 710 MeV Bi ions. High resolution lattice imaging of an irradiated Si_3N_4 specimen (plan view) will be performed to conclusively determine whether or not the ion track center is amorphous.

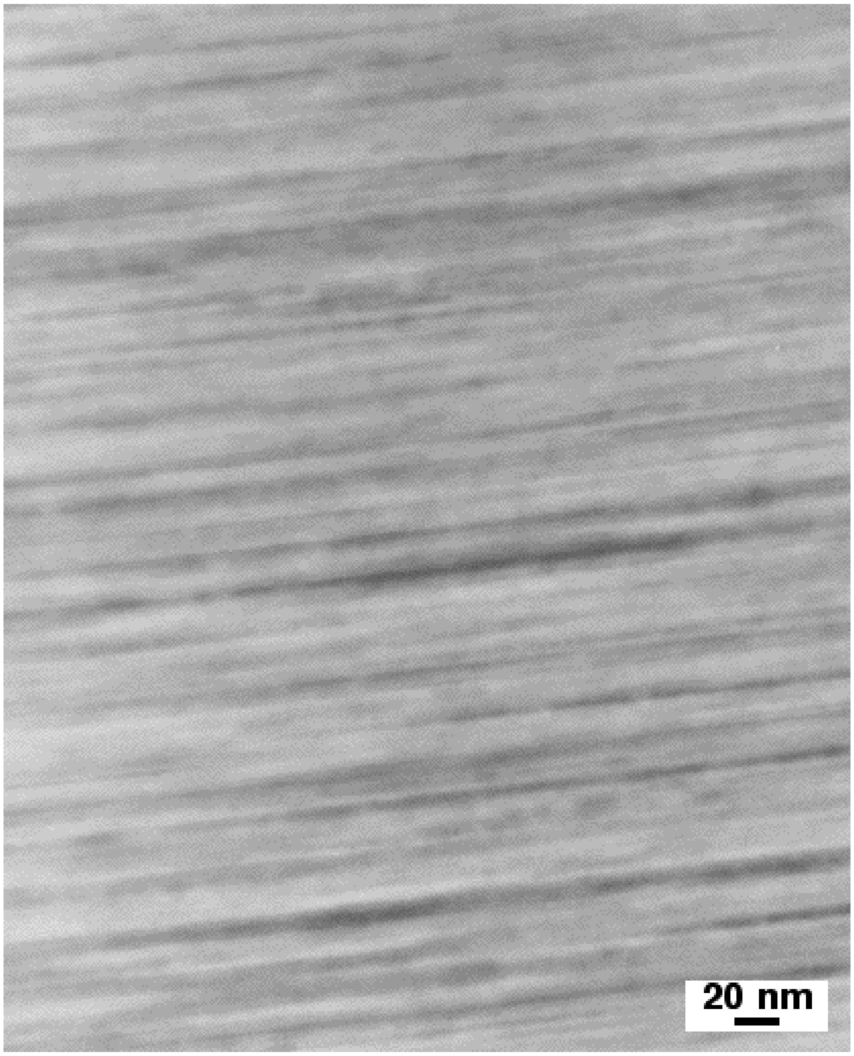

Fig. 3. Microstructure of Si_3N_4 irradiated with 710 MeV Bi ions.

In order to further investigate the threshold electronic stopping power for track formation in Si_3N_4, the microstructure of specimens irradiated with 245 MeV Kr ions to a fluence of $1x10^{13}/cm^2$ was examined. Although evidence for radiation damage to a depth of ~20 µm was visible in optical micrographs of a cross-section specimen, there was no evidence for ion track formation during extensive TEM examination. Ion tracks were also not observed in the SiC or AlN specimens irradiated with 245 MeV Kr ions.

Figure 4 compares the calculated depth-dependent electronic stopping powers for 710 MeV Bi and 245 MeV Kr ions in Si_3N_4. The maximum electronic stopping power for 245 MeV Kr ions is ~14.5 kV/nm, occurring at a depth of ~7 µm. Therefore, the absence of visible ion tracks in Si_3N_4 irradiated with 245 MeV Kr ions indicates that the threshold electronic stopping power for track formation is >15 keV/nm for Xe ions.

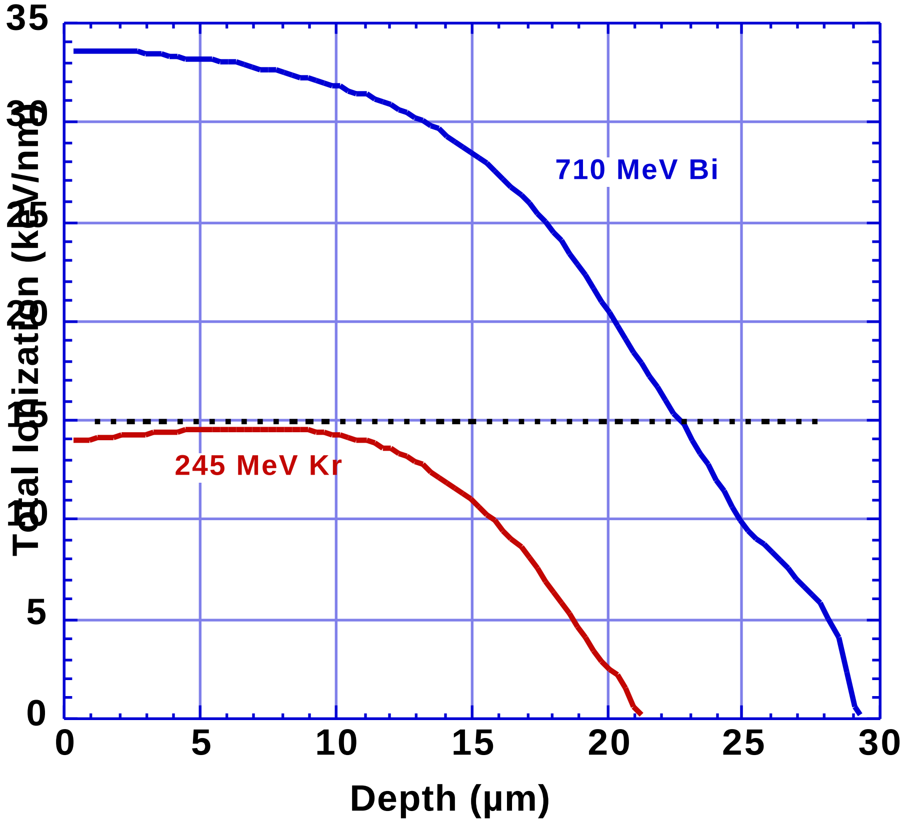

Fig. 4. Comparison of the electronic stopping powers for swift heavy ions in Si_3N_4.

DISCUSSION

In three previous studies of SiC irradiated with swift heavy ions [3-5], there was no evidence for ion track formation. Krstic and coworkers did not observe any swelling in SiC irradiated with 72 MeV I^+ ions (peak electronic stopping power of ~15 keV/nm) up to fluences as high as $1x10^{17}/cm^2$ [4]. Lhermitte-Sebire et al. [3] did not observe evidence for track formation in SiC irradiated with 5.5 GeV Xe ions, where the maximum calculated electronic stopping power was 21.9 keV/nm at a depth of 390 µm. A recent positron annihilation study did not observe evidence for amorphization in SiC irradiated at 300 K with 246 MeV Kr ions (maximum S_e=14.5 keV/nm) up to a fluence of $1x10^{14}$ ions/cm^2 [5]. The present study indicates that track formation does not occur in SiC for electronic stopping powers as high as 34 keV/nm. We are not aware of any previous studies of track formation in AlN or Si_3N_4.

Latent tracks were registered in Si_3N_4, which has the lowest thermal conductivity among the 3 ceramics listed in Table 1. This implies that the observations in this investigation may be interpreted in the framework of the thermal-spike model. The basic assumption of the thermal-spike model connects the latent track formation with quenching of molten matter along the ion path [1,9-11]. Since the experimentally determined value is a track size, R_0, the applicability of approach is usually concluded from the comparison of measured and calculated values of R_0. In the microscopic transient thermodynamic model [9-11] it can be done by solving two coupled equations with one only free parameter – the electron-lattice mean free path $\lambda = (D_e\tau_e)^{1/2}$, where D_e is the thermal electron diffusivity and τ_e the electron-lattice interaction time. This parameter λ is determined by fitting the experimental radii found for a variety of specific inelastic energy loss values S_e,. Since track radii were only observed for one ion beam energy in the present study (710 MeV Bi ions incident on Si_3N_4), further studies using additional ion beams are needed before a quantitative evaluation of the suitability of the thermal spike model can be made.

The alternative phenomenological track formation model proposed by Szenes [12,13] assumes a Gaussian temperature distribution within the ion track. The model predicts that track formation consists of two stages: a low energy deposition regime where the track radius is given by R_0^2~ln S_e, and a higher energy deposition regime where R_0^2~S_e (linear regime). The low-energy regime is associated with the so-called velocity effect: low-velocity ions induce tracks more effectively for a given S_e. The linear regime of track formation has been observed to occur for many insulators over a wide range of electronic stopping powers. Our previously published data on track radii in $MgAl_2O_4$ irradiated with Kr and Xe ions [2] are consistent with the relation summarized above: R=1.0 nm for S_e=16 keV/nm (Kr ions) and R=1.3 nm for S_e=26 keV/nm (Xe ions). In these two cases, the ratio of R_0^2/S_e varies from 15.4 to 16. Further experiments are required in order to check the validity of the linear regime for Si_3N_4.

CONCLUSIONS

Both SiC and AlN have a very high resistance to ion track damage. No evidence for track formation was obtained in these two materials up to electronic stopping powers of 34 keV/nm (710 MeV Bi ions).

Ion tracks are visible in Si_3N_4 irradiated with 710 MeV Bi ions for electronic stopping powers above ~15 keV/nm. Ion tracks were not observed in Si_3N_4 irradiated with 245 MeV Kr ions (maximum electronic stopping power of 14.5 keV/nm). Preliminary analysis of the ion tracks in Si_3N_4 suggests that the track center may be amorphous. Further experimental data obtained with different ion beams are needed to determine whether the thermal spike model or the phenomenological model proposed by Szenes is a more appropriate description of the ion track creation process.

Acknowledgements

This research was sponsored in part by the Office of Fusion Energy Sciences, U.S. Department of Energy under contract DE-AC05-00OR22725 with UT-Battelle, LLC and by the Russian Foundation for Basic Research, grant N 00-02-16559.

REFERENCES

1. M. Toulemonde, S. Bouffard, and F. Studer, Nucl. Instr. Meth. B **91**, 108 (1994).
2. S.J. Zinkle, Hj. Matzke, and V.A. Skuratov, in *Microstructural Processes During Irradiation*, MRS Symposium Proceedings, edited by S.J. Zinkle, G.E. Lucas, R.C. Ewing, and J.S. Williams (Materials Research Society, Warrendale, PA, 1999), Vol. 540, p. 299.
3. I. Lhermitte-Sebire, J. Vicens, J.L. Chermant, M. Levalois, and E. Paumier, Philos. Mag. A **69** (2), 237 (1994).
4. V.D. Krstic, M.D. Vlajic, and R.A. Verrall, Key Engineering Materials **122-124**, 387 (1996).
5. L. Liszkay, K. Havancsák, M.-F. Barthe et al., in *Proc. 12th International Conference on Positron Annihilation,* Munich, Germany, August 6-12, 2000, in press.
6. J.F. Ziegler, J.P. Biersak, and U. Littmark, *The Stopping and Range of Ions in Solids* (Pergamon Press, New York, 1985).
7. T. Yano and T. Iseki, J. Nucl. Mater. **203**, 249 (1993).
8. C-M Wang, X. Pan, M. Rühle, F.L. Riley, and M. Mitomo, J. Mater. Sci. **31**, 5281 (1996).
9. M. Toulemonde, J.M. Costantini, Ch. Dufour et al., Nucl. Instr. Meth. B **116**, 37 (1996).
10. A. Meftah, M. Djebara, N. Khalfaoui et al., Mater. Sci. Forum **248-249**, 53 (1997).
11. M. Toulemonde, Ch. Dufour, A. Meftah, and E. Paumier, Nucl. Instr. Meth. B **166-167**, 903 (2000).
12. G. Szenes, Phys. Rev. B **51** (13), 8026 (1995).
13. G. Szenes, Nucl. Instr. Meth. B **116**, 141 (1996).

8.0 BREEDING MATERIALS

No contributions.

9.0 RADIATION EFFECTS, MECHANISTIC STUDIES, AND EXPERIMENTAL METHODS

The Influence of PKA Direction on Displacement Cascade Evolution - Roger E. Stoller (Oak Ridge National Laboratory)

EXTENDED ABSTRACT

An extensive database of atomic displacement cascades in iron has been developed using molecular dynamic (MD) simulations. More than 300 cascades have been completed at 100K at energies between 100 eV and 100 keV, with fewer simulations at 600 and 900K. A systematic evaluation of the database has revealed an unexpected effect of PKA direction in MD simulations of 300 eV cascades in iron at 100K. A type of planar channeling was observed when the PKA direction lies in the close-packed {110} planes. An example of a cascade with a [114] direction is shown in Figure 1. Parts (a) and (b) of this figure show the peak damage condition in two different orientations, and part (c) shows the final configuration of stable defects. In this case, 6 stable vacancies and interstitials were created, whereas the average from a large number of cascades initiated in a high-index direction is about 2. The two-dimensional nature of cascade development leads to more efficient separation of vacancies and interstitials, thereby reducing in-cascade

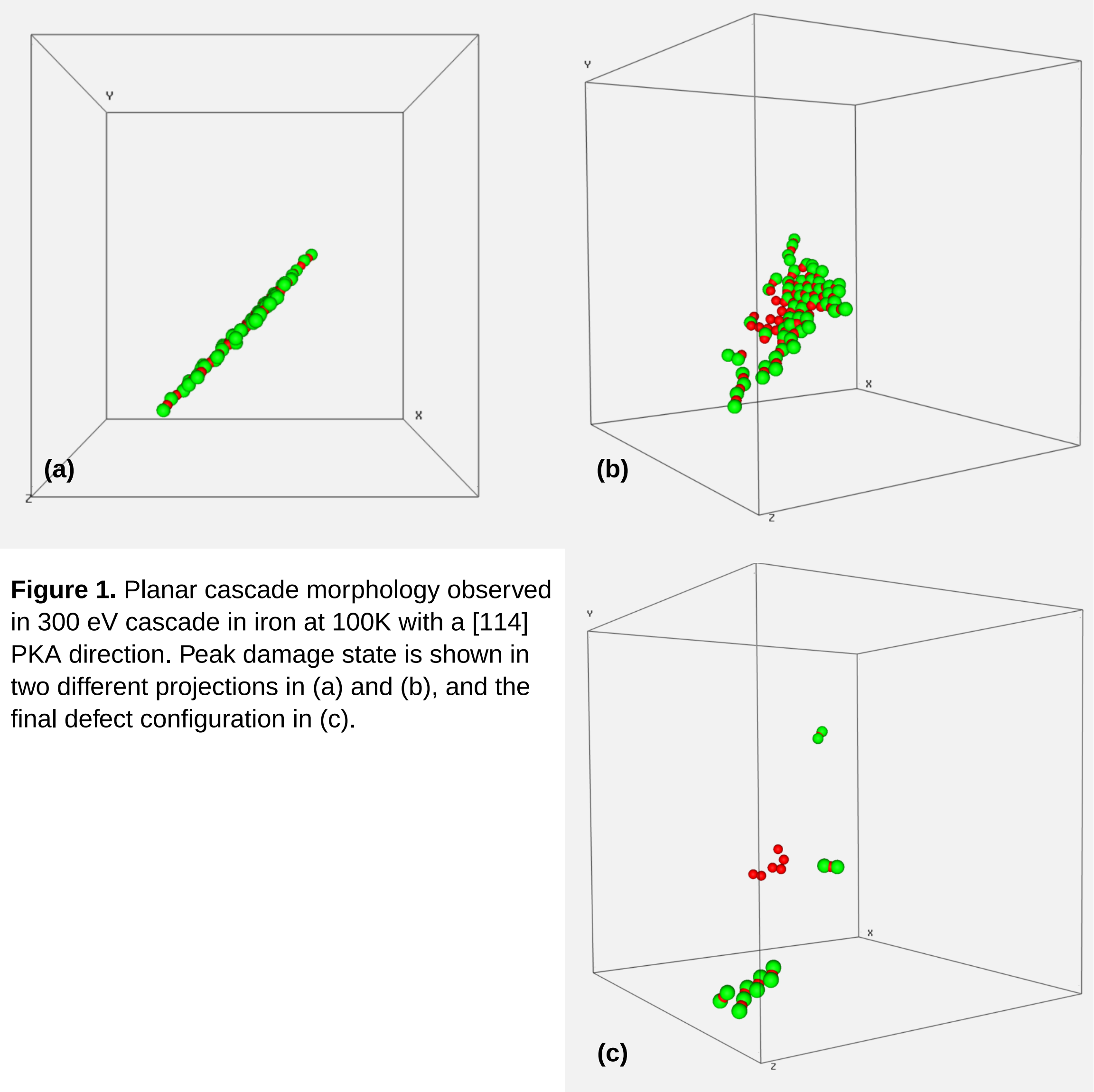

Figure 1. Planar cascade morphology observed in 300 eV cascade in iron at 100K with a [114] PKA direction. Peak damage state is shown in two different projections in (a) and (b), and the final defect configuration in (c).

recombination. Thus, a greater fraction of the radiation-produced interstitials and vacancies survive in cascades with a PKA directions that lies in a {110} plane.

The cascade shown in Figure 1 is perfectly planar, and the most extreme example out of the sixteen [114] cascades simulated. However, all the cascades were somewhat disk-like, leading to higher average defect survival. The magnitude if this effect is shown in Figure 2, where the average number of stable displacements is plotted for four different PKA directions: [135], [114], [121], and [123]. The [135] and [123] are relatively high index directions and the [114] and [121] lie in {110} planes. The average number of surviving displacements has been normalized by the value predicted by the standard NRT model [1]. The impact of PKA direction on in-cascade point defect clustering is less systematic since there is more cascade-to-cascade scatter in this parameter than in defect survival [2].

The PKA direction effect gradually disappears at higher energies as the atomic recoils have a greater probability of breaking out of the plane and generating a three-dimensional cascade. However, the data indicate that some dependence on PKA direction persists up to about 2 keV. The difference between the [135] and [114] averages is statistically significant at the 95% confidence level for the 300 eV simulations. The [114] defect survival was 15% higher than [135] at 2 keV, although this difference is not statistically significant at the 90% confidence level.

These results are probably most significant for low temperature irradiation conditions because increased thermal motion of the atoms may mitigate the effect at higher temperatures. The influence of irradiation temperature on the observed behavior is under investigation. Since the effect of PKA direction on defect survival persists up to cascade energies as high as 1-2 keV (~2.5 keV PKA energy), a thorough investigation of PKA direction effects in low-energy cascades should be carried out before choosing a single direction for high energy cascade simulations. Finally, it is interesting to note that the PKA directions which gave higher than average survival were not those directions with a low displacement threshold [3]. Thus, this effect should also be considered when interpreting the results of experiments intended to measure atomic displacement thresholds.

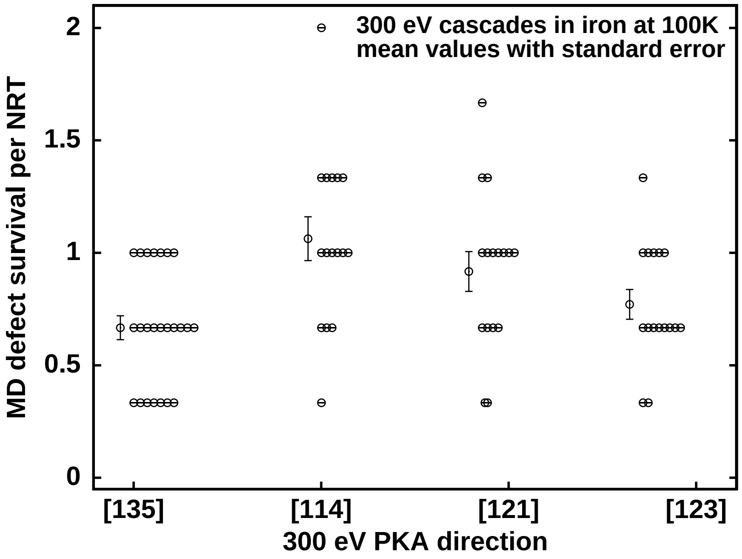

Figure 2. Effect of PKA direction on the number of stable displacements in MD cascade simulations, normalized by the NRT displacements.

ACKNOWLEDGEMENTS

This research was also supported by the Division of Materials Sciences and Engineering, U.S. Department of Energy and the Office of Nuclear Regulatory Research, U.S. Nuclear

Regulatory Commission under interagency agreement DOE 1886-N695-3W with the U.S. Department of Energy, under contract DE-AC05-00OR22725 with UT-Battelle, LLC.

REFERENCES

[1] M. J. Norgett, M. T. Robinson, and I. M. Torrens, Nucl. Eng. and Des. 33 (1975) 50.
[2] R.E. Stoller and A. F. Calder, J. Nucl. Mater., 283-287 (2001) 746.
[3] D. J. Bacon, A. F. Calder, J. M. Harder, and S. J. Wooding, J. Nucl. Mater. 205 (1993) 52.

(extended abstract of paper to be published by Materials Research Society in proceedings of Symposium R: Microstructural Processes in Irradiated Materials, Fall MRS Meeting)

THE EFFECT OF TEST MACHINE COMPLIANCE ON THE MEASURED SHEAR PUNCH YIELD STRESS AS PREDICTED USING FINITE ELEMENT ANALYSIS

- Mychailo B. Toloczko*, Katsunori Abe (Tohoku University, Japan), Margaret L. Hamilton, Frank A. Garner, and Richard J. Kurtz (Pacific Northwest National Laboratory)[*]

ABSTRACT

In previous research involving the use of the shear punch test, it was assumed that the displacement of the punch tip was only slightly different than the crosshead displacement. The present work explores this assumption and its ramifications by simulating the shear punch test with finite element analysis (FEA). The simulations suggest that punch tip displacement is much less than previously assumed, and that for the test frames which have been used, crosshead displacement is over an order of magnitude greater than punch tip displacement. This difference in displacements is thought to be due to test machine and punch compliance, and a simple elasticity calculation of the compliance of the punch, the test machine, and a specimen gives a result which is in agreement with the FEA simulations. The effect of using punch tip displacement on the observed effective shear yield stress was evaluated using FEA simulated shear punch tests on several different metals. Yield was measured at several different offset shear strains with a 1.0% offset shear yield strength measurement providing the best correlation with 0.2% offset uniaxial yield strength. When using the 1.0% offset shear yield values, the previously observed material-to-material variability in the tensile-shear correlation all but disappeared. Based on this work, it appears that the material-to-material variations in prior correlations between uniaxial yield strength and shear yield strength is due to a combination of large test machine compliance and material-to-material differences in the work hardening exponent.

---

[*] Pacific Northwest National Laboratory (PNNL) is operated for the U.S. Department of Energy by Battelle Memorial Institute under contract DE-AC06-76RLO-1830.

Introduction

The shear punch test is a small specimen test technique for extracting yield strength, ultimate strength, and uniform elongation values from metals using TEM disks [1-5]. It is a blanking operation where a 1 mm diameter flat faced cylindrical punch is driven through a TEM disk at a constant rate. A schematic of a shear punch test apparatus is shown in Fig. 1. Ideally, the load on the punch is measured as a function of punch tip displacement, but due to the difficulty in actually measuring the punch tip displacement, it has been previously assumed that crosshead displacement is approximately equal to punch tip displacement, and thus, the load on the punch has been measured as a function of crosshead displacement. Shear punch load versus crosshead displacement traces are similar in appearance to uniaxial tensile test traces. Yield is measured from these traces at deviation from linear elastic loading, and ultimate is measured at the peak load. The “effective” shear stress[1] is calculated assuming that the only stress generated during a test is a shear stress in the rz plane of a cylindrical coordinate system with z-axis parallel to the punch axis. Thus, the “effective” shear stress is:

$$\sigma = \frac{P}{2\pi r t} \tag{1}$$

where P is the load on the punch, r is the average of the punch and receiving die radii, and t is the specimen thickness. True uniform elongation is estimated from the ratio of the shear ultimate strength to the shear yield strength [3].

In a recent FEA based study of the shear punch test [6], the authors of the study observed that, 1) the elastic loading slope of an FEA generated load versus punch tip displacement

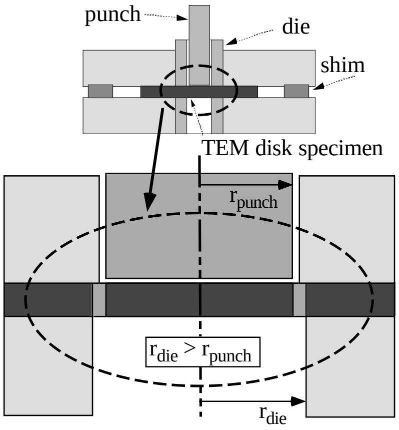

Figure 1. Sketch of the shear punch fixture.

---

[1] For the sake of brevity, the “effective shear stress” will simply be called the “shear stress”.

trace was much steeper than observed in real shear punch tests, 2) the strain hardening behavior was much different than observed in real shear punch tests, and 3) the yield point observed in the FEA simulations was lower than what was observed in real tests. Since the authors were focused on other results obtained from the FEA simulations, the aforementioned differences between the FEA simulations and the real test traces were not given any further consideration.

The present work represents an effort to examine those aspects of the FEA simulated shear punch test which were not examined in the first paper [6]. It was determined that the compliance of a typical mechanical properties test frame is much greater than the elastic compliance of a typical shear punch test specimen (when loaded in the shear punch test). It was this large test machine compliance which led to the difference in the shape of a real shear punch test trace and an FEA generated shear punch test trace. It was found that the correlation between shear yield strength and ***uniaxial*** yield strength improved when using shear yield strength values obtained from load versus punch tip traces generated in FEA simulations of the shear punch test.

Experimental: The Finite Element Analysis Simulation

The MARC finite element analysis software was used to simulate the shear punch test. To reduce computing time and costs, an axisymmetric mesh was utilized and is shown in Fig. 2. There are three main components to the mesh: the specimen, the punch, and the receiving

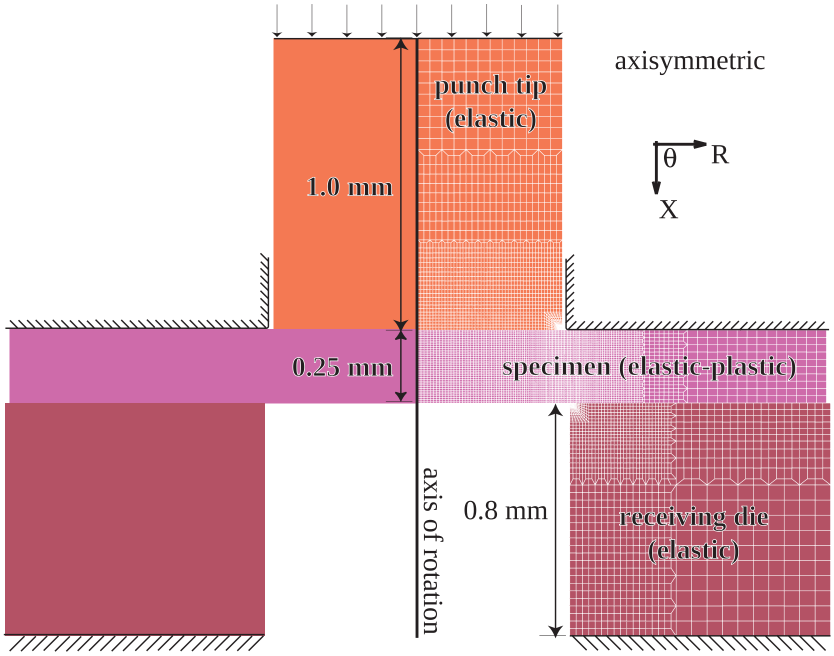

Figure 2. Sketch of the mesh used in the present study.

die. The specimen was modeled as elastic-plastic. In an effort to make the simulation as realistic as possible, the punch and the receiving die were modeled as elastic. This allows for a small amount of elastic deformation in these components which alters the stress distribution in the specimen mesh[2]. The specimen has a thickness of 0.25 mm and a diameter of 3 mm. The mesh consisted of 4340 elements. The punch diameter is 1.016 mm. In real shear punch tests, the punch is about 20 mm in length, but for the simulations, only 1 mm of the 20 mm length was modeled. The diameter of the receiving die is 1.0414 mm, and as with the punch, only a small portion of the length of the entire receiving die was modeled (0.8 mm). The lengths of the punch and the die were chosen so that the stresses at the top of the punch and the bottom of the die were fairly uniform. This guarantees that the stress concentrations at the punch tip and die tip can relax in the same manner which they do in a real test. The punch and the receiving die meshes were composed of 1527 and 1395 elements respectively. As with any finite element analysis, material properties must be inserted into the model. For this simulation, the punch and the receiving die were assigned the elastic properties of BCC steel ($E = 200$ GPa, $\nu = 0.28$). The specimen was assigned the uniaxial deformation behavior of several different materials of interest as described in the next paragraph. The FEA boundary conditions were as follows:

1) Translations in the radial direction were prevented because the model is axisymmetric.
2) The bottom of the receiving die was held stationary in the axial direction.
3) An immovable boundary was placed in contact with a portion of the top of the specimen to simulate the presence of the upper-half of the shear punch fixture. No clamping force was applied to the specimen with this boundary condition.
4) Friction between the components was set equal to zero. The previous FEA based study has shown the effect of friction between components to be minimal [6].

During a simulation, the top of the punch was moved at a constant rate. Under the assumption that real shear punch tests are performed in the strain rate independent realm, the FEA simulations were run in static mode. Due to the difficulty in simulating the cutting and failure behavior which occur in a real shear punch test, the FEA simulations were run to only a small amount beyond yield.

Simulated shear punch tests were performed on several different materials. Different materials were “tested” by assigning true stress versus true plastic strain data and elastic

---

[2] Simulations using a rigid punch and receiving die were also performed but are not reported here. By comparing these results using a rigid punch and receiving die to the results obtained using an elastic punch and receiving die, it was found that using an elastic punch and receiving die significantly altered the stress state in the FEA specimen (reduced stress concentrations) and had a significant influence on the apparent transition from linear elastic loading to plastic deformation in a load versus punch tip displacement trace.

deformation properties from different materials to the specimen elements. The true stress versus true plastic strain data were obtained from miniature tensile tests performed on 316 SS, HT9 (a 12Cr-1Mo martensitic stainless steel), several dispersion strengthened copper alloys, a precipitate strengthened copper alloy, vanadium alloys, and aluminum alloys. A brief summary of the materials can be found in Table 1. Further details about these materials can be found in Ref. 2.

During a simulation, the MARC program keeps track of the load on the punch and the displacement of the top of the punch. To obtain the punch tip displacement, it was necessary to run simulations using a rigid punch and receiving die. By comparing the elastic loading obtained from a rigid component test to an elastic component test, it was possible to measure the compliance of the punch and receiving die. This compliance value was then used to estimate the punch tip displacement as a function of the displacement at the top of the punch using the following formula:

$$x = x' - PC' \tag{2}$$

where x is the punch tip displacement, x' is the displacement at the top of the punch, P is the load on the punch, and C' is the measured compliance of the punch and receiving die. Using the calculated punch tip displacement data, load versus punch tip displacement traces were created.

FEA generated shear stress versus punch tip displacement traces were compared to shear stress versus crosshead displacement traces obtained from real shear punch tests. These shear punch tests were performed several years ago using a machine with a compliance that is typical of that for tensile tests. Further details of these shear punch tests have been published [2, 7].

Table 1. Materials and thermomechanical treatments studied in this work.

Alloy	Thermomechanical Treatments
Al 5052	0 (solution annealed), H38 (aged and CW)
Al 6061	0 (solution annealed), T6 (aged)
316	SA, 20% CW, 40% CW, 2 age/CW treatments
HT9	normalized, 4 different tempering treatments
316, 316L	SA, CW
CuAl25	50% CW
MZC-3	aged and cold-worked
$CuHfO_2$	20% CW
V-5Cr-5Ti	950°C/1h/furnace cool
V-3Ti-0.3Si	1150°C/1h/furnace cool

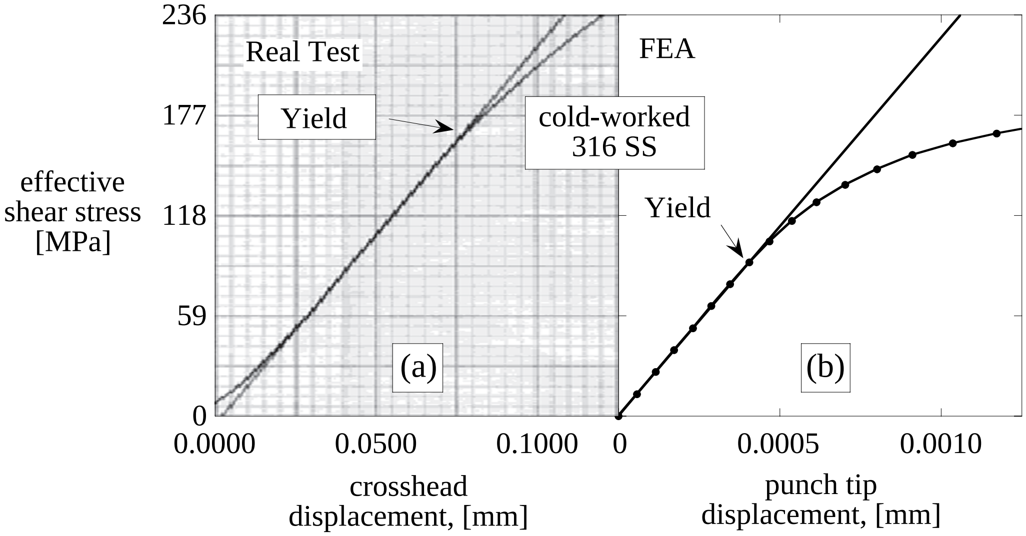

Figure 3. a) Shear stress versus crosshead displacement trace for a real shear punch test of a cold-worked 316 SS, and b) shear stress versus punch tip displacement trace for an FEA simulated shear punch test on the same steel.

Results and Discussion

Compliance

While simulated tests were performed on many different materials, the results can be most efficiently conveyed by showing the behavior of one combination of material and thermomechanical treatment, namely using one of the cold-worked 316 SS conditions. Fig. 3a shows a shear stress versus crosshead displacement trace obtained from a real shear punch test on a cold-worked 316 SS specimen, while Fig. 3b shows a shear stress versus punch tip displacement trace obtained from an FEA simulation of a shear punch test on the same material. The key aspect of this comparison is that the elastic loading slope for the FEA simulation is 2 orders of magnitude steeper than the elastic loading slope of the real shear punch test (look at the x-axis scales in figures). This result mirrors the result obtained in the previous FEA based study of the shear punch test [6]. Since the main difference between an FEA simulation and a real shear punch test is the location at which displacement is measured, it is reasonable to assume that this is leading to the dissimilar traces. This could be determined by measuring the compliance of the test machine, but performing such a compliance measurement is not a simple task because of the geometry of the shear punch test.

An alternative method for obtaining the test machine compliance is to calculate it directly using the dimensions of the major components in the load-train of the test machine and using Young's modulus. First, consider the relative compliance of the punch and a specimen. The punch which was used for the shear punch tests has a diameter of 1.016 mm and a length of approximately 20 mm. Assuming a Young's modulus of 200 GPa, this leads to a compliance of approximately 1.2×10^{-4} mm/N. This can be compared to the calculated elastic compliance of a specimen. For a shear modulus of approximately 75 GPa (steel), and for a 0.25 mm thick specimen under an idealized shear deformation shown in Fig. 4, the elastic compliance of the specimen due to shear deformation is estimated to be 2×10^{-7} mm/N. Due to the way load is applied during a shear punch test, a specimen is also compressed. Assuming the majority of the compression occurs in an annular region with in radius of 0.85 mm and outer radius of 1.15 mm, the compliance due to the compression is estimated to be approximately 6.6×10^{-7} mm/N. The total estimated compliance of a specimen is then approximately 8.6×10^{-7} mm/N. Hence, the estimated ***punch*** compliance is approximately a factor of 140 greater than the estimated elastic compliance of a steel specimen. An idealized calculation of the compliance of the remainder of the load-train would increase this ratio to approximately 150. Thus, these simple elasticity calculations tend to confirm the results obtained by comparing the elastic loading observed in the FEA simulations to the elastic loading observed in real shear punch tests.

Following the idea that the differences in the traces for the FEA simulations and the real shear punch tests is due to test machine compliance, a compliance was added to the FEA punch tip displacement data. By adding a compliance, the punch tip displacement was converted to a hypothetical crosshead displacement. The equation which describes this hypothetical crosshead displacement is

$$\delta = x + PC \tag{3}$$

where δ is the hypothetical crosshead displacement, x is the displacement of the punch tip, P is the load on the specimen, and C is the estimated test machine compliance (including the punch). C was found by comparing the elastic loading slope in shear punch test traces obtained from real tests and from FEA simulations. For the 316 SS trace in Fig. 3a, C is approximately 5.5×10^{-4} mm/N. The resulting shear stress versus hypothetical crosshead displacement trace is compared to the real test trace in Fig. 5. The FEA generated trace has been transformed into a trace that looks nearly identical to the real trace. The yield point estimated from the transformed FEA trace is 165 MPa whereas the yield point estimated from the real test trace is 163 MPa. This further confirms the idea that crosshead

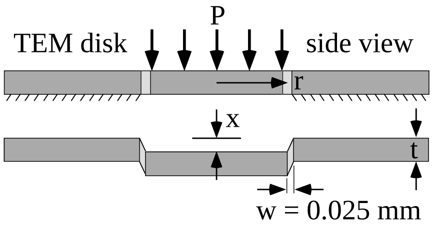

Figure 4. Idealized deformation during a shear punch test.

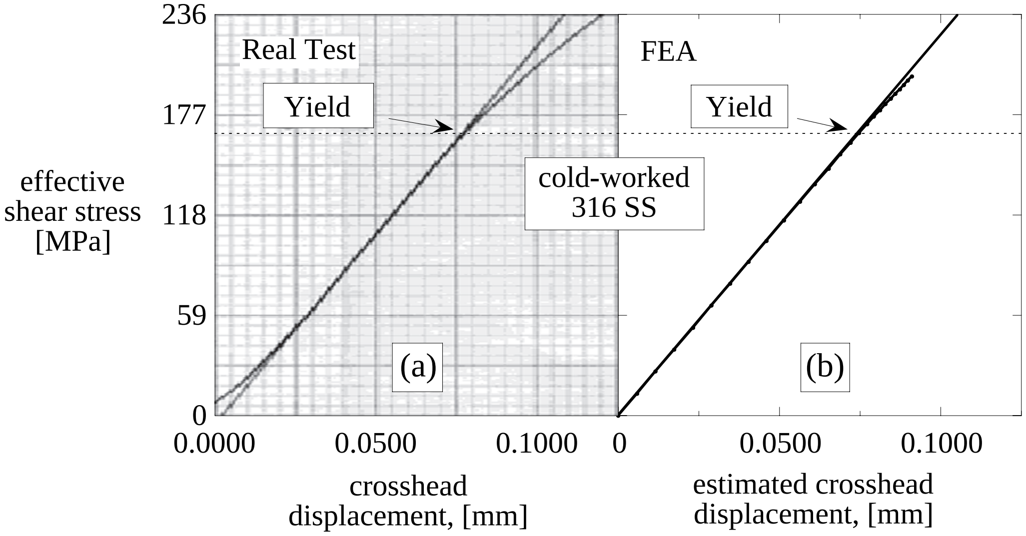

Figure 5. Comparison of a real trace and an FEA simulated trace where the FEA punch tip displacement data has been converted to a hypothetical crosshead displacement data using Eq. 3.

displacement measured in real tests is much larger than the actual punch tip displacement. It also shows that a large amount of compliance can strongly alter the appearance of a load versus displacement trace.

Shear yield stress measurement and correlation to uniaxial yield stress

For the shear punch tests performed to date, load has been measured as a function of crosshead displacement. Shear yield has been measured from these traces at deviation from apparent linear elastic loading. Shear yield values measured in this way have, in general, correlated very well with uniaxial tensile data [1-3, 5]. However, there is some material-to-material variability in the yield correlation. To examine the effect of test machine compliance on the observed shear yield stress, shear yield stress was measured from the FEA generated shear stress versus punch tip displacement traces. Since punch tip displacement data were used, it was deemed reasonable to re-assess the method by which shear yield is measured. Besides simply measuring the shear yield at deviation from linear elastic loading, the shear yield was also measured at an “offset shear strain” in a manner analogous to the 0.2% offset uniaxial yield stress measurement technique. The (fractional) shear strain was calculated using the following formula:

$$\varepsilon_{rz} = \frac{1}{2}\frac{x}{w} \tag{4}$$

where w is the difference in the punch and receiving die radii (Fig. 4). The factor of 1/2 results from using the tensor definition of shear strain. The optimum offset shear strain was chosen based on how well the shear yield values correlated with real 0.2% offset uniaxial strain measurements. Shear yield measured at offset shear strains ranging from 0% (deviation from linearity) to 1.0% were tried, and the correlations resulting from these two extremes are shown in Fig. 6a and Fig. 6b. It is clear that measurement of shear yield at 1.0% offset shear strain resulted in the best correlation with the data collapsing nearly perfectly onto a straight line.

Fig. 6b can be compared with Fig. 7a and Fig. 7b which show the yield correlation when measuring shear yield at deviation from linearity using either (a) real shear stress versus crosshead displacement traces or (b) FEA generated shear stress versus estimated crosshead displacement traces. The 1.0% offset shear yield measurements produce a noticeably better correlation (Fig. 6b) compared to shear yield measured at deviation from linearity (Fig. 7a and Fig. 7b). Two tangible factors likely contribute to the improvement in the correlation. First, shear stress versus punch tip displacement traces provide a much more accurate representation of the stress-strain relationship in a material during a shear punch test. And second, with this improvement, it is possible to measure the shear yield stress in a manner similar to the method by which yield is measured from uniaxial tensile test traces. The fact that an offset shear strain resulted in the best correlation is reasonable because it is known that the relative uniaxial yield strength of different materials depends on what offset strain is used when measuring the yield point[3] [8]. A somewhat intangible factor

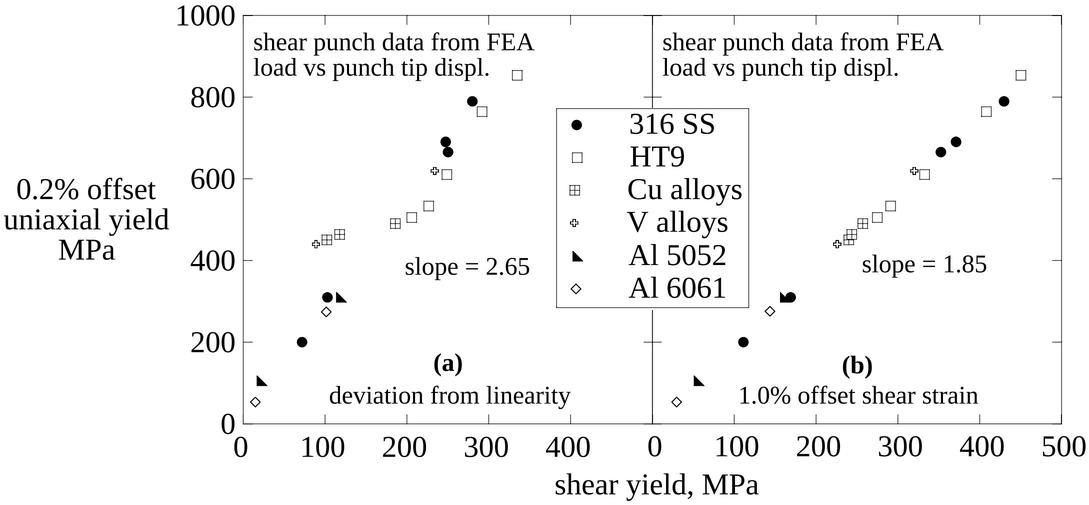

Figure 6. Comparison of correlations where shear yield was either measured (a) at deviation from linearity in an FEA shear stress versus punch tip displacement trace or (b) at a 1.0% offset strain in an FEA shear stress versus punch tip displacement trace.

---

[3] The relative variation is because, in general, different materials exhibit different strain hardening behavior. Some materials exhibit relatively little strain hardening, and the yield stress increases very little with increases in offset strain while other materials exhibit high strain hardening, and the yield stress increases very rapidly with increasing offset strain.

which may also contribute to the improvement in the correlation is material strain rate effects. During the FEA simulations, the materials were tested in static mode where strain rate effects are not present. In comparison, during a real test, there may be material strain rate effects. With a large amount of test machine compliance, the displacement rate of the punch tip will be time dependent. Relative to the speed of the crosshead, the punch tip speed is given by:

$$v_x = v_\delta - C\frac{dP}{dt} \tag{5}$$

were v_x is the punch tip speed and v_δ is the crosshead speed. During elastic loading, dP/dt is constant, and the difference in speed between the crosshead and the punch tip will also be constant. However, once the loading trace goes non-linear, dP/dt will no longer be a constant, and the difference in speeds will change. Since dP/dt will decrease, the punch tip will move at a faster and faster speed. The peak punch tip speed will be reached at maximum load, and at this point, the punch tip speed will equal the crosshead speed. Thus, during the course of a test where a large amount of test machine compliance is present, the punch tip speed may increase by several orders of magnitude. It therefore seems quite plausible that there may be strain rate effects in real tests when a large amount of test machine compliance is present. For a large amount of test machine compliance, it is thought that because materials usually have a positive strain rate exponent and because the punch tip speed increases during a test, the observed loads would be artificially high. Since the strain rate exponent is temperature dependent, this effect may be magnified at elevated test temperatures.

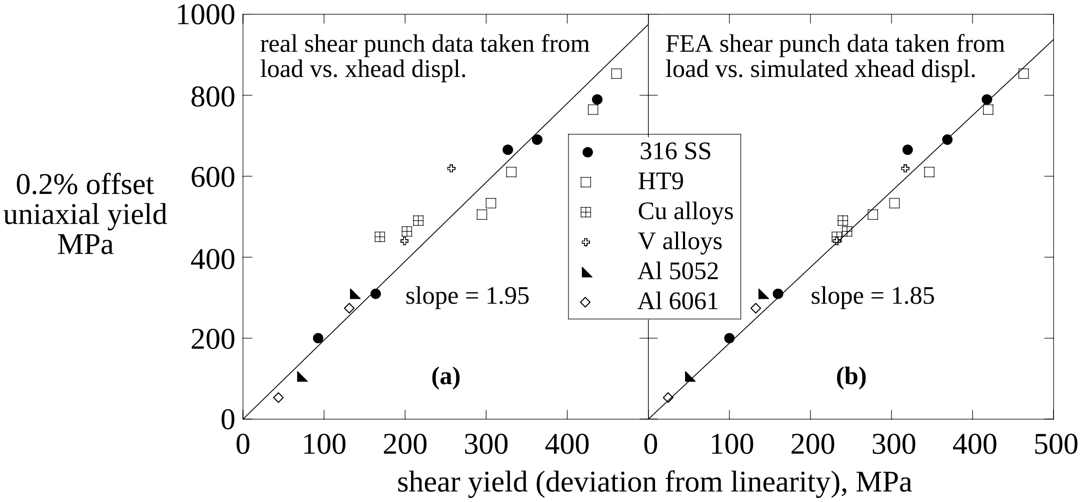

Figure 7. Comparison of correlations where shear yield was measured at deviation from linearity using either (a) real shear stress versus crosshead displacement traces or (b) using FEA generated shear stress versus simulated crosshead displacement traces.

The improvement in the correlation between uniaxial yield strength and FEA based shear yield strength suggests that the correlation between uniaxial yield strength and ***real*** shear yield strength measurements could be improved if a shear punch test fixture which more directly measures punch tip displacement could be constructed. Such a fixture has been designed and constructed, but evaluation and testing could not be completed in time for this paper.

Summary and Conclusions

In a previous finite element analysis based study of the shear punch test, it was noted that shear stress versus punch tip displacement traces obtained from FEA simulations looked much different than that obtained from real tests. The results of the present study suggest that the apparent differences in the original FEA traces and real traces is due to an incorrect assumption that crosshead displacement is nearly equal to punch tip displacement. It appears that punch tip displacement during a shear punch test is much smaller than previously assumed, and that an amount of test machine compliance which is considered normal for a tensile test is unacceptably large for a shear punch test if displacement is to be measured at the crosshead.

The present study also suggests that the previously observed material-to-material variability in the correlation between shear yield strength and uniaxial yield strength is due to a combination of large test machine compliance and material-to-material variability in the work hardening exponent. By measuring shear yield at an offset shear strain in FEA generated shear stress versus punch tip displacement traces, the correlation between uniaxial yield and FEA derived shear yield strength was significantly improved. A new shear punch fixture which eliminates most test machine compliance has been constructed, and evaluation of the new fixture in progress.

REFERENCES

[1] G. E. Lucas, G. R. Odette, and J. W. Sheckherd, “Shear Punch and Microhardness Tests for Strength and Ductility Measurements,” *The Use of Small Scale Specimens for Testing Irradiated Material, ASTM STP 888*, W.R. Corwin and G. E. Lucas, Eds., American Society for Testing and Materials, 1986, pp. 112-140.

[2] M. L. Hamilton, M. B. Toloczko, and G. E. Lucas, “Recent Progress in Shear Punch Testing,” *Miniaturized Specimens for Testing of Irradiated Materials*, Hans Ullmaier and Peter Jung, Eds., Forschungszentrum Jülich GmbH, January, 1995, pp. 46-58.

[3] M. B. Toloczko, M. L. Hamilton, and G. E. Lucas, “Ductility Correlations Between Shear Punch and Uniaxial Tensile Test Data,” *9th International Conference on Fusion Reactor Materials*, October 1999, Colorado Springs, Colorado, to be published in the *Journal of Nuclear Materials*.

[4] M. B. Toloczko, G. E. Lucas, G. R. Odette, R. E. Stoller, and M. L. Hamilton, "An Investigation of Microstructures and Yield Strengths in Irradiated Austenitic Stainless Steels using Small Specimen Techniques," *17th Symposium on the Effects of Radiation on Materials, ASTM STP 1270*, David S. Gelles, Randy K. Nanstad, Arvind S. Kumar, and Edward A. Little, Eds., American Society for Testing and Materials, 1996, pp. 902-918.

[5] G. L. Hankin, M. B. Toloczko, M. L. Hamilton, and R. G. Faulkner, "Validation of the Shear Punch-Tensile Correlation Technique using Irradiated Materials," *Journal of Nuclear Materials,* Vols. 258-263, 1998, pp. 1651-1656.

[6] G. L. Hankin, M. B. Toloczko, K. I. Johnson, M. A. Khaleel, M. L. Hamilton, F. A. Garner, R. W. Davies, and R. G. Faulkner, "An Investigation into the Origin and Nature of the Slope and x-axis Intercept of the Shear Punch-Tensile Yield Strength Correlation using Finite Element Analysis," *Effects of Radiation on Materials: 19th International Symposium, ASTM STP 1366*, M. L. Hamilton, A. S. Kumar, S. T. Rosinski, and M. L. Grossbeck, Eds., American Society for Testing and Materials, West Conshohocken, PA, 2000, pp. 1018-1028.

[7] M. L. Hamilton, M. B. Toloczko, D. J. Edwards, W. F. Sommer, M. J. Borden, J. A. Dunlap, J. F. Stubbins, and G. E. Lucas, "Correlation Between Shear Punch and Tensile Data for Neutron-Irradiated Aluminum Alloys," *Effects of Radiation on Materials: 17th International Symposium, ASTM STP 1270*, David S. Gelles, Randy K. Nanstad, Arvind S. Kumar and Edward A. Little, Eds., American Society for Testing and Materials, 1996, pp. 1057-1067.

[8] "Standard Test Methods for Tension Testing of Metallic Materials [Metric]," *1997 Annual Book of ASTM Standards*, Vol. 03.01, American Society for Testing and Materials, 1997, pp. 77-97.

Correlation of Nanoindentation and Conventional Mechanical Property Measurements -

Philip M. Rice (IBM Almaden Research Center) and Roger E. Stoller (Oak Ridge National Laboratory)

EXTENDED ABSTRACT

A series of model ferritic alloys and two commercial steels [1,2] were used to develop a correlation between conventional mechanical property measurements and nano-indentation hardness measurements. The NanoIndenter-II® [3] was used with loads as low as 0.05 g_f and the results were compared with conventional Vickers microhardness measurements using 200 and 500 g_f loads. When the nanohardness data were corrected to account for the difference between projected and actual indenter contact area, good correlation between the Vickers and nanohardness measurements was obtained for hardness values between 0.7 and 3 GPa. The relationship between Vickers and nanohardness measurements is shown in Figure 1.

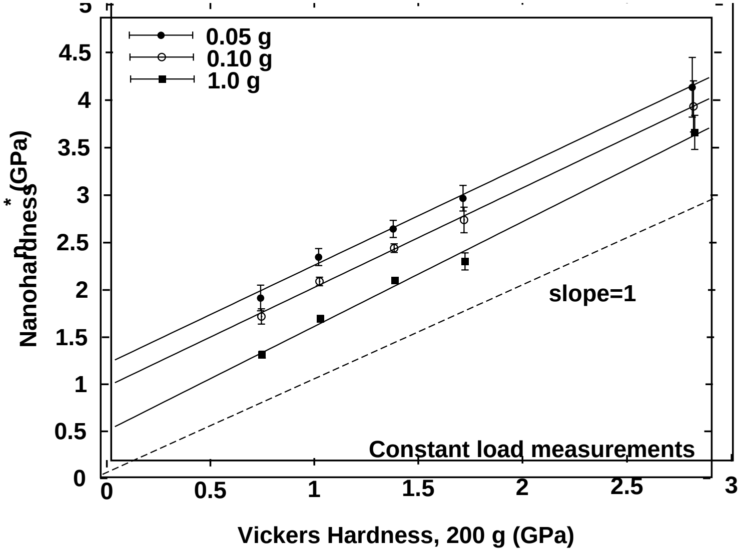

Figure 1. Comparison of 200-g_f Vickers hardness and constant-load nanohardness measurements

The nanohardness values show the well-known apparent increase in hardness with decreasing indent depth [4], which is responsible for the different zero-intercepts in Figure 1. The physical origin of the zero-offset in Figure 3 is not known, but the hardness changes are consistent for all the alloys. Thus, only the intercept, and not the slope of the ΔH_N vs. ΔH_V line changes and changes in hardness are well correlated. Overall, the slope of each line is within a few percent of the bottom dashed line which was drawn with a slope of 1.0. based on the average slope of the lines in Figure 1 and additional data, the following correlation is found between the two hardness measurements: $\Delta H_V/\Delta H_N$=0.937 GPa/GPa.

Tensile property measurements were made on these same alloys using 0.020 in.-thick sheet tensile samples. A linear correlation was found between the change in Vickers hardness and tensile yield strength in these ferritic and ferritic/martensitic steels with yield strengths in the range of 150 to 750 MPa. This correlation is shown in Figure 2. Using the available data, a correlation between nanohardness and tensile yield strength can be obtained in two ways. The first is derived from the linear relationships shown between Vickers hardness and yield strength in Figure 2 (slope=0.2836 MPa/MPa), and between nanohardness and Vickers hardness in Figure 1 (Eqn. (1)). The product of these slopes yields $\Delta H_N/\Delta\sigma_y$=266 GPa/MPa. Alternately, the tensile data can be plotted against the nanohardness data and the average slope obtained directly. In this case, the correlation obtained is (as it must be) nearly same:

$$\Delta\sigma_y\,[MPa] = 274\Delta H_N\,[GPa] \qquad (1)$$

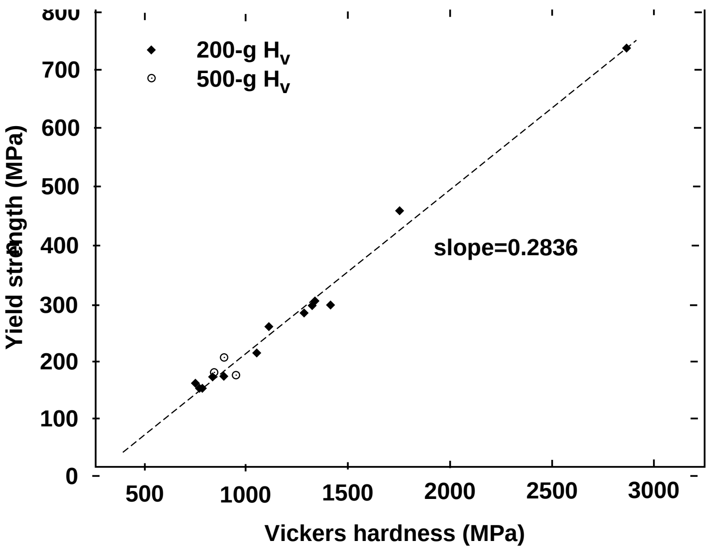

Figure 2. Comparison of yield strength and Vickers hardness for all materials in study.

The successful correlation of nanohardness measurements with bulk mechanical properties is significant not only because of the validation of the nanoindentation technique, but also because of its implications for ion irradiation studies. This validation supports the application of ion irradiations to simulate the effects of neutron irradiation, allowing studies to be carried out without the complications associated with testing radioactive specimens. For example, reliable estimates of mechanical property changes can be obtained for the high dose conditions reached at the end of fission reactor lifetimes. Similarly, the technique can be used to more rapidly screen alloys for irradiation performance and to investigate variables such as alloy composition or thermal-mechanical treatment. With the cross-section technique [1,2], is possible to use the nanoindenter to obtain data for a range of doses on a single specimen. In conjunction with TEM observation, changes in mechanical properties can be correlated with microstructural changes, and parameters such as the strength of microstructural obstacles preventing dislocation motion can be measured.

ACKNOWLEDGEMENTS

This research was also supported by the Division of Materials Sciences and Engineering, U.S. Department of Energy and the Office of Nuclear Regulatory Research, U.S. Nuclear Regulatory Commission under interagency agreement DOE 1886-N695-3W with the U.S. Department of Energy, under contract DE-AC05-00OR22725 with UT-Battelle, LLC., and by an appointment of P. M. Rice to the Oak Ridge National Laboratory Postdoctoral Research Associates Program administered jointly by the Oak Ridge National Laboratory and the Oak Ridge Institute for Science and Education. The authors thank Profs. G. R. Odette and G. E. Lucas of UCSB for providing the model alloys and R. D. Klingensmith of UCSB for tensile testing of the model alloys.

REFERENCES

[1] P. M. Rice and R. E. Stoller, Journal of Nuclear Materials **244** 219 (1997).
[2] P. M. Rice and R. E. Stoller, *Hardening Behavior of Ferritic Alloys at High Doses and After Thermal Aging*, NUREG/CR-6643 (ORNL/TM-1999/297), Oak Ridge National Laboratory, Oak Ridge, TN, April 2000.
[3] W.C. Oliver, and G.M. Pharr, Journal of Materials Research, **7** (6), 1564 (1992).
[4] J. B. Pethica, R. Hutchings, and W. C. Oliver, Philosophical Magazine A **48**, 593 (1983).

(extended abstract of paper to be published by Materials Research Society in proceedings of Symposium Q: Fundamentals of Nanoindentation and Nanotribology II, Fall MRS Meeting).

EFFECT OF PERIODIC TEMPERATURE VARIATIONS ON THE MICROSTRUCTURE OF NEUTRON-IRRADIATED METALS- S.J. Zinkle, N. Hashimoto, D.T. Hoelzer, A.L. Qualls (Oak Ridge National Laboratory) and T. Muroga (National Institute for Fusion Science)

OBJECTIVE

The objective of this report is to investigate the effect of periodic variations in irradiation temperature on the microstructural evolution of several structural materials.

SUMMARY

Specimens of pure copper, a high-purity austenitic stainless steel, and V-4Cr-4Ti were exposed to eight cycles of either constant temperature or periodic temperature variations during neutron irradiation in the High Flux Isotopes Reactor to a cumulative damage level of 4 to 5 displacements per atom. Specimens were exposed to a low temperature during the initial 10% of accrued dose in each of the eight cycles, and were exposed to a higher temperature during the remaining 90% of accrued dose in each cycle. Different specimens were exposed to low/high irradiation temperatures of 225/340˚C and 350/520˚C. The microstructure was compared with that of companion specimens that were continuously maintained at 340 ˚C and 520˚C, respectively during the entire irradiation. The low-temperature excursions produced enhanced nucleation and growth of radiation-induced defects (precipitates, dislocation loops) in V-4Cr-4Ti and stainless steel.

PROGRESS AND STATUS

INTRODUCTION

It is well known that the irradiation temperature can have a profound impact on the microstructure that develops in materials [1]. In qualitative terms, nucleation of defect clusters is maximized at lower temperatures whereas growth and coarsening of clusters are maximized at higher temperatures. Modest temperature excursions are expected to be a common occurrence in any commercial nuclear system due to scheduled startup and shutdown events. These varying-temperature excursions allow the possibility of enhanced nucleation and growth of radiation-induced defect clusters compared to a constant-temperature irradiation. Several previous ion irradiation and low-dose neutron irradiation studies [2-10] have found that these temperature excursions may exert a significant influence on the microstructural evolution, particularly if the temperature excursion transcends the recovery Stage V temperature regime (which corresponds to thermal dissociation of small vacancy clusters). The recovery Stage V occurs at ~325˚C in austenitic stainless steel [11-13] and ~375˚C in V-4Cr-4Ti [14]. Void formation was generally enhanced and loop formation suppressed for the cyclic temperature irradiation [4] or preirradiation at low temperatures [2].

Several studies have investigated the effect of constant versus varying temperature on the microstructure of irradiated austenitic stainless steel [4-6,8,15], vanadium [7,10], and vanadium alloys [7]. In some cases, rather spectacular differences were observed. For example, Yoshida and coworkers [5] observed that varying temperature (either 200/400˚C or 300/500˚C) neutron irradiation of Fe-16Cr-17Ni-0.25Ti austenitic stainless steel produced dramatically higher void swelling levels compared to constant temperature irradiation at 400˚C. Similarly, enhanced void nucleation has been observed in numerous binary vanadium alloys which were preirradiated at low temperature, compared to constant temperature irradiation [7]. Low temperature preirradiation has been observed to cause an enhancement in the defect cluster density in many cases [5,6], but in some cases either no effect [8] or a decrease in loop density [10] has been observed compared to the constant temperature irradiation condition.

In the present paper, results will be presented for V-4Cr-4Ti and stainless steel irradiated at 520˚C (constant temperature) vs. 350/520˚C (varying temperature), and for pure copper irradiated at a constant temperature of 340˚C. This irradiation experiment was performed as part of the JUPITER Japan-USA collaboration on fusion materials.

EXPERIMENTAL PROCEDURE

The materials used for this study were "P7" austenitic stainless steel (Fe-17Cr-16.7Ni-2.5Mo), V-4Cr-4Ti (Teledyne Wah Chang heat 832665), and Johnson-Matthey "Puratronic" 99.999% copper. All of the specimens were irradiated in the annealed condition as 3 mm diameter by 0.5 mm thick transmission electron microscope disks. The annealing conditions were 1050˚C for 0.5 h (stainless steel), 1000˚C for 2 h (V-4Cr-4Ti), and 550˚C for 2 h (Cu). The specimens were irradiated for a total of 8 irradiation cycles in the High Flux Isotopes Reactor at ORNL, which resulted in a fast neutron fluence (E>0.1 MeV) of ~8×10^{21} n/m^2. This corresponds to a damage level of ~4 dpa in the stainless steel and vanadium specimens, and ~5 dpa in copper. Electrical heaters and a mixture of helium and argon gases were used to control the irradiation temperatures. The temperatures were continuously monitored and controlled during the irradiation. The capsule was divided into four independently-controlled zones in order to achieve four different irradiation temperature profiles [16]. The temperature profiles for each of the 8 HFIR irradiation cycles were as follows: Zone A, constant temperature of 340˚C; Zone B, constant temperature of 520˚C; Zone C, first 10% of dose at 350˚C and remaining 90% at 520˚C; Zone D, first 10% of dose at 225˚C and remaining 90% at 340˚C. Further experimental details are described elsewhere [16]. Following irradiation, the TEM specimens were jet electropolished and examined in a JEOL 2000FX or Philips CM30 electron microscope.

RESULTS

The dominant microstructural feature in V-4Cr-4Ti irradiated at both a constant temperature of 520˚C and the variable (350/520˚C) condition was a high density of disk-shaped precipitates on {001} matrix habit planes. Figure 1 shows an example of the precipitates observed in V-4Cr-4Ti irradiated at a constant temperature of 520˚C. Void or dislocation loop formation was not observed in either specimen. A very low density of network dislocations was observed in both specimens.

The microstructure of V-4Cr-4Ti irradiated at constant (520˚C) vs. varying (350/520˚C) temperature was qualitatively similar. However, as shown in Fig. 2, the varying temperature irradiation produced precipitates of a finer size and higher density compared to the constant temperature irradiation condition. According to preliminary measurements, the constant temperature irradiation produced precipitates with a mean diameter of 24 nm and a density of ~4×10^{21}/m^3. The varying temperature irradiation produced precipitates with a mean diameter of 11 nm and a density of ~1.2×10^{22}/m^3. Additional quantitative measurements of the precipitate size and density are in progress.

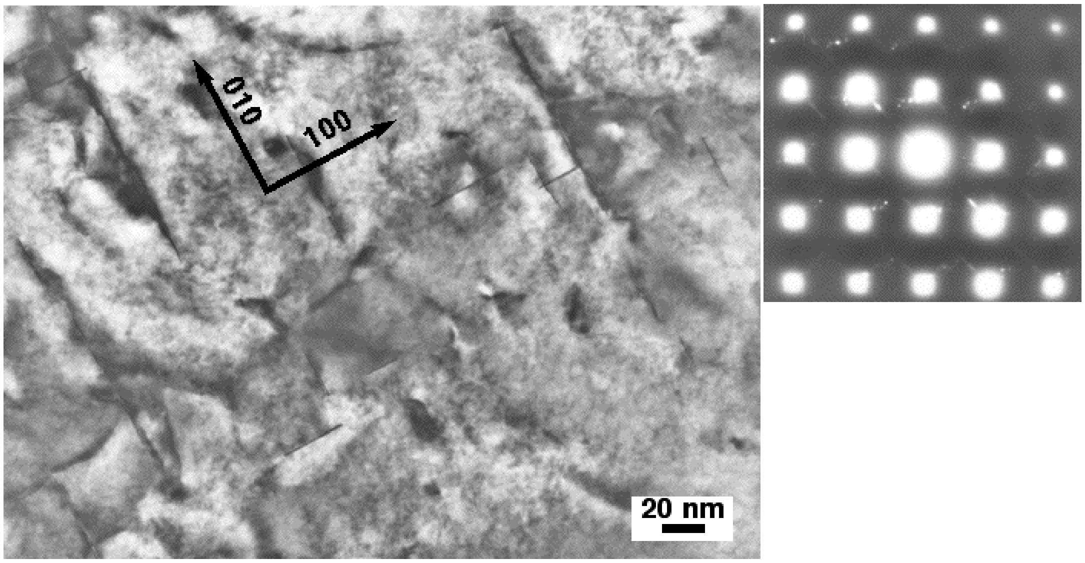

Fig. 1. Precipitates observed on {001} matrix habit planes in V-4Cr-4Ti irradiated to 4 dpa at 520˚C. Streaks associated with the precipitates are visible in the diffraction pattern.

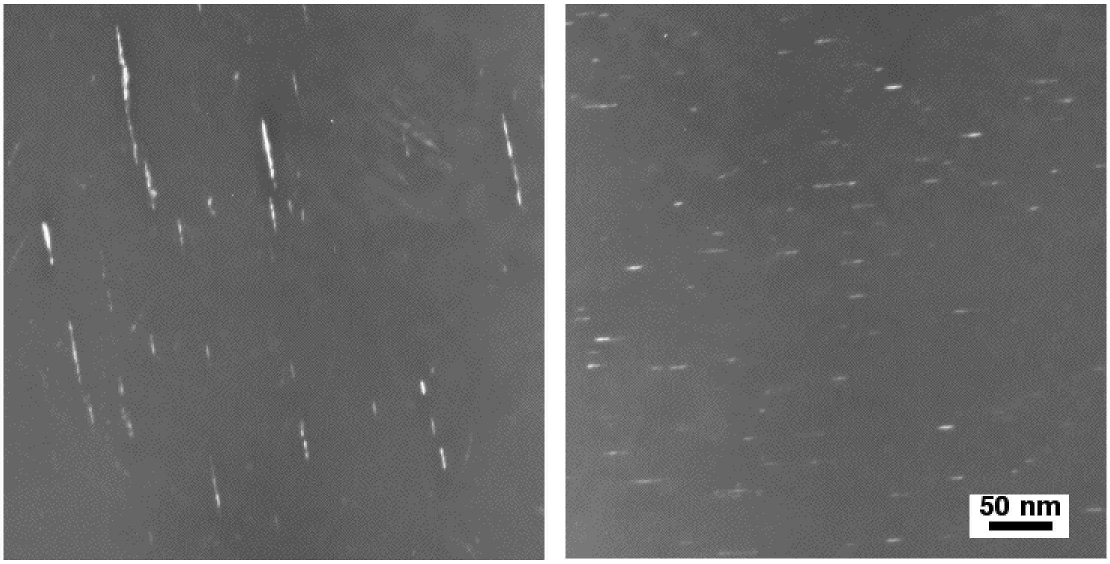

Fig. 2. Comparison of the precipitates observed in V-4Cr-4Ti irradiated to 4 dpa at 520˚C (left fig., constant temperature) vs. 350/520˚C (right fig., varying temperature). Centered dark field image.

A moderate density of small defect clusters (dislocation loops, stacking fault tetrahedra) and voids were produced in stainless steel during irradiation at either constant (520˚C) or varying (350/520˚C) irradiation conditions. The general microstructural features were qualitatively similar for the two irradiation conditions, although there were some quantitative differences. Figure 3 compares the general microstructure of stainless steel for the two irradiation conditions. The varying temperature irradiation produced enhanced growth of defect clusters compared to the constant irradiation condition. Although the defect cluster density was ~$3\times10^{21}/m^3$ for both irradiation conditions, the mean defect cluster diameter was significantly larger for the varying temperature condition (6 nm) compared to the constant temperature condition (2.5 nm).

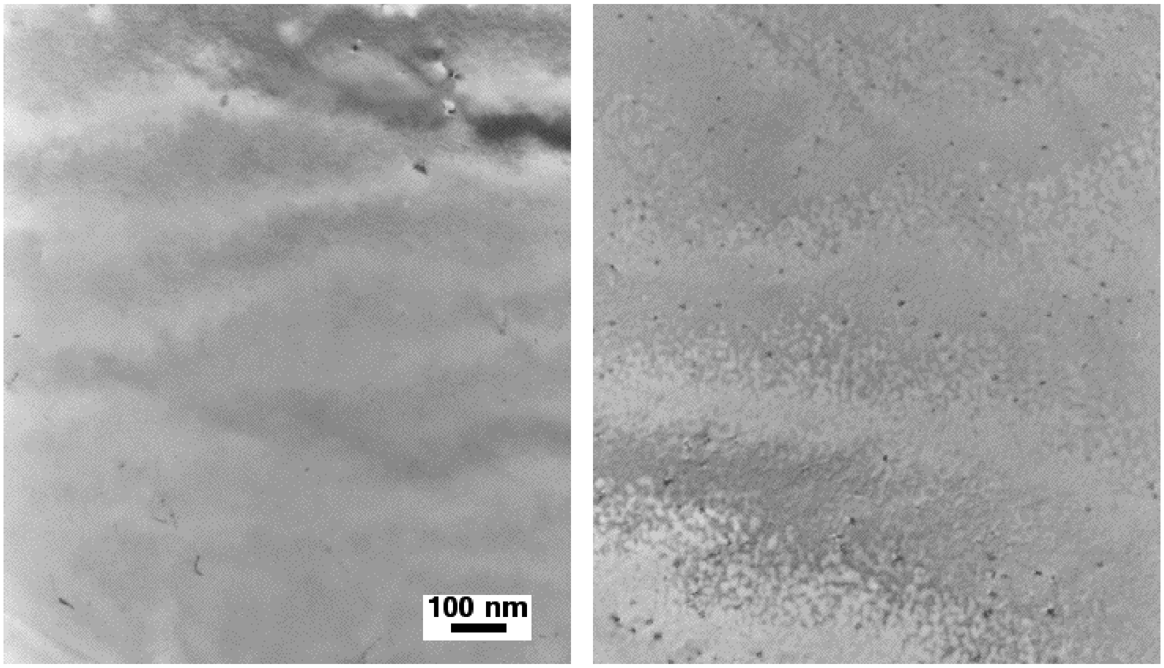

Fig. 3. Comparison of the defect clusters observed in stainless steel irradiated to 4 dpa at 520˚C (left fig., constant temperature) vs. 350/520˚C (right fig., varying temperature).

As shown in Fig. 4, a low density of small cavities was observed in stainless steel for both irradiation conditions. Although the number density appeared to be slightly higher for the varying temperature condition, the amount of void swelling was very small (<0.01%) for both conditions. Higher dose irradiations would be needed to examine the possibility of significant differences in the void swelling behavior for constant vs. varying temperature irradiation conditions.

Irradiation of pure copper at a constant temperature of 340˚C produced a large amount of cavity swelling. The mean void diameter and density were 80 nm and $8x10^{19}/m^3$, which yields a volume swelling of ~2.2%. The void density is about a factor of two larger than previously reported for copper irradiated to ~1 dpa at a constant temperature of 350˚C [17,18]. There was no evidence for crystallographic ordering of the cavities in the present study. A very low density of small stacking fault tetrahedra was also observed. Figure 5 shows an example of cavity formation adjacent to a grain boundary. The width of the zone denuded of cavities adjacent to the grain boundaries was ~0.45 µm. The slightly higher cavity density and smaller grain boundary denuded zone width in the present study compared to previous constant temperature irradiation studies at 350 ˚C [17,18] may be in part attributable to the lower irradiation temperature and higher damage rate in this study.

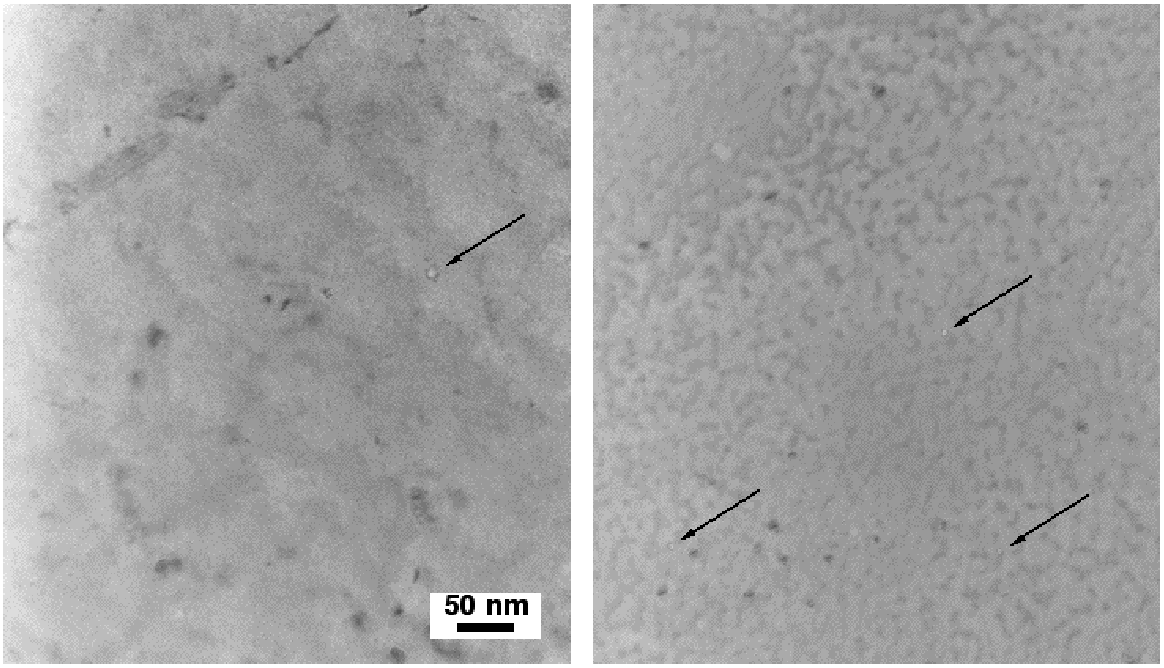

Fig. 4. Examples of the small cavities observed in stainless steel irradiated to 4 dpa at 520˚C (left fig., constant temperature) vs. 350/520˚C (right fig., varying temperature).

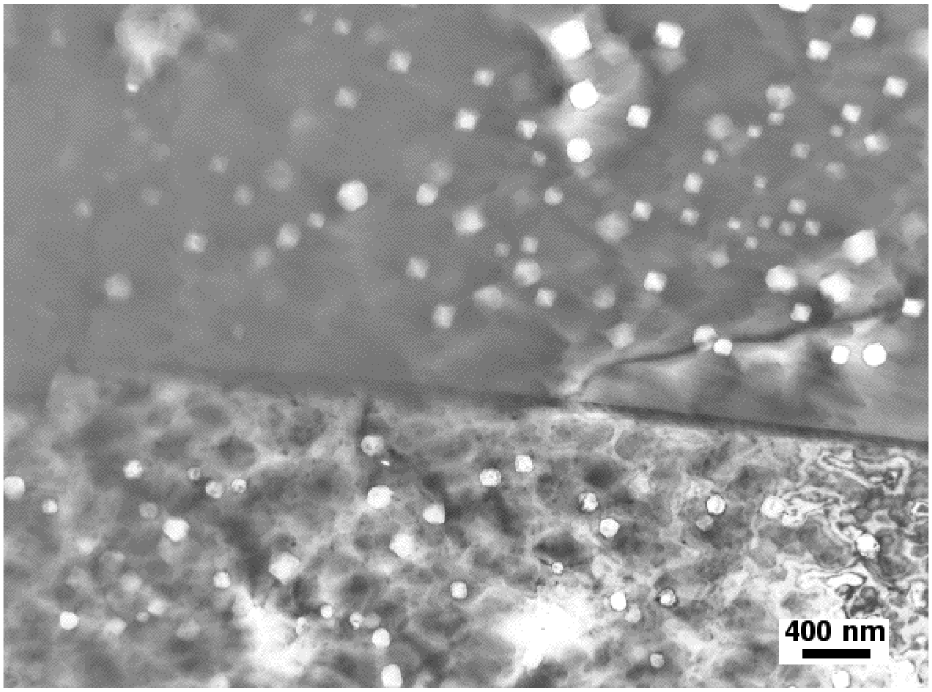

Fig. 5. Cavity swelling adjacent to a grain boundary in copper irradiated to 5 dpa at 340˚C

DISCUSSION

Qualitatively similar microstructures were observed in V-4Cr-4Ti and stainless steel for the constant and varying temperature irradiation conditions investigated in this study. In quantitative terms, the varying temperature irradiation generated a higher density of smaller precipitates in V-4Cr-4Ti and a larger average defect cluster size in stainless steel. The precipitate density observed for V-4Cr-4Ti ($4\text{x}10^{21}$ and $12\text{x}10^{21}/\text{m}^3$) was slightly higher than that observed in the same alloy heat following a constant temperature neutron irradiation to 0.1 dpa at 505˚C ($2.6\text{x}10^{21}/\text{m}^3$) [14].

CONCLUSIONS

Low temperature excursions can produce enhanced nucleation and growth of radiation-induced defects (precipitates, dislocation loops) in V-4Cr-4Ti and stainless steel. The quantitative effect of low-temperature excursions was relatively small for the materials and conditions investigated in the present study (8 cycles of varying 350/520˚C temperature vs. constant 520˚C temperature, with 0.05 dpa at the lower temperature and 0.45 dpa at the higher temperature for each cycle). Further analysis is needed to investigate the quantitative influence of varying temperatures under other irradiation conditions (different temperatures, different doses at low temperature, etc.).

Acknowledgements

This research was supported by the Japan/US collaborative JUPITER program on fusion materials research and sponsored in part by the Office of Fusion Energy Sciences, U.S. Department of Energy under contract DE-AC05-00OR22725 with UT-Battelle, LLC.

REFERENCES

1. M. Kiritani, J. Nucl. Mater. **160**, 135 (1988).
2. M. Kiritani, T. Yoshiie, S. Kojima, Y. Satoh, and K. Hamada, J. Nucl. Mater. **174**, 327 (1990).
3. M. Kiritani, T. Endoh, K. Hamada et al., J. Nucl. Mater. **179-181**, 1104 (1991).
4. M. Kiritani, T. Yoshiie, M. Iseki et al., J. Nucl. Mater. **212-215**, 241 (1994).
5. N. Yoshida, Q. Xu, H. Watanabe, Y. Miyamoto, and T. Muroga, J. Nucl. Mater. **212-215**, 471 (1994).
6. Q. Xu, H. Watanabe, T. Muroga, and N. Yoshida, J. Nucl. Mater. **212-215**, 258 (1994).
7. H. Matsui, K. Kuji, M. Hasegawa, and A. Kimura, J. Nucl. Mater. **212-215**, 784 (1994).
8. Q. Xu, H. Watanabe, and N. Yoshida, J. Nucl. Mater. **233-237**, 1057 (1996).
9. T. Muroga, S. Ohnuki, F.A. Garner, and S.J. Zinkle, J. Nucl. Mater. **258-263**, 130 (1998).
10. K. Ochiai, H. Watanabe, T. Muroga, N. Yoshida, and H. Matsui, J. Nucl. Mater. **271-272**, 376 (1998).
11. N. Yoshida, Q. Xu, H. Watanabe, T. Muroga, and M. Kiritani, J. Nucl. Mater. **191-194**, 1114 (1992).
12. S.J. Zinkle, P.J. Maziasz, and R.E. Stoller, J. Nucl. Mater. **206**, 266 (1993).
13. M. Horiki and M. Kiritani, J. Nucl. Mater. **239**, 34 (1996).
14. P.M. Rice and S.J. Zinkle, J. Nucl. Mater. **258-263**, 1414 (1998).
15. D.J. Mazey, T.M. Williams, and D.E.J. Bolster, J. Nucl. Mater. **154**, 186 (1988).
16. A.L. Qualls and T. Muroga, in *Fusion Materials Semiannual Progress Report for Period ending June 30, 2000, DOE/ER-0313/28*, (Oak Ridge National Lab, 2000), p. 266.
17. S.J. Zinkle and K. Farrell, J. Nucl. Mater. **168**, 262 (1989).
18. S.J. Zinkle, K. Farrell, and H. Kanazawa, J. Nucl. Mater. **168**, 262 (1991).

10.0 DOSIMETRY, DAMAGE PARAMETERS, AND ACTIVATION CALCULATIONS

No contributions.

11.0 MATERIALS ENGINEERING AND DESIGN REQUIREMENTS

No contributions.

12.0 IRRADIATION FACILITIES AND TEST MATRICES

No contributions.